Université Lille Nord de France

Université de Lille 1 Sciences et Technologies

POLYTECH LILLE

Laboratoire Mécanique Lille

Order Number: ....

lbl-institute **Université Lille 1 - Sciences et Technologies**

Doctoral School **ED Régionale SPI 72**

University Department **Laboratoire de Mécanique de Lille (LML)**

Thesis defended by **Anselmo Soeiro Pereira**

Defended on **29th November, 2016**

In order to become Doctor from Université Lille 1 - Sciences et Technologies

Academic Field **Mécanique**

Speciality **Mécanique des Fluides**

Thesis Title

Transient aspects of the polymer induced drag reduction phenomenon

Thesis supervised by	Prof. Gilmar Mompean	Supervisor
	MCF Laurent Thais	Co-Supervisor

Committee members

Referees	Prof. Francisco Chinesta	Ecole Centrale de Nantes
	Prof. Fernando Pinho	Université de Porto
Examiners	Dr. Isabelle Hénaut	IFP Energies nouvelles
	Dr. Rudy Valette	École Nationale Supérieure des Mines de Paris
Supervisors	Prof. Gilmar Mompean	Université Lille 1 - Polytech-Lille
	MCF Laurent Thais	Université Lille 1 - Polytech-Lille

lbl-institute **Université Lille 1 - Sciences et Technologies**

Doctoral School **ED Régionale SPI 72**

University Department **Laboratoire de Mécanique de Lille (LML)**

Thesis defended by **Anselmo Soeiro Pereira**

Defended on **29th November, 2016**

In order to become Doctor from Université Lille 1 - Sciences et Technologies

Academic Field **Mécanique**

Speciality **Mécanique des Fluides**

Thesis Title

Transient aspects of the polymer induced drag reduction phenomenon

Thesis supervised by

Prof. Gilmar Mompean	Supervisor
MCF Laurent Thais	Co-Supervisor

Committee members

Referees	Prof. Francisco Chinesta	Ecole Centrale de Nantes
	Prof. Fernando Pinho	Université de Porto
Examiners	Dr. Isabelle Hénaut	IFP Energies nouvelles
	Dr. Rudy Valette	École Nationale Supérieure des Mines de Paris
Supervisors	Prof. Gilmar Mompean	Université Lille 1 - Polytech-Lille
	MCF Laurent Thais	Université Lille 1 - Polytech-Lille

lbl-institute **Université Lille 1 - Sciences et Technologies**

École doctorale **ED Régionale SPI 72**

Unité de recherche **Laboratoire de Mécanique de Lille (LML)**

Thèse présentée par **Anselmo Soeiro Pereira**

Soutenue le **29 novembre 2016**

En vue de l'obtention du grade de docteur de l'Université Lille 1 - Sciences et Technologies

Discipline **Mechanics**

Spécialité **Fluids Mechanics**

Titre de la thèse

Des aspects transitoires du phénomène de réduction de la traînée induite par des polymères

Thèse dirigée par	Prof. Gilmar Mompean	Directeur
	MCF Laurent Thais	co-directeur

Composition du jury

Rapporteurs	Prof. Francisco Chinesta	Ecole Centrale de Nantes
	Prof. Fernando Pinho	Université de Porto
Examinateurs	Dr. Isabelle Hénaut	IFP Energies nouvelles
	Dr. Rudy Valette	École Nationale Supérieure des Mines de Paris
Directeurs de thèse	Prof. Gilmar Mompean	Université Lille 1 - Polytech-Lille
	MCF Laurent Thais	Université Lille 1 - Polytech-Lille

Keywords: direct numerical simulation, turbulent flow, fene-p model, drag reduction, transitory aspects, polymer degradation.

Mots clés : simulation numérique directe, écoulement turbulent, modèle fene-p, réduction de la traînée, aspects transitoires, dégradation du polymère.

This thesis has been prepared at

Laboratoire de Mécanique de Lille (LML)
Av. Paul Langevin
Cité Scientifique
59650 Villeneuve d'Ascq
France

☎ (33)(0)3 20 33 71 52
(33)(0)3 20 33 71 53
lml@univ-lille1.fr
Web Site http://lml.univ-lille1.fr/

À celle dont l'amour et l'amitié m'accompagnent, ma chère épouse, Camila.

Esse negócio de entender de uma coisa, tem que amar. Quando você ama, isso cria uma capacidade. Você se interessa pela coisa, você começa a olhar.

Tom Jobim

J'ai toujours préféré la folie des passions à la sagesse de l'indifférence.

Anatole France (Le Crime de Sylvestre Bonnard)

If his chest had been a mortar, he burst his hot heart's shell upon it.

Herman Melville (Moby Dick)

Remerciements

Le travail présenté dans cette thèse a été réalisé au sein de l'École Polytechnique Universitaire de Lille et du Laboratoire de Mécanique de Lille (LML). Je tiens donc tout d'abord à remercier l'ensemble du personnel enseignant et administratif pour leur accueil et leur convivialité.

Je remercie particulièrement Monsieur Gilmar MOMPEAN, professeur à l'École Polytechnique Universitaire de Lille, pour sa direction scientifique et ses précieuses remarques qui ont permis l'aboutissement de ce travail ainsi que pour l'amitié que nous avons développée tout au long de ces quatre dernières années. Je tiens également à remercier Monsieur Laurent THAIS, maître de conférences à l'École Polytechnique Universitaire de Lille, pour sa disponibilité, son aide et les connaissances scientifiques qu'il a apportées à cette recherche.

Je tiens également à exprimer ma gratitude au Conseil National pour le Développent Scientifique (CNPq) du Brésil pour le soutien financier de cette recherche au travers du Programme Science sans Frontières.

Cette thèse a bénéficié d'un accès aux moyens de calcul de l'Institut du Développement et des Ressources en Informatique Scientifique (IDRIS) au travers des allocations de ressources i2014b2277 et i20162a2277. Je tiens donc à remercier le personnel de l'IDRIS pour leur disponibilité à la réalisation de ce travail.

Je remercie vivement Monsieur Edson José SOARES, professeur à l'Université Fédérale de l'Espírito Santo, ainsi que Monsieur Roney Leon THOMPSON, professeur à l'Université Fédérale de Rio de Janeiro, des chercheurs remarquables et des amis très chers avec qui j'ai partagé des moments inoubliables tout au long de mon parcours scientifique et sans qui cette thèse n'aurait pas été la même.

J'adresse un remerciement tout particulier à Messieurs Francisco CHINESTA et Fernando PINHO de m'avoir fait l'honneur d'être rapporteurs de cette thèse, ainsi qu'à Madame Isabelle Hénaut et Monsieur Rudy VALETTE pour avoir accepté de faire partie du jury.

Je voudrais aussi exprimer ma gratitude éternelle à ma chère épouse, Camila, d'être compréhensive, tolérante et courageuse, une compagne formidable.

Un grand merci à mes parents, Anselmo et Euzimar, et à ma famille au Brésil, pour m'avoir toujours soutenu et supporté durant le déroulement de cette recherche. Je remercie également à ceux qui représentent pour moi ma famille française, Anne-Marie LEROY, Jean-Pierre LEROY, Emmanuelle LEROY, Sandro DECOTTIGNIES CERQUEIRA et ma filleule, la petite Béatrice Rosita Marie CERQUEIRA. Je tiens enfin à remercier à tous les doctorants, ici représentés par Ramon MARTINS, avec qui j'ai pu partager de bons moments pendant l'élaboration de cette thèse.

Transient aspects of the polymer induced drag reduction phenomenon

Abstract

The addition of a small amount of polymers of high molecular weight can lead to a pressure drop decrease in turbulent flows. Over the years, numerous experimental and numerical studies have been conducted in attempts to make practical use of polymer-induced drag reduction, including long-distance transport of liquids, oil well operations, firefighting, transport of suspensions and slurries, and biomedical applications. The polymers successively stretch and coil by interacting with the turbulent structures, which changes the turbulent flow and further imposes a transient behaviour on the drag reduction (DR) as well as the subsequent mechanical polymer degradation. As a result, DR undergoes at least three stages over time: A, B, and C. In stage A, referred to as the *developing time*, DR departs from zero and assumes negative values due to a significant polymer stretching at the beginning of the process, which requires energy from the flow. After the minimum DR is reached, the polymers start their coil-stretch cycle and, in consequence, DR increases in response to the development of turbulent structures, achieving a maximum value, which makes for the beginning of stage B. However, during their coil-stretch cycle, polymers can be mechanically degraded as a result of an intense polymer stretching, which reduces their ability to act as energy exchange agents. Hence, when polymer degradation becomes pronounced, DR decreases until achieving a final value which indicates that the degradation has stopped and the molecular weight distribution has reached a steady state. The polymer degradation process characterizes the stage C. In the present work, numerical analyses are conducted aiming to investigate the stages A, B and C. The transient aspects of the polymer induced drag reduction phenomenon are explored with the aid of direct numerical simulations of turbulent plane Poiseulle and Couette flows of viscoelastic FENE-P fluids taking into account a wide range of Reynolds number, Weissenberg number and maximum polymer molecule extensibility. Stages A and B are carefully studied from tensor, statistical, energy budget and spectral perspectives. Additionally, a new and simple polymer scission model based on the molecule strain level is developed in order to numerically reproduce the stage C. It is found that the significant transient behaviour of DR within stage A is related to important exchanges of energy between the polymers, the mean flow and the turbulent structures, which is accentuated as the elasticity increases. In stage B, the dynamics of the flow is described by an autonomous regeneration cycle. The effects of polymers on such a cycle are attenuated by the molecules degradation during the stage C.

Keywords: direct numerical simulation, turbulent flow, fene-p model, drag reduction, transitory aspects, polymer degradation.

Laboratoire de Mécanique de Lille (LML)
Av. Paul Langevin – Cité Scientifique – 59650 Villeneuve d'Ascq – France

Des aspects transitoires du phénomène de réduction de la traînée induite par des polymères

Résumé

La dilution en très faible concentration de chaînes polymériques longues dans un fluide newtonien peut réduire considérablement la traînée turbulente, phénomène nommé ici DR (*drag reduction*). Au cours des dernières années, de nombreuses études expérimentales et numériques ont été menées motivées par les applications pratiques de la DR, à savoir le transport à grandes distances des liquides par pipelines, le transport des boues et des suspensions et des applications médicales. Les polymères s'étirent et s'enroulent successivement, en interaction avec les structures turbulentes, ce qui modifie l'écoulement turbulent, imposant à DR un comportement transitoire et provoquant la dégradation polymérique. Il en résulte que la DR traverse au moins trois stades. Lors du premier, connu sous le nom de temps de développement, la DR démarre à zéro et descend à des valeurs négatives en raison d'un étirement considérable du polymère au début du processus, ce qui exige de l'énergie de l'écoulement. Une fois atteint le niveau minimal de réduction de la traînée, les polymères commencent leur cycle d'étirement-enroulement et, par conséquent, la DR augmente en réponse au développement de structures turbulentes, pour en arriver à une valeur maximale, menant au début du deuxième stade. Cependant, lors de leur cycle d'étirement-enroulement, les polymères peuvent subir une dégradation mécanique à la suite d'un étirement polymérique intense, ce qui réduit leurs capacités de servir d'agents d'échange d'énergie. Lorsque la dégradation polymérique devient assez prononcée, la DR redescend pour atteindre une valeur finale qui indique que la dégradation s'est arrêtée et que la distribution de la masse moléculaire s'est stabilisée. Le processus de dégradation polymérique caractérise le troisième stade. Dans le présent travail, des analyses numériques ont été menées dans le but d'examiner ces trois stades. Les aspects transitoires du phénomène de réduction de la traînée induite par des polymères sont explorés à l'aide de simulations numériques directes d'écoulements turbulents viscoélastiques FENE-P en géométries du type Poiseuille plan et Couette plan, sur un large éventail de nombres de Reynolds, de nombres de Weissenberg et d'extension maximale de la chaîne polymérique. Les deux premiers stades sont soigneusement étudiés à partir des analyses tensorielle, statistique, énergétique et spectrale. De surcroît, un nouveau modèle de dégradation polymérique basé sur le niveau d'étirement des molécules est proposé afin de reproduire numériquement le stade final. Il a été constaté que le comportement transitoire significatif de la DR lors du premier stade est lié à d'importants échanges d'énergie entre les polymères, l'écoulement moyen et les structures turbulentes, s'intensifiant à mesure que l'élasticité augmente. Lors du deuxième stade, la dynamique de l'écoulement est décrite par un cycle de régénération autonome. Les effets des polymères sur ce cycle s'atténuent par la dégradation moléculaire qui survient lors du troisième stade.

Mots clés : simulation numérique directe, écoulement turbulent, modèle fene-p, réduction de la traînée, aspects transitoires, dégradation du polymère.

Sommaire

List of Tables

List of Figures

Nomenclature

Act	active regime
DR	drag reduction
Hib	hibernating regime
MKE	mean kinetic energy
TKE	turbulent kinetic energy

β_0	viscosity ratio
Δ_x^+	grid resolution (in wall units) in x
Δ_y^+	grid resolution (in wall units) in y
$\Delta_{z,min}^+$	minimum grid resolution (in wall units) in z
$\Delta_{z,max}^+$	maximum grid resolution (in wall units) in z
δ_{ij}	Kronecker's delta
κ	von Kármán coefficient (log-law)
λ	elastic relaxation time [s]
ν_{tot}	total (solvent + polymer) zero-shear kinematic viscosity $[m^2/s]$
ν_N	solvent kinematic viscosity $[m^2/s]$
ν_{p0}	polymer kinematic viscosity $[m^2/s]$
$\boldsymbol{\Xi}^+$	instantaneous extra-stress tensor in wall units
Ξ_{ij}^+	components of the instantaneous extra-stress tensor in wall units
$\overline{\boldsymbol{\Xi}^+}$	time-averaged extra-stress tensor in wall units
$\overline{\Xi_{ij}^+}$	components of the time-averaged extra-stress tensor in wall units
$\boldsymbol{\Xi}'^+$	fluctuation of the extra-stress tensor in wall units
Φ	angle between the principal directions of two tensors
${\Xi'_{ij}}^+$	fluctuation of the components of the extra-stress tensor in wall units
ρ	density $[Kg/m^3]$
τ_w	wall shear stress (solution) $[N/m^2]$
$\tau_{w,N}$	wall shear stress (solvent) $[N/m^2]$
τ_{ij}^+	time average of the fluctuation velocity products $\tau_{ij}^+ = \overline{u'_i u'_j}^+$
$\boldsymbol{\omega}$	instantaneous vorticity vector
ω_i	component of the instantaneous vorticity vector in the i direction
ω_i'	component of the fluctuating vorticity vector in the i direction
$\nabla \boldsymbol{u}$	velocity gradient tensor $[1/s]$
$\nabla \boldsymbol{u}^+$	velocity gradient tensor in wall units

A	amplitude coefficient (perturbation)
A_1	intercept (log-law)
$\boldsymbol{C}$	instantaneous conformation tensor
C_{ij}	components of the instantaneous conformation tensor
$\overline{\boldsymbol{C}}$	time-averaged conformation tensor
$\overline{C_{ij}}$	components of the time-averaged conformation tensor
$\boldsymbol{C'}$	conformation tensor fluctuation
$\overline{C'_{ij}}$	components of the fluctuating conformation tensor
DR	drag reduction level
DR_{min}	minimum value of DR
DR_{max}	maximum value of DR
$\boldsymbol{e_x}$	unit vector in the streamwise direction
$\boldsymbol{e_y}$	unit vector in the spanwise direction
$\boldsymbol{e_z}$	unit vector in the wall-normal direction
f	Peterlin function
h	channel-half height [m]
L	maximum polymer molecule extensibility
Lx, Ly and Lz	channel extent in x, y and z, respectively [m]
Nx	number of mesh points in streamwise direction
Ny	number of mesh points in spanwise direction
Nz	number of mesh points in wall-normal direction
Q	Q-criterion
Q_{norm}	normalized Q-criterion
$\boldsymbol{\tau'}$	instantaneous Reynolds stress tensor
$Re_{\tau 0}$	zero shear friction Reynolds number
Re_h	Reynolds number based on the plate velocities
$\boldsymbol{S}$	rate-of-strain tensor [$1/s$]
S_{ij}	components of the rate-of-strain tensor [$1/s$]
$\boldsymbol{S}^+$	rate-of-strain tensor in wall units
S^+_{ij}	components of the rate-of-strain tensor in wall units
t_d	developing time [s]
t_r	resistance time [s]
p^+	instantaneous pressure in wall units
$\overline{P}^+$	time-averaged pressure in wall units
p'^+	pressure fluctuation in wall units
Sc_c	Schmidt number
U_h	streamwise velocity of the top and the bottom plates [m/s]
u_τ	zero-shear friction velocity [m/s]
u_x and u_1	instantaneous streamwise velocity [m/s]
u_y and u_2	instantaneous spanwise velocity [m/s]
u_z and u_3	instantaneous wall-normal velocity [m/s]
$\overline{U_x}$	time-averaged streamwise velocity [m/s]
$\overline{U_y}$	time-averaged spanwise velocity [m/s]
$\overline{U_z}$	time-averaged wall-normal velocity [m/s]
u'_x	streamwise velocity fluctuation [m/s]
u'_y	spanwise velocity fluctuation [m/s]
u'_z	wall-normal velocity fluctuation [m/s]
u^+_{rx}	instantaneous relative streamwise velocity in wall units

u_x^+ and u_1^+	instantaneous streamwise velocity in wall units
u_y^+ and u_2^+	instantaneous spanwise velocity in wall units
u_z^+ and u_3^+	instantaneous wall-normal velocity in wall units
$\overline{U_{rx}}^+$	time-averaged relative streamwise velocity in wall units
$\overline{U_x}^+$	time-averaged streamwise velocity in wall units
$\overline{U_y}^+$	time-averaged spanwise velocity in wall units
$\overline{U_z}^+$	time-averaged wall-normal velocity in wall units
$u_x'^+$	streamwise velocity fluctuation in wall units
$u_y'^+$	spanwise velocity fluctuation in wall units
$u_z'^+$	wall-normal velocity fluctuation in wall units
$\boldsymbol{W}$	rate-of-rotation tensor $[1/s]$
W_{ij}	components of the rate-of-rotation tensor $[1/s]$
$\boldsymbol{W}^+$	rate-of-rotation tensor in wall units
W_{ij}^+	components of the rate-of-rotation tensor in wall units
$Wi_{\tau 0}$	friction Weissenberg number
Wi_h	Weissenberg number
x_1 and x	channel streamwise direction $[m]$
x_2 and y	channel spanwise direction $[m]$
x_3 and z	channel wall-normal direction $[m]$
x_1^+ and x^+	channel streamwise direction in wall units
x_2^+ and y^+	channel spanwise direction in wall units
x_3^+ and z^+	channel wall-normal direction in wall units
T_i^+	time derivative energy term (i direction)
A_i^+	instantaneous advection work (wall units) in the i direction
P_i^+	instantaneous pressure work (wall units) in the i direction
V_i^+	instantaneous viscous work (wall units) in the i direction
N_i^+	instantaneous Newtonian work (wall units) in the i direction
E_i^+	instantaneous polymer work (wall units) in the i direction
$T_i'^+$	fluctuations of the time derivative energy term (i direction)
$A_i'^+$	advection work fluctuation (wall units) in the i direction
$P_i'^+$	pressure work fluctuation (wall units) in the i direction
$V_i'^+$	viscous work fluctuation (wall units) in the i direction
$N_i'^+$	Newtonian work fluctuation (wall units) in the i direction
$E_i'^+$	polymer work fluctuation (wall units) in the i direction
$T_{m,i}^+$	average in time of T_i^+
$A_{m,i}^+$	time-averaged advection work (wall units) in the i direction
$P_{m,i}^+$	time-averaged pressure work (wall units) in the i direction
$V_{m,i}^+$	time-averaged viscous work (wall units) in the i direction
$N_{m,i}^+$	time-averaged Newtonian work (wall units) in the i direction
$E_{m,i}^+$	time-averaged polymer work (wall units) in the i direction
$T_{mm,i}^+$	part of $T_{m,i}^+$ related to the mean flow
$A_{mm,i}^+$	part of $A_{m,i}^+$ related to the mean flow
$P_{mm,i}^+$	part of $P_{m,i}^+$ related to the mean flow
$V_{mm,i}^+$	part of $V_{m,i}^+$ related to the mean flow
$N_{mm,i}^+$	part of $N_{m,i}^+$ related to the mean flow
$E_{mm,i}^+$	part of $E_{m,i}^+$ related to the mean flow

$T^+_{mt,i}$	part of $T^+_{m,i}$ related to the fluctuating fields
$A^+_{mt,i}$	part of $A^+_{m,i}$ related to the fluctuating fields
$P^+_{mt,i}$	part of $P^+_{m,i}$ related to the fluctuating fields
$V^+_{mt,i}$	part of $V^+_{m,i}$ related to the fluctuating fields
$N^+_{mt,i}$	part of $N^+_{m,i}$ related to the fluctuating fields
$E^+_{mt,i}$	part of $E^+_{m,i}$ related to the fluctuating fields
K_m	mean kinetic energy
$-P^+_m$	production of turbulent kinetic energy
$-P^+_{pm}$	production of mean polymeric energy
ϵ^+_m	dissipation rate of mean kinetic energy
$D^+_{m\nu}$	viscous diffusion of mean kinetic energy
D^+_{mP}	pressure transport of mean kinetic energy
D^+_{mt}	turbulent transport of mean kinetic energy
D^+_{pm}	mean polymeric transport of mean kinetic energy
K_t	turbulent kinetic energy
ϵ^+_t	dissipation rate of turbulent kinetic energy
$D^+_{t\nu}$	the viscous diffusion of turbulent kinetic energy
D^+_{tP}	pressure transport of turbulent kinetic energy
D^+_{mt}	turbulent transport of turbulent kinetic energy
P^+_{pt}	production of turbulent polymeric energy
D^+_{pt}	polymeric transport of turbulent kinetic energy
k_x	wavenumbers
$E_{1,1}$	1D spectra of turbulent kinetic energy

Chapter 1

Introduction

1.1 Motivation

Turbulence represents one of the most challenging subjects of physics. Such a flow regime dramatically increases in complexity when small amounts of polymers are diluted in Newtonian fluids, giving to the problem a viscoelastic character. These molecules induce an expressive drag reduction [28, 93, 61] whose practical uses include long-distance transport of liquids [80], oil well operations [15], firefighting [27], transport of suspensions and slurries [29], and biomedical applications [32]. In this context, [97] showed in a pioneering experimental work that if the friction drag for pipe flows is plotted in Prandtl–Kármán coordinates, it departs from the Prandtl–Kármán law (the onset of drag reduction) to its bound, the so-called maximum drag reduction (MDR) or Virk's asymptote, as a result of an increase in either the Reynolds number, the polymer concentration, or the polymer's molecular weight.

Over the years, researchers have successfully analysed relevant aspects of this phenomenon and a significant literature is available, e.g. [36, 98, 63, 96, 12, 13, 60, 33, 44]. However, up to now, there has been no definitive consensus concerning the interactions between the turbulent energy and the deformations of the polymer.

Phenomenological explanations for polymer drag reduction (DR) gravitate around two major theories. According to the viscous theory, independently proposed by Lumley [52] and Seyer and Metzner [81] and supported by Ryskin [79], polymer stretching in a turbulent flow produces an increase in the effective viscosity in a region outside of the viscous sublayer and in the buffer layer, which suppresses turbulent fluctuations, increasing the thickness of the buffer layer and reducing the wall friction. The elastic theory postulated by Tabor and de Gennes [84] assumes that the elastic energy stored by the polymer becomes comparable to the kinetic energy in the buffer layer. Since the corresponding viscoelastic length scale is larger than the Kolmogorov scale, the usual energy cascade is inhibited, which thickens the buffer layer and reduces the drag [see

also 43]. Numerically, polymer-induced drag reduction theories have been intensively investigated for over a decade since the first simulations conducted by Toonder et al. [94] and Orlandi [62], such as Sureshkumar et al. [83], Min et al. [59], L'vov et al. [53], de Angelis et al. [20], Dubief et al. [24], Benzi et al. [9], Dallas et al. [19], and Thais et al. [86].

Despite the discrepancies between the two most prominent theories, what seems to be in accordance with both scenarios is the relevance of the polymer-turbulence interactions, which further imposes a transient behaviour on the drag reduction [105] as well as a subsequent polymer degradation, a consequence of polymer elongation [58, 64, 82]. The relation between the polymer extension level and drag reduction was discussed by Dimitropoulos et al. [21] with the aid of direct numerical simulation (DNS) analysis to compute DR in a turbulent boundary layer flow of a FENE-P fluid. According to the authors, the development of polymer extension and streamwise vortices along the length of the plate is asynchronous. In other words, the turbulent structures take some time to rearrange following a high deformation at the very beginning of the process, which leads to a variation of DR level along the boundary. This numerical observation was recently experimentally confirmed in a series of works by Pereira and Soares [65], Pereira et al. [64] and Andrade et al. [2], who, using a rotating cylindrical double gap device, reported that DR undergoes, at least, three stages over time, as shown in Figure 1.1 where transient aspects of the polymer induced drag reduction phenomenon are illustrated. Initially, during the stage A, DR presents negative values due to an instantaneous increment of local extensional viscosity caused by a high and abrupt polymer stretching at the very beginning of the test, which requires enhanced energy input that comes from the flow. The molecules then start their coil-stretch cycle and DR, after reaching a minimum value, DR_{min}, increases in response to the development of turbulent structures, achieving a maximum value, denoted DR_{max}. The time to achieve DR_{max} is refereed as the *developing time*, t_d. Following t_d, DR_{max} is maintained for a period called *resistance time*, t_r (stage B). Finally, during the stage C, DR decreases as a result of polymer scissions, attaining a final and asymptotic value, a time during which the polymer degradation stops and the molecular weight distribution reaches a steady state.

The expressive transient behaviour described above is not predicted by the DR mechanisms proposed in the literature, which reveals that the DR phenomenon is not completely understood and many aspects of the problem remain unclear. Any attempt to completely elucidate polymer-induced drag reduction must consider, at least, four important issues: the mechanism of polymer coil–stretch; the development of turbulent structures in viscoelastic flows; the exchange of energy between the turbulence and the polymers; and the breaking of the polymer molecules. In the present dissertation, these four important points will be systematically analysed from a numerical standpoint.

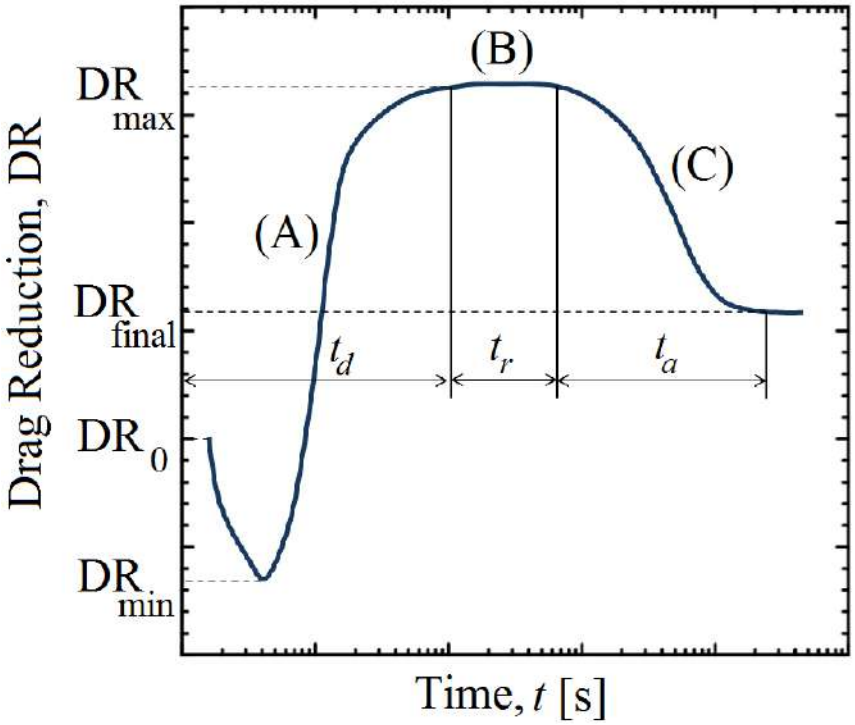

Figure 1.1 – Sketch of the polymer-induced drag reduction over time.

1.2 About this thesis

1.2.1 Objective

The DR curve illustrated in Figure 1.1 was never numerically reproduced since, up to now, there is no polymer degradation model available in the literature capable to take into account the molecule scissions in a turbulent viscoelastic flow scenario. In addition, the DR development from its very beginning was scarcely investigated. The majority of the papers concerning the drag reduction are, thus, restricted to the state B in Figure 1.1, neglecting very important transient aspects of the drag reduction mechanism.

The main objective underlying the present dissertation is to study the strong transient behaviour of the polymer induced drag reduction phenomenon by developing numerical methodologies which allow the complete reproduction of the blue curve displayed in Figure 1.1. In this sense, direct numerical simulations of turbulent flows of a viscoelastic FENE-P fluid are performed in order to investigate the development of turbulent structures in viscoelastic flows, the exchange of energy between the turbulence and the polymers, the mechanism of polymer coil–stretch, and the breaking of the polymer molecules. The latter point is analysed in the light of a new polymer scission methodology based on the molecule strain level.

1.2.2 Organization of the contents

The present thesis is a synopsis of publications prepared during the stay of the author at the *École Polytechnique Universitaire de Lille* (09/2012-09/2016). Most of the chapters in the present dissertation are transcriptions of published or submitted journal articles. Consequently, unavoidable redundancies exist between the introductory sections of some chapters, since these chapters consist of the text of journal articles under their original form.

The sequential organization of chapters follows the chronological order of development of this doctoral work through the pursuit of the understanding of DR. In order to help the reader to focus on the logical evolution of these researches, we summarize here the contents of this dissertation:

- Chapter 2: *The polymer coil–stretch mechanism in turbulent drag reducing flows* (Pereira et al. [67, 71])

  In this initial chapter, we use the DNS database produced by our Research Group between 2011 and 2013 [89, 87, 86, 88] to study the polymer coil–stretch process in turbulent plane Poiseuille flows of a viscoelastic FENE-P fluid taking into account a wide range of zero-shear friction Reynolds numbers (from 180 up to 1000). Tensorial and statistical analyses are developed. The flow is divided into two distinct regions, following the Q-criterion of flow classification [see 38]: an elliptical (or vortical) and a hyperbolic (or extensional) part. The polymer work fluctuation is then investigated within these regions, separately. The analyses that came out from these tools enable the proposition of a polymer coil–stretch mechanism (stage B in Figure 1.1).

- Chapter 3: *On the drag reducing plane Couette flows* (Pereira et al. [70])

  Aiming to analyse the drag reduction phenomenon in a flow scenario dominated by large-scale motions, in Chapter 3 we perform direction numerical simulations of turbulent plane Couette flows of viscoelastic FENE-P fluids. Such configuration is characterized by the presence of large-scale structures only observed in plane Poiseuille flows at high Reynolds numbers ($Re_{\tau 0} > 1000$; see also [75]). The results enable the addition of new details concerning the effects of the polymers on the autonomous regeneration cycle conceived for Newtonian flows by Jiménez and Pinelli [42], expanded to viscoelastic flows by Dubief et al. [24] and revisited in Chapter 2. The new DNS set of turbulent viscoelastic plane Couette flows is used in the following chapters.

- Chapter 4: *Transient aspects of the drag reducing plane Couette flows* (Pereira et al. [72])

This chapter is devoted to the evolution of DR over its developing time (stage A in Figure 1.1). We show that the initial interactions between the mean shear flow, turbulent structures, and molecules are the key to understanding the step-by-step evolution of the drag reduction phenomenon. The effects of elasticity on the developing time are also clarified.

- Chapter 5: *Elliptical, parabolic, and hyperbolic exchanges of energy in drag reducing plane Couette flows* (Pereira et al. [69]).

  In Chapter 5, we investigate the polymer-turbulence interactions within elliptical, parabolic and hyperbolic parts, separately, from a kinetic energy budget perspective. We have found that even more activity is located within the confines of the hyperbolic (extensional) structures when compared to what happens in the elliptical (vortical) ones, which highlights the importance of considering the role of hyperbolic domains on the drag reduction mechanism. In addition, we also show that the initial evolution of DR discussed in Chapter 4 is dramatically affected by the initial flow condition (velocity field).

- Chapter 6: *Active and hibernating turbulence in drag reducing plane Couette flows* (Pereira et al. [66])

  When the level of elasticity becomes pronounced, turbulent flows start to oscillate between the active and the hibernating regime [105] more frequently. The former regime is related to the basic dynamical elements of Newtonian near-wall turbulence, exhibiting a higher drag. In contrast, during the latter regime, the turbulent structures almost disappear, which reduced the drag. In Chapter 6 we show that the polymer-turbulence interactions in these two fundamental states are considerably different. Especially during the hibernating state, polymers act as an important source of turbulent energy, which can be an explanation for the MDR limit.

- Chapter 7: *Drag reducing flows considering the effects of polymer degradation* (Pereira et al. [68])

  Finally, in Chapter 7, we develop a new polymer degradation methodology based on the molecule strain level in order to numerically reproduced the molecular scission (stage C in Figure 1.1). The effects of polymer degradation on the drag reduction phenomenon are then evaluated.

1.3 General physical formulation and numerical methodology

In the present dissertation, two channel flow configurations are used: plane Poiseuille (Figure 1.2*a*) and plane Couette (Figure 1.2*b*). These flow configurations are commonly adopted in direct numerical simulations due their simplicity as well as their attractiveness for theoretical studies of near wall turbulent interactions. The former is certainly the most explored one in the drag reduction context. On the other hand, although DNS results of turbulent viscoelastic plane Couette flows are scarce in the DR literature, the plane Couette geometry represents a useful alternative to probe large-scale effects in wall-bounded flow since it is dominated by strong inner/outer layer interactions similar to those founded in high-Reynolds-number Poisseuile flows ($Re_{\tau 0} > 1000$; see also [75]).

The channel streamwise direction is $x_1 = x$, the spanwise direction is $x_2 = y$, and the wall-normal direction is $x_3 = z$. In the plane Poiseuille geometry, the flow between the two parallel stationary plates is induced by a constant streamwise pressure gradient, as illustrated in Figure 1.2(a). Nevertheless, the imposed pressure gradient is null in the plane Couette configuration and the flow is driven by both the top and the bottom plates, which have the same magnitude of velocity in the streamwise direction (U_h) but opposite senses, as indicated in Figure 1.2(b).

The instantaneous velocity field in the respective directions is $(u_x, u_y, u_z) = (u_1, u_2, u_3)$. In order to conduct a comparative analysis of the inner layer dynamics of the plane channel flow, wall scaling is used and based on zero-shear rate variables with the length and time scaled by ν_{tot}/u_τ and ν_{tot}/u_τ^2, where $\nu_{tot} = \nu_N + \nu_{p0}$ is the total (solvent + polymer) zero-shear viscosity, and u_τ is the zero-shear friction velocity. Using this scaling, the dimensionless conservation equations are

$$\frac{\partial u_j^+}{\partial x_j^+} = 0\,, \tag{1.1}$$

$$\frac{\partial u_i^+}{\partial t^+} + u_j^+ \frac{\partial u_i^+}{\partial x_j^+} = -\frac{\partial p^+}{\partial x_i^+} + \beta_0 \frac{\partial^2 u_i^+}{\partial x_j^{+\,2}} + \frac{\partial \Xi_{ij}^+}{\partial x_j^+}\,. \tag{1.2}$$

In Eq. 1.2, the superscript '+' indicates the wall unit normalization, p^+ is the pressure, β_0 is the ratio of the Newtonian solvent viscosity (ν_N) to the total zero-shear viscosity (ν_{tot}). The extra-stress tensor components are denoted by Ξ_{ij}^+. The formalism of Eq. 1.2 includes the assumption of a uniform polymer concentration which is governed by the viscosity ratio β_0, where $\beta_0 = 1$ yields the limiting behaviour of the Newtonian case.

The extra-stress tensor components (Ξ_{ij}^+) in Eq. 1.2 represent the polymer's contribution to the tension of the solution. This contribution is accounted for by a single spring-dumbbell model. We employ here the FENE-P kinetic theory [14], which is the

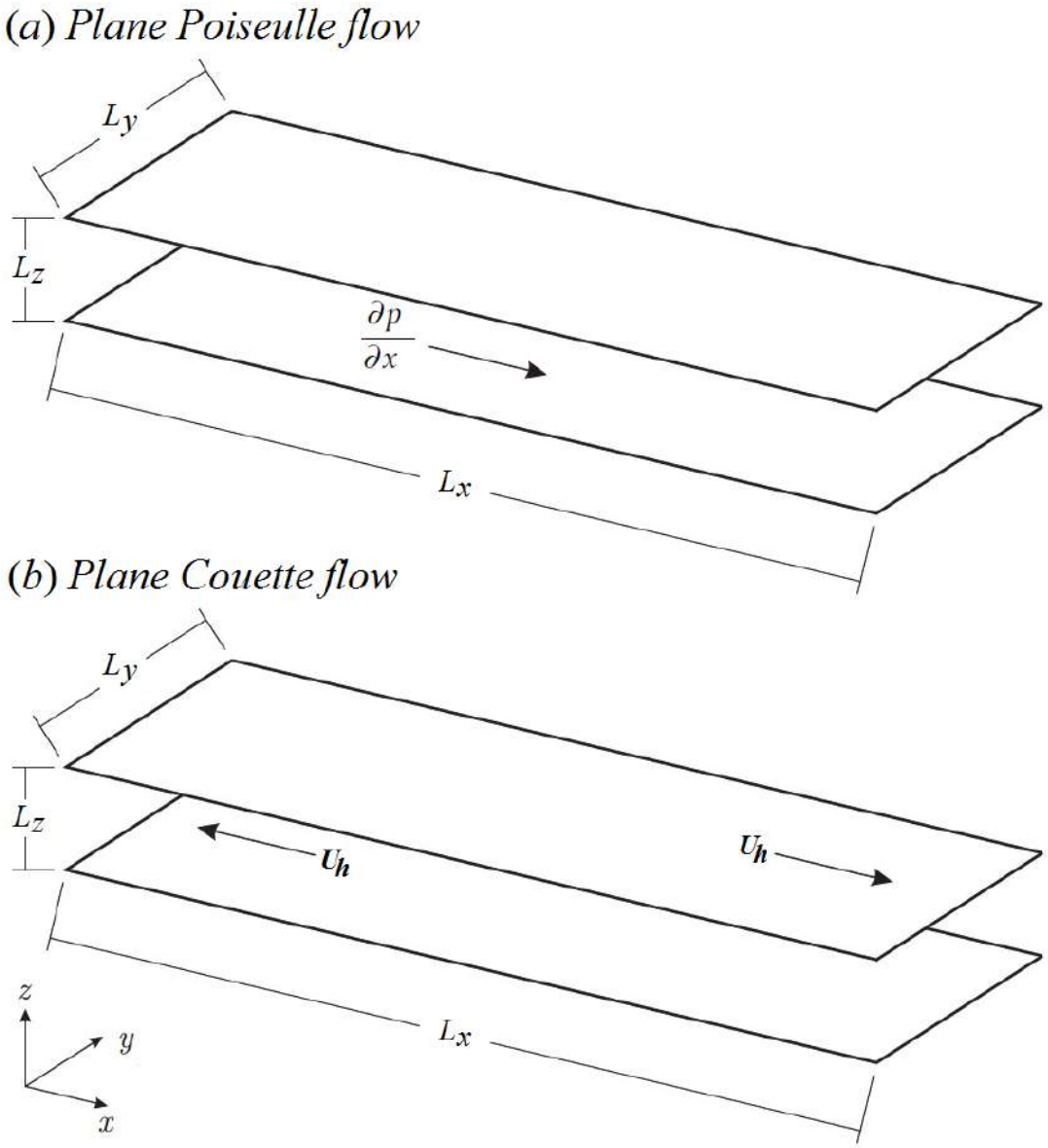

Figure 1.2 – Geometries of the plane Poisseuille (*a*) and Couette (*b*) flows with coordinate system.

most preferred one due to its physically realistic finite extensibility of the polymer molecules and to its relatively simple second-order closure. This model employs the phase-averaged conformation tensor $C_{ij} = \left\langle q_i q_j \right\rangle$, where the q_i are the components of the *end-to-end vector* of each individual polymer molecule. The extra-stress tensor is then

$$\Xi_{ij}^{+} = \alpha_0 \left(f\left\{ tr\left(\boldsymbol{C}\right)\right\} C_{ij} - \delta_{ij} \right), \tag{1.3}$$

where $\alpha_0 = (1-\beta_0)/Wi_{\tau 0}$, and with $Wi_{\tau 0} = \lambda u_\tau^2/\nu_{tot}$ the friction Weissenberg number representing the ratio of the elastic relaxation time (λ) to the viscous timescale. Additionally, δ_{ij} is the Kronecker's delta and $f\left\{ tr\left(\boldsymbol{C}\right)\right\}$ is given by the Peterlin approximation

$$f\left\{ tr\left(\boldsymbol{C}\right)\right\} = \frac{L^2 - 3}{L^2 - tr\left(\boldsymbol{C}\right)}, \tag{1.4}$$

where L is the maximum polymer molecule extensibility and $\{tr(.)\}$ represents the trace operator. This system of equations is closed with an evolution equation for the conformation tensor

$$\frac{DC_{ij}}{Dt^{+}} = \left(C_{ik} S_{kj}^{+} + S_{ik}^{+} C_{kj} \right) - \left(C_{ik} W_{kj}^{+} + W_{ik}^{+} C_{kj} \right) - \frac{f\left(tr\left(\boldsymbol{C}\right)\right) C_{ij} - \delta_{ij}}{Wi_{\tau 0}}, \tag{1.5}$$

where $S_{ij}^{+} = \left(\partial u_i^{+}/\partial x_j^{+} + \partial u_j^{+}/\partial x_i^{+} \right)/2$ and $W_{ij}^{+} = \left(\partial u_i^{+}/\partial x_j^{+} - \partial u_j^{+}/\partial x_i^{+} \right)/2$ are, respectively, the terms of the rate-of-strain, $\boldsymbol{S}^{+}$, and the rate-of-rotation, $\boldsymbol{W}^{+}$, tensors.

Since the numerical scheme for our DNS is detailed in Thais et al. [89], we present here a brief description of the mathematical and numerical approaches. The hybrid MPI/OPENMP algorithm used was tailored to run properly in massively parallel architectures. The hybrid spatial scheme includes Fourier spectral accuracy in the two homogeneous directions (x and y) and sixth-order compact finite differences for the first and second-order wall-normal derivatives (z direction). The time marching can be up to fourth-order accurate by the use of the Adams–Moulton scheme for the viscous terms and Adams–Bashforth for the explicit terms. Pressure–velocity coupling is facilitated by a higher order generalization of the semi-implicit fractional step method on a non-staggered grid arrangement analysed by Armfield and Street [4]. In order to attenuate high wave-number energy accumulation, de-aliasing and fourth-order filtering are performed in the two homogeneous and wall-normal directions, respectively. Typically, this algorithm makes possible high-resolution, high drag reduction viscoelastic DNS, at relatively high flow Reynolds numbers.

Chapter 2

The polymer coil–stretch mechanism in turbulent drag reducing flows

The polymer coil–stretch mechanism in turbulent drag reducing flows is analysed using direct numerical simulations of viscoelastic FENE-P fluids. The study is carried out taking into account low and high drag reduction regimes. The polymer stretching and the alignment between the conformation tensor and other relevant entities are investigated using statistical and tensor analysis. The significant alignment between the former and the velocity fluctuations product tensor indicates that the initial polymer stretching due to the mean shear is increased by the flow stress fluctuations, providing a supplementary polymer extension. In addition, interactions between the turbulence and the polymer are evaluated from an instantaneous turbulent energy exchange perspective by considering streamwise work fluctuating terms in elliptical and hyperbolic flow regions, separately. Near the wall, polymers not only release energy to the streaks, but also to the elliptical (or vortical) and hyperbolic (or extensional) structures. However, polymers can be also dragged around near wall vortices, passing through hyperbolic regions and experiencing a significant straining within both these turbulent structures and storing their energy. Hence, polymers weaken elliptical and hyperbolic structures leading to a tendency of a dominant parabolic character in the flow domain. Polymer release of energy occurs primarily in the streamwise direction, which is in agreement with the enhanced streamwise velocity fluctuation observed in drag reducing flows. A detailed polymer coil–stretch mechanism is provided.

2.1 Introduction

The addition of a small amount of polymers of high molecular weight can lead to a pressure drop decrease in turbulent flows. Since the first observations reported by Forrest and Grierson [28], Toms [93] and Mysels and Metzner [61], numerous

experimental studies have been conducted in attempts to make practical use of polymer-induced drag reduction (DR), including long-distance transport of liquids [80], oil well operations [15], fire fighting [27], transport of suspensions and slurries [29], and biomedical applications [32]. In a remarkable and pioneering paper, Virk et al. [97] performed a careful analysis with an experimental turbulent pipe flow apparatus and showed that if the friction drag for pipe flows is plotted in Prandtl–Kármán coordinates, it departs from the Prandtl–Kármán law (the onset of DR) to its bound, the so-called maximum drag reduction (MDR) or Virk's asymptote, as a result of an increase in either the Reynolds number, the polymer concentration, or the polymer's molecular weight. Over the years, researchers have successfully analysed relevant aspects of this phenomenon and a significant literature is available, e.g. [36, 98, 63, 96, 12, 13, 60, 33, 44]. However, up to now, there has been no definitive consensus concerning the interactions between the turbulent energy and the deformations of the polymer.

Phenomenological explanations for polymer drag reduction gravitate around two major theories. According to the viscous theory, independently proposed by Lumley [52] and Seyer and Metzner [81] and supported by Ryskin [79], polymer stretching in a turbulent flow produces an increase in the effective viscosity in a region outside of the viscous sublayer and in the buffer layer, which suppresses turbulent fluctuations, increasing the thickness of the buffer layer and reducing the wall friction. The elastic theory postulated by Tabor and de Gennes [84] assumes that the elastic energy stored by the polymer becomes comparable to the kinetic energy in the buffer layer. Since the corresponding viscoelastic length scale is larger than the Kolmogorov scale, the usual energy cascade is inhibited, which thickens the buffer layer and reduces the drag [43].

Numerically, polymer-induced drag reduction theories have been intensively investigated for over a decade since the first simulations conducted by Toonder et al. [94] and Orlandi [62]. Using an inelastic generalized Newtonian fluid to analyse pipe [94] and channel [62] flows, both researchers argued that DR seems to be closely related to the anisotropy of the *elongational viscosity*, a parameter that measures the resistance of the fluid against stretching deformations. Such an argument was also presented by Sureshkumar et al. [83], who performed the first direct numerical simulation (DNS) of turbulent channel flow of a viscoelastic finitely extensible nonlinear elastic in the Peterlin approximation (FENE-P) fluid [73], at a zero-shear friction Reynolds number of 125. Their results suggest a partial suppression of turbulence within the buffer layer after the onset of drag reduction, which is linked with an enhanced effective viscosity attributed to the extension of polymers dispersed in the flow.

The explanations proposed in the three papers referred to above [94, 62, 83] seem to corroborate Lumley's theory. In an attempt to quantify this viscous scenario, L'vov et al. [53] used conservation principles to show that an additional effective viscosity growing linearly with the distance from the wall in the buffer layer has similar effects to

those observed by the addition of flexible polymers in turbulent flows. This theoretical prediction was later confirmed by de Angelis et al. [20], who performed a DNS of Newtonian turbulent flows with an added viscosity profile obtaining results previously observed in viscoelastic FENE-P simulations. Additionally, using this simple linear viscosity model, de Angelis et al. [20] were able to predict the maximum drag reduction asymptote, a point discussed in detail by Benzi et al. [9].

It is important to note that the elastic theory has also been actively explored. Min et al. [59] conducted a DNS of turbulent drag reducing channel flows in which the dilute polymer solution is simulated using the Oldroyd-B model. Their results showed good agreement with previous theoretical and experimental predictions of the onset of DR at specific friction Weissenberg numbers, which is interpreted based on the elastic theory. Min et al. [59] and Dallas et al. [19] describe an elastic scenario in which the elastic energy stored in the near-wall region due to the uncoiling of polymer molecules is transported to and, to some extent, released in the buffer and log-law layers. This storage of energy around the near-wall vortices was confirmed by Dubief et al. [24], who performed a DNS of turbulent polymer solutions in a channel using the FENE-P model, although, in contrast to Min et al. [59] and Dallas et al. [19], they proposed an autonomous regeneration cycle of polymer wall turbulence in which the coherent release of energy occurs in the very near-wall region, just above the viscous sublayer. In order to clarify the dynamics of the polymer–turbulence interaction, Thais et al. [87] used the DNS of a fully developed turbulent channel flow of Newtonian and viscoelastic FENE-P fluids, at zero shear friction Reynolds numbers up to 1000, and carefully examined the budgets of turbulent kinetic energy and the elastic energy budget in drag-reducing flows. The authors showed that the elastic energy production is small in the very near-wall region, growing with the distance from the wall and reaching a maximum value in the log-law region. This elastic energy production acts simultaneously as the dominant source of elastic energy and as the dominant sink of turbulent energy. This is rather in line with Tabor and De Gennes's description. However, recently, Thais et al. [86] emphasized that at $Re_{\tau 0} = 1000$, the elastic coupling between the turbulence and the polymer does not depend on the drag reduction regime (the level of viscoelasticity), which is in disagreement with the elastic theory.

Despite the discrepancies between the two most prominent theories, what seems to be in accordance with both scenarios is the relevance of the polymer coil–stretch process, which further imposes a transient behaviour on the drag reduction as well as a subsequent polymer degradation, a consequence of polymer elongation [58, 64, 82]. In order to understand the polymer coil–stretch process, Bagheri et al. [6] presented direct numerical simulations of turbulent channel flow with passive Lagrangian linear (Oldroyd-B) and nonlinear (FENE) polymers. For the FENE model, the polymers are more elongated within the near-wall region although such extension becomes less

heterogeneous as the Weissenberg number increases. Furthermore, a much stronger orientational trend is seen close to the wall, where the polymers are well aligned along the streamwise direction. The authors also verified the alignment of the end-to-end vector with respect to the principal directions of the rate-of-strain tensor and the vorticity vector. Nevertheless, they did not identify possible tensors capable of stretching the polymers, which would reveal more details about the uncoiling mechanism.

It is clear that the DR phenomenon is not completely understood and many aspects of the problem remain unclear. Any attempt to completely elucidate polymer-induced drag reduction must consider, at least, four important issues: the mechanism of polymer coil–stretch; the development of turbulent structures in viscoelastic flows; the exchange of energy between the turbulence and the polymers; and the breaking of the polymer molecules.

In the present work, we investigate the polymer coil–stretch process with the aid of direct numerical simulations of the turbulent plane Poiseuille flow of a viscoelastic FENE-P fluid taking into account a large range of zero-shear friction Reynolds numbers (from 180 up to 1000). Tensorial and statistical analyses are developed in an attempt to highlight the role played by three relevant kinematic tensor entities in the polymer extension mechanism: the velocity fluctuation product tensor (which can be physically interpreted as an instantaneous Reynolds stress), the rate-of-strain tensor, and the rate-of-rotation tensor. As the primary focus, the relative polymer stretch and the alignment between the conformation tensor and these three important tensor entities will be confronted. Additionally, joint probability density functions will be used in order to correlate the polymer–turbulence exchanges of energy and polymer orientations. Lastly, the flow will be divided into two distinct regions, following the Q-criterion of vortex identification [38]: an elliptical (or vortical) part where the second invariant of the velocity gradient tensor is positive, and a hyperbolic (or extensional) part which is determined by the negative values of the second invariant of the velocity gradient tensor. The polymer work fluctuation will then be investigated within these regions, separately. The analyses that came out from these tools enable the proposition of a polymer coil–stretch mechanism based on the autonomous regeneration cycle reported by Dubief et al. [24], which in turn was based on that conceived for Newtonian turbulent flows, previously presented by Jiménez and Pinelli [42].

Following the description of the physical formulation and numerical methodology presented in Section 2.2, our main results are separated into three parts: Sections 2.3, 2.4, and 2.5. In the first part (Section 2.3), some classical time-averaged quantities are initially presented. In Section 2.4, we analyse the distribution of polymer stretch along the wall distance, of which the effects on near-wall vortices and the dependence on L and $Wi_{\tau 0}$ are investigated as well, as exposed in subsection 2.4.1. Tensor analyses are conducted in subsection 2.4.2 in an attempt to verify the alignment between the

conformation tensor and the other three relevant entities. In Section 2.5, joint probability density functions are used in order to correlate the polymer–turbulence exchanges of energy and polymer alignments (subsection 2.5.1). Additionally, the coil–stretch polymer process is linked with the coherent structures within the flow (subsection 2.5.2). In Section 2.6, these interactions are finally employed to describe a detailed cyclic mechanism of the polymer–turbulence interaction.

2.2 Numerical methodology

The parameters for the turbulent Newtonian and FENE-P channel flows studied here are summarized in table 2.1. Our simulated cases were chosen keeping in mind that viscoelastic fluids can have significantly different statistical behaviour from a Newtonian fluid. For a given turbulence level, as parametrized by the zero shear friction Reynolds number $Re_{\tau 0}$ (defined as $Re_{\tau 0} = u_\tau h/\nu_0$), this effect can vary with the friction Weissenberg number, $Wi_{\tau 0}$ (where $Wi_{\tau 0} = \lambda {u_\tau}^2/\nu_0$) and the maximum polymer extension length, L. In this paper, four Newtonian flow and seven viscoelastic flows were examined, keeping the viscosity ratio β_0 fixed at 0.9 and taking into account four different values of the zero-shear friction Reynolds number ($Re_{\tau_0} = 180$, $Re_{\tau_0} = 395$, $Re_{\tau_0} = 590$ and $Re_{\tau_0} = 1000$) and two different values of the friction Weissenberg number and the maximum polymer molecule extensibility ($Wi_{\tau_0} = 50$; $Wi_{\tau_0} = 115$; $L = 30$; $L = 100$), which provided drag reduction regimes from 28.5% up to 62.3%. The drag reduction level is defined by

$$DR[\%] = \overline{\left(1 - \frac{< \tau_w(t) >}{< \tau_{w,N}(t) >}\right)} \times 100, \tag{2.1}$$

where $< \tau_w(t) >$ and $\tau_{w,N}(t)$ denote the area-averaged wall shear stress at a given instant t for the polymer solution and the Newtonian solvent, respectively, evaluated at the same zero shear friction Reynolds number. Time averaging of DNS data (represented by the bar) is taken in time over some 500 flow snapshots spanning several eddy turnover times, while spatial averaging (indicated by '$\langle\ \rangle$') is taken in the two homogeneous channel directions (x, y).

Two drag reducing regimes are shown in table 2.1: the high drag reduction (HDR; $DR > 40\%$) and the low drag reduction (LDR; $DR \leqslant 40\%$). Physically, the main difference between these two regimes consists in the fact that for LDR flows, the Reynolds stresses play a major role, whereas in the HDR regime, the near-wall dynamics of the flow is dominated by the polymer stresses [102].

The channel extent for the flow cases at Re_{τ_0} up to of 590 was $Lx \times Ly \times Lz = 8\pi \times 1.5\pi \times 2.0$. For the highest zero-shear friction Reynolds number flow, $Lx \times Ly \times Lz =$

$6\pi \times 1.5\pi \times 2.0$. The number of mesh points ($Nx \times Ny \times Nz$) shown in table 2.1 for each case corresponds to a grid resolution of $8.8 \leq \Delta x^+ \leq 12.3$, $5.4 \leq \Delta y^+ \leq 7.3$, and $0.2 \leq \Delta z^+ \leq 12.1$. The superscript '+' indicates normalization by the friction velocity, defined by $u_\tau = \sqrt{\tau_w/\rho}$, and the total kinematic zero-shear rate viscosity. The Schmidt number $Sc_c = 0.1$ was necessary to keep the algorithm stable and the conformation tensor symmetric positive-definite.

$Re_{\tau 0}$	$Wi_{\tau 0}$	L	β_0	N_x **x** N_y **x** N_z	Δ_x^+ **x** Δ_y^+ **x** $\Delta_{z,min}^+$	$\Delta_{z,max}^+$	DR [%]
180	0	0	1	512 x 128 x 129	8.8 x 6.6 x 0.2	7.1	0
180	50	30	0.9	512 x 128 x 129	8.8 x 6.6 x 0.2	7.1	28.5 (LDR)
180	115	30	0.9	512 x 128 x 129	8.8 x 6.6 x 0.2	7.1	38.4 (LDR)
180	50	100	0.9	512 x 128 x 129	8.8 x 6.6 x 0.2	7.1	47.0 (HDR)
180	115	100	0.9	512 x 128 x 129	8.8 x 6.6 x 0.2	7.1	62.3 (HDR)
395	0	0	1	1024 x 256 x 257	9.7 x 7.3 x 0.2	7.9	0
395	115	100	0.9	1024 x 256 x 257	9.7 x 7.3 x 0.2	7.9	62.0 (HDR)
590	0	0	1	1536 x 512 x 257	9.7 x 5.4 x 0.5	10.4	0
590	115	100	0.9	1536 x 512 x 257	9.7 x 5.4 x 0.5	10.4	61.0 (HDR)
1000	0	0	1	1536 x 768 x 385	12.3 x 6.1 x 0.5	12.1	0
1000	115	100	0.9	1536 x 768 x 385	12.3 x 6.1 x 0.5	12.1	58.0 (HDR)

Table 2.1 – Parameters for the DNS of Newtonian and FENE-P turbulent channel flows.

2.3 Statistics of the flow

2.3.1 Time-averaged statistics

The distributions of the mean velocity in wall-coordinates, $\langle \overline{U_x}^+ \rangle$, for turbulent channel flows of Newtonian and viscoelastic solutions are displayed in figure 2.1(a). The bar indicates time average and '$\langle\ \rangle$' denotes the $x-y$ plane average. The gray circles present the Newtonian mean velocity profile at $Re_{\tau_0} = 180$ while the other symbols present the viscoelastic flows. In the *viscous sublayer* ($0 < z^+ < 5$), where the total stress is predominantly associated with viscous effects, the mean velocities converge to the same linear shape $\langle \overline{U_x}^+ \rangle = z^+$ represented by the solid grey line. As the wall distance increases, the Reynolds stress becomes important and comparable to the viscous stress within the Newtonian *buffer layer* ($5 < z^+ < 30$). Then, the Newtonian mean velocity departs quickly from the linear profile, taking on a logarithmic dependence on z^+ (grey dashed line) in the Newtonian *log-law region*, $z^+ > 30$,

$$\langle \overline{U_x}^+ \rangle = \frac{1}{\kappa} \ln(z^+) + A_1 \,, \tag{2.2}$$

where κ is commonly called the von Kármán coefficient ($1/\kappa$ is the slope), and A_1 is the intercept at $z^+ = 1$. For Newtonian channel flows over a hydraulically smooth wall, $\kappa = 0.4$ and $A_1 = 5.5$ [45]. In order to better describe our results, we use the boundaries of the viscous sublayer, the buffer layer and the log-law Newtonian regions to define regions I, II and III, respectively.

The interactions between the viscoelastic fluid dynamics and the turbulent flow dynamics result in changes in the mean velocity profile relative to the Newtonian fluid. The polymer drag reduction phenomenon leads to an increased bulk mean velocity, as observed by comparing the viscoelastic profiles plotted in figure 2.1. When a high enough polymer concentration is used, the maximum level of drag reduction (MDR) is attained. In that state, the velocity profile is commonly represented by the Virk's asymptote [98],

$$\langle \overline{U_x}^+ \rangle = 11.7 \ln(z^+) + 17.8 , \tag{2.3}$$

which is a matter of recent controversy [104]. This velocity profile, illustrated by the orange dash-dotted line and partially fitted by the most viscoelastic case (orange inverted triangles), was derived by L'vov et al. [53] using a DNS of FENE-P turbulent flows and assuming that the Reynolds stress momentum flux is negligible and the pressure gradient is balanced by the effective polymer/viscous force [10, 76, 8]. Additionally, the MDR scenario was recently explored by Dubief et al. [22], who performed direct numerical simulations of FENE-P inertial channel flows in an attempt to investigate the mechanism of the turbulence primarily driven by the polymers, which is called the *elasto-inertial turbulence*. The authors pointed out that in the MDR state, the fluctuations in polymer stresses create turbulent kinetic energy. This fact suggests that the maximum drag reduction asymptote can not be surpassed since the polymer coil–stretch process is itself a source of turbulence. Hence, the elasto-inertial turbulence phenomenon may provide a reasonable explanation for the MDR. Nevertheless, as pointed by the authors, further analysis is required to validate this rationale.

Experimental and recent numerical results based on DNS [25, 77, 26, 87] indicate a parallel upward shift of the logarithmic region of the mean velocity profile with increasing DR, which is clearly perceived at high Reynolds numbers [86]. Such a behaviour suggests a significant extension of the buffer layer region into the channel caused by the polymers. For viscoelastic fluids, the cross-over to a presumed *Newtonian plug-flow* occurs at a distance from the wall where the Reynolds stress momentum flux is no longer negligible compared to that of the polymer/viscous stress. Figures 2.1(b), (c), and (d) show the normal components of the Reynolds stress tensor, whose components are defined as the *time standard deviation* of the velocity fluctuation product ($\overline{u'_i u'_j}^+$). The mean effect of the polymer on the turbulence is anisotropic and induces an increase in the streamwise normal Reynolds stress component (figure 2.1b), while

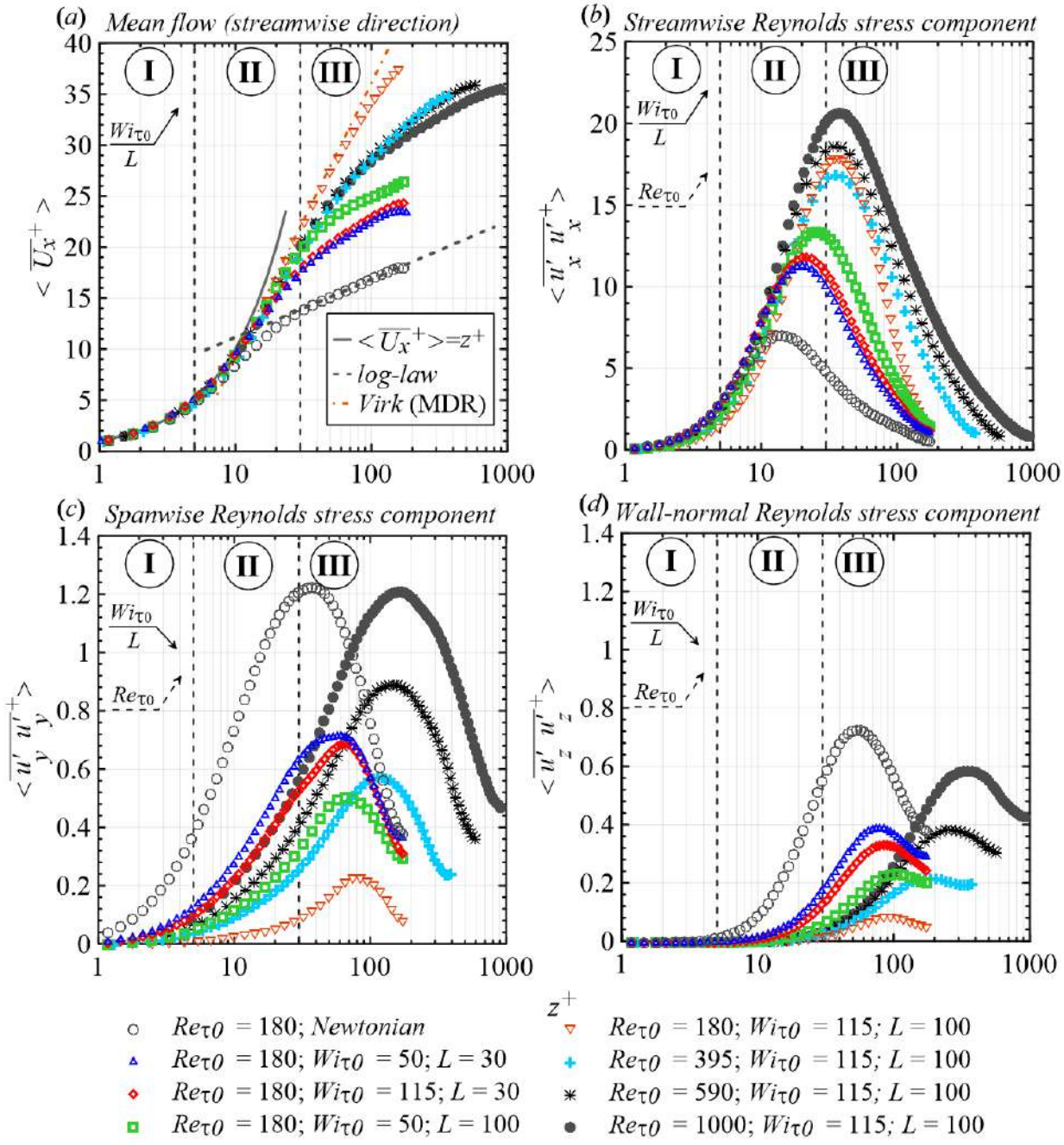

Figure 2.1 – Mean velocity profiles in the streamwise direction (a),$\langle \overline{U_x}^+ \rangle$, and normal components of the Reynolds stress (b, c, and d) for Newtonian and viscoelastic channel flows, against the normalized wall distance.

weakening both the spanwise (figure 2.1*c*) and the wall-normal (figure 2.1*d*) terms, as experimentally found by many researchers such as Pinho and Whitelaw [74], Warholic et al. [99] and White et al. [103]. This effect is more pronounced as the elasticity increases, as indicated by the solid black arrows. In the most elastic flow at $Re_{\tau_0} = 180$ (orange inverted triangles), for instance, the peak of $\langle \overline{u'_x u'_x}^+ \rangle$ moves from $z^+ \approx 12$ (region II) to $z^+ \approx 32$ and its value is one order of magnitude greater than the Newtonian one (grey open circles). In addition, the other components also shift away from the wall, but their peaks decrease by one order of magnitude compared to the Newtonian flow. Since vortices produce significant transverse fluctuations, the reduction of both u'_y and u'_z suggests a strong interaction between these intermittent structures and polymers [24]. Lastly, the dashed arrows indicate that the normal Reynolds stress components are an increasing function of $Re_{\tau 0}$. Their peaks move towards the channel centre with increasing Reynolds number.

The variations in polymer mean stresses across the channel can be highlighted by analysing the polymer mean stretch, which is linked with the former by the Peterlin function (equation 1.4). The distribution of the relative polymer mean stretch $\langle \mathrm{tr}\left(\overline{\boldsymbol{C}}\right)/\mathrm{L}^2 \rangle$ as a function of z^+ is displayed in figure 2.2(*a*), for all viscoelastic cases studied in the present paper. As a common point, the polymer molecules exhibit a significant extension at the wall, which increases in the buffer layer, where its peak is attained. This peak magnitude, as well as its location, is a decreasing function of L, but increases with increasing $Wi_{\tau 0}$ (these trends are discussed in subsection 2.4.1). As the wall distance increases further, $\langle rmtr\left(\overline{\boldsymbol{C}}\right)/L^2 \rangle$ becomes less pronounced until achieving its minimum level at $z^+ = 180$. A very simple method to clarify the polymer stretching mechanism consists in solving equation 1.5 using different mean velocity profiles. The result is illustrated in figure 2.2(*b*), where the less elastic flow is considered (grey open circles), as well as the polymer extension produced in this fluid by three mean velocity profiles: turbulent-channel-like $\overline{U_x} = (9/8)[1 - (z/h)^8]$ [19]; laminar-channel-like, $\overline{U_x} = (3/2)[1-(z/h)^2]$; and laminar-Couette-like, $\overline{U_x} = (z/h)$. As the derivative of the mean velocity with respect to the wall-normal direction increases, the polymers stretch considerably, due to the increase of the shear stress. More specifically, the profile of $\langle \mathrm{tr}\left(\overline{\boldsymbol{C}}\right)/\mathrm{L}^2 \rangle$ follows the mean viscous shear stress feature. In a pure Couette shear flow (black star symbol), the polymers exhibit a weak and constant extension, $\langle \mathrm{tr}\left(\overline{\boldsymbol{C}}\right)/\mathrm{L}^2 \rangle \approx 0.06$. On the other hand, for a pure channel shear flow (blue plus symbol), the relative polymer stretch decreases monotonically and linearly from $\langle \mathrm{tr}\left(\overline{\boldsymbol{C}}\right)/\mathrm{L}^2 \rangle \approx 0.25$ to $\langle \mathrm{tr}\left(\overline{\boldsymbol{C}}\right)/\mathrm{L}^2 \rangle = 0$ across the channel. Lastly, comparing the relative polymer extensions obtained from a turbulent-like mean velocity profile (orange inverted triangles) and DNS results (grey open circles), it is interesting to observe that both curves depart from the same level (≈ 0.54), at $z^+ = 0$. However, as the wall distance increases, the discrepancy between them becomes pronounced. In fact, near the wall, the increasing $\langle \mathrm{tr}\left(\overline{\boldsymbol{C}}\right)/\mathrm{L}^2 \rangle$ noticed

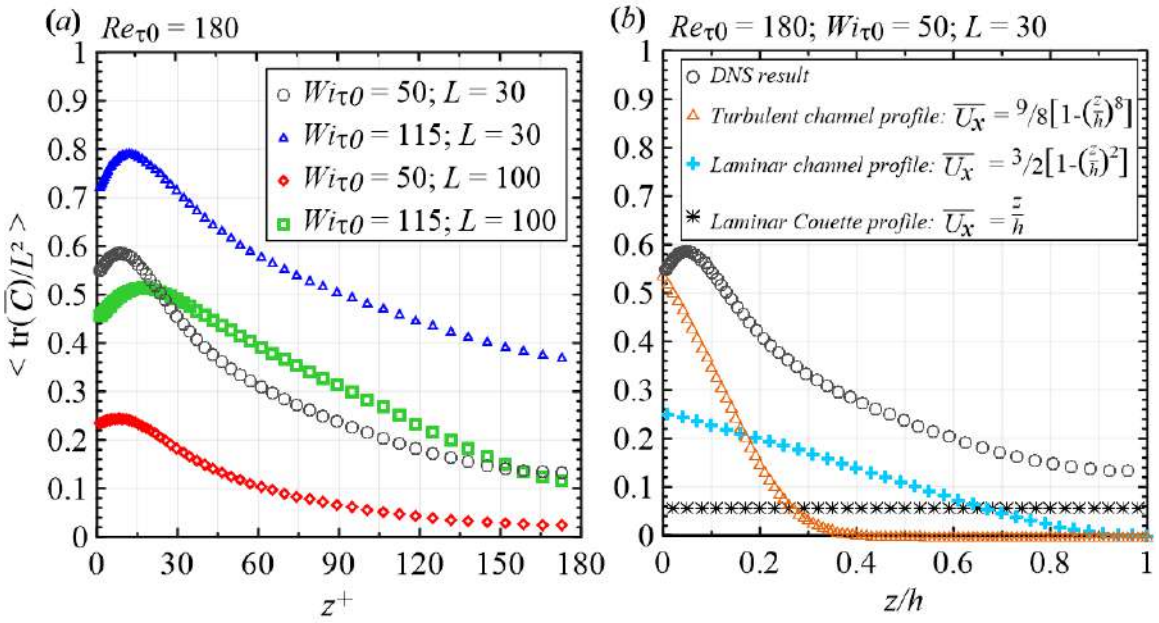

Figure 2.2 – (*a*) Evolution of the mean relative polymer extension, $\langle \mathrm{tr}\left(\overline{C}\right)/\mathrm{L}^2 \rangle$, against the normalized wall distance. (*b*) Effects of mean shear stress profile on polymer extension.

for the grey circles curve suggests that in this region there is a particular intermittent flow topology capable of producing an increase in the polymer extension beyond the viscous mean shear level represented by the orange inverted triangles. In other words, the viscous mean stress is responsible for a relevant polymer stretching, which is incremented since the turbulent structures interact with the polymer molecules, providing a supplementary polymer extension. We believe these intermittent polymer–turbulence interactions are also responsible for the polymer coil–stretch process, which will be analysed in later subsections from statistical and tensorial perspectives.

All the trends discussed above considering $Re_{\tau 0} = 180$ are also observed at higher zero-shear friction Reynolds numbers, as previously reported by Thais et al. [87, 86].

2.4 Polymer stretching and alignment

In order to analyse the effects of instantaneous polymer stretching on the flow, the following data and results were evaluated at the same instant of simulation, after a statistical steady state was achieved. Such an instantaneous analysis is justified by the fact that in turbulent flows, the polymer action is likely to be as intermittent as the near-wall vortices [24]. Hence, these intermittent events may be hidden by a time-averaging procedure. In other words, such an analysis of the instantaneous quantities could reveal rare but important events for the DR phenomenon.

Although in this Subsection we analyse the effects of the elasticity on the stretching

and alignment of the polymers at a low zero-shear friction Reynolds number, $Re_{\tau_0} = 180$, it is important to emphasize that the trends shown below are observed for all viscoelastic cases studied. In other words, the physical aspects of DR discussed here are not affected by low–Reynolds number effects.

2.4.1 Polymer stretching

The three-dimensional structures shown in figure 2.3 represent the isosurfaces of the vortical regions, defined as the positive second invariant of the velocity gradient tensor, $\nabla \boldsymbol{u}$, in Newtonian (a) and viscoelastic (b, c, d, and e) flows. For incompressible flows, the second invariant of $\nabla \boldsymbol{u}$, Q, can be used to identify vortical structures, the so-called *Q-criterion* [38], and simplified as

$$Q = \frac{1}{2}\left(\|\boldsymbol{W}\|^2 - \|\boldsymbol{D}\|^2\right) > 0\,, \tag{2.4}$$

which indicates the spatial regions where the Euclidean norm of the rate-of-rotation tensor, $\|\boldsymbol{W}\|$, dominates that of the rate-of-strain, $\|\boldsymbol{D}\|$ (the Euclidean norm of a generic second order tensor $\boldsymbol{A}$ is $\|\boldsymbol{A}\| = \sqrt{tr\left(\boldsymbol{A}\cdot\boldsymbol{A}^{\boldsymbol{T}}\right)}$). These structures follow an organized hierarchy across the channel. In the vicinity of the wall ($z^+ < 20$), eddies are found to be pairs of counter-rotating quasi-streamwise vortices, while for $z^+ > 30$, these eddies resemble *hairpins* (the so-called *horseshoe vortices*). The formation of such morphologies is induced by combined *second-quadrant ejection* ($u'_x < 0, u'_z > 0$; Q2 event) and *fourth-quadrant sweep* ($u'_x > 0, u'_z < 0$; Q4 event) events within the flow [1]. Specifically, the hairpin vortices are composed of three well defined parts. The *legs* are regions of rotation quasi-aligned with the streamwise direction. The *head* is a rotation part aligned with the spanwise direction. The *necks* are the connections between the legs and the head of the hairpin. These three parts, as well as the velocity fluctuations associated with them, can be seen in detail in figure 2.4, where a typical hairpin extracted from our less elastic flow ($Re_{\tau 0} = 180$, $Wi_{\tau 0} = 50$ and $L = 30$) is coloured by the Q events.

Comparing figures 2.3(a), (b), (c), (d) and (e), it can be seen that the number of vortices with a value of the Q-criterion equal to 0.7 decreases with increasing elasticity ($Wi_{\tau 0}$ and L). For $Wi_{\tau 0} = 115$ and $L = 100$, which provides $DR = 62.3\%$, the vortices with $Q = 0.7$ are completely gone and the vortices with $Q = 0.1$ (figure 2.3e) are only found close to the walls. In viscoelastic flows, the vortical structures are significantly weaker than in the Newtonian flow, which is considered fundamental evidence of the polymer–turbulence interactions and the consequent drag reduction [46, 47, 102]. As the elasticity increases, some characteristics of the vortices change: their thicknesses and streamwise lengths increase, while their strengths weaken, which is clearly observed by comparing figures 2.3(a) and (e). Furthermore, the vortices become more parallel

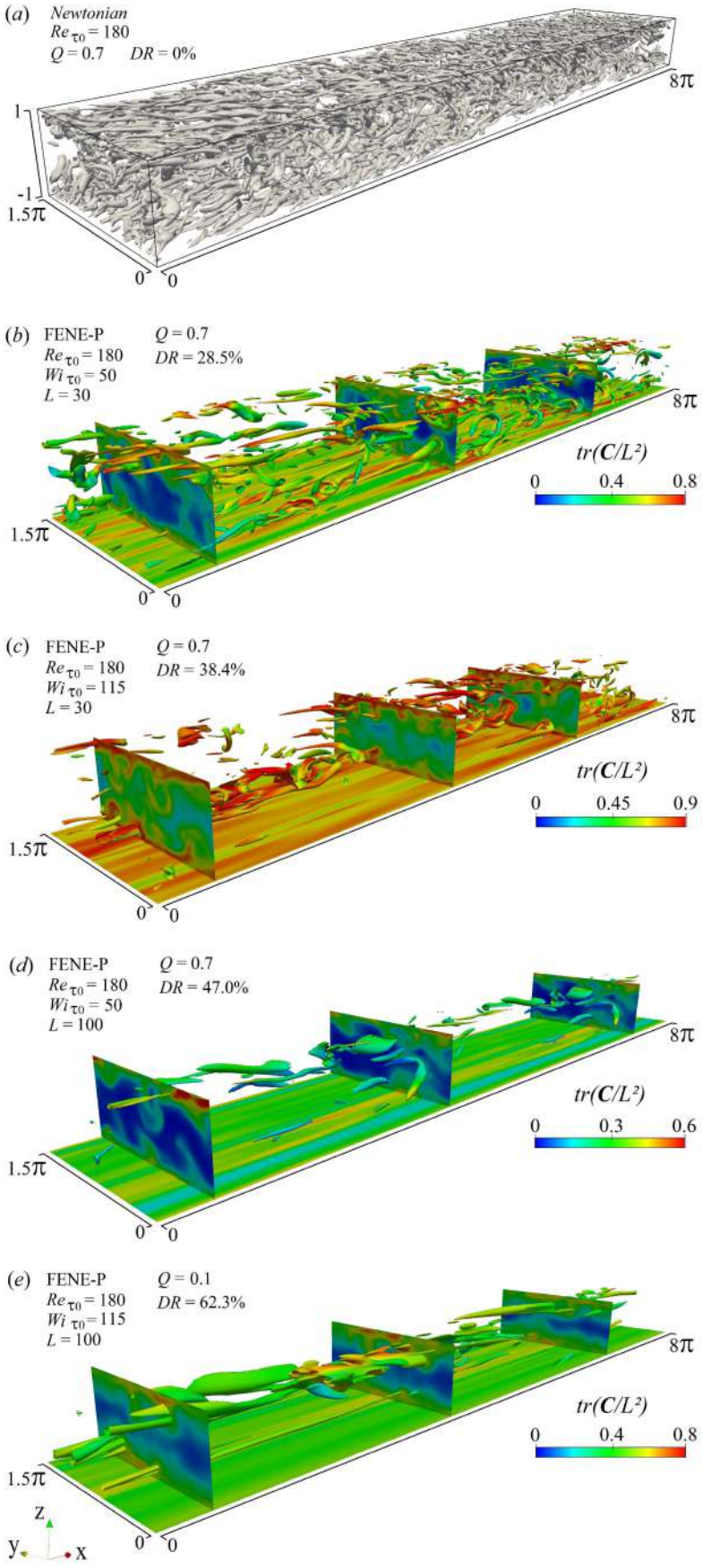

Figure 2.3 – The three-dimensional structures represent isosurfaces of vortical regions defined as a positive value of the second invariant of velocity gradient tensor, $\nabla \boldsymbol{u}$. The colours indicate the polymer stretching, $\mathrm{tr}(\boldsymbol{C})/\mathrm{L}^2$.

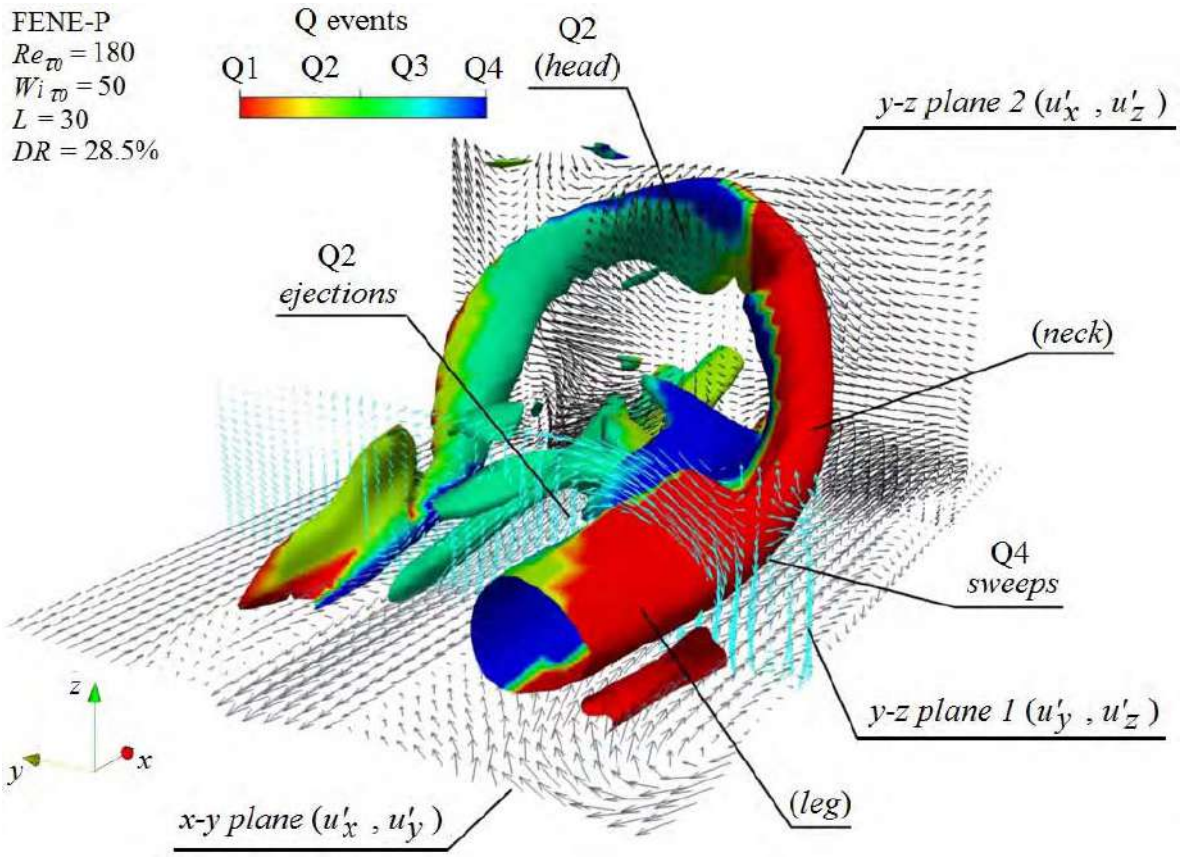

Figure 2.4 – Typical hairpin extracted from a viscoelastic flow ($Re_{\tau 0} = 180$; $Wi_{\tau 0} = 50$; $L = 30$) with $Q = 0.7$ and coloured by the Q1 ($u'_x > 0, u'_z > 0$), Q2 ($u'_x < 0, u'_z > 0$), Q3 ($u'_x < 0, u'_z < 0$), and Q4 ($u'_x > 0, u'_z < 0$) events.

to the wall. In the log-law region, the hairpin head is strongly weakened. It has been experimentally and numerically shown that in drag reducing flows, the streamwise component of the Reynolds normal stresses increases relative to the Newtonian case, while the other components of the Reynolds stress tensors decrease [100, 99, 77, 46, 87]. These variations seem to be closely connected with the coil–stretch polymer transition and the consequent vortex structural changes [21]. The colours in figures 2.3(b), (c), (d) and (e) indicate the relative polymer stretch, $\mathrm{tr}(\boldsymbol{C})/\mathrm{L}^2$. The $y-z$ planes show that for all four viscoelastic flows, the polymers are more stretched close to the wall (yellow and red regions). In contrast, the polymer extensions are less pronounced in the middle of the channel (blue regions). The isosurface colours and those of the intersections between vortical structures and $y-z$ planes show that the polymers are more extended around the near-wall vortices.

The stretching of the polymers can be seen more clearly in figure 2.5(a), where the evolution of the $x-y$ plane average normalized trace of the instantaneous conformation tensor, $\langle \mathrm{tr}(\boldsymbol{C})/\mathrm{L}^2 \rangle$, is plotted against the wall distance z^+ (solid symbols) together with the normalized streamwise normal component of the conformation tensor, $\langle C_{xx}/L^2 \rangle$ (open symbols). The percentage of polymer extension, $\langle \mathrm{tr}(\boldsymbol{C})/\mathrm{L}^2 \rangle$, is relatively high at the wall, achieving a peak in the very near-wall region ($z^+ < 20$), the exact location of which varies with L and $Wi_{\tau 0}$. This peak is commonly associated with the streamwise vortices [19, 24, 21]. After this point, $\langle \mathrm{tr}(\boldsymbol{C})/\mathrm{L}^2 \rangle$ starts to decrease, until reaching its minimum at the channel centre. In comparing the grey solid circles with the red solid diamonds, or the blue solid triangles with the green solid squares, it can be clearly seen that $\langle \mathrm{tr}(\boldsymbol{C})/\mathrm{L}^2 \rangle$ decreases with increasing L, for fixed $Re_{\tau 0}$ and $Wi_{\tau 0}$, which suggests that the large polymer molecules could be less susceptible to chain scission degradation [65]. A further comparison of the grey solid circles with the blue solid triangles, or of the red solid diamonds with the green solid squares, reveals that the relative polymer extension becomes greater as the friction Weissenberg number increases, since higher values of the polymer time scale induce the polymer molecules to be influenced by a wider spectrum of time scales of the flow [19]. Figure 2.5(a) also shows that the dominant contribution to the trace of the conformation tensor comes from C_{xx}, i.e. $\langle \mathrm{tr}(\boldsymbol{C})/\mathrm{L}^2 \rangle \approx \langle C_{xx}/L^2 \rangle$ (especially near the wall and for the highest value of L, $L = 100$). This distribution suggests a significant stretching of the polymers in the streamwise direction. The other component with a non-zero wall value is the off-diagonal component C_{xz}, normalized and displayed in figure 2.5(d). However, its value at the wall is almost two orders of magnitude smaller than that of the C_{xx} component. Moreover, as $Wi_{\tau 0}$ and L increase, the profile of $\langle C_{xz}/L^2 \rangle$ follows the same tendencies noted in figure 2.5(a), reaching its peaks at z^+ not much different from those observed for C_{xx}. The peak magnitude of the off-diagonal component C_{xz} is comparable to that of the C_{zz} component (plotted in figure 2.5b), although both are only slightly smaller than the peak magnitude of the

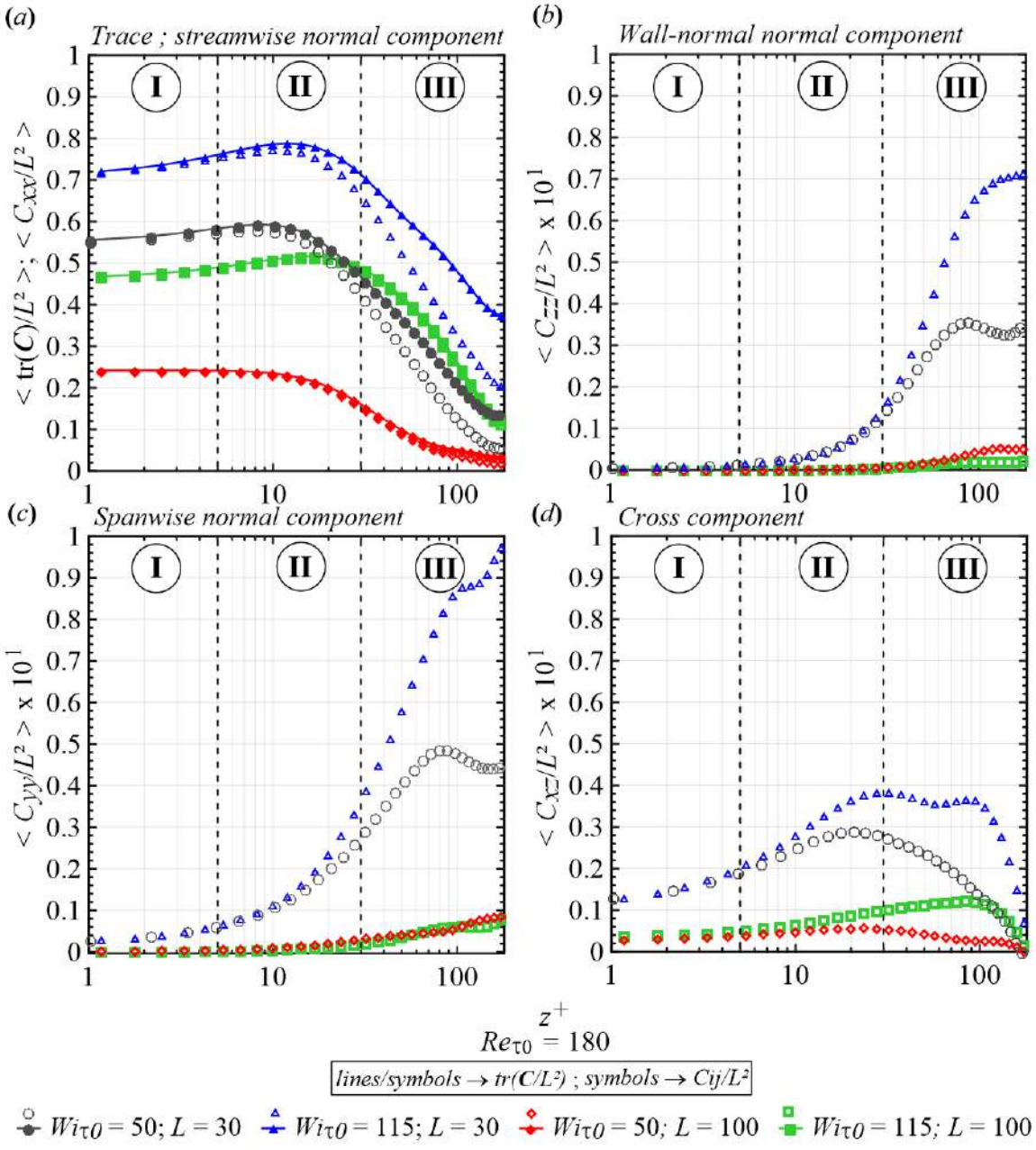

Figure 2.5 – Normalized conformation tensor as a function of the normalized wall distance. Streamwise normal components of $\boldsymbol{C}$ and $\mathrm{tr}(\boldsymbol{C})/\mathrm{L}^2$ (open and solid in *a*, respectively). Spanwise normal component of $\boldsymbol{C}$ (*b*). Wall-normal normal component of $\boldsymbol{C}$ (*c*). Cross components (*d*).

C_{yy} component (shown in figure 2.5c). It is worth noting that $\langle C_{xz}/L^2 \rangle$ is an increasing function of the molecular relaxation time (the variations of which are here computed by changing $Wi_{\tau 0}$ at fixed $Re_{\tau 0}$) although a saturation effect is observed when increasing the elasticity (the red diamonds and green square curves are close). This saturation effect is also seen for C_{zz} (figure 2.5b) and C_{yy} (figure 2.5c). The peak magnitude of the normal components C_{zz} and C_{yy} are both one order of magnitude smaller than that of the C_{xx} component, starting with a zero wall value. Lastly, as $Wi_{\tau 0}$ increases, C_{zz} and C_{yy} increase. The opposite behaviour is observed with increasing L. These two normal components exhibit maximum values beyond the buffer layer ($60 < z^+ < 90$), as previously reported by Thais et al. [87], which is currently linked to the straining flows around the vortices [24, 21].

In figure 2.5, it is worth noting that $C_{xx} \gg C_{yy} > C_{zz} \approx C_{xz}$ indicates a strong anisotropic behaviour of the conformation tensor. This anisotropy seems to dramatically influence the statistics of the fluctuating velocity fields, especially at small scales. The analysis of the trace of the conformation tensor reveals two locations of interest that will be systematically explored in this paper: $z^+ = 8.2$, the approximate position where $\langle \mathrm{tr}(\boldsymbol{C})/\mathrm{L}^2 \rangle$ is a maximum; $z^+ = 180$, where the trace of the conformation tensor reaches its minimum value with respect to L^2.

The probability distribution functions (PDFs) of $\mathrm{tr}(\boldsymbol{C})/\mathrm{L}^2$ are displayed in figure 2.6. The grey circles indicate the PDF for the whole channel, while the blue triangles and red diamonds are for the $x-y$ planes located at $z^+ = 8.2$ and $z^+ = 180$, respectively. Figure 2.6(a) shows the results for the less elastic flow, for which $Wi_{\tau 0} = 50$, $L = 30$, and $DR = 28.5\%$. The relative polymer extensions shown in this figure vary between 0 and 0.9, although the curve of grey circles indicates that most of the molecules have a stretch percentage of 55%, which is equally observed at $z^+ = 8.2$. Moreover, close to the wall, the polymer molecules present a more reduced stretch range, $0.3 < \mathrm{tr}(\boldsymbol{C})/\mathrm{L}^2 < 0.8$ (there are no coiled molecule in this $x-y$ plane). At the centre of the channel ($z^+ = 180$), a large number of polymer molecules are coiled and most of them are weakly stretched ($\mathrm{tr}(\boldsymbol{C})/\mathrm{L}^2 = 0.05$). A comparison between figures 2.6(a) and 2.6(c) shows that as L increases, keeping $Wi_{\tau 0}$ fixed, the polymer extension percentage decreases and the number of coiled molecules increases. The same trend is observed comparing figures 2.6(b) and 2.6(d). Regarding figure 2.6(c), in the $x-y$ plane located at $z^+ = 180$ almost all polymer molecules have a null stretching percentage. As discussed before, the relative polymer extension becomes greater as the friction Weissenberg number increases, since higher values of the polymer time scale are influenced by a wider spectrum of time scales of the flow. This is clearly observed by comparing figures 2.6(a) and (b). In figure 2.6(b), where $Wi_{\tau 0} = 115$ and $L = 30$, an increase in $Wi_{\tau 0}$ widens the range of polymer stretching ($3/900 < \mathrm{tr}(\boldsymbol{C})/\mathrm{L}^2 < 0.95$). The majority of polymer molecules are highly extended (0.78). Furthermore, in the $x-y$ plane located close to the wall, only strongly

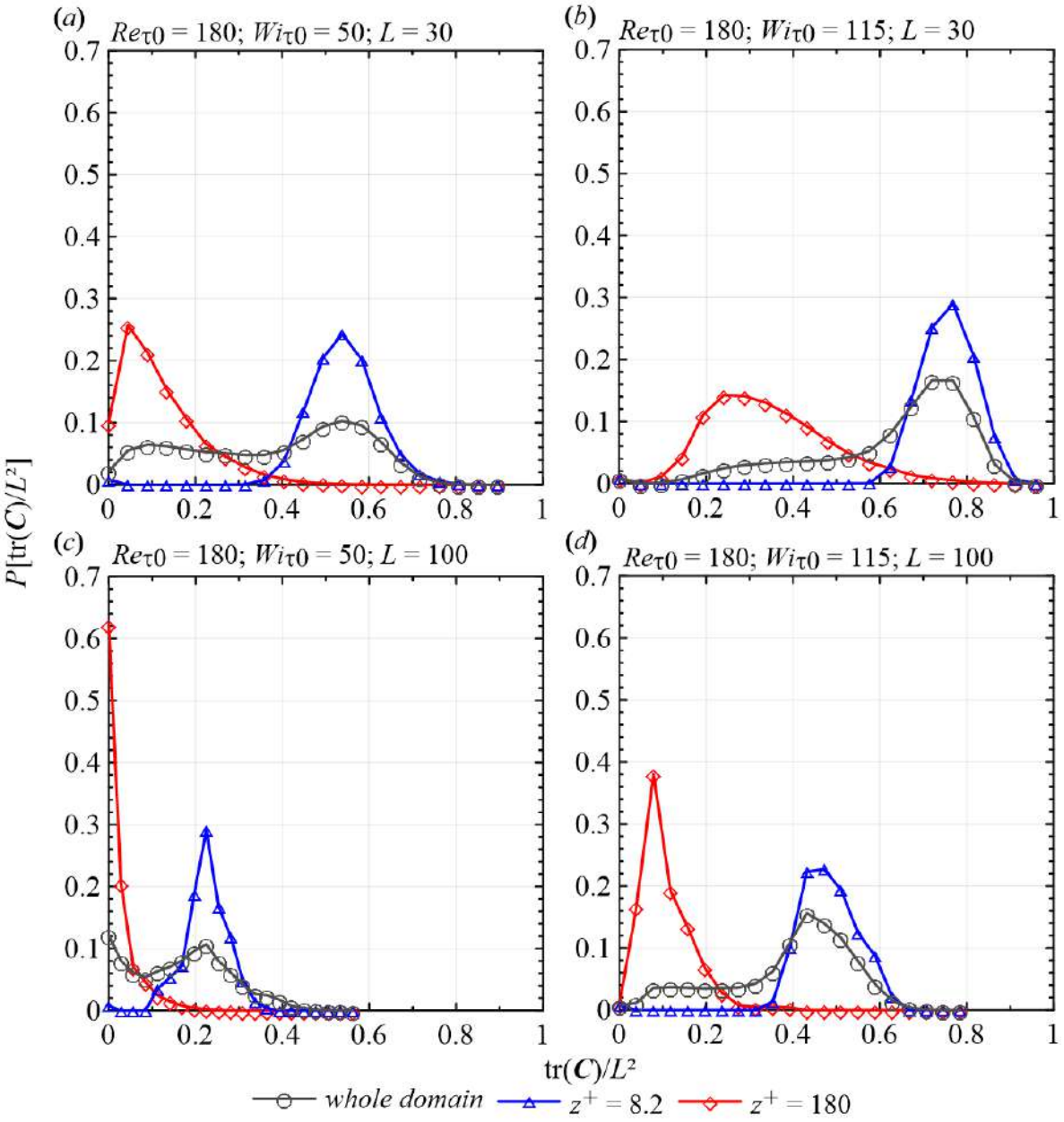

Figure 2.6 – Probability distribution functions of the polymer extensions, $\mathrm{tr}(\boldsymbol{C})/\mathrm{L}^2$.

stretched molecules are noted, and even at the middle of the channel it is possible to find considerably extended ones. The probability distribution functions for the most elastic flow are displayed in figure 2.6(d). We note that these PDF curves are comparable to those in figure 2.6(a), and have the same trends.

2.4.2 Polymer alignment

Figure 2.7 shows the average values in the $x-y$ plane of the cosines of the angles Ψ between the first principal direction, e_1, of our three relevant tensor entities (the eigenvector related to the largest eigenvalue) and the three unit vectors e_x (streamwise; figure 2.7a), e_y (spanwise; figure 2.7b), and e_z (wall-normal, figure 2.7c) against the normalized wall distance, for the Newtonian case.

The alignment between the first principal direction of the velocity fluctuation product tensor, $\boldsymbol{\tau}'$ (whose components are defined by $u_i'u_j'$), and e_x, indicated in figure 2.7(a) by the blue open triangles, is accentuated near the wall, growing within the buffer layer, where $\langle \mathbf{cos}\Psi\left(e_1^{\tau'}, e_x\right)\rangle$ achieves its peak magnitude (≈ 0.85) at $z^+ \approx 8.2$. This is consistent with the fact that $u_x'u_x'$ is the most important component of $\boldsymbol{\tau}'$ in the near-wall region. However, as the wall distance increases, $u_y'u_y'$, $u_z'u_z'$, and $u_x'u_z'$ become important while $u_x'u_x'$ decreases, considerable reducing $\langle \mathbf{cos}\Psi\left(e_1^{\tau'}, e_x\right)\rangle$ in the middle of the channel (≈ 0.57). A different behaviour is observed by analysing the angles between $e_1^{\tau'}$ and both the spanwise and wall-normal directions as functions of z^+, as shown in figures 2.7(b) and (c), respectively. Firstly, at the wall, $\langle \mathbf{cos}\Psi\left(e_1^{\tau'}, e_y\right)\rangle \approx 0.48$ while $\langle \mathbf{cos}\Psi\left(e_1^{\tau'}, e_z\right)\rangle = 0$ due to the wall effects ($u_z'u_z' = 0$). Although an increase in $\langle \mathbf{cos}\Psi\left(e_1^{\tau'}, e_z\right)\rangle$ with z^+ is noted, the buffer layer favours the alignment between $\boldsymbol{\tau}'$ and the streamwise direction. Consequently, $\langle \mathbf{cos}\Psi\left(e_1^{\tau'}, e_y\right)\rangle$ decreases, reaching a minimum value of 0.37 at $z^+ \approx 15$. Lastly, in the middle of the channel, both $\langle \mathbf{cos}\Psi\left(e_1^{\tau'}, e_y\right)\rangle$ and $\langle \mathbf{cos}\Psi\left(e_1^{\tau'}, e_z\right)\rangle$ are approximately 0.5, indicating a random tendency of the alignment of $\boldsymbol{\tau}'$ with both the y and z directions.

The orientation of the rate-of-strain tensor presented in figure 2.7(a), (b) and (c) exhibits an interesting behaviour as the wall distance increases. Since in the viscous sublayer the Reynolds stress tensor is negligible compared to the viscous stress tensor [24], the flow in this region is laminar and, consequently, $\langle \mathbf{cos}\Psi\left(e_1^{D}, e_x\right)\rangle \approx \sqrt{2}/2$, $\langle \mathbf{cos}\Psi\left(e_1^{D}, e_y\right)\rangle \approx 0$, and $\langle \mathbf{cos}\Psi\left(e_1^{D}, e_z\right)\rangle \approx \sqrt{2}/2$. In contrast, in the log-law region, the flow is driven by the turbulence, and $\langle \mathbf{cos}\Psi\left(e_1^{D}, e_x\right)\rangle \approx \langle \mathbf{cos}\Psi\left(e_1^{D}, e_y\right)\rangle \approx \langle \mathbf{cos}\Psi\left(e_1^{D}, e_z\right)\rangle \approx 0.5$, which emerges from a weak velocity gradient, of which the tendency of direction is not clear.

The green open squares in figures 2.7(a), (b) and (c) show the orientation of the vorticity vector. Following the rate-of-strain tensor, beyond the buffer layer ($60 < z^+ < 180$), a chaotic alignment is perceived, since $\langle \mathbf{cos}\Psi\left(\boldsymbol{\omega}, e_x\right)\rangle = \langle \mathbf{cos}\Psi\left(\boldsymbol{\omega}, e_y\right)\rangle =$

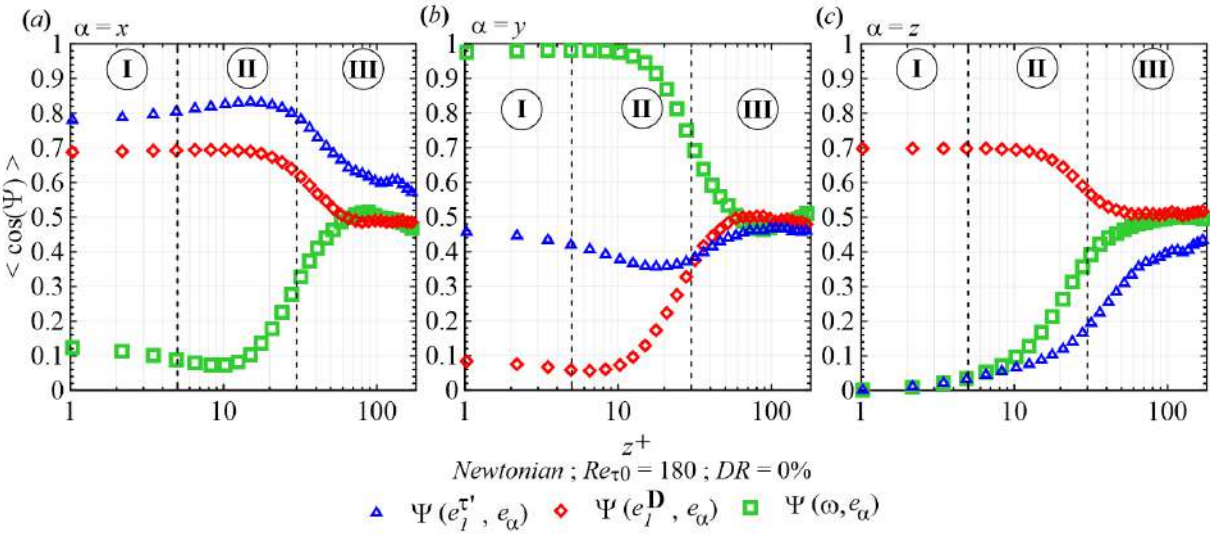

Figure 2.7 – Average values in the $x-y$ plane of the cosines of the angles between the principal directions of a given tensor and the three unit vectors e_x, e_y, and e_z (which represent the streamwise, spanwise and wall-normal directions) against the normalized wall distance.

$\langle \mathbf{cos}\Psi(\boldsymbol{\omega}, e_z)\rangle \approx 0.5$. However, close to the wall ($z^+ < 20$), the vorticity vector tends to be strongly aligned with the spanwise direction.

Following the method described above, the effects of a polymer on the average orientation of our three relevant tensor entities are plotted against the wall distance in figures 2.8 and 2.9 for two drag reduction regimes: the less elastic ($DR = 28.5\%$, $Wi_{\tau 0} = 50$ and $L = 30$) and the most elastic ($DR = 62.3\%$, $Wi_{\tau 0} = 115$ and $L = 100$). In this subsection, we use the acronyms LDR and HDR to refer to these two cases. The orientation of the conformation tensor is also considered.

The polymer alignment in the LDR case is shown in figures 2.8(a), (b) and (c). The grey open symbols indicate that in the viscous sublayer, the conformation tensor is well oriented along the streamwise direction. This preferential alignment between e_1^C and e_x is maintained within the buffer layer. However, it weakens as $\langle \mathbf{cos}\Psi\left(e_1^C, e_y\right)\rangle$ and $\langle \mathbf{cos}\Psi\left(e_1^C, e_z\right)\rangle$ increase from $z^+ = 30$ to $z^+ = 180$, at which point both profiles reach a peak (≈ 0.4) and $\langle \mathbf{cos}\Psi\left(e_1^C, e_x\right)\rangle$ exhibits its minimum value (≈ 0.6). Nevertheless, it is worth noting that even in the LDR middle region region, where the Reynolds stresses are more pronounced, a slight preferential orientation of $\boldsymbol{C}$ with e_x is observed. A comparison of figures 2.8 and 2.9 reveals that $\mathbf{cos}\Psi\left(e_1^C, e_x\right)$ is an increasing function of the elasticity. In the HDR case, the angle between e_1^C and e_x is approximately zero for all z^+, indicating that the polymers are strongly aligned with the streamwise direction throughout the whole channel.

The alignment between the first principal direction of $\boldsymbol{\tau}'$ and e_x for the LDR case displayed in figure 2.8(a) is accentuated at the wall (≈ 0.85), where $\langle \mathbf{cos}\Psi\left(e_1^{\tau'}, e_x\right)\rangle$ is approximately 6% greater than that of the Newtonian case. In addition, the peak

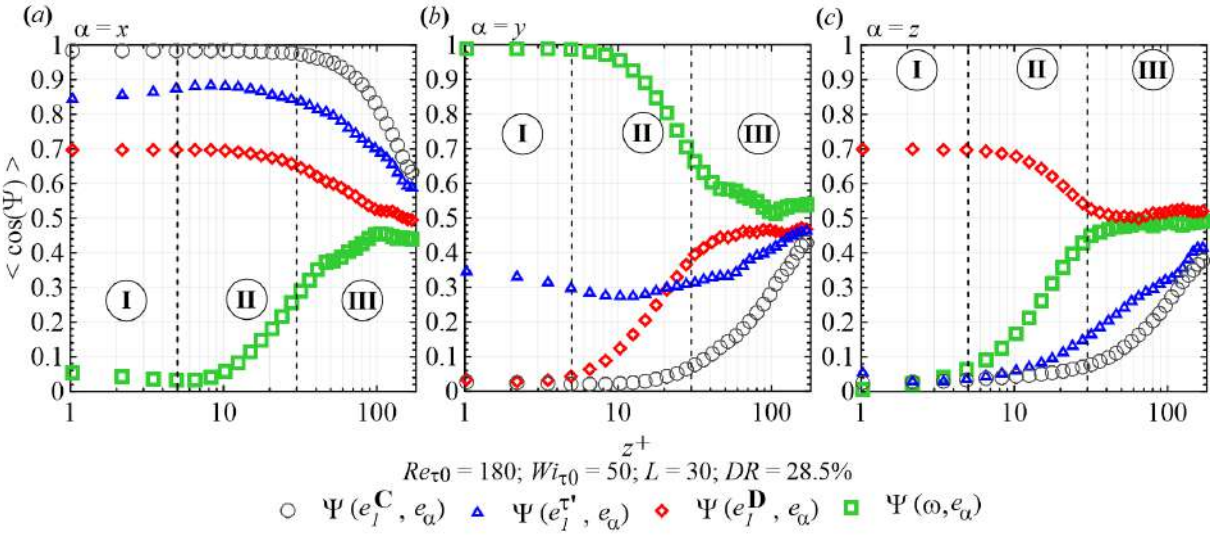

Figure 2.8 – Average values in the $x-y$ plane of the cosines of the angles between the principal directions of a given tensor and the three unit vectors e_x, e_y, and e_z against the normalized wall distance.

magnitude of $\langle \mathbf{cos}\Psi\left(e_1^{\tau'}, e_x\right)\rangle$, which is located in the buffer layer ($z^+ \approx 8.2$), is also 6% larger than for the Newtonian flow. As the wall distance increases, the alignment between $e_1^{\tau'}$ and e_x decreases, achieving its minimum value ($\langle \mathbf{cos}\Psi\left(e_1^{\tau'}, e_x\right)\rangle \approx 0.6$) at the middle of the channel. Analysing the angles between $e_1^{\tau'}$ and both spanwise and wall-normal directions, we initially note that at the wall, $\langle \mathbf{cos}\Psi\left(e_1^{\tau'}, e_y\right)\rangle \approx 0.35$ and $\langle \mathbf{cos}\Psi\left(e_1^{\tau'}, e_z\right)\rangle = 0$. The increasing fluctuation in the streamwise velocity in the buffer layer favours the alignment between $\boldsymbol{\tau}'$ and e_x, which reduces $\langle \mathbf{cos}\Psi\left(e_1^{\tau'}, e_y\right)\rangle$ to its minimum value (≈ 0.3) at $z^+ \approx 15$. After this point, similar to the Newtonian behaviour, $\langle \mathbf{cos}\Psi\left(e_1^{\tau'}, e_y\right)\rangle$ and $\langle \mathbf{cos}\Psi\left(e_1^{\tau'}, e_z\right)\rangle$ increase, reaching their peak magnitude (≈ 0.45) at the middle of the channel. Since, at this location, $\langle \mathbf{cos}\Psi\left(e_1^{\tau'}, e_x\right)\rangle \approx 0.6$, we can conclude that the addition of a polymer reduces the initial random tendency of the orientation of $\boldsymbol{\tau}'$ observed for the Newtonian flow. This polymer effect is more clearly perceived in figures 2.9(a), (b) and (c). In the HDR case, $\langle \mathbf{cos}\Psi\left(e_1^{\tau'}, e_x\right)\rangle$ changes from 0.96, at the wall, to the maximum value of 0.98 within the buffer layer. In contrast, $\langle \mathbf{cos}\Psi\left(e_1^{\tau'}, e_x\right)\rangle$ decreases along the region III, reaching its minimum value (≈ 0.85) at $z^+ = 180$. Additionally, $\langle \mathbf{cos}\Psi\left(e_1^{\tau'}, e_y\right)\rangle$ changes from 0.12, at $z^+ = 0$, to 0.1, in the buffer layer, after which it starts to increase, achieving its peak magnitude (≈ 0.26) at $z+ = 180$. Moreover, $\langle \mathbf{cos}\Psi\left(e_1^{\tau'}, e_z\right)\rangle$ smoothly increases from zero to 0.22 across one-half of the channel. Lastly, it is important to note that in the HDR case, $\langle \mathbf{cos}\Psi\left(e_1^{\tau'}, e_x\right)\rangle > 0.85$ and $\langle \mathbf{cos}\Psi\left(e_1^{\tau'}, e_z\right)\rangle < \langle \mathbf{cos}\Psi\left(e_1^{\tau'}, e_y\right)\rangle < 0.3$ for all z^+. In other words, the addition of polymers induces a preferable alignment of $\boldsymbol{\tau}'$ with the streamwise direction in the whole channel.

The effects of a polymer on the orientation of the rate-of-strain in the LDR case

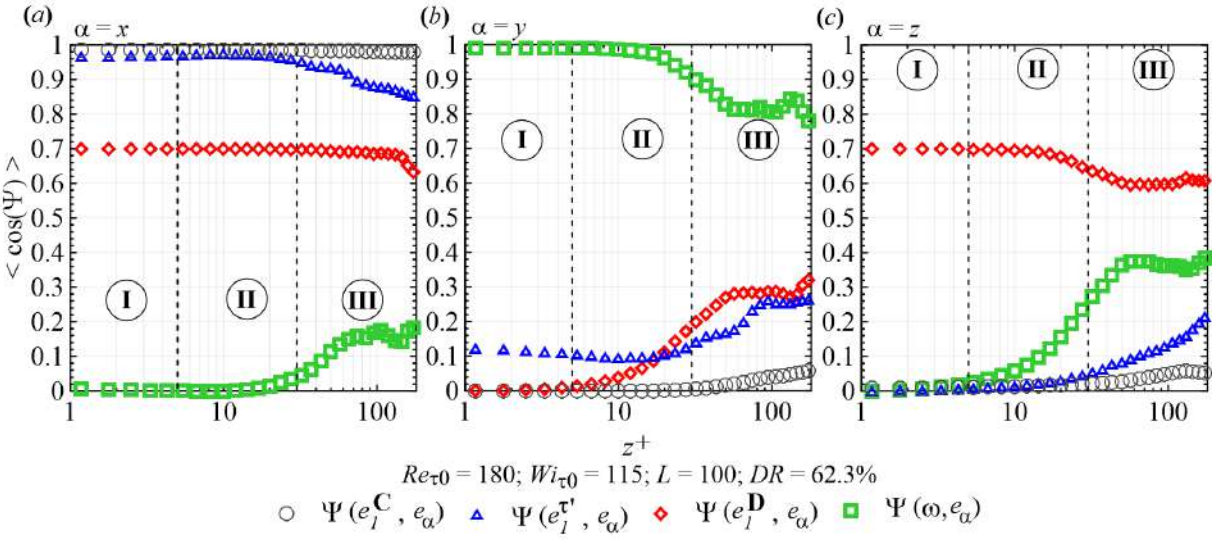

Figure 2.9 – Average values in the $x-y$ plane of the cosines of the angles between the principal directions of a given tensor and the three unit vectors e_x, e_y, and e_z, against the normalized wall distance.

are indicated by the red open diamonds in figures 2.8(a), (b) and (c). In the viscous sublayer, a laminar characteristic eigenvector emerges. Consequently, $\langle \mathbf{cos}\Psi\left(e_1^D, e_x\right)\rangle = \langle \mathbf{cos}\Psi\left(e_1^D, e_z\right)\rangle \approx \sqrt{2}/2$, and $\langle \mathbf{cos}\Psi\left(e_1^D, e_y\right)\rangle \approx 0$. These typical orientations gradually change to random orientations at $z^+ = 180$, which differs from the fast transition observed in the Newtonian case, for which a chaotic tendency of alignment is noted throughout the entire log-law region. In the HDR regime, the alignment is not random, as can be seen in figures 2.9(a), (b) and (c). The angle between e_1^D and e_x is equal to 45^o from the wall to $z^+ = 155$. In addition, $\langle \mathbf{cos}\Psi\left(e_1^D, e_y\right)\rangle < 0.5$ and $\langle \mathbf{cos}\Psi\left(e_1^D, e_z\right)\rangle > 0.4$ for all z^+. Such a behaviour is consistent with the fact that polymers weaken the normal components of $\boldsymbol{D}$ while no significant difference is perceived for its off-diagonal terms compared with the Newtonian case. Thus, polymers act in the flow by partially suppressing the turbulence, making the rate-of-strain tensor more laminar.

Figures 2.8(a), (b) and (c) also show the orientation of the vorticity vector in the LDR regime. The green open squares indicate that although the variations of $\langle \mathbf{cos}\Psi\left(\boldsymbol{\omega}, e_\alpha\right)\rangle$ across the half channel are smoother than those for the Newtonian flow, there are similarities between both the LDR and the Newtonian cases, such as the preferable alignment of $\boldsymbol{\omega}$ with the y direction in the viscous sublayer, and the chaotic orientation of this vector within the log-law region. Nevertheless, the analysis of the alignment of the vorticity for the HDR flow displayed in figures 2.9(a), (b) and (c) reveals that an increasing elasticity amplifies $\langle \mathbf{cos}\Psi\left(\boldsymbol{\omega}, e_y\right)\rangle$, which results from the fact that polymers weaken both $\langle \omega_x \rangle$ and $\langle \omega_z \rangle$ in the region III, but do not affect $\langle \omega_y \rangle$.

Figures 2.7, 2.8 and 2.9 bring out the complexity of the near-wall dynamics in a Newtonian turbulent flow and how much this region is affected by polymers. In

the high drag reduction regime, polymer effects are perceived even far from the wall ($60 < z+ < 180$). The most evident polymer effects shown in these figures are the strong alignment of $\boldsymbol{C}$ and $\boldsymbol{\tau}'$ with x, which increase with increasing elasticity. These preferable streamwise orientations indicate not only that the most significant turbulence–polymer energy exchanges should occur in the x direction, but also that $\boldsymbol{C}$ and $\boldsymbol{\tau}'$ present an significant alignment between them, which can be linked with the coil–stretch process of the polymer. Thus, in order to clarify the role played by the three considered tensors in the polymer extension mechanism, it is convenient to compute their alignments with respect to the local conformation tensor (the eigenvectors of $\boldsymbol{C}$ are the local reference frames), as shown in figures 2.10 and 2.11 for the same LDR and HDR regimes previously analysed in this subsection.

The cosines of the angles between the eigenvectors of $\boldsymbol{C}$ and $e_1^{\tau'}$ in the LDR case are displayed in figure 2.10. Following the blue open triangles in figure 2.10(a), we notice that $\langle \mathbf{cos}\Psi\left(e_1^C, e_1^{\tau'}\right)\rangle$ departs from an accentuated value at the wall (≈ 0.85). Furthermore, the alignment between e_1^C and $e_1^{\tau'}$ becomes more pronounced while moving along the viscous sublayer, achieving its peak magnitude (≈ 0.9) at $z^+ = 8.2$, the exact same location as the maximum polymer extension ($\langle \mathrm{tr}(\boldsymbol{C})/\mathrm{L}^2\rangle \approx 0.8$) observed in figure 2.5. This peak is maintained until $z^+ \approx 12$, from which point $\langle \mathbf{cos}\Psi\left(e_1^C, e_1^{\tau'}\right)\rangle$ starts to decrease to its minimum value (≈ 0.58), located at the middle of the channel. In contrast, $\langle \mathbf{cos}\Psi\left(e_2^C, e_1^{\tau'}\right)\rangle$ and $\langle \mathbf{cos}\Psi\left(e_3^C, e_1^{\tau'}\right)\rangle$ exhibit opposite behaviours along the channel, as shown by the blue open triangles in figures 2.10(b) and (c), respectively. The former is small at the wall and, after reaching its minimum value (≈ 0.27) at $z^+ = 8.2$, tends to 0.5. The latter is very close to zero in the viscous sublayer. However, it slightly increases as the wall distance increases, achieving a peak of 0.4 at $z^+ = 180$. In the HDR case, shown in figures 2.11(a), (b) and (c), $\langle \mathbf{cos}\Psi\left(e_1^C, e_1^{\tau'}\right)\rangle$ changes from 0.96, at the wall, to 0.98 at $z^+ \approx 10$, which represents a peak magnitude 9% greater than that of the LDR case. This value is sustained until $z^+ \approx 15$, from which point the alignment between e_1^C and $e_1^{\tau'}$ gently decreases to its minimum value (≈ 0.85), situated at the centre of the channel. In the opposite sense, increasing elasticity decreases $\langle \mathbf{cos}\Psi\left(e_2^C, e_1^{\tau'}\right)\rangle$ and $\langle \mathbf{cos}\Psi\left(e_3^C, e_1^{\tau'}\right)\rangle$. It is worth noting that the alignment between the first eigenvectors of $\boldsymbol{C}$ and $\boldsymbol{\tau}'$ is significant even at the middle of the channel, where $\langle \mathbf{cos}\Psi\left(e_1^C, e_1^{\tau'}\right)\rangle$ is about 47% greater than in the case of the LDR. This indicates that the interaction between $\boldsymbol{C}$ and $\boldsymbol{\tau}'$ is an increasing function of the elasticity, whose effects are perceptible not only near the wall, but also in the region III.

In the viscous sublayers of both the low and the high drag reduction regimes (figures 2.10 and 2.11, respectively), while e_2^C and e_1^D are almost orthogonal, there is an angle of $\approx 45^o$ between e_3^C and e_1^D, as well as between e_1^C and e_1^D. Interestingly, $\Psi\left(e_1^C, e_1^D\right)$ is maintained across the channel. In contrast, in the LDR scenario, both $\Psi\left(e_3^C, e_1^D\right)$ and $\Psi\left(e_2^C, e_1^D\right)$ become random as the wall distance increases. However, in the HDR

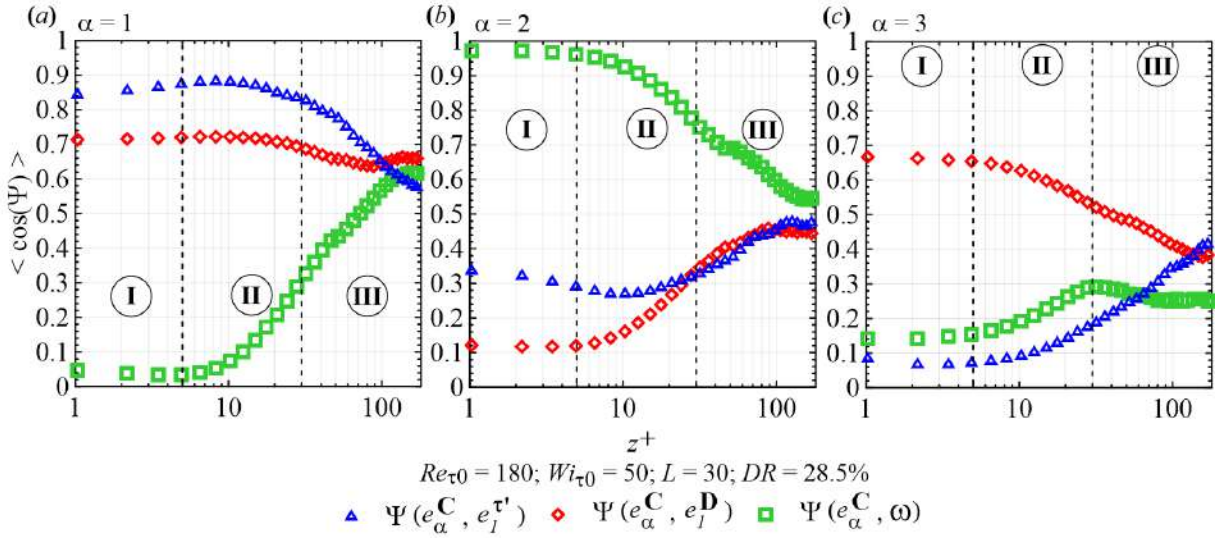

Figure 2.10 – Average values in the $x-y$ plane of the cosines of the angles between the principal directions of the conformation tensor and other relevant entities.

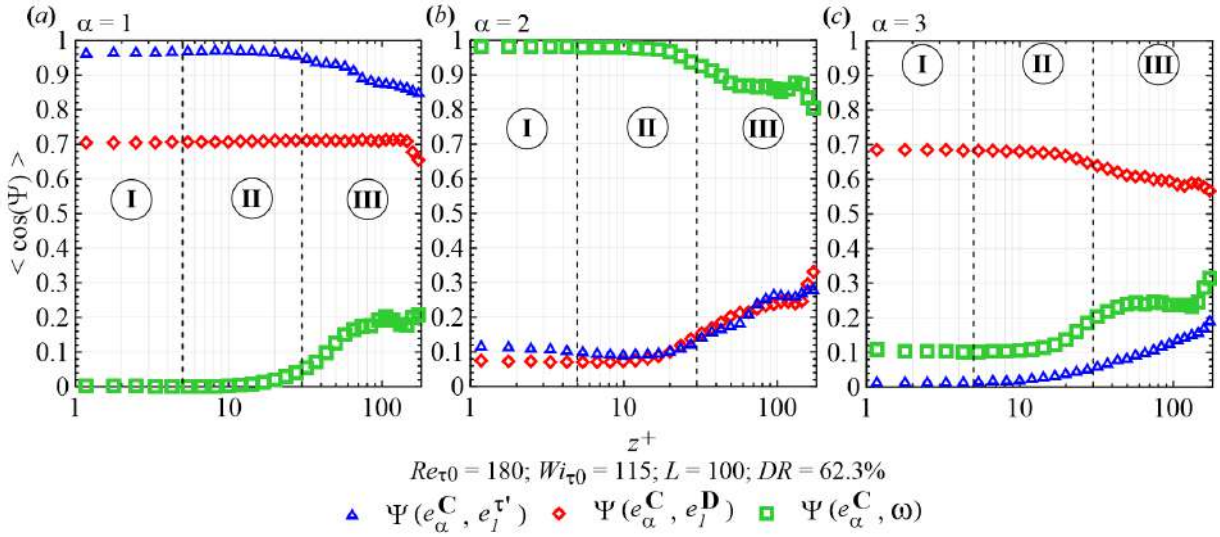

Figure 2.11 – Average values in the $x-y$ plane of the cosines of the principal directions of the conformation tensor and other relevant entities.

regime, this tendency of chaotic alignment within the region III is attenuated, and, in consequence, $\langle \mathbf{cos}\Psi\left(e_3^C, e_1^D\right)\rangle \approx 0.6$ and $\langle \mathbf{cos}\Psi\left(e_2^C, e_1^D\right)\rangle \approx 0.25$. Thus, as $Wi_{\tau 0}$ and L increase, the polymer becomes more exposed to the rate-of-strain tensor not only in I and II, but also in the region III.

Near the wall, the polymer molecules exhibit a weak tendency to lie in the plane perpendicular to $\boldsymbol{\omega}$ since $\langle \mathbf{cos}\Psi\left(e_1^C, \boldsymbol{\omega}\right)\rangle$ and $\langle \mathbf{cos}\Psi\left(e_3^C, \boldsymbol{\omega}\right)\rangle$ are almost zero, as can be seen in figures 2.10 and 2.11. However, one can note that in this region, $\langle \mathbf{cos}\Psi\left(e_2^C, \boldsymbol{\omega}\right)\rangle \approx 1.0$. This occurs because, near the wall, e_2^C is oriented along the e_y direction (not shown here), as is $\boldsymbol{\omega}$ (see figures 2.8 and 2.9).

2.5 Polymer–turbulence energy transfer

2.5.1 Global exchanges of energy

As pointed out in previous subsections, near-wall polymers are highly aligned with $\boldsymbol{\tau}'$ and, consequently, strongly exposed to flow stress fluctuations. The latter are responsible for the generation of intermittent quasi-streamwise vortices, which play a very important role in the momentum exchange as well as in the increase of the turbulent friction drag [50]. Hence, our tensorial and statistical analyses suggest that polymers primarily interact with these intermittent structures, exchanging energy with them. Aiming to characterize such energy exchanges, we consider the work fluctuation terms. These energy terms are that exclusively related to the fluctuating fields which appear in the right-hand side of the work fluctuation equation, which in turn is obtained by decomposing the variables of the momentum equation into mean flow ($\overline{U}_\alpha^+$, $\bar{p}^+$ and $\bar{\Xi}_{\alpha j}^+$) and fluctuations ($u_\alpha'^+$, p'^+ and $\Xi_{\alpha j}'^+$), and then multiplying the resulting equation by the streamwise velocity fluctuation ($u_\alpha'^+$). The work terms exclusively linked with the fluctuating fields are then: $E_\alpha'^+ = \left(u_\alpha'^+ \frac{\partial \Xi_{\alpha j}'^+}{\partial x_j^+}\right)$, $A_\alpha'^+ = \left[-u_\alpha'^+ \frac{\partial\left(u_\alpha'^+ u_j'^+\right)}{\partial x_j^+}\right]$, $P_\alpha'^+ = \left(-u_\alpha'^+ \frac{\partial p'^+}{\partial x^+}\right)$ and $V_\alpha'^+ = \left[(\beta_0)\, u_\alpha'^+ \frac{\partial^2 u_\alpha'^+}{\partial x_j^{+2}}\right]$. Since the turbulent energy exchanges in the x direction constitute more than 90% of that considering the streamwise, the spanwise and the wall-normal directions, we analyse here only the streamwise work fluctuation terms ($\alpha = x$). Hence, the instantaneous polymer work term, $E_x'^+$, indicates the amount of energy stored ($E_x'^+ < 0$) or released ($E_x'^+ > 0$) by the polymers from the fluctuating velocity field in the streamwise direction, $u_x'^+$ (the fluctuations are denoted by the superscript '$\prime$'). The supplementary fluctuating work terms denote the advection, $A_x'^+$, the pressure redistribution, $P_x'^+$, and the viscous stress, $V_x'^+$. The sum $A_x'^+ + P_x'^+ + V_x'^+$ is referred to as the *Newtonian fluctuating work*, $N_x'^+$.

In figures 2.12 and 2.13, the $x-y$ plane average of the instantaneous streamwise work fluctuating terms against the normalized wall distance are considered. In addition,

both $\langle \mathrm{tr}(\boldsymbol{C})/L^2 \rangle$ and $\langle \mathbf{cos}\Psi\left(e_1^{\boldsymbol{C}}, e_1^{\boldsymbol{\tau}'}\right)\rangle$ are plotted. These quantities are denoted by the solid symbols in figures 2.12(d) and 2.12(f), respectively. Different levels of elasticity are considered in figure 2.12 fixing the Reynolds number, while the effects of Re_{τ_0} are shown in figure 2.13 maintaining $Wi_{\tau_0} = 115$ and $L = 100$. Our lowest Reynolds number case ($Re_{\tau_0} = 180$) and the seven viscoelastic flows detailed in table 2.1 are considered.

Very close to the wall (I), where the turbulent stresses are negligible, the work fluctuation terms are close to zero. The streamwise vicous work fluctuation (figures 2.12c and 2.13c) and the streamwise polymer work fluctuation (figures 2.12d and 2.13d) exhibit initially an opposite behaviour. For the less elastic case (blue open triangles), the former decreases from the wall to $z^+ \approx 10$, where its minimum value is located. The latter, one order of magnitude smaller than V_x', increases throughout the viscous sublayer, reaching its peak magnitude at $z^+ \approx 5$. It is worth noting that both the inflexion point of $\langle {E_x'}^+ \rangle$ and the minimum value of $\langle {V_x'}^+ \rangle$ are located at the same wall distance for each case analysed here. Additionally, the maximum values of $\langle \mathrm{tr}(\boldsymbol{C})/L^2 \rangle$ (solid symbols in figures 2.12c and 2.13c) and $\langle \mathbf{cos}\Psi\left(e_1^{\boldsymbol{C}}, e_1^{\boldsymbol{\tau}'}\right)\rangle$ (solid symbols in figures 2.12d and 2.13d), quantities which develop parallel profiles, are observed at the same location ($z^+ \approx 10$ for the less elastic case). Both the advection and pressure terms become less pronounced as elasticity increases, playing a less important role in the fluctuating energy budget under LDR flow conditions (figure 2.12). In the opposite trend, more significant values of $\langle {A_x'}^+ \rangle$ and $\langle {P_x'}^+ \rangle$ are observed at higher Re_{τ_0} (figure 2.13).

The black arrows in figure 2.12 indicate that increasing elasticity makes $\langle {A_x'}^+ \rangle$, $\langle {P_x'}^+ \rangle$, and $\langle {V_x'}^+ \rangle$ close to zero. This effect of increasing elasticity is more pronounced in the viscous term and, consequently, in the Newtonian term $({A_x'}^+ + {P_x'}^+ + {V_x'}^+)$ of which the minimum value changes from $\langle {N_x'}^+ \rangle \approx \breve{}0.225$ for the Newtonian case to $\langle {N_x'}^+ \rangle \approx -0.07$ for the most elastic case (not shown). Furthermore, the minimum and the maximum values observed in figure 2.12 move away from the wall as Wi_{τ_0} and L increase. On the other hand, as indicated by the black arrows in figure 2.13, for a fixed elasticity, the magnitude of the energy budget terms increases with increasing Reynolds number.

Intermittent energy transfers may be hidden even by instantaneous spatial averaging procedures. Further evidence regarding such energy transfers are provided by figure 2.14, which shows five different joint probability density functions (JPF) for the $x-y$ planes related to the less elastic case and located at $z^+ \approx 5.0$, where $\langle {E_x'}^+ \rangle$ is a maximum, as well as that situated at $z^+ \approx 50$, where $\langle {E_z'}^+ \rangle$ is a minimum (not shown here). The black solid line represents the JPF of E_α' vs u_α' (where α can denote either x or z), whereas the red solid line represents the JPF which considers the instantaneous streamwise polymer work fluctuation and the cosine of the angle between the first principal directions of $\boldsymbol{C}$ and $\boldsymbol{\tau}'$. Similar JPFs are displayed in figure 2.15 for the Newtonian work fluctuation at the same $x-y$ planes. The work fluctuation terms were normalized by their temporal root mean square spatially averaged over the corresponding $x-y$ plane. In this figure,

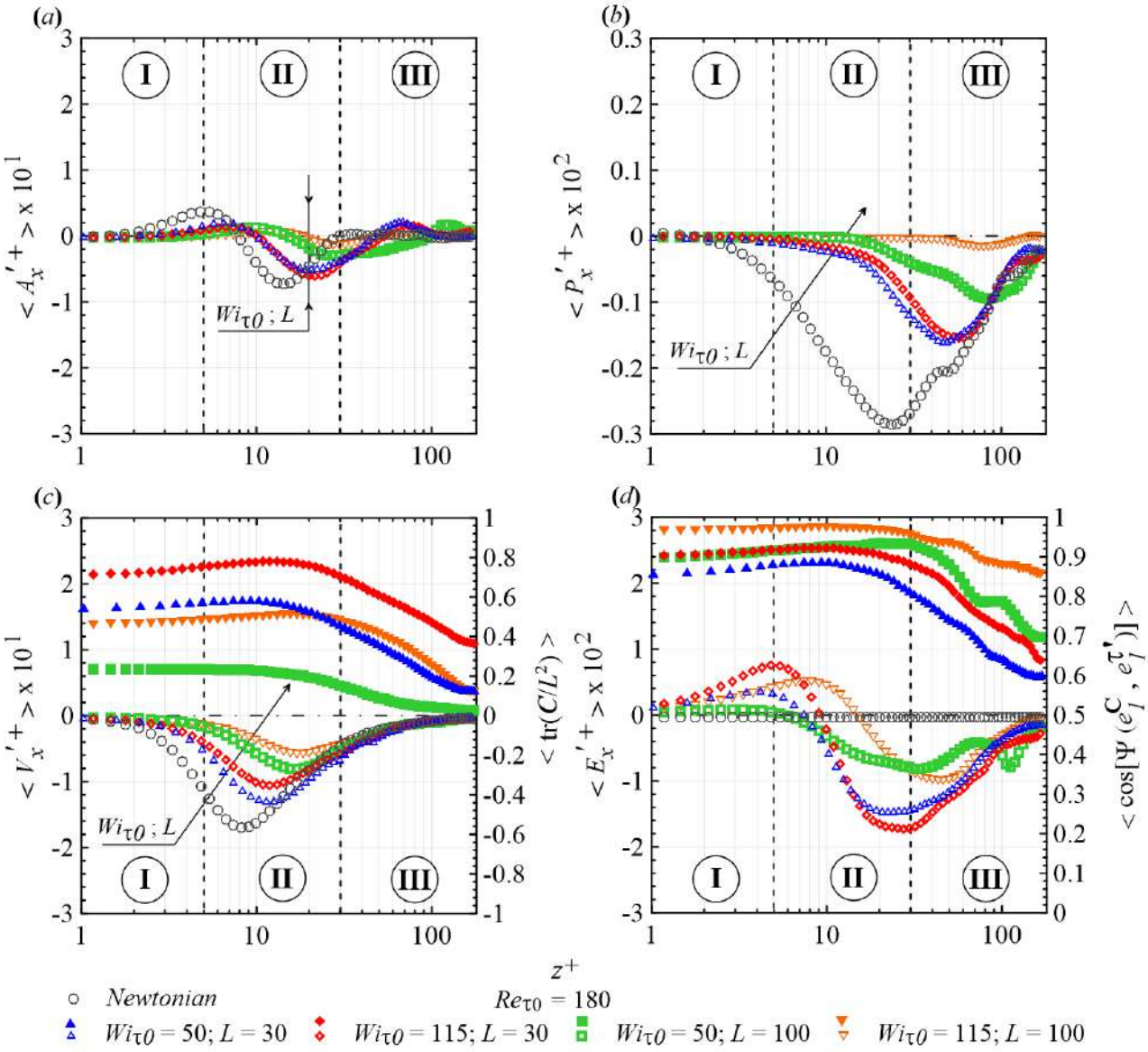

Figure 2.12 – The open symbols show the normalized instantaneous streamwise work fluctuating terms against the normalized wall distance. The solid symbols in (*c*) and (*d*) show the profiles of $\langle \mathrm{tr}(\boldsymbol{C})/\mathrm{L}^2 \rangle$ and $\langle \mathbf{cos}\Psi\left(e_1^C, e_1^{\tau'}\right) \rangle$ across the channel half-width, respectively.

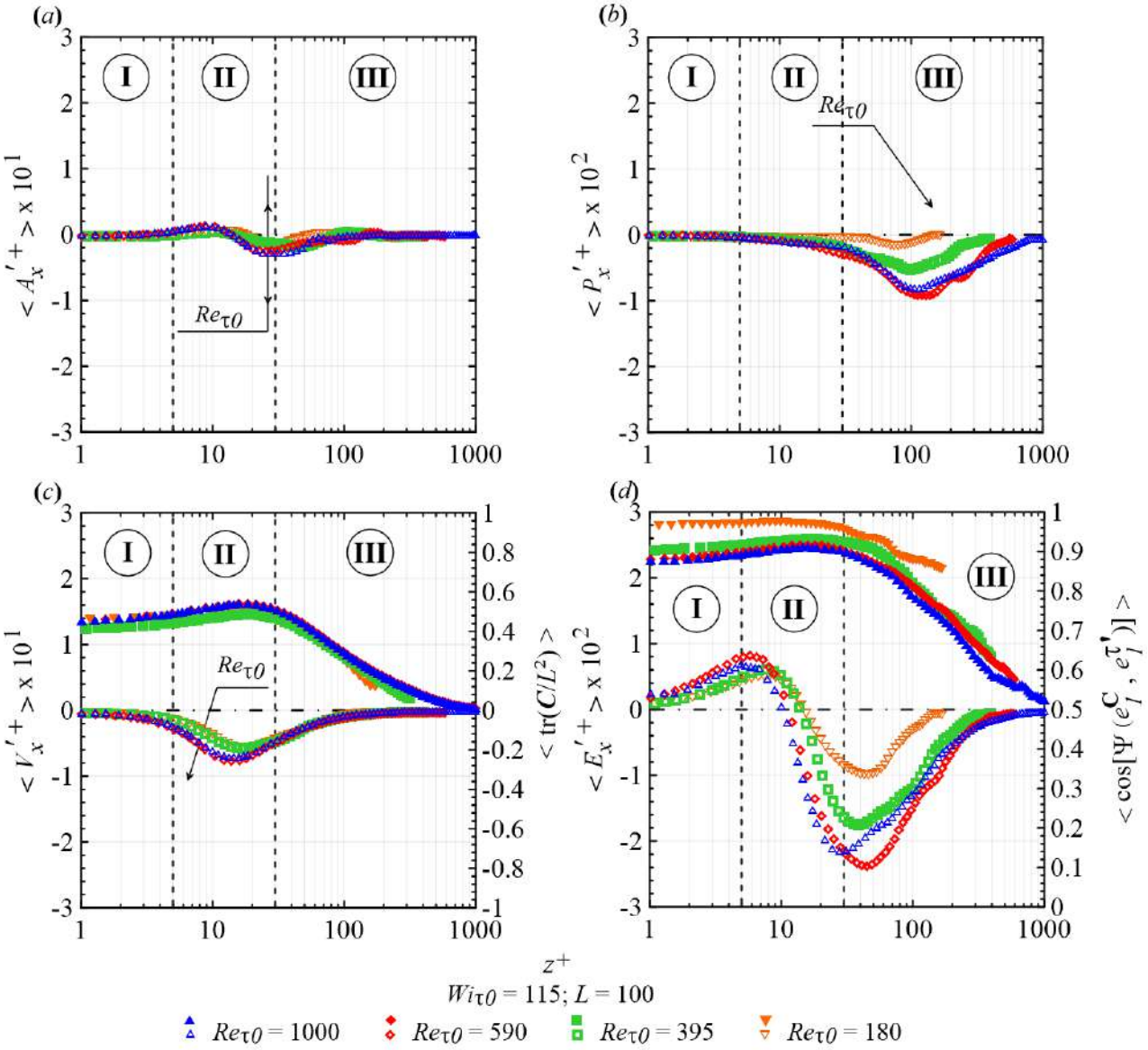

Figure 2.13 – The open symbols show the normalized instantaneous streamwise work fluctuating terms against the normalized wall distance. The solid symbols in (*c*) and (*d*) show the profiles of $\langle \mathrm{tr}(\boldsymbol{C})/\mathrm{L}^2 \rangle$ and $\langle \mathbf{cos}\Psi\left(e_1^{C}, e_1^{\tau'}\right) \rangle$ across the channel half-width, respectively.

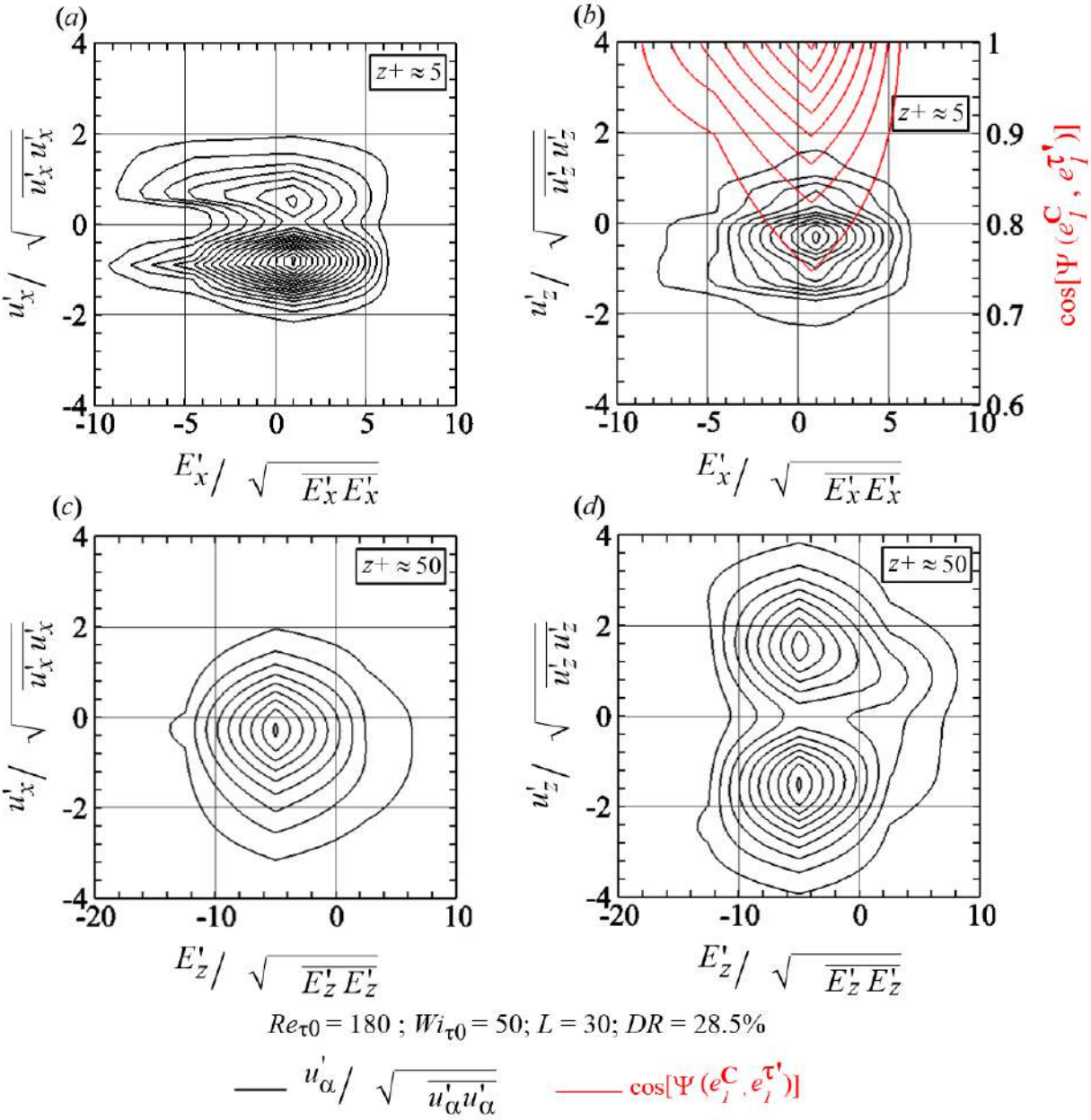

Figure 2.14 – Joint probability density functions of instantaneous polymer work vs instantaneous velocity fluctuation for the $x-y$ planes located at $z^+ = 5.0$ (a and b) and $z^+ = 50$ (c) and d). Fluctuations terms are normalized by their temporal root mean square spatially averaged over the corresponding $x-y$ plane.

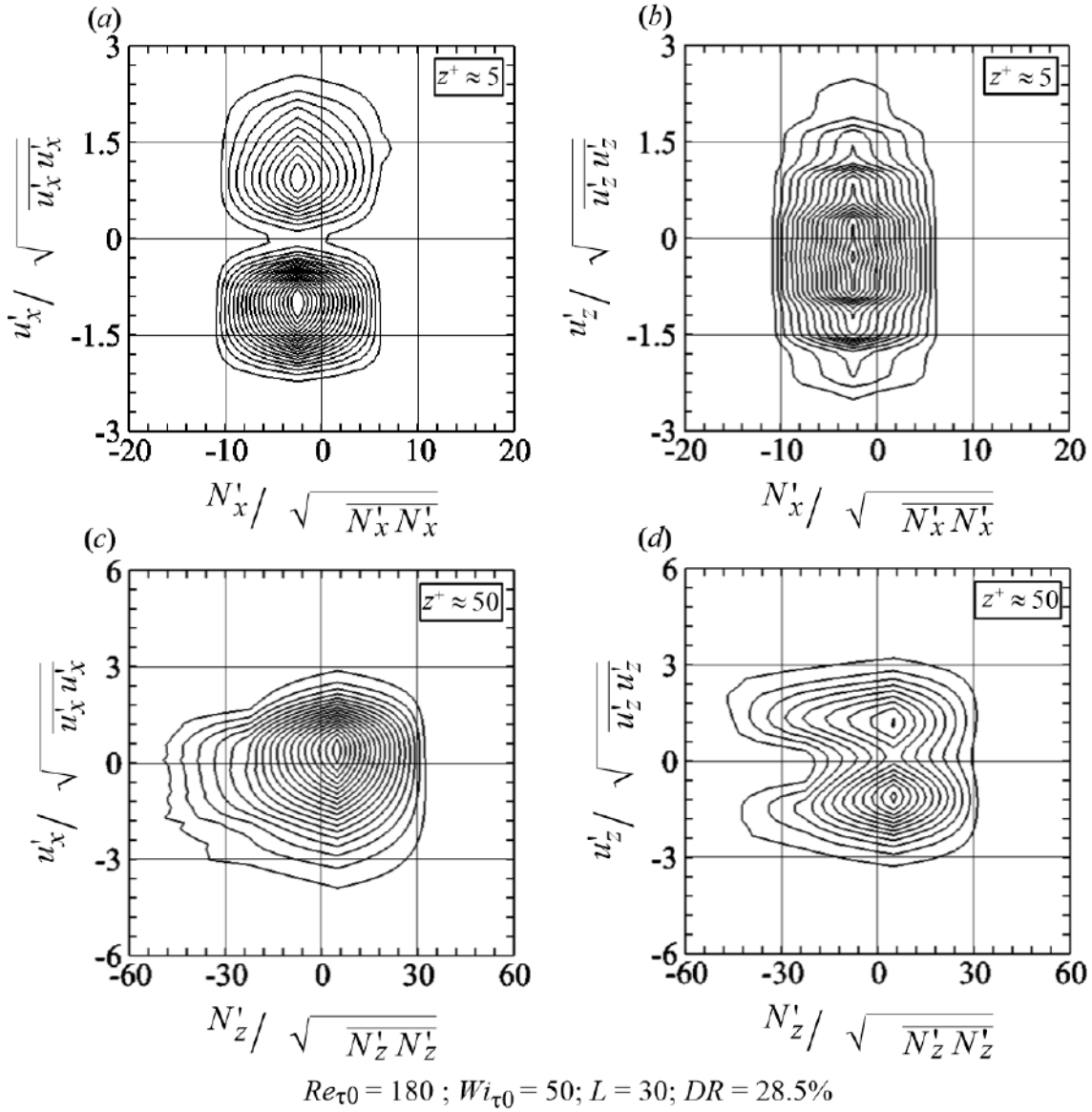

Figure 2.15 – Joint probability density functions of instantaneous Newtonian work vs instantaneous velocity fluctuation over the $x-y$ planes located at $z^+ = 5.0$ (a and b) and $z^+ = 50$ (c) and d). Fluctuations terms are normalized by their respective temporal root mean square spatially averaged over the corresponding $x-y$ plane.

the most probable events are indicated by internal lines. Although only our less elastic fluid is treated in this figure, all the supplementary viscoelastic cases present qualitatively similar trends.

Firstly, with regard to figure 2.14(a), it is important to observe that the polymer molecules are allowed to coil ($E_x' > 0$) and stretch ($E_x' < 0$) within the near-wall region ($z^+ \approx 5.0$). At such a location, the polymer molecules are predominantly injecting energy into the flow ($E_x' > 0$) and, as a consequence, increasing both the negative and the positive streamwise velocity fluctuations as well as the absolute value of T_x' (see figure 2.12). Moreover, this injection of energy is closely related (has a higher probability) to negative values of u_z', as shown in figure 2.14(b). Interestingly, the red solid lines in figure 2.14(b) reveal that more pronounced polymer–turbulence exchanges of energy occur when the conformation tensor is predominantly oriented along the first principal direction of $\boldsymbol{\tau}'$ ($\cos\Psi\left(\mathrm{e}_1^{\boldsymbol{C}}, \mathrm{e}_1^{\boldsymbol{\tau}'}\right) \approx 1$), which reinforces the relevance of the aligment between $\boldsymbol{C}$ and $\boldsymbol{\tau}'$ for the polymer–turbulence exchange of energy.

Figure 2.14 also shows that at $z^+ \approx 50$, polymers primarily extract energy from the flow ($E_z' < 0$), which preferentially occurs where $u_x' < 0$ (figure 2.14c) and $u_z' < 0$ (figure 2.14d). However, the suppression of ejection flows ($u_x' < 0$ and $u_z' > 0$; Q2 region) is also a moderately likely event.

Comparing figures 2.14 and 2.15, it is interesting to note that in the very near-wall region, E_x' and N_x' tend to have opposite signs. Hence, at $z^+ \approx 5$, injection events are strongly related to $E_x' > 0$ and $N_x' < 0$. Similarly, at $z^+ \approx 50$, the ejection and injection events are linked with $E_z' < 0$ and $N_z' > 0$.

2.5.2 Elliptical and hyperbolic exchanges of energy

In order to better understand the polymer coil–stretch process from the energy perspective, we divide the flow into three different regions by using the Q-criterion discussed in subsection 2.4.1. Instead of the usual approach, where a threshold is chosen to produce a Boolean picture of the flow, as in figure 2.3, for example, we adopt the Q-criterion as a measure of the intensity of stretching/rotation activity, i.e. we plot the Q field. To this end, Q is normalized in order to produce values between 0 and 1 [54] and thus takes the form

$$Q_{norm} = \frac{1}{\pi}\cos^{-1}\left(\frac{\|\boldsymbol{W}\|^2 - \|\boldsymbol{D}\|^2}{\|\boldsymbol{W}\|^2 + \|\boldsymbol{D}\|^2}\right). \tag{2.5}$$

Normalized values $0 \leq Q_{norm} < 0.5$ represent *swirling-like* or *elliptical* regions, whereas $0.5 < Q_{norm} \leq 1$ indicates a *non-swirling-like* or *hyperbolic* region. A value of $Q_{norm} = 0.5$ represents transition surfaces where the magnitudes of $\boldsymbol{W}$ and $\boldsymbol{D}$ are equal. This normalized vortex identification criterion was applied to the centre $x - z$ plane (at $y = 0.75\pi$) for all viscoelastic flows corresponding to $Re_{\tau 0} = 180$, as shown in figure 2.16.

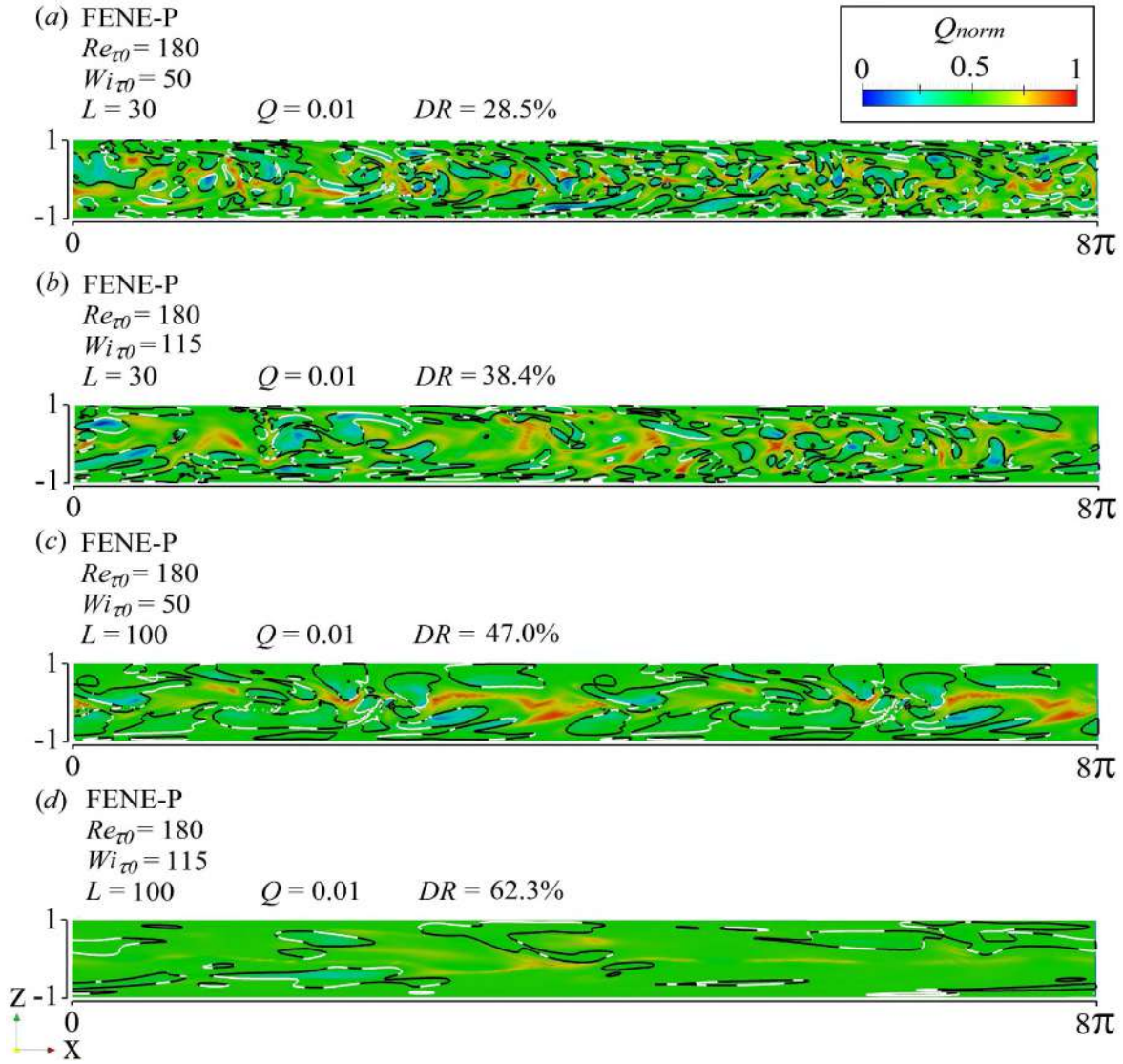

Figure 2.16 – Contour of normalized Q-criterion, Q_{norm}. The lines around vortical regions (blue and green regions) represent intersections between the $x-y$ plane and vortices with $Q = 0.01$. These lines are black or white, which indicates polymer stretching or coiling, respectively.

The vortical regions (swirling-like) are shown in blue, while the extensional regions (non-swirling-like) are shown in red. Green indicates the transition regions, generally referred to as *parabolic*, where the intensities of the rotational and extensional motions are close to each other. The lines around vortical regions represent the intersections between the $x-y$ plane and vortices with $Q = 0.01$ (consequently, the lines surround the blue parts). These lines are black or white, which indicates polymer stretching ($E'_x < 0$) or coiling ($E'_x > 0$) in the streamwise direction, respectively.

Analysing figure 2.16, we first notice that both the vortical and extensional motion are weakened by increasing elasticity. Hence, green regions are more frequent in the HDR cases (*c* and *d*). Furthermore, the lines indicate that the morphology of the vortices changes with an increase of $Wi_{\tau 0}$ and/or L, since their thicknesses and streamwise

lengths increase, while they become more parallel to the wall, something also seen in figure 2.3. Concerning the polymer–vortex interactions, it is apparent that the lines around the elliptical parts are predominantly black. Such a result reveals that polymers essentially stretch in such a region, extracting energy from the vortices. In addition, we note that far from the wall, polymers also store a significant amount of energy from the hyperbolic regions, which are mostly surrounded by black lines as well (not shown for clarity).

The extraction of energy from the elliptical and hyperbolic structures by the polymer is further explored in figure 2.17, where the contours of the normalized Q-criterion were applied to the centre $y-z$ plane (at $x = 4.0\pi$) for our less elastic case. The arrows in figure 2.17(a) indicate the direction and the sense of the vectors resulting from u'_y and u'_z, while those in figure 2.17(b) illustrate the direction and the sense of the vectors resulting from polymer force fluctuations ($f'_\alpha = E'_\alpha/u'_\alpha$) in both the spanwise and wall-normal directions (the vector magnitudes are not considered in these figures). Comparing both of these figures, it is apparent that, fundamentally, the polymer forces oppose the vortical motion (blue regions) by imposing a counter-torque around such structures. However, it is important to stress that in the extensional structures (yellow and red regions) the polymer forces also oppose the fluctuating velocities. Similar results were obtained for the other case (not shown here).

The energy exchanges between the polymers and turbulent structures are highlighted by the open symbols in figures 2.18 and 2.19, where the $x-y$ plane average of the streamwise polymer work fluctuations (a) and the streamwise Newtonian work fluctuations (b) are plotted against the wall distance for both the elliptical (c and d) and the hyperbolic (e and f) regions, separately. Additionally, a similar analysis is displayed for $\langle \mathbf{cos}\Psi\left(e_1^C, e_1^{\tau'}\right)\rangle$ plotted against z^+ (solid symbols in figures a, c and, e).

Considering the whole channel evaluated in figures 2.18(a), 2.18(b), 2.19(a) and 2.19(b) it is found that polymers essentially release energy within the viscous sublayer, since $\langle E_x'^+(z^+ < 5)\rangle > 0$. In contrast, after reaching its maximum value at $z^+ \approx 5.0$, $\langle E_x'^+\rangle$ becomes negative and reaches expressive negative values in the region II ($20 \leq z^+ \leq 30$). Negative values of $\langle E_x'^+\rangle$ are also observed within the region III. Hence, the polymers store turbulent energy in both the region II and III ($E'_\alpha < 0$), and release it into the viscous sublayer ($E'_x > 0$) by coiling along the streamwise direction, which increases the streamwise velocity fluctuations (see figure 2.1b).

Inside the elliptical and hyperbolic structures, the streamwise polymer work fluctuation profiles follow the same trends as those described for the whole channel. Polymers release energy to elliptical (figures 2.18c and 2.19c) and hyperbolic (figures 2.18e and 2.19e) parts located in the near-wall region (I), which had been previously extracted from such structures in the regions II and III. These results corroborate those shown in figure 2.16. On the other hand, in the wall-normal direction as well as in the spanwise

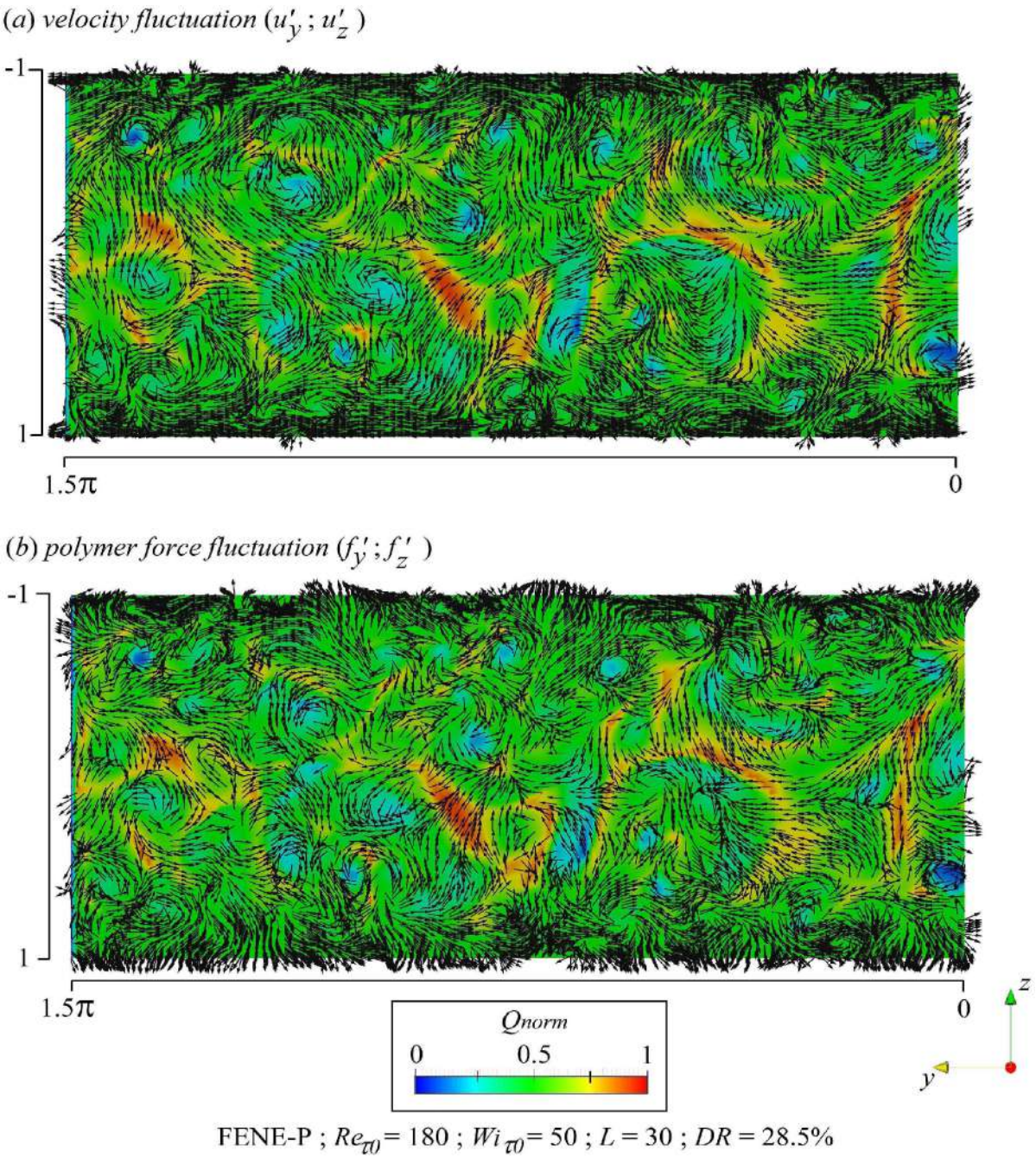

Figure 2.17 – Velocity (a) and polymer body force (b) fluctuation vectors on the $y-z$ plane at $x = 4.0\pi$. Contours of the normalized Q-criterion, Q_{norm}, are also overlaid, with blue regions indicating large swirling strength and red regions representing large extensional deformations.

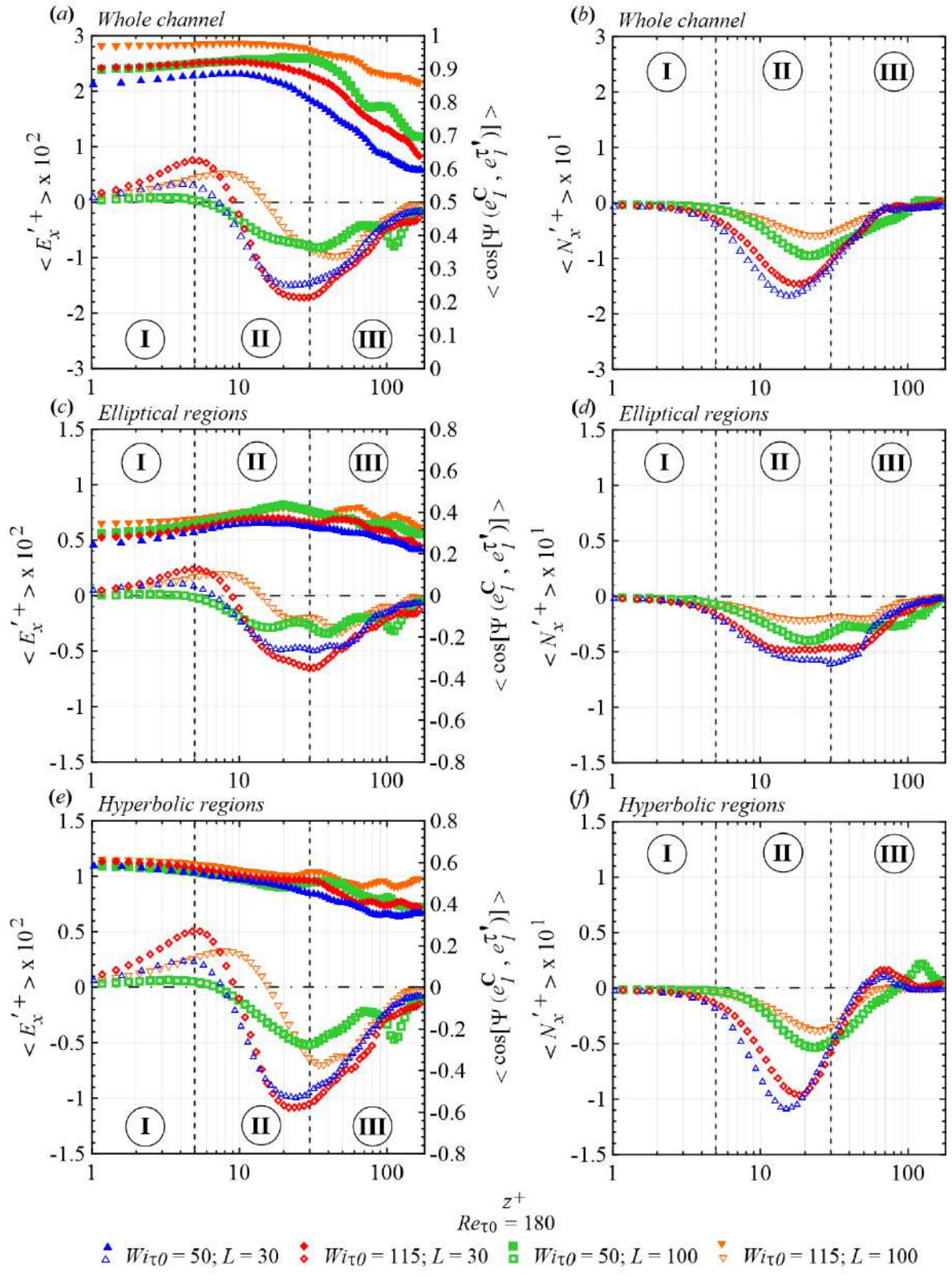

Figure 2.18 – The open symbols show the normalized streamwise polymer (left column) and Newtonian (right column) work fluctuations against the wall (z^+) distance considering the whole channel (*a* and *b*) as well as the elliptical (*c* and *d*) and hyperbolic (*e* and *f*) regions, separately. The solid symbols in (*a*), (*c*) and (*e*) show the profile of $\langle \mathbf{cos}\Psi\left(e_1^C, e_1^{\tau'}\right)\rangle$ against the wall distance, in the same three domains.

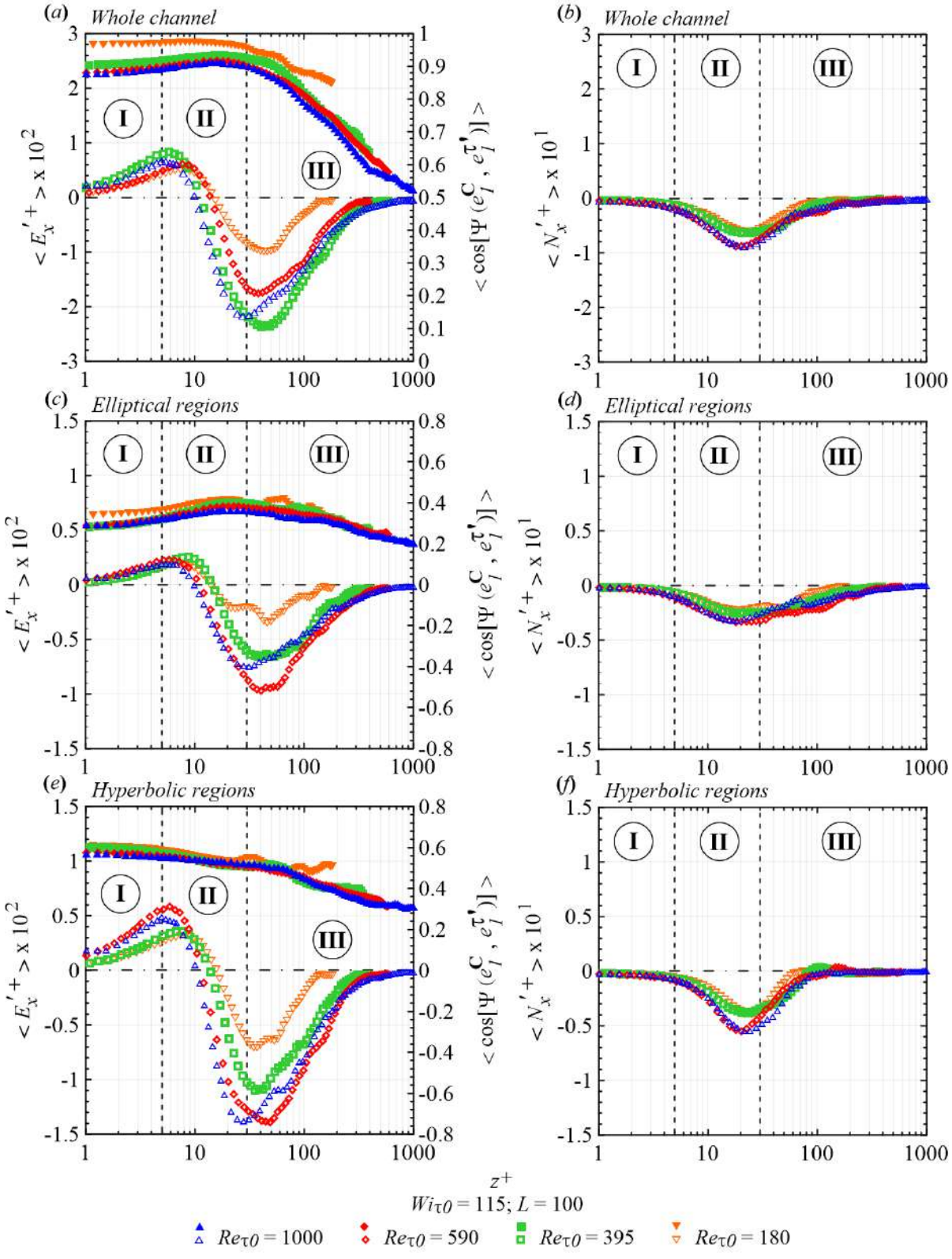

Figure 2.19 – The open symbols show the normalized streamwise polymer (left column) and Newtonian (right column) work fluctuations against the wall (z^+) distance considering the whole channel (*a* and *b*) as well as the elliptical (*c* and *d*) and hyperbolic (*e* and *f*) regions, separately. The solid symbols in (*a*), (*c*) and (*e*) show the profile of $\langle \mathbf{cos}\Psi\left(e_1^C, e_1^{\tau'}\right)\rangle$ against the wall distance, in the same three domains.

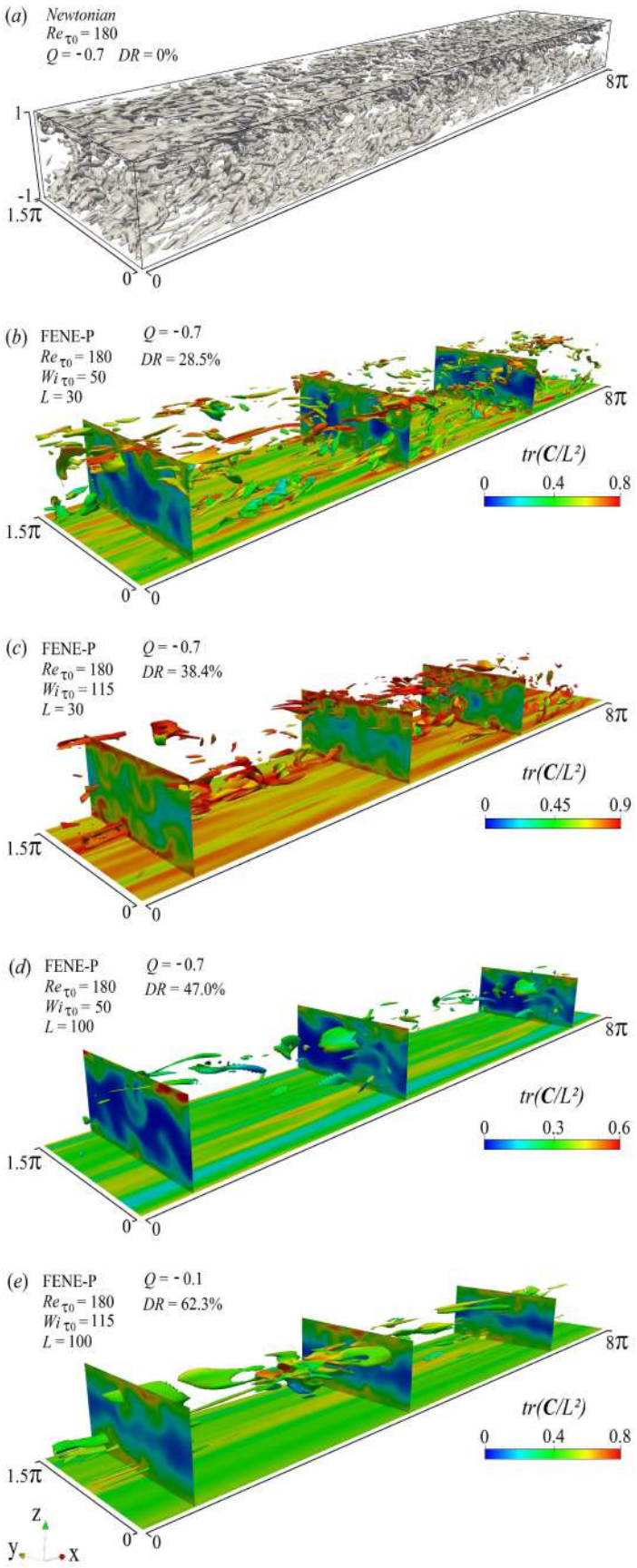

Figure 2.20 – The three-dimensional structures represent the isosurfaces of hyperbolic regions defined as a negative value of the second invariant of the velocity gradient tensor, $\nabla \boldsymbol{u}$. The colours indicate polymer stretching, $\mathrm{tr}(\boldsymbol{C})/\mathrm{L}^2$.

direction (not shown here), the polymer molecules predominantly store turbulent energy from the elliptical and hyperbolic structures by stretching in the region III, which reinforces our remarks concerning figure 2.17. It is important to emphasize that the polymer–turbulence exchanges of energy are more pronounced in hyperbolic regions, especially in the streamwise direction. Lastly, regarding $\langle \mathbf{cos}\Psi\left(e_1^{\boldsymbol{C}}, e_1^{\boldsymbol{\tau}'}\right)\rangle$ (solid symbols), the more significant alignments between $\boldsymbol{C}$ and $\boldsymbol{\tau}'$ are situated in the hyperbolic regions (figures 2.18*e* and 2.19*e*). These alignments decrease monotonically from the viscous sublayer to the centre of the channel.

More significant elastic and inertial effects are observed for $\langle N_x'^{+}\rangle$ (figures 2.18*b* and 2.19*b*), which is essentially negative along z^+ and reaches its minimum value in the buffer layer ($z^+ \approx 20$). This term is one order of magnitude greater than $\langle E_x'^{+}\rangle$ and becomes close to zero as Wi_{τ_0} and L increase, and Re_{τ_0} decreases. Within the elliptical region (figures 2.18*d* and 2.19*d*), no positive values of $\langle N_x'^{+}\rangle$ are observed (figures 2.18*d* and 2.19*d*). However, in the hyperbolic regions (figures 2.18*f* and 2.19*f*), after achieving its minimum value, $\langle N_x'^{+}\rangle$ increases and reaches a positive peak magnitude at $z^+ \approx 70$.

Concerning figures 2.18 and 2.19, it is also important to note that, for each viscoelastic case, the profiles given by the sum of the energy terms shown in figures 2.18(*c*) and (*e*), and in figures 2.19(*c*) and (*e*) at each z^+ are approximately equal to those displayed in figures 2.18(*a*) and 2.19(*a*), respectively, which is also valid for figures 2.18(*b*), (*d*) and (*f*), and figures 2.19(*b*), (*d*) and (*f*). Such a result indicates that the amount of energy exchanged between the polymers and turbulence in the parabolic regions is negligible compared to that occurring in elliptical or hyperbolic regions.

In order to illustrate the role played by the addition of a polymer in the hyperbolic structures of the domain, consider the hyperbolic counterpart of figure 2.3. Since the magnitude of the second invariant of the velocity gradient is not altered when one interchanges the Euclidean norms of $\boldsymbol{D}$ and $\boldsymbol{W}$, a negative value of Q with the same magnitude as the ones depicted in figure 2.3 would give the hyperbolic structure an intensity corresponding to the elliptical structure intensity of that figure, as measured by Q. In this connection, what is seen in figure 2.20 is a distribution over the domain of hyperbolic structures corresponding to: $Q = -0.7$ for the Newtonian (figure 2.20*a*); $Q = -0.7$ for the viscoelastic case with $Wi_{\tau 0} = 50$, $L = 30$ (figure 2.20*b*); $Q = -0.7$ for the viscoelastic with $Wi_{\tau 0} = 115$, $L = 30$ (figure 2.20*c*); $Q = -0.7$ for the viscoelastic case with $Wi_{\tau 0} = 50$, $L = 100$ (figure 2.20*d*); and $Q = -0.1$ for the viscoelastic case with $Wi_{\tau 0} = 115$, $L = 100$ (figure 2.20*e*). A direct comparison between figures 2.3 and 2.20 shows a remarkable similarity in the intensity of the structures. Although there are clear differences in the morphology of the corresponding hyperbolic structures, figure 2.20 shows that these turbulent entities are also weakened by the action of the polymer. As the elastic character of the polymer becomes more prominent, the hyperbolic structures are reduced in intensity and size in a quite similar fashion to what happened with the

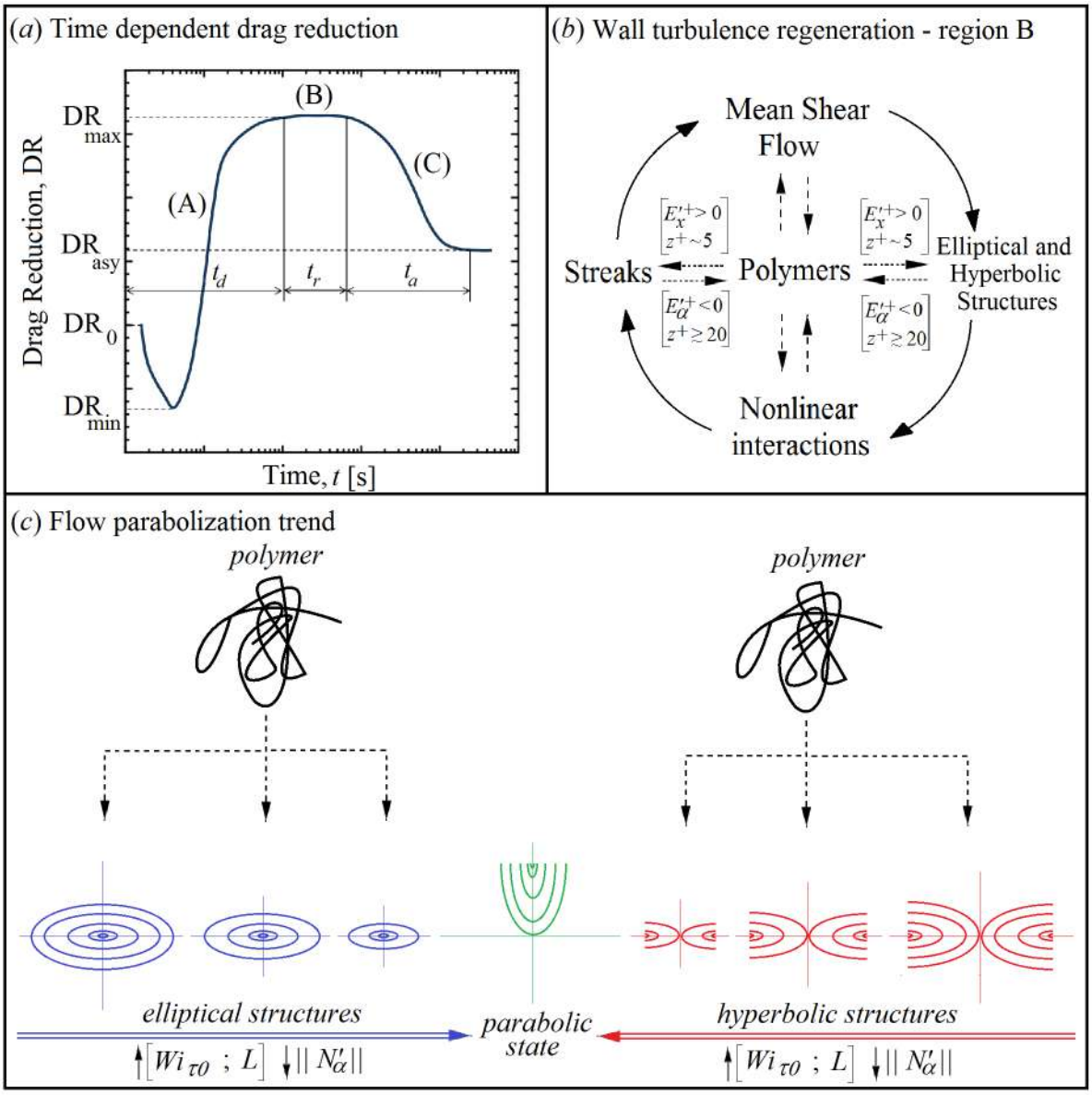

Figure 2.21 – Sketch of the polymer-induced drag reduction mechanism.

elliptical structures displayed in figure 2.3. We can deduce that the polymer molecules interact with the turbulence, damping the elliptical and hyperbolic turbulent structures and leading to a tendency of a dominant parabolic character in the flow domain.

2.6 The DR mechanism

Recently, Andrade et al. [2] experimentally showed that the polymer drag reduction phenomenon undergoes at least three stages over time: A, B, and C, as shown in figure 2.21(a). In stage A, referred to as the *developing time* (t_d), the DR is first negative, due to an instantaneous increase in the local extensional viscosity caused by a large and abrupt polymer stretching. This initial process requires a significant energy input, which comes

predominantly from the mean flow [72], besides a lesser but still important amount of energy that is extracted from the elliptical and hyperbolic structures, since the polymers are strongly exposed to $\boldsymbol{\tau}'$. After reaching a minimum value (DR_{min}), the polymers start their coil–stretch cycle and, in consequence, the DR increases in response to the polymer-flow interactions, achieving a maximum value (DR_{max}), which makes for the beginning of stage B. The duration of stage B is referred to as the *resistance time* (t_r). Such a stage is characterized by a negligible polymer degradation, during which the DR is maintained at its maximum value. In order to describe the polymer coil–stretch mechanisms during stage B, we invoke the autonomous regeneration cycle discussed by Dubief et al. [24], in which we include new details concerning the polymer–turbulent exchanges of energy shown in figure 2.21(b). This autonomous cycle is originally based on that put forward by Jiménez and Pinelli [42] and conceived for Newtonian turbulent flows. In the viscous sublayer, the polymers are highly exposed to the mean flow, which acts as a source of elastic potential energy [86]. Additionally, just above the viscous sublayer ($z^+ \approx 5$), the polymers enhance the streamwise momentum in the elliptical and hyperbolic regions by releasing streamwise turbulent energy ($E'_x > 0$) to such structures (see figure 2.18). However, polymers can be also pulled around the near-wall vortices, passing through hyperbolic regions and experiencing a significant strain within both these turbulent structures. Thereby, as shown in figure 2.18, the polymers store turbulent energy from the elliptical and hyperbolic parts ($E'_\alpha < 0$) in the regions II and III (where they probably also release a non-negligible amount of energy to the mean flow). Lastly, the polymer can be injected (or re-injected) into the very near-wall region, there releasing streamwise turbulent energy and being more exposed to the mean shear. It is worth mentioning that, as shown by the red JPF in figure 2.14(b), more pronounced polymer–turbulence exchanges of energy occur where $\cos\Psi\left(\mathrm{e}_1^{\boldsymbol{C}}, \mathrm{e}_1^{\boldsymbol{\tau}'}\right) \approx 1$.

Since the amount of energy stored by the polymer from the fluctuating velocity field in the regions II and III is greater than that released just above the viscous sublayer, there is a weakening of the elliptical and hyperbolic turbulent structures, as indicated by both the blue and red arrows in figure 2.21(c), resulting in the growth of the parabolic domain. This flow parabolization trend is accompanied by the reduction of the Newtonian work fluctuation as the elasticity increases.

During their coil–stretch cycle, polymer molecules can be mechanically degraded as a result of excessive polymer stretching, which reduces their ability to act as energy exchange agents. Hence, when polymer degradation becomes pronounced, the DR decreases, as represented by stage C in figure 2.21(a), until achieving an asymptotic value (DR_{asy}), which indicates that the degradation has stopped and the molecular weight distribution has reached a steady state.

The coil–stretch mechanism discussed above and sketched in figure 2.21 highlights

the role played by the polymers in the self-sustained wall turbulence interacting with the mean shear, nonlinear interactions, near-wall elliptical and hyperbolic structures in viscoelastic drag reducing flows, considering a DR which evolves over time from the very start of the phenomenon until reaching its asymptotic value.

2.7 Concluding Remarks

The statistical and tensorial analysis of the polymer coil–stretch mechanism in a drag reducing channel flow were conducted by using direct numerical simulations employing the viscoelastic FENE-P model. Four Newtonian flow and seven viscoelastic flows were examined, keeping the viscosity ratio β_0 fixed at 0.9 and taking into account four different values of the zero-shear friction Reynolds number ($Re_{\tau_0} = 180$, $Re_{\tau_0} = 395$, $Re_{\tau_0} = 590$ and $Re_{\tau_0} = 1000$) and two different values of the friction Weissenberg number and the maximum polymer molecule extensibility ($Wi_{\tau_0} = 50$; $Wi_{\tau_0} = 115$; $L = 30$; $L = 100$), which provided drag reduction regimes from 28.5% up to 62.3% (the simulation details are in table 2.1, Section 2.2).

The polymer modifies the mean flow velocity, increasing its streamwise component, which departs from the Prandtl–Kármán law (the onset of DR) up to Virk's asymptote, as $Wi_{\tau 0}$ and L increase. A similar effect is found for the streamwise Reynolds stress normal component, although the other normal components of this tensor decrease (figure 2.1 in Section 2.3). Concerning the relative polymer extension, the polymer molecules exhibit a significant stretch level close to the wall, which reaches its maximum within the buffer layer but is minimal, yet still relevant, at the centre of the channel. Such an extension profile can not, however, be sustained exclusively by the mean flow, although the mean viscous shear stress is the most relevant stretch agent in the very near-wall region (figure 2.2 in Section 2.3). As pointed out in Section 2.4, the stretching produced by the mean flow is increased, since the turbulent structures interact with the polymers molecules, providing a supplementary polymer extension. In fact, polymer molecules are strongly exposed to flow stress fluctuations, which is evidenced by the high degree of alignment between the instantaneous conformation tensor and the instantaneous velocity fluctuation product tensor (especially in the very near-wall region). As $Wi_{\tau 0}$ and L increase, this alignment between both the first principal directions of the conformation tensor ($\boldsymbol{C}$) and the velocity fluctuation product tensor ($\boldsymbol{\tau}'$) becomes more pronounced.

The thickening of the buffer layer was also evidenced by the tensorial and statistical analysis, as shown in subsection 2.4.2. For the most viscoelastic flow, for instance, the angle between $e_1^{\boldsymbol{D}}$ and e_x is equal to 45^o from the wall to $z^+ = 155$, a typical orientation which indicates that the polymers act on the flow by partially suppressing the turbulence, making the rate-of-strain tensor more laminar, viscometrically speaking.

The Q-criterion was used as a measure of the intensity of elliptical (vortices) and hyperbolic structures. A normalized dimensionless version of this criterion was constructed in order to partition the domain into elliptical, hyperbolic, and parabolic regions. The strong interactions between the polymers and intermittent turbulent structures were investigated using perspective of the Q-criterion (Section 2.5). Figure 2.17 showed that the previously documented counter-torque action [46] on the turbulent elliptical structures (vortices) corresponding to blue regions where $Q_{norm} < 0.5$ (or $Q > 0$) is accompanied by a counter-stretch force acting on the hyperbolic structures corresponding to red regions where $Q_{norm} > 0.5$ (or $Q < 0$). To illustrate the polymer–turbulence interactions in the hyperbolic structures, figure 2.20 showed how these structures are weakened as the elasticity is increased from the Newtonian to our maximum drag reduction case. The similarities with respect to the effect on the elliptical structures in terms of the intensity of the structures are remarkable (see figure 2.3). The conclusion reached at this point was schematically represented in figure 2.21(c). An important consequence of the addition of a polymer to turbulent shear flows is the weakening of elliptical and hyperbolic structures, inducing the enhancement of the parabolic domain, which is typical of a viscometric laminar response to an imposed shear flow.

The instantaneous turbulent energy exchange represented by the streamwise work fluctuation terms (Section 2.5) was analysed in this paper by splitting the domain into elliptical and hyperbolic flow regions. Such analyses, combined with the tensorial and statistical ones, allowed us to include more details concerning the polymer coil–stretch mechanism on the autonomous regeneration cycle discussed by Dubief et al. [24] and originally based on that put forward by Jiménez and Pinelli [42] conceived for Newtonian turbulent flows. The Newtonian fluctuating term, $\langle N_x'^{+} \rangle$ exceeds by one order of magnitude the elastic fluctuating term, $\langle E_x'^{+} \rangle$, and, therefore, needs to be taken into account in the description of the DR mechanism. We have noticed higher intensities of these quantities in the hyperbolic domain than in the elliptical ones. In the very near-wall region, polymers not only release energy to the streaks [24], but also to the elliptical and hyperbolic structures. However, these two turbulent structures are damped within the buffer layer. Joint probability functions have shown that more pronounced polymer–turbulence exchanges of energy occur when the conformation tensor is predominantly oriented along the first principal direction of $\boldsymbol{\tau}'$ (figure 2.14). Fundamentally, in elliptical regions, the polymer stores turbulent energy by applying a counter-torque around the vortices, damping the ejection (Q2) and sweep (Q4) events, while, in the hyperbolic regions, polymers take energy from the flow by opposing the extensional deformation. Lastly, it is important to remark that a polymer release of energy occurs almost exclusively in the streamwise direction since $\langle E_y'^{+} \rangle \leq 0$ and $\langle E_z'^{+} \rangle \leq 0$ across the channel half-width (not shown here), which is in agreement with

the increase in the velocity streamwise fluctuation observed in drag reducing flows. Polymers store energy from the mean flow [86] in order to have a considerable stretch in the very near-wall region, and we believe that they can also release energy to the mean flow within the buffer layer, a fact with which the increase in u_x' could be also related, since the mean flow also acts as a source of turbulent kinetic energy in this region.

Chapter 3

On the drag reducing plane Couette flows

Turbulent drag reducing plane Couette flows are analysed using direct numerical simulations of viscoelastic FENE-P fluids. The study is carried out taking into account low and high drag reduction regimes obtained for a large range of Reynolds number (based on the velocities of the plates), Weissenberg number and maximum polymer molecule extensibility. Both the mean and turbulent fields are investigated. The interactions between polymers and turbulence are carefully explored from an energy budget perspective in a flow scenario dominated by large-scale structures. The analyses are complemented by the longitudinal 1D spectra of turbulent kinetic energy. The results are employed to describe a detailed cyclic mechanism of energy exchange between polymers and turbulence in drag reducing flows.

3.1 Introduction

Turbulence represents one of the most challenging subjects of physics. Such a flow regime dramatically increases in complexity when small amounts of polymers are diluted in Newtonian fluids, giving to the problem a viscoelastic character. These molecules induce an significant drag reduction [28, 93, 61] whose practical uses include long-distance transport of liquids [80], oil well operations [15], firefighting [27], transport of suspensions and slurries [29], and biomedical applications [32]. In this context, [97] showed in a pioneering experimental work that if the friction drag for pipe flows is plotted in Prandtl–Kármán coordinates, it departs from the Prandtl–Kármán law (the onset of DR) to its bound, the so-called maximum drag reduction (MDR) or Virk's asymptote, as a result of an increase in either the Reynolds number, the polymer concentration, or the polymer's molecular weight.

Over the years, researchers have experimentally analysed relevant aspects of the

drag reduction phenomenon (DR) and a significant literature is available [36, 98, 63, 96, 12, 13, 60, 33, 44, 65, 82]. Additionally, an extensive number of direct numerical simulations (DNS) of turbulent flows of a viscoelastic finitely extensible nonlinear elastic in the Peterlin approximation (FENE-P) fluid have been conducted [83, 59, 53, 20, 9, 21, 19, 87] in order to investigate the two most prominent theories concerning the exceedingly non-linear nature of DR: the viscous theory [52, 81] and the elastic theory [84]. White and Mungal [102] provide a review of some recent progress in understanding the fundamentals of polymer drag reduction.

Marginally to the prolific discussions around the two main theories referred above, there is an effort on understanding the effects of the interactions between the polymers and the turbulence by investigating how these two entities, representatives of the material and the flow, are correlated to each other. In this connection, it has been observed that, in the viscous sublayer, the polymers are highly exposed to the mean flow, which acts as a source of elastic potential energy [86]. In addition, just above the viscous sublayer, the polymers increase the streamwise momentum of the flow by releasing turbulent energy to its vortical regions [24]. In addition, polymers can be also pulled around the near-wall vortices, passing through vortical regions and experiencing a significant strain within these regions. Consequently, the polymers store turbulent energy from the vortical structures as the wall distance increases by applying a counter-torque around the vortices, which attenuate the drag [47]. Lastly, the polymer can be injected (or re-injected) into the very near-wall region, there releasing streamwise turbulent energy and being more exposed to the mean shear. The energy exhanges between polymers and vortical structures were considered by Dubief et al. [24], who propose a cyclic drag reduction mechanism based on these interactions. This cyclic DR mechanism was recently incremented by Pereira et al. [71], who bring to light new details about the polymer-flow interactions. According to the authors, turbulent extensional structures, as captured by the Q-criterion [38], are also directly damped by the molecules. The preliminary results have shown that the process which occurs within the extensional (or hyperbolic) domain is not less important than the corresponding process in the vortical (or elliptical) parts, which is more established in the literature. In other words, what was shown by Pereira et al. (2016) is that the action of the polymer on turbulence induces a flow evolution towards a parabolic state where elliptical and hyperbolic structures get weaker as a consequence of elastic effects.

The details concerning the DR mechanism recently reported by Pereira et al. reveals that many aspects of the interaction between polymers and turbulent structures remain unclear. These interactions can be intensified in a turbulent plane Couette flow since such a configuration is inherently characterized by the presence of large-scale structures having a typical length up to $30h$ and spanwise size of $4h$ [7, 49], where h is the channel-half height. Turbulent plane Couette flows of Newtonian fluids are described by a

strong inner/outer layer interaction similar to those founded in high-Reynolds-number channels ($Re_{\tau 0} > 1000$; [75]). Hence, as indicated by Bernardini et al. [11], the plane Couette geometry can represent a useful alternative to probe large-scale effects in wall-bounded flow. Here, we consider such geometry in attempt to analyses the polymer-flow interactions in a flow dynamic scenario dominated by large-scale motions.

In the present work, we investigate the drag reduction phenomenon with the aid of direction numerical simulations of turbulent plane Couette flows of viscoelastic FENE-P fluids taking into account a large range of Reynolds number based on the plate velocities ($1000 \leq Re_h \leq 4000$), Weissenberg number based on the plate velocities ($1 \leq Wi_h \leq 10$) and maximum polymer molecule extensibility ($10 \leq L \leq 100$). Statistical analyses are developed in an attempt to highlight the interactions between the polymers and the turbulence in a flow context dominated by large-scale structures. The results which emerge from a careful energy budget investigation enable the addition of new details concerning the effects of the polymers on the autonomous regeneration cycle conceived for Newtonian flows by Jiménez and Pinelli [42], expanded to viscoelastic flows by Dubief et al. [24] and recently revisited by Pereira et al. [71]. A new set of numerical simulations of turbulent plane Couette flows of viscoelastic fluids is described and compared with simulations of plane Poiseuille flows.

The outline of the work is as follows. The description of the physical formulation and numerical methodology are presented in Section 3.2. Our main results are separated in three parts: Sections 3.3, 3.4 and 3.5. Firstly, in Section 3.3, some classical time-averaged quantities are explored. In Section 3.4, we present a detailed energy budget investigation. The energetic analysis is complemented by the longitudinal 1D spectra of turbulent kinetic energy shown in Section 3.5. Finally, in Section 3.6, our results are employed to describe the mechanism of interaction between polymers and turbulence in drag reducing flows.

3.2 Numerical methodology

The parameters for the turbulent Newtonian and FENE-P plane Couette flows studied here are summarized in table 3.1. Our simulated cases were chosen keeping in mind that viscoelastic fluids can have significantly different statistical behaviour from a Newtonian fluid. For a given turbulence level, as parametrized by the Reynolds number, Re_h, based on the plate velocities (defined as $Re_h = hU_h/\nu_{tot}$), this effect can vary with the Weissenberg number, Wi_h (where $Wi_h = \lambda U_h/h$) and the maximum polymer extension length, L. In this work, four Newtonian flows and sixteen viscoelastic flows were examined, keeping the viscosity ratio β_0 fixed at 0.9 and taking into account four different values of the Reynolds number based on the plate velocities ($Re_h = 1000$, $Re_h = 2000$, $Re_h = 3000$ and $Re_h = 4000$). A large range of Weissenberg number based

on the plate velocities ($1 \leq Wi_h \leq 10$) and maximum polymer molecule extensibility ($10 \leq L \leq 100$) were explored, which provided drag reduction regimes (DR) from 0.9% up to 52.8%. The drag reduction level is defined by

$$DR = \left(1 - \frac{\langle \tau_w \rangle}{\langle \tau_{w,N} \rangle}\right) \times 100, \tag{3.1}$$

where $\langle \tau_w \rangle$ and $\langle \tau_{w,N} \rangle$ denote the $x-y$ plane average of the shear stress at the wall for the polymer solution and the Newtonian solvent, respectively.

The geometry extent for the flow cases at $Re_h = 1000$ was $Lx \times Ly \times Lz = 20\pi \times 6\pi \times 2.0$ [5]. For the other Reynolds number flows, $Lx \times Ly \times Lz = 12\pi \times 4\pi \times 2.0$ [11]. The number of mesh points ($Nx \times Ny \times Nz$) for the cases at $Re_h = 1000$, $Re_h = 2000$ and $Re_h = 3000$ was $Nx \times Ny \times Nz = 384 \times 256 \times 127$. In addition, at $Re_h = 4000$, $Nx \times Ny \times Nz = 768 \times 512 \times 257$. These number of mesh points corresponds to a grid resolution of $7.4 \leq \Delta x^+ \leq 16.6$, $3.5 \leq \Delta y^+ \leq 8.3$, and $0.2 \leq \Delta z^+ \leq 5.4$, as shown in table 3.1.

Case	Re_h	$Re_{\tau 0}$	Wi_h	$Wi_{\tau 0}$	L	Δx^+ **x** Δy^+ **x** Δz^+_{min}	Δz^+_{max}	DR[%]
N1	1000	65.5	0	0	0	10.7 x 4.8 x 0.2	1.9	0
A	1000	65.2	1	4.3	10	10.7 x 4.8 x 0.2	1.9	0.9 (LDR)
B	1000	65.0	2	8.5	10	10.6 x 4.8 x 0.2	1.9	1.5 (LDR)
C	1000	64.5	3	12.5	10	10.6 x 4.8 x 0.2	1.8	3.0 (LDR)
D	1000	62.9	4.3	17.0	10	10.3 x 4.6 x 0.2	1.8	7.7 (LDR)
E	1000	59.2	4.3	15.1	30	9.7 x 4.4 x 0.2	1.7	18.4 (LDR)
F	1000	57.8	4.3	14.4	50	9.5 x 4.3 x 0.2	1.7	22.1 (LDR)
G	1000	57.0	4.3	14.0	100	9.3 x 4.2 x 0.2	1.7	24.3 (LDR)
H	1000	62.1	7.5	28.9	10	10.2 x 4.6 x 0.2	1.8	9.6 (LDR)
I	1000	61.7	10	38.0	10	10.0 x 4.5 x 0.2	1.8	11.4 (LDR)
J	1000	55.7	10	31.0	30	9.1 x 4.1 x 0.2	1.6	27.8 (LDR)
N2	2000	118.4	0	0	0	11.6 x 5.8 x 0.3	3.8	0
K	2000	97.6	10	47.6	30	9.6 x 4.8 x 0.3	3.1	32.1 (LDR)
L	2000	89.0	10	39.6	100	8.7 x 4.4 x 0.2	2.9	43.5 (HDR)
N3	3000	169.5	0	0	0	16.6 x 8.3 x 0.4	5.4	0
M	3000	136.5	10	62.1	30	13.4 x 6.7 x 0.4	4.4	35.2 (LDR)
O	3000	119.1	10	47.3	100	11.7 x 5.9 x 0.3	3.9	50.6 (HDR)
N4	4000	220.0	0	0	0	10.8 x 5.4 x 0.2	3.8	0
P	4000	172.0	4.3	31.8	100	8.4 x 4.2 x 0.2	3.0	38.9 (LDR)
Q	4000	151.1	10	57.2	100	7.4 x 3.7 x 0.2	2.6	52.8 (HDR)

Table 3.1 – Parameters for the DNS of Newtonian and FENE-P turbulent plane Couette flows.

Averaging of DNS data is taken in time over some 500 flow snapshots spanning several eddy turn-over times. Two drag reducing regimes are obtained from our drag reducing flows: the high drag reduction (HDR; $DR > 40\%$) observed for the cases A, B, C, D, E, F, G, H, I, J, K, M and P; the low drag reduction (LDR; $DR \leqslant 40\%$) related to the

cases L, O and Q. Physically, the main difference between these two regimes consists in the fact that for LDR flows, the Reynolds stresses play a major role, whereas in the HDR regime, the near-wall dynamics of the flow is dominated by the polymer stresses [102].

Figure 3.1 shows that DR is an increasing function of Wi_h (a), L (b), and Re_h (c). The numerical data illustrated by the blue triangles are well fitted by the red diamonds given by

$$\frac{DR}{Wi_h L} = \frac{a_1 Re_h^{3/7}}{a_2 Wi_h L + a_3}. \tag{3.2}$$

Equation 3.2 was obtained by Pereira and Soares [65] how experimentally analysed the DR phenomenon in a cylindrical double gap rheometer device. Here, the constants $a_1 = 2.0$, $a_2 = 1.1$ and $a_3 = 200$. It is shown that DR saturates at high values of Wi_h and L, which means that the drag reduction is bounded at high values of elasticity Virk's description of the phenomenon [97, 98]. Furthermore, this equation evidenced an important connection between experimental and numerical results.

3.3 Statistics of the flow

3.3.1 Velocity and pressure statistics

The distributions of the mean velocity in wall-coordinates for turbulent plane Couette flows of Newtonian and viscoelastic solutions are displayed in figure 3.2(a). In order to compare our profiles with the classical ones available in the literature, the velocity of the bottom plate was subtracted from the velocity field, resulting in a relative streamwise mean component, $\overline{U_{rx}}$ given by $\overline{U_{rx}} = \overline{U_x} - (-U_h)$. In addition, figures 3.2(b), (c), and (d) show the normal components of the Reynolds stress tensor, $\boldsymbol{\tau}^+$, whose components are defined as the time average of the fluctuation velocity products ($\tau_{ij}^+ = \overline{u'_i u'_j}^+$). In figure 3.2, the bar indicates time average and '$\langle\ \rangle$' denotes the $x-y$ plane average. The effects of Re_h, Wi_h and L on these quantities are analysed.

The results displayed in figure 3.2 are qualitatively similar to those obtained from drag reducing channel flow [71]. The gray circles indicate the Newtonian profiles while the other symbols are related to viscoelastic flows. In the *viscous sublayer* ($0 < z^+ < 5$, region I), where viscous effects are more pronounced, the mean velocities for all cases exhibit a linear shape $\langle \overline{U_{rx}}^+ \rangle = z^+$ represented by the solid grey line (3.2a). Nevertheless, as pointed out by the gray circles in figures 3.2(b), (c), and (d), the Reynolds stress becomes important and comparable to the viscous stress within the Newtonian *buffer layer* ($5 < z^+ < 30$, region II). In this region, the Newtonian mean velocity detaches from the linear profile, assuming a logarithmic dependence on z^+ in the Newtonian *log-law region* ($z^+ > 30$, region III). This log-law velocity profile $\langle \overline{U_{rx}}^+ \rangle = \frac{1}{\kappa}\ln(z^+) + A_1$ is plotted in figure 3.2(a) for a von Kármán coefficient $\kappa = 0.41$ ($1/\kappa$ is the slope) and

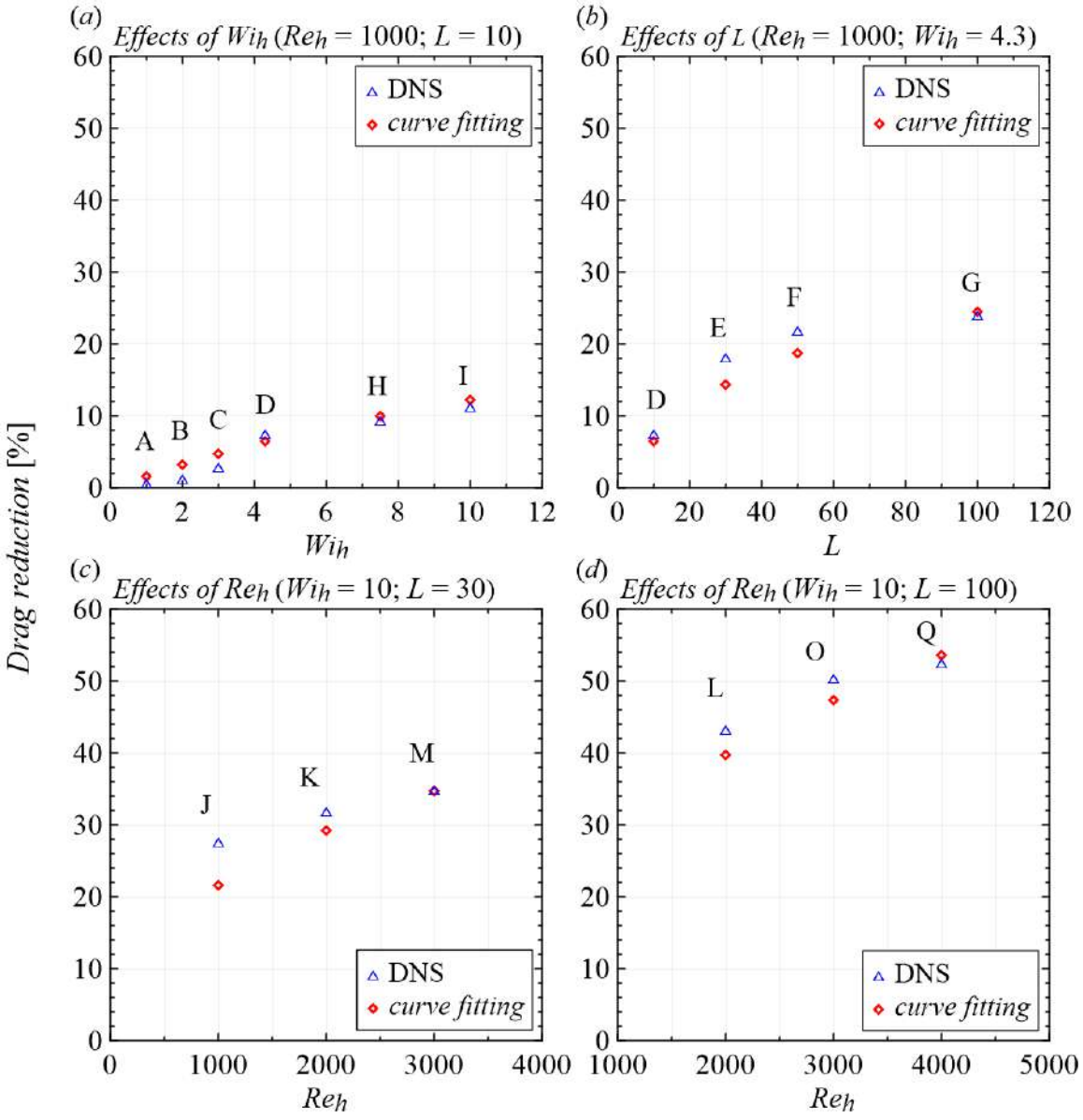

Figure 3.1 – Effects of Wi_h (a), L (b) and Re_h (c and d) on the drag reduction level.

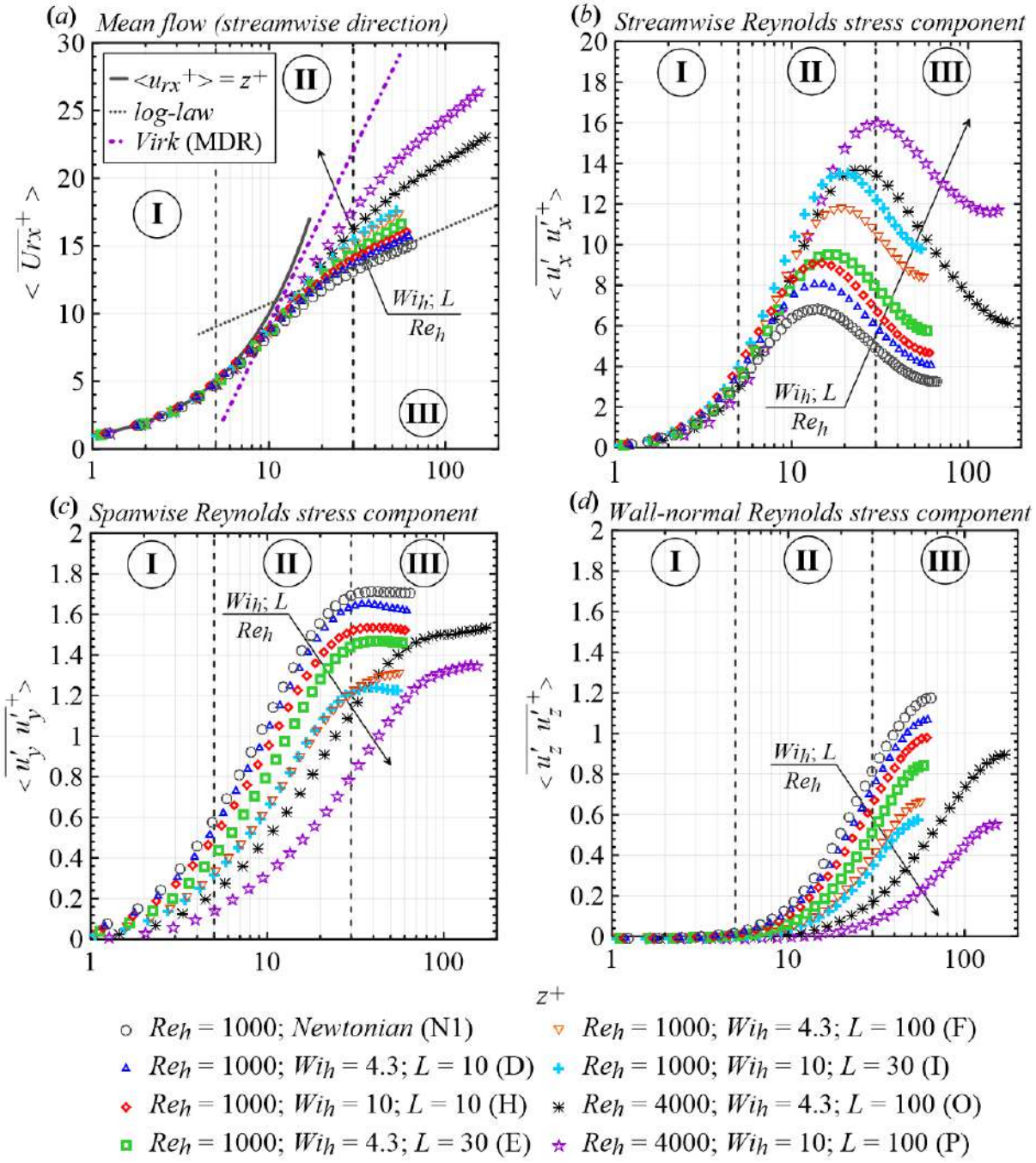

Figure 3.2 – Relative mean velocity profiles in the streamwise direction (a),$\langle \overline{U_{rx}}^+ \rangle$, and normal components of the Reynolds stress (b, c, and d) for Newtonian and viscoelastic plane Couette flows against the normalized wall distance.

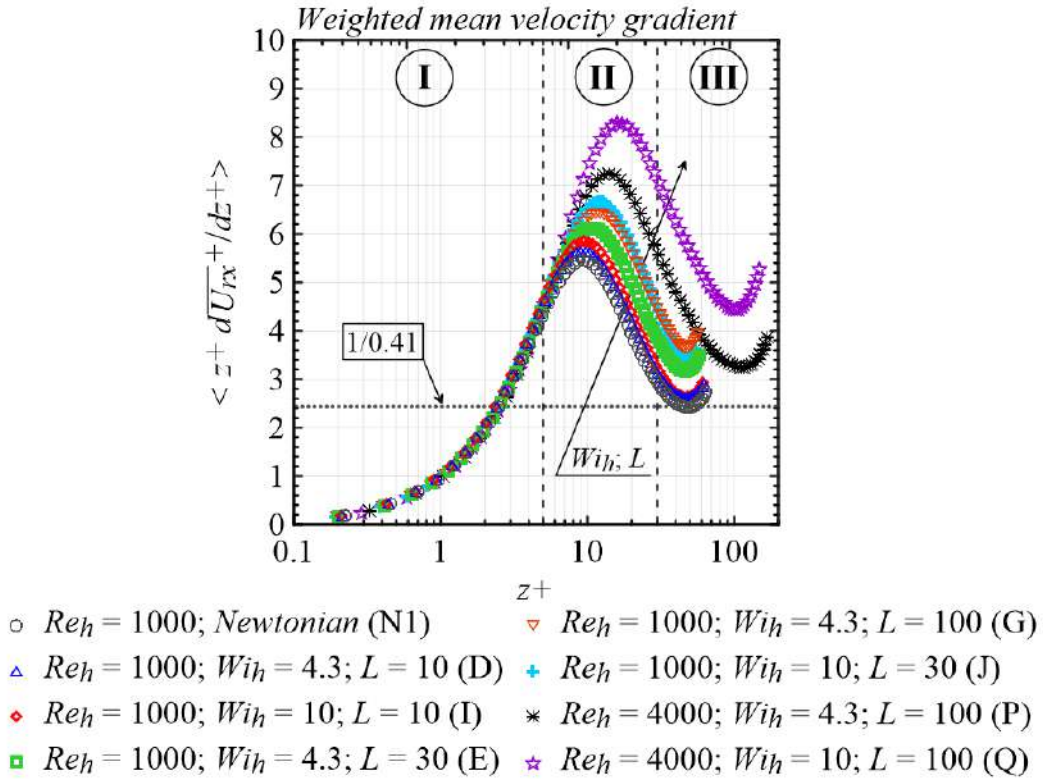

Figure 3.3 – Weighted mean velocity gradient across the half-width plane Couette for Newtonian and FENE-P turbulent flows. The dot straight line has a constant value of 1/0.41.

$A_1 = 5.1$ (the intercept at $z^+ = 1$), as recently reported by Avsarkisov et al. [5]. The addition of flexible polymers in turbulent flow can gradually increase $\langle \overline{U_{rx}}^+ \rangle$ towards the maximum drag reduction level (MDR) represented here by the orange dash-dotted line ($\langle \overline{U_{rx}}^+ \rangle = 11.7 \ln(z^+) + 17.8$; see [98]). The increasing elasticity also increases the streamwise Reynolds stress component in regions II and III, while the other normal components ($\langle \overline{u'_y u'_y}^+ \rangle$ and $\langle \overline{u'_z u'_z}^+ \rangle$) are continuously attenuated. This anisotropic effect of the polymers on the Reynolds stress components was previously reported by many researchers, such as Pinho and Whitelaw [74], Warholic et al. [99] and White et al. [103] who performed experimental and/or numerical analyses in drag reducing channel and pipe flows. Despite this anisotropic effect, it is worth noting that the peak magnitude of the Reynolds stress components moves away from the wall throughout the level of elasticity, suggesting the thickening of the buffer layer predicted by both the viscous [52] and the elastic [84] theories.

Comparing the mean velocity profiles shown in figure 3.2(a), it is interesting to observe that the curves of LDR cases are shifted upwards, developing velocity profiles which are parallel to the Newtonian one. In addition, the HDR flows exhibit a different mean velocity curve with the slope $1/\kappa$ increasing towards the MDR. Such a behaviour suggests a significant extension of the buffer layer into the plane Couette flow and can

be further evidenced by analysing the log-indicator function plotted in figure 3.3. As recently reported by Avsarkisov et al. [5], the Newtonian curves collapse up to their first minimum at $z^+ \approx 60$, which, according to Hoyas and Jiménez [37], can be taken as a lower limit for the Newtonian outer layer ($z^+ \geq 60$). At this location, $\langle z^+ \frac{\partial \overline{U_{rx}}^+}{\partial z^+} \rangle \approx 1/0.41$ for the Newtonian turbulent flows. For the LDR cases shown in figure 3.3(a), this minimal value is an increasing function of Wi_h and L. However, when the HDR regime is achieved (figure 3.3b), the log-indicator curve dramatically changes and its minimum peak magnitude becomes unidentifiable, indicating the thickening of the buffer-layer and the consequent suppression of the log-law region.

The interactions between polymers and turbulent fields also modify the time standard deviation statistics of the fluctuating vorticity normalised by viscous scales, $\boldsymbol{\omega}'^+$, as illustrated in figure 3.4 for different viscoelastic cases. As the elasticity increases, a persistent attenuation of the streamwise vorticity fluctuations, $\omega_x'^+$, is perceived along the normalised wall distance (figure 3.4a). Additionally, the distance between the local minimum and maximum of $\omega_x'^+$ are displayed away from each other when increasing the elasticity, which can be interpreted as an increase in the average size of the streamwise vortices induced by the polymers [19]. Interestingly, the polymer effects on both the spanwise ($\omega_y'^+$) and wall-normal ($\omega_z'^+$) vorticity fluctuations exhibit a transitional character (figures 3.4b and c, respectively). The presence of the molecules partiality suppresses the former in the near-wall region (I) and increases it further away while DR becomes more pronounced. The latter departs from zero at the wall due to the no-slip boundary conditions and achieves its peak magnitude in region II, where it is inhibited and shifted away from the wall as DR increases. However, in region III, an opposite trend is observed since polymers produce an increase in $\omega_z'^+$. We believe that this transitional behaviour of $\omega_y'^+$ and $\omega_z'^+$ is possibly related to the increase in $u_x'^+$ evidenced in figure 3.2.

It is worth noting that the most significant polymer effect on $\boldsymbol{\omega}'^+$ is the attenuation of its streamwise component across the plane Couette geometry. The weakening of the streamwise vortices as well as their morphological changes have been reported by many authors trough numerical channel flow analyses (see, for instance, [21, 46, 47, 71]). Here, these changes are illustrated from a coherent structure perspective by considering the isosurfaces given by $\overline{U_z}/U_h = 0.008$ (red) and $\overline{U_z}/U_h = -0.008$ (blue) in figure 3.5. The effects of Wi_h and L are analysed by keeping Re_h fixed at 1000. The long counter-rotating pairs which emerges from such analysis are generated by low–speed velocity streaks which appear due to a quasi-periodic process in the core region of the turbulent plane Couette flow [35, 48, 75, 11, 57]. This process does not occur in turbulent plane Poiseuille flows and it is considerable affected by the presence of polymers, as observed by comparing the flows displayed in figures 3.5(a) and (b). For the Newtonian fluid shown in figure 3.5(a), five counter-rotating pair are found in the

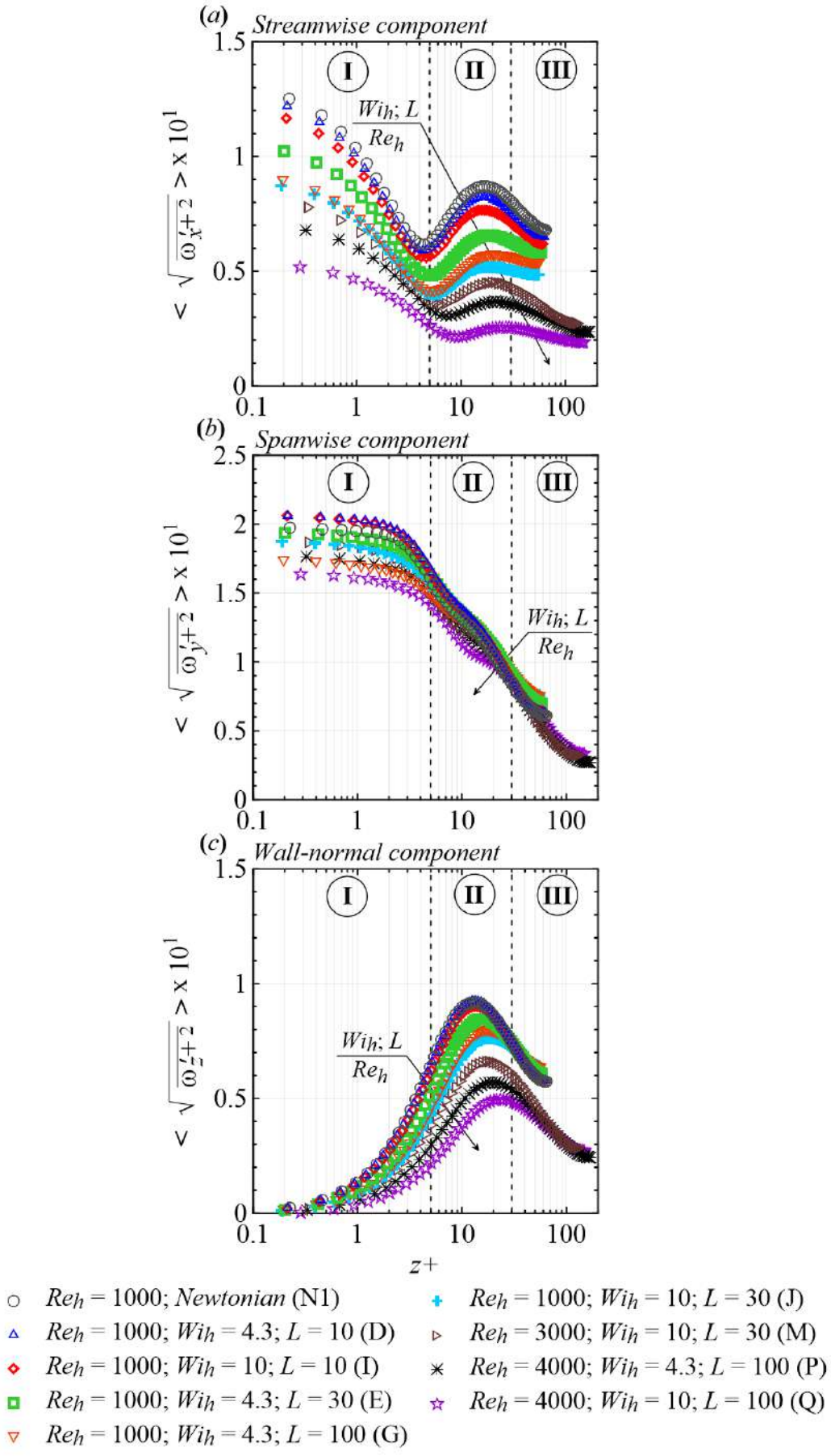

Figure 3.4 – Standard deviation of the normalized vorticity components across the half-width plane Couette for Newtonian and FENE-P turbulent flows.

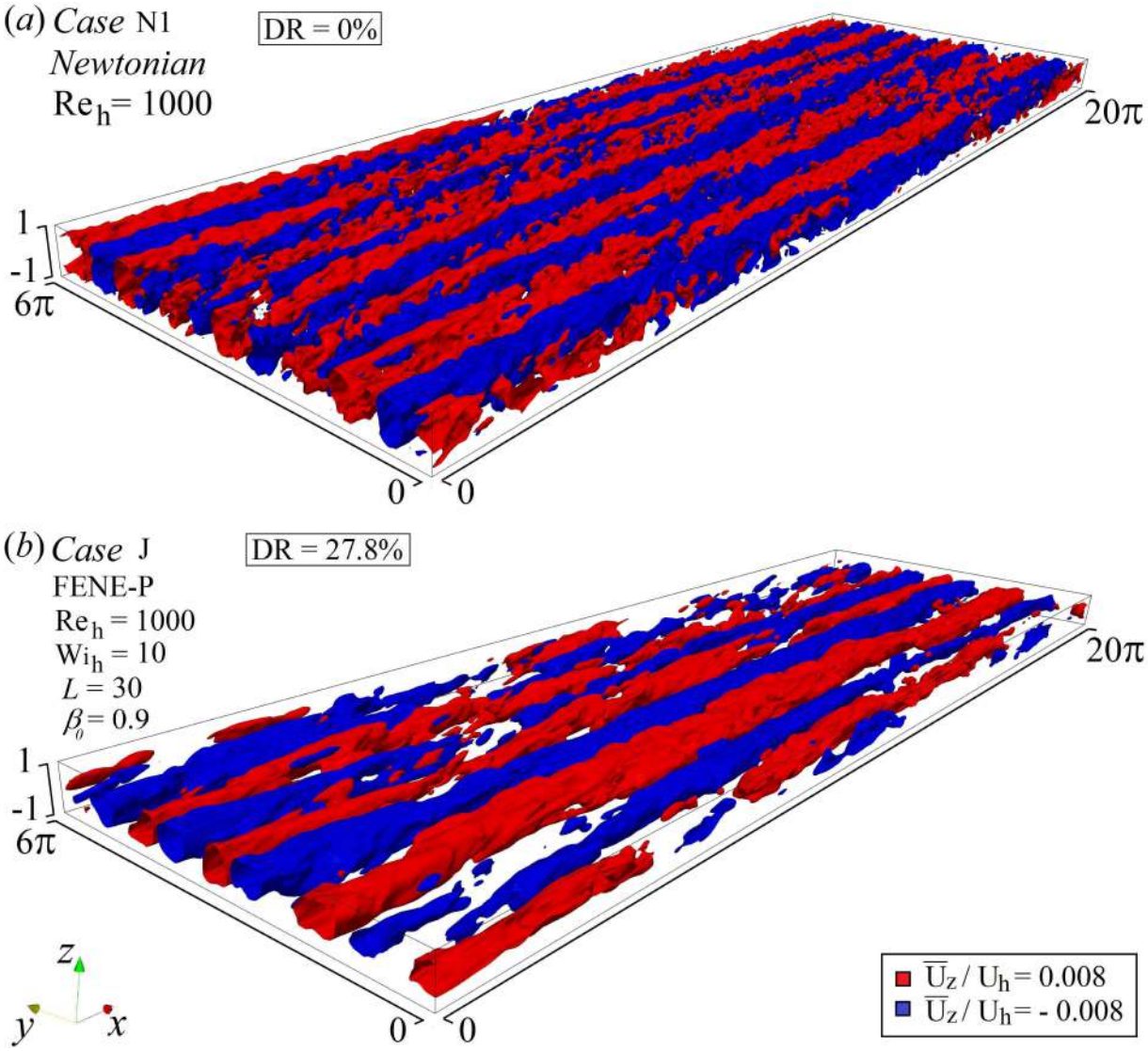

Figure 3.5 – Coherent structures given by $\overline{U_z}/U_h = 0.008$ (red) and $\overline{U_z}/U_h = -0.008$ (blue) through all the plane Couette geometry.

box. However, as the elasticity gradually increases, the rotating structures become less numerous and, consequently, in figure 3.5(b) only 4 counter-rotating pairs are observed. Comparing figures 3.5(a) and (b), it is noted that the molecules not only weaken and suppress the rotating structures, but also widen them, as previously indicated in figure 3.4(a).

The anisotropy invariant map of the Reynolds stress anisotropy tensor ($b_{ij} = \langle \tau_{ij}^{+} \rangle / (\langle tr(\boldsymbol{\tau}^{+}) \rangle - \delta_{ij}/3)$ shown in figures 3.6 (for Newtonian cases) and 3.7 (for viscoelastic cases) provides more details about the morphological changes in turbulence caused by the polymers. The map consist in cross-plotting the second and third invariants of b_{ij}. The former, II_b, is given by $II_b = -b_{ij}b_{ji}/2$, while the latter, III_b, is calculated as $III_b = b_{ij}b_{jk}b_{ki}/3$. The top boundary of the map ($II_b + 3III_b = -1/9$) designates a 2-D anisotropic turbulence (ellipsoid). The top vertex ($\frac{2}{27}$, $\frac{1}{3}$) indicates the 1-D state (line; most anisotropic state). The vertex located at the point ($\frac{-1}{108}$, $\frac{1}{12}$) represents the 2-D isotropic turbulence (disk), while the bottom one (0,0) characterises the 3-D isotropic turbulence (sphere). The boundary in between, $(-III_b/2)(-II_b/3)^{3/2} = 1$, indicates a 3-D pancake-like turbulence (oblate spheroid). Lastly, the bottom boundary, $(III_b/2)(-II_b/3)^{3/2} = 1$, defines a 3-D cigar-like turbulence (prolate spheroid). Near the wall, all turbulent flows analysed here exhibit a 2-D anisotropic behaviour. However, drag reducing flows can be dramatically more anisotropic than the Newtonian ones, since there is significant migration in the FENE-P cases towards the top vertex when increasing DR (the case J almost reaches the one-component apex of the map). In other words, in drag reducing flows, $\overline{u'_x u'_x}^{+}$ tends to be much larger than $\overline{u'_y u'_y}^{+}$ and $\overline{u'_z u'_z}^{+}$ since both the spanwise and the wall-normal normal components are strongly reduced by the polymers. Also consistent with the thickened buffer layer region in the FENE-P cases, the migration location to the axisymmetric boundary of the invariant map has shifted from $z^{+} = 6.69$ for the Newtonian case at $Re_h = 4000$ to $z^{+} = 11.6$ for the LDR case at $Re_h = 4000$, $Wi_h = 10$ and $L = 100$.

Lastly, despite the fact that the mean pressure gradient is null in the turbulent plane Couette flow as shown in figure 3.8(a), i.e. the flow is driven by the plate motions, fluctuations in the pressure gradient field are perceived. One can note in figure 3.8(b) that these fluctuations are relatively high in Newtonian flows (grey circles), reaching their peak of magnitude in region III. However, the pressure gradient fluctuations are considerable attenuated with increasing elasticity throughout the whole plane Couette geometry. In comparing, for instance, the grey open circles with the blue plus symbols, it can be clearly seen that, for all z^{+}, viscoelastic case exhibits a fluctuating gradient pressure which is approximately two times smaller than that of the Newtonian case. Additionally, the peak magnitude of the viscoelastic cases shift away from the wall when increasing DR.

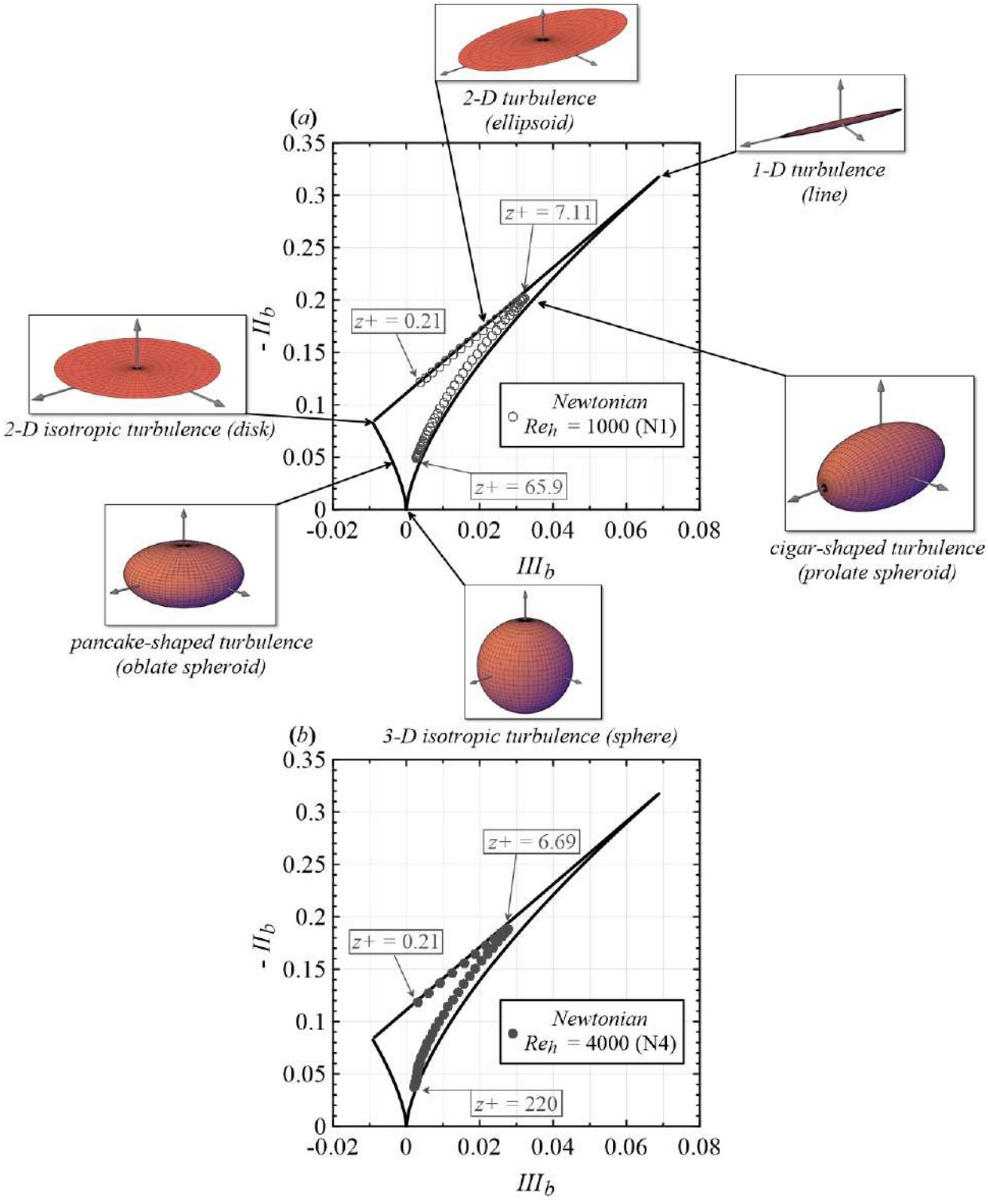

Figure 3.6 – Anisotropy-invariant map of Reynolds stress tensor for two Newtonian flows: $Re_h = 1000$ (a) and $Re_h = 4000$ (b).

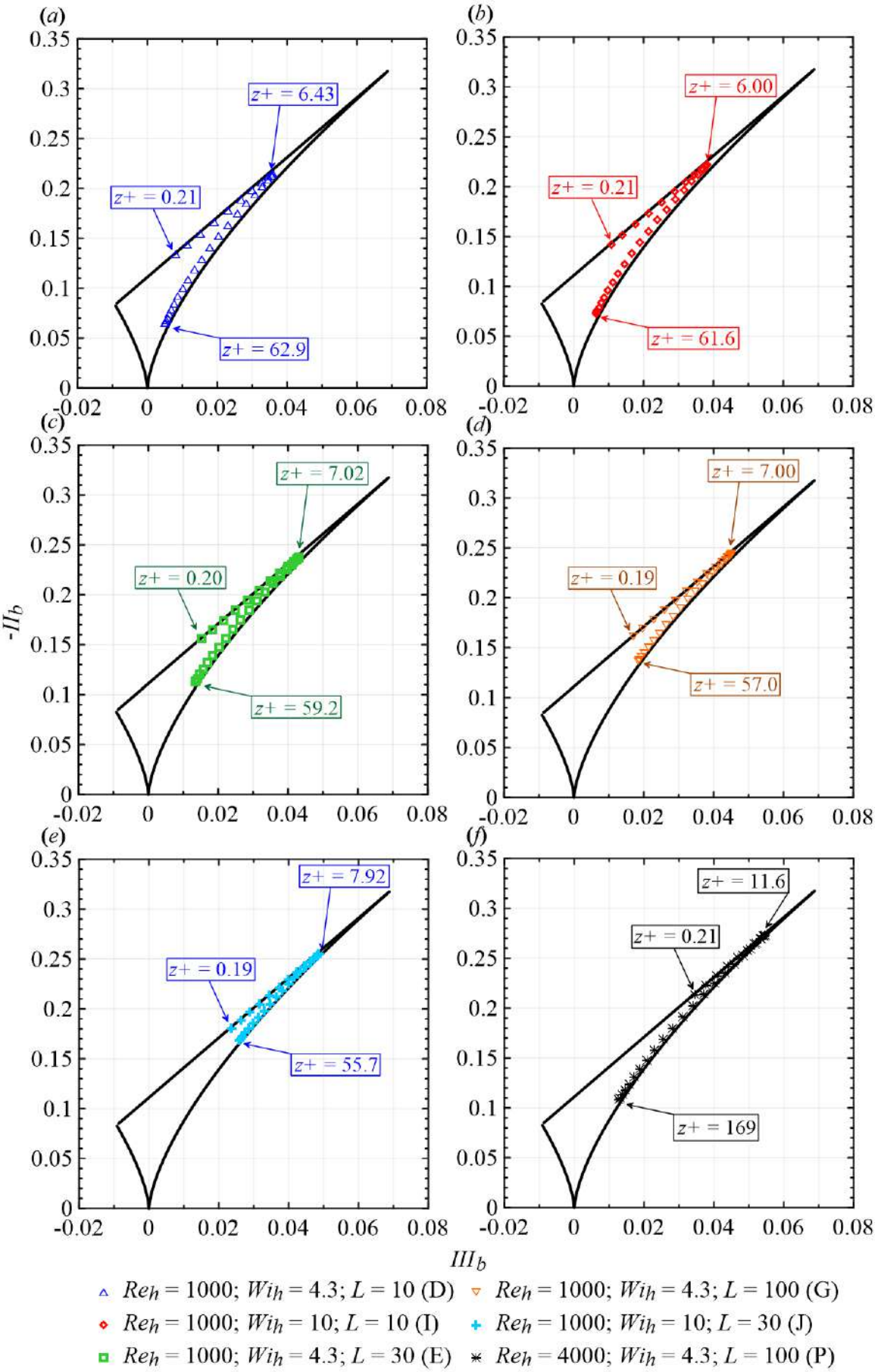

Figure 3.7 – Anisotropy-invariant map of Reynolds stress tensor for six FENE-P flows.

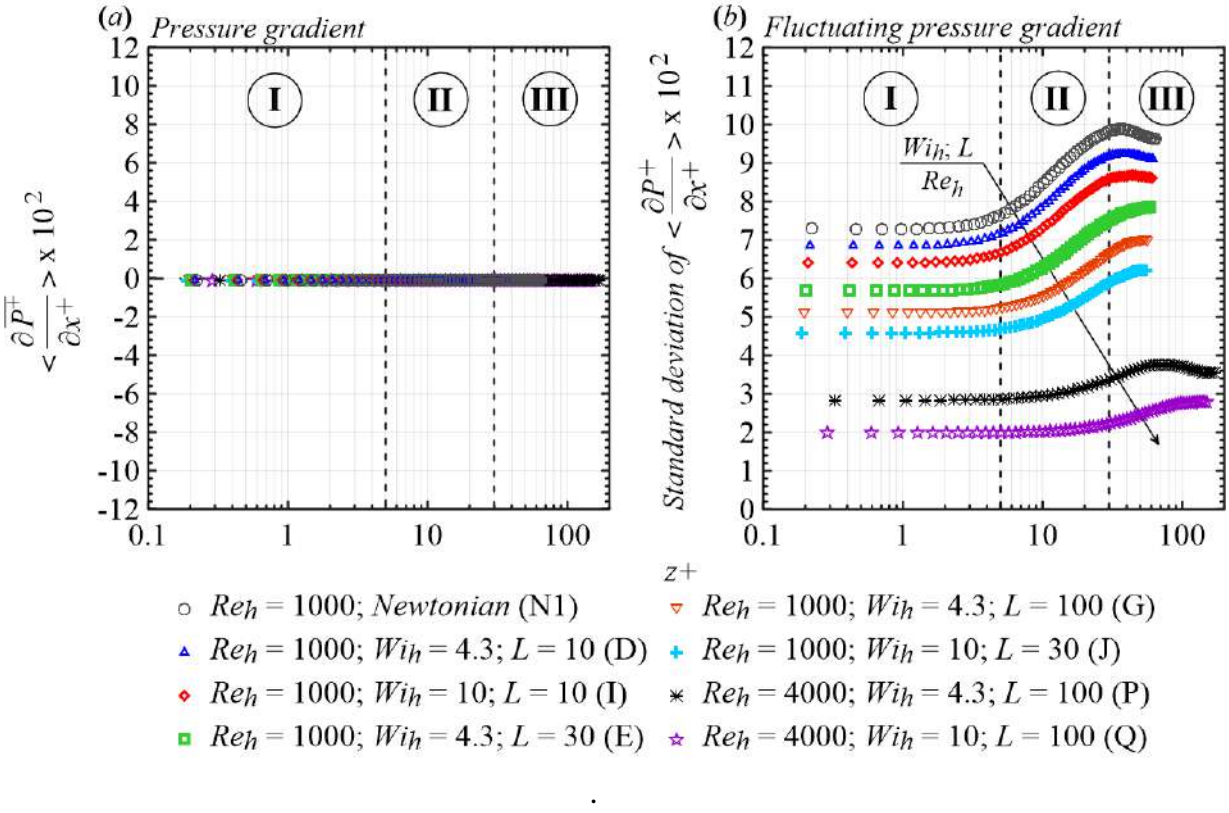

Figure 3.8 – Average value in the $x-y$ plane of the mean normalized gradient pressure as a function of the normalized wall distance (a). Standard deviation of the normalized gradient pressure as a function of the normalized wall distance (b)

3.3.2 Polymer statistics

The interaction between polymers and turbulence also reflects on the molecules conformations (3.9). The stretching of the polymers can be seen in figure 3.9(a), where the evolution of the $x-y$ plane average normalized trace of the time-averaged conformation tensor, $\langle tr(\boldsymbol{C})/L^2\rangle$, is plotted against the normalized wall distance (solid symbols) together with the normalized streamwise normal component of the conformation tensor, $\langle C_{xx}/L^2\rangle$ (open symbols). Following the results founded in plane Poiseuille flows (see, for instance, [24, 21, 87, 71]), figure 3.9(a) indicates that the dominant contribution to the trace of the conformation tensor comes from C_{xx}, since $\langle tr(\boldsymbol{C})/L^2\rangle \approx \langle C_{xx}/L^2\rangle$ (especially near the wall and for the highest value of L). These two quantities are relatively high at the wall and their values tend to be incremented as DR increases, until achieving their magnitude peak in region II. This peak is commonly associated with the streamwise fluctuating vorticity presented in figure 3.4(a) [24, 21, 19] and its exact location varies with Re_h, Wi_h and L. For the case J (blue plus symbols, $DR = 27.8\%$), for instance, the maximum $\langle tr(\boldsymbol{C})/L^2\rangle$ (≈ 0.47) is situated at $z^+ \approx 8$. However, for the case M (black asterisks, $DR = 38.9\%$), the maximum $\langle tr(\boldsymbol{C})/L^2\rangle$ is shifted from the wall, been located at $z^+ \approx 15$. After this point, both $\langle tr(\boldsymbol{C})/L^2\rangle$ and $\langle C_{xx}/L^2\rangle$ start to decrease, until reaching their minimum at the plane Couette centre. These quantities decrease with increasing L, for fixed Re_h and Wi_h, suggesting that the large polymer molecules could be less susceptible to chain scission degradation [65]. On the other hand, $\langle tr(\boldsymbol{C})/L^2\rangle$ and $\langle C_{xx}/L^2\rangle$ become greater as the friction Weissenberg number increases, since higher values of the polymer time scale induce the polymer molecules to be influenced by a wider spectrum of time scales of the flow [19]. As indicated by the black arrows in figures 3.9(a), (b), (c), and (d), similar effects of L and Wi_h on C_{yy}, C_{zz} and C_{xz} are observed. The latter exhibits a non-zero wall value, as displayed in figure 3.9(d) and its peak is almost one order of magnitude smaller than that of the C_{xx} component, been achieved at z^+ not much different from those observed for C_{xx}. The peak magnitude of the off-diagonal component C_{xz} is comparable to that of the C_{zz} component (plotted in figure 3.6c), although both are only slightly smaller than the peak magnitude of the C_{yy} component (shown in figure 3.6b). Lastly, is interesting to observe that, different from the plane Poiseuille flow, $\langle C_{yy}/L^2\rangle$ and $\langle C_{zz}/L^2\rangle$ exhibit maximum values at the centre of the geometry, which is probable related to the intense spanwise and wall-normal velocity fluctuations at this location.

The results discussed in figure 3.9 suggest a preponderant polymer activity in the streamwise direction. Supplementary information concerning this polymer preferential direction can be obtained from an anisotropy invariant map of the extra-stress tensor analogous to that of the Reynolds stress. In this connection, the extra-stress anisotropy tensor is defined as $e_{ij} = \Xi^+_{ij}/tr(\boldsymbol{\Xi}^+) - \delta_{ij}/3$ [87]. Its second and third invariants are given

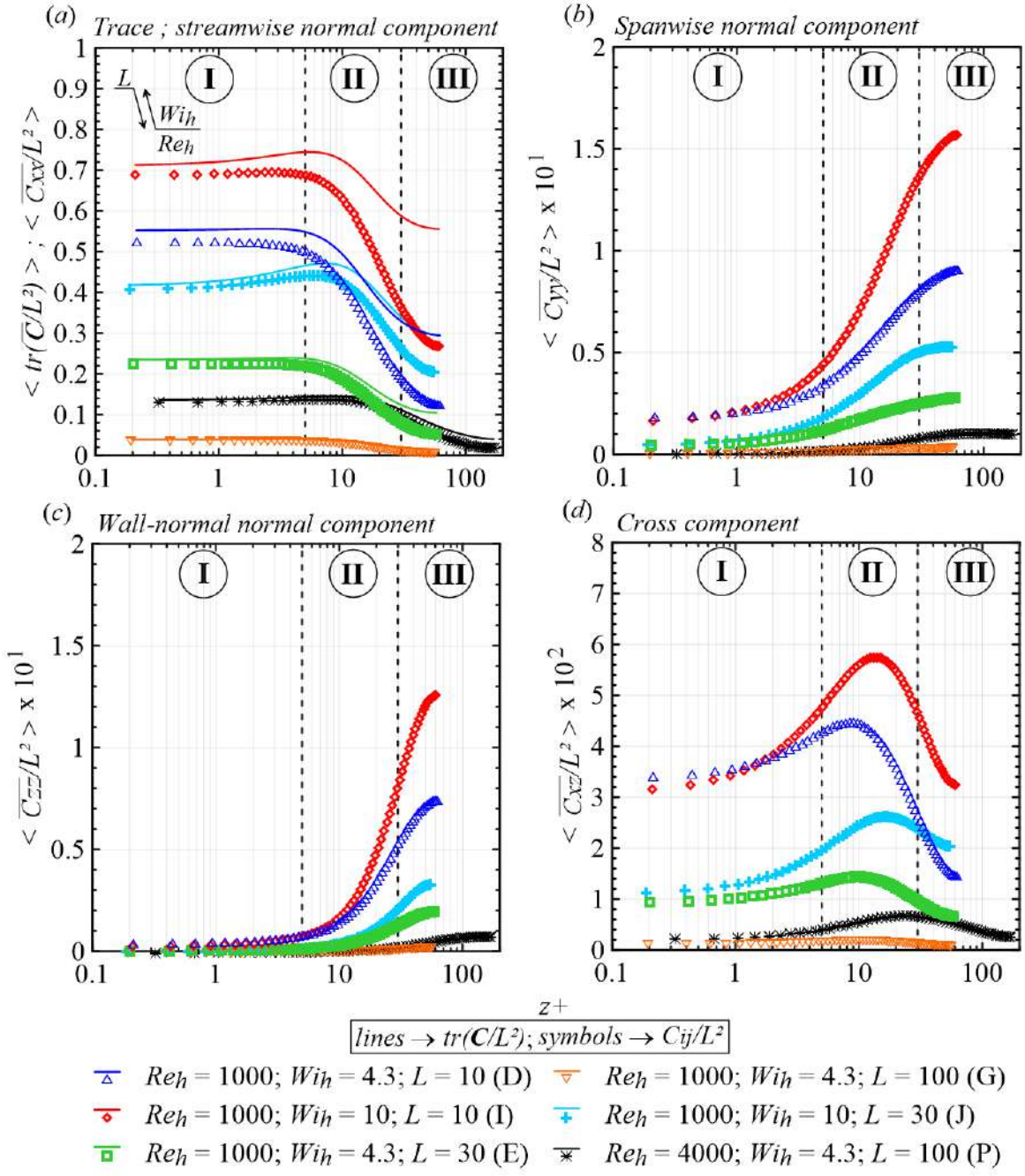

Figure 3.9 – Normalized conformation tensor as a function of the normalized wall distance. Streamwise normal components of $\boldsymbol{C}$ and $tr(\boldsymbol{C})/L^2$ (open and solid in *a*, respectively). Spanwise normal component of $\boldsymbol{C}$ (*b*). Wall-normal normal component of $\boldsymbol{C}$ (*c*). Cross components (*d*).

by $II_e = -e_{ij}e_{ji}/2$ and $III_e = e_{ij}e_{jk}e_{ki}/3$, respectively. The results are shown in figure 3.10 for six viscoelastic cases, which further exemplifies the significant dominance the streamwise conformation tensor component has on the polymeric stress field. The invariant map is positioned along the bottom boundary, in between the 3-D isotropic vertex (0,0) and the 1-D state (the most anisotropic state), throughout the entire geometry. Near the wall, the highly dominant streamwise polymer conformation component makes $e_{ij} = \Xi^+_{ij}/tr(\boldsymbol{\Xi}^+) - \delta_{ij}/3$ anisotropic. Similar to the tendencies noted in figure 3.8, the increasing elasticity displaces the invariant map towards this 1-D anisotropic state.

Further comparisons between the Reynolds stress tensor and the extra-stress tensor from a shear stress balance perspective reveal important difference between the low drag reduction regime (LDR), $DR \leq 40\%$, and the high drag reduction one (HDR), $DR > 40\%$. Physically, the main difference between these two regimes consists in the fact that for LDR flows, the Reynolds stresses play a major role, whereas in the HDR regime, the near-wall dynamics of the flow is dominated by the polymer stresses [102]. In figure 3.11, two viscoelastic cases are illustrated keeping Re_h and L fixed. In the LDR case displayed in figure 3.11(a), $DR = 38.9\%$, $Re_h = 4000$, $Wi_h = 4.3$ and $L = 100$ (case P). For the HDR regime illustrated in figure 3.11(b), $DR = 52.8\%$, $Re_h = 4000$, $Wi_h = 10$ and $L = 100$ (case Q). In both cases, the viscous shear stress (grey open circles), given by $2\beta_0\overline{S_{xz}}^+$ where $\overline{S_{ij}}^+ = (\partial\overline{U_i}^+/\partial x_j^+ + \partial\overline{U_j}^+/\partial x_i^+)/2$, is close to 1 within the viscous sublayer (region I). However, it decreases greatly within region II, whereas both the Reynolds and polymer shear stresses increase (blue open triangles and red open diamonds, respectively). For the LDR flow, it is clearly observed that $\langle\overline{u'_x u'_z}^+\rangle$ is the most important shear term in regions II and III, going up to 82% of the total stress ($2\beta_0\overline{S_{xz}}^+ - \overline{u'_x u'_z}^+ + \overline{\Xi_{xz}}^+$) represented by the solid black line. In contrast, in the HDR case, $\langle\overline{u'_x u'_z}^+\rangle$ is considerably suppressed, while the polymers produce a stronger shear stress than in the LDR. These changes make the polymer shear stress contribution surpass the Reynolds shear stress in the larger part of region II ($5 < z^+ < 20$).

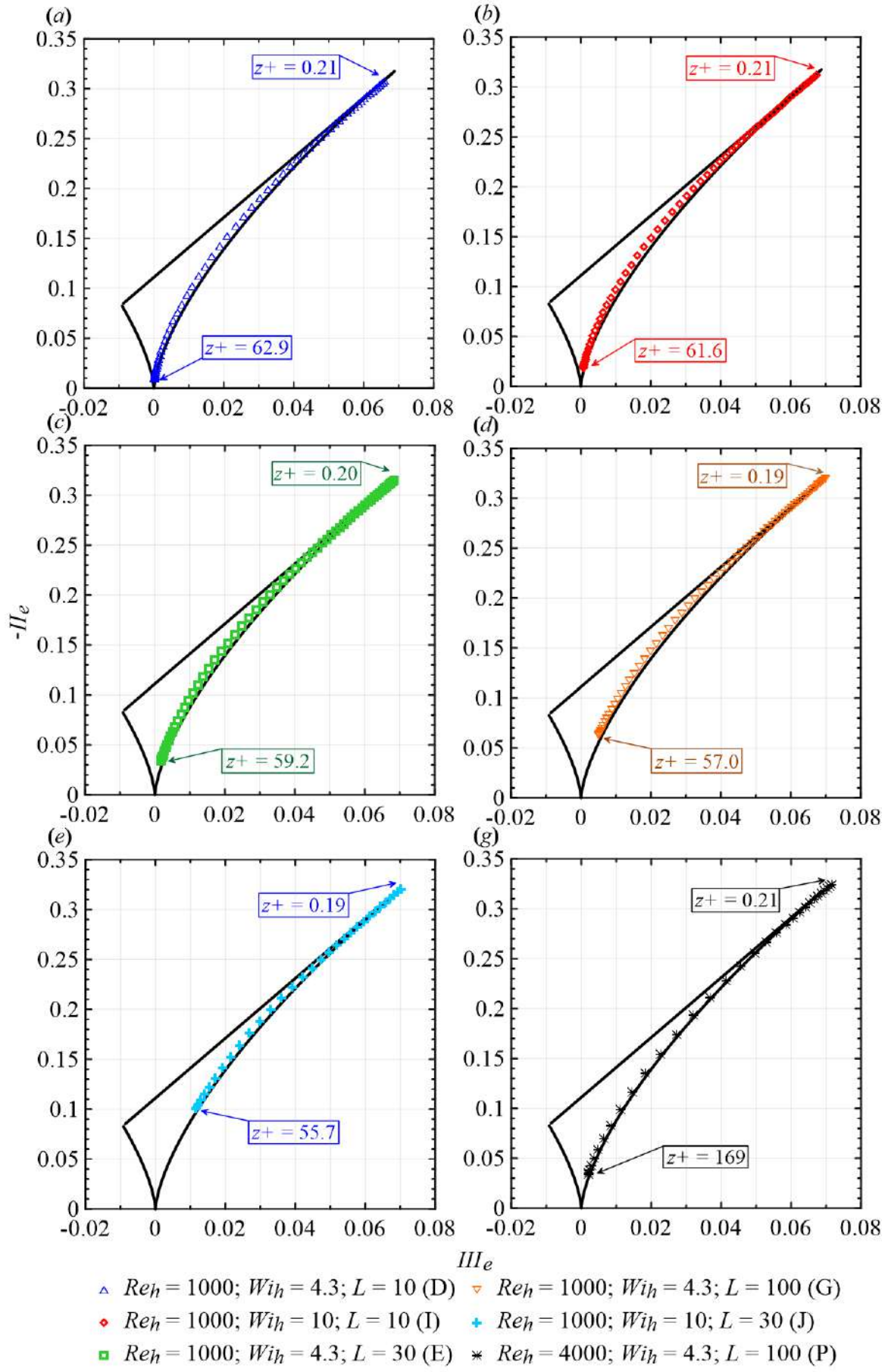

Figure 3.10 – Anisotropy-invariant map of extra-stress tensor for six FENE-P flows.

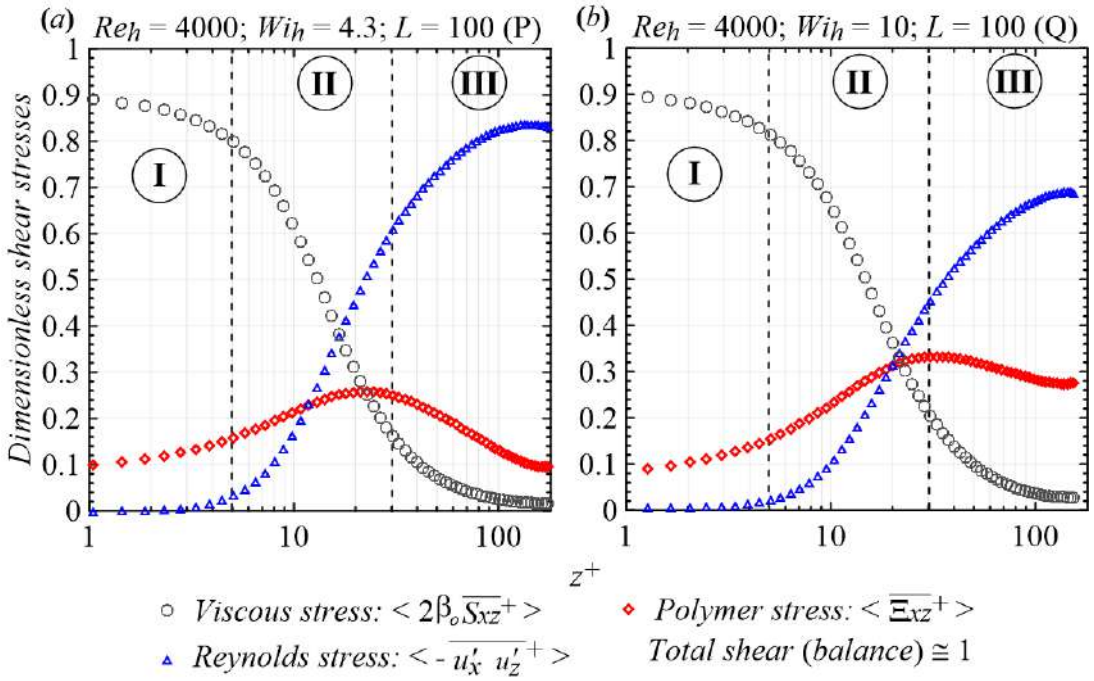

Figure 3.11 – The balance of shear stress for two viscoelastic flows.

3.4 Energy budgets

The results discussed above indicate a significant interaction between the polymers and the flow, which is analysed in the present section from an energy budget perspective. Aiming to characterize such energy exchanges, we consider the time average work equation

$$\underbrace{\left[\overline{\frac{1}{2}\frac{\partial\left(u_\alpha^{+2}\right)}{\partial t^+}}\right]}_{T^+_{m,\alpha}} = \underbrace{\left[\overline{-u_\alpha^+\frac{\partial\left(u_\alpha^+u_i^+\right)}{\partial x_i^+}}\right]}_{A^+_{m,\alpha}} + \underbrace{\left[\overline{-u_\alpha^+\frac{\partial p^+}{\partial x_\alpha^+}}\right]}_{P^+_{m,\alpha}} + \underbrace{\left[\overline{(\beta_0)\,u_\alpha^+\frac{\partial^2 u_\alpha^+}{\partial x_i^{+2}}}\right]}_{V^+_{m,\alpha}} + \underbrace{\left[\overline{u_\alpha^+\frac{\partial \Xi^+_{\alpha i}}{\partial x_i^+}}\right]}_{E^+_{m,\alpha}}, \tag{3.3}$$

where the time-averaged amount of energy which is stored ($E^+_{m,\alpha} < 0$) or released ($E^+_{m,\alpha} > 0$) by polymers from the velocity in the α direction, u_α^+, is represented by $E^+_{m,\alpha}$. The complementary work terms denote the advection $A^+_{m,\alpha}$, the pressure redistribution $P^+_{m,\alpha}$, and the viscous stress $V^+_{m,\alpha}$. The sum $A^+_{m,\alpha} + P^+_{m,\alpha} + V^+_{m,\alpha}$ is referred as time average *Newtonian work*, $N^+_{m,\alpha}$, and $T^+_{m,\alpha}$ is the time derivative term. The velocity, pressure and extra-stress fields in equation 3.3 can be decomposed into mean ($\overline{U_i^+}$, $\overline{P^+}$, $\overline{\Xi^+_{ij}}$) and fluctuating ($u_i'^+$, p'^+, Ξ'^+_{ij}) fields, which leads to the equation:

$$\begin{aligned}\underbrace{\left[\frac{1}{2}\frac{\partial\left(\overline{U_\alpha^+}^2\right)}{\partial t^+}\right]}_{T^+_{mm,\alpha}} + T^+_{mt,\alpha} = &\underbrace{\left[-\overline{U_\alpha^+}\frac{\partial\left(\overline{U_\alpha^+}\,\overline{U_i^+}\right)}{\partial x_i^+}\right]}_{A^+_{mm,\alpha}} + A^+_{mt,\alpha} + \underbrace{\left[-\overline{U_\alpha^+}\frac{\partial\overline{P^+}}{\partial x_\alpha^+}\right]}_{P^+_{mm,\alpha}} + P^+_{mt,\alpha} + \\ &\underbrace{\left[(\beta_0)\,\overline{U_\alpha^+}\frac{\partial^2\overline{U_\alpha^+}}{\partial x_i^{+2}}\right]}_{V^+_{mm,\alpha}} + V^+_{mt,\alpha} + \underbrace{\left[\overline{U_\alpha^+}\frac{\partial\overline{\Xi^+_{\alpha i}}}{\partial x_i^+}\right]}_{E^+_{mm,\alpha}} + E^+_{mt,\alpha},\end{aligned} \tag{3.4}$$

where the amount of energy which is stored ($E^+_{mm,\alpha} < 0$) or released ($E^+_{mm,\alpha} > 0$) by polymers from the mean velocity in the α direction, $\overline{U_\alpha^+}$, is represented by $E^+_{mm,\alpha}$. The complementary work terms denote the mean advection $A^+_{mm,\alpha}$, the mean pressure redistribution $P^+_{mm,\alpha}$, and the mean viscous stress $V^+_{mm,\alpha}$. The sum $A^+_{mm,\alpha} + P^+_{mm,\alpha} + V^+_{mm,\alpha}$ is referred as *mean Newtonian work*, $N^+_{mm,\alpha}$, and $T^+_{mm,\alpha}$ is the time derivative term associated with the mean velocity. The work terms related to the fluctuating fields are

expressed as:

$$\begin{cases} T^+_{mt,\alpha} = T^+_{m,\alpha} - T^+_{mm,\alpha}\,; \\ A^+_{mt,\alpha} = A^+_{m,\alpha} - A^+_{mm,\alpha}\,; \\ P^+_{mt,\alpha} = P^+_{m,\alpha} - P^+_{mm,\alpha}\,; \\ V^+_{mt,\alpha} = V^+_{m,\alpha} - V^+_{mm,\alpha}\,; \\ E^+_{mt,\alpha} = E^+_{m,\alpha} - E^+_{mm,\alpha}\,. \end{cases} \tag{3.5}$$

It is worth mentioning that the energy exchanges in the x direction ($\alpha = x$) constitute more than 90% of that considering the streamwise, the spanwise and the wall-normal directions. Hence, in figure 3.12, only the $x-y$ plane average of the streamwise work terms provided by equation 3.4 against the normalized wall distance are considered.

Figure 3.12 shows the time averages of the streamwise work terms related to mean fields (left side column) and to fluctuating fields (right side column) across the plane Couette half-width for Newtonian and FENE-P turbulent flows at $Re_h = 1000$. Firstly, concerning the mean energy terms (left side column), it is observed that the $\langle E^+_{mm,\alpha}\rangle$ and $\langle V^+_{mm,\alpha}\rangle$ are the most important terms. The former, displayed in figure 3.12(g) departs from its minimum negative value at the wall $\langle E^+_{mm,\alpha}\rangle$, which is maintained across the larger part of region I. In other word, near the wall, polymers store a significant amount of energy from the mean flow. This storage of energy within region I becomes more pronounced while increasing the elasticity. However, around the upper limit of the viscous sublayer, $\langle E^+_{mm,\alpha}\rangle$ starts to increase until reaching its maximum positive value within region II, where a non-negligible quantity of energy is released to the mean flow. Small positive values of $\langle E^+_{mm,\alpha}\rangle$ are also observed in region III. This polymer release of energy in regions II and III are an increasing function of Wi_h and L and they are probably linked with the increase in the streamwise mean velocity pointed out in figure 3.2(a). The intense storage of energy by the polymers in the viscous sublayer favours the enhancement of the mean viscous work (figure 3.12e), which in turn starts to depart from a non-null value at the wall (viscoelastic cases) instead of zero (Newtonian case). Nevertheless, comparing the viscoelastic cases with the Newtonian one, it worth noting that the peak magnitude of $\langle V^+_{mm,\alpha}\rangle$ situated in the region II decreases with increasing Wi_h and L. The same trend is observed in $\langle V^+_{mt,\alpha}\rangle$ (figure 3.12f). Such a behaviour is possibly related to the increase in the streamwise velocity in region II caused by the polymers (see figures 3.2a and b). The polymer release of energy to the mean flow in region II and III also increases the magnitude of $\langle A^+_{mm,\alpha}\rangle$ within these regions. However, this term is one order of magnitude smaller than $\langle A^+_{mt,\alpha}\rangle$, which indicates that the advection work is dominated by the fluctuating velocity field. Since the fluctuating velocity field is partially suppressed by the polymers (see figures 3.2c and d), one can note in figure 3.12(b) that $\langle A^+_{mt,\alpha}\rangle$ tends to decrease in region II, although it is slightly increased in region III due to the morphological changes in the turbulent structures

reported by [72]. Regarding the exchanges of energy between the polymers and the fluctuating velocity field, $\langle E^+_{mt,\alpha}\rangle$ (figure 3.12*h*), it is interesting to observe that, near the wall, the molecules release energy to the fluctuating velocity field ($\langle E^+_{mt,\alpha}\rangle > 0$ for $z^+ < 5$). In contrast, in regions II and III, $\langle E^+_{mt,\alpha}\rangle$ assumes a significantly negative value, indicating a considerable damping of the fluctuations. Lastly, it is important to observed that the mean pressure redistribution $\langle P^+_{mm,\alpha}\rangle \approx 0$ across the geometry since the mean pressure gradient is null, while $\langle P^+_{mm,\alpha}\rangle$ is reduced when increasing Wi_h and L due to the partial suppression in the pressure gradient fluctuations caused by the polymers (see figure 3.8*b*).

Comparing figures 3.12(*g*) and (*h*), the polymer-flow interactions can be summarized as follows. In the viscous sublayer, polymers store energy from the mean flow in order to have a considerable stretch in the near-wall region. In the regions II and III, however, the molecules release energy to the mean flow, a fact with which the increase in u'_x could be also related, since the mean flow also acts as a source of turbulent kinetic energy in this region as reported by Thais et al. [86]. Additionally, polymer interacts directly with the fluctuating part of the flow, damping it in region II and releasing part of this energy to the fluctuating velocity field in region I.

In order to compare our results with that presented by Thais et al. [86] who numerically analysing turbulent plane Poiseuille flows of FENE-P fluids, we consider the transport of mean kinetic energy as well as that of turbulent kinetic energy in figures 3.13 and 3.14, respectively.

The transport equation for the mean kinetic energy (MKE), $K^+_m = \left(\overline{U^+_i}^2\right)/2$, is obtained

$$\frac{DK^+_m}{Dt^+} = -P^+_m - P^+_{pm} - \underbrace{\beta_0\left(\frac{\partial \overline{U^+_i}}{\partial x^+_j}\right)^2}_{\epsilon^+_m} + \underbrace{\beta_0\left(\frac{\partial^2 K^+_m}{\partial x^{+2}_j}\right)}_{D^+_{mv}} - \underbrace{\frac{\partial\left(\overline{P^+}\ \overline{U^+_i}\right)}{\partial x^+_i}}_{D^+_{mP}} - \underbrace{\frac{\partial\left(\overline{U^+_i}\,\overline{\tau^+_{ij}}\right)}{\partial x^+_j}}_{D^+_{mt}} + \underbrace{\frac{\partial\left(\overline{U^+_i}\ \overline{\Xi^+_{ij}}\right)}{\partial x^+_j}}_{D^+_{pm}}, \tag{3.6}$$

where $-P^+_m$ is an energy exchange term acting as a sink of mean kinetic energy to the turbulent kinetic energy (production of turbulent kinetic energy),

$$P^+_m = -\tau^+_{ij}\overline{S^+_{ji}}, \tag{3.7}$$

and $-P^+_{pm}$ is also an energy exchange term but acting as a sink of mean kinetic energy to

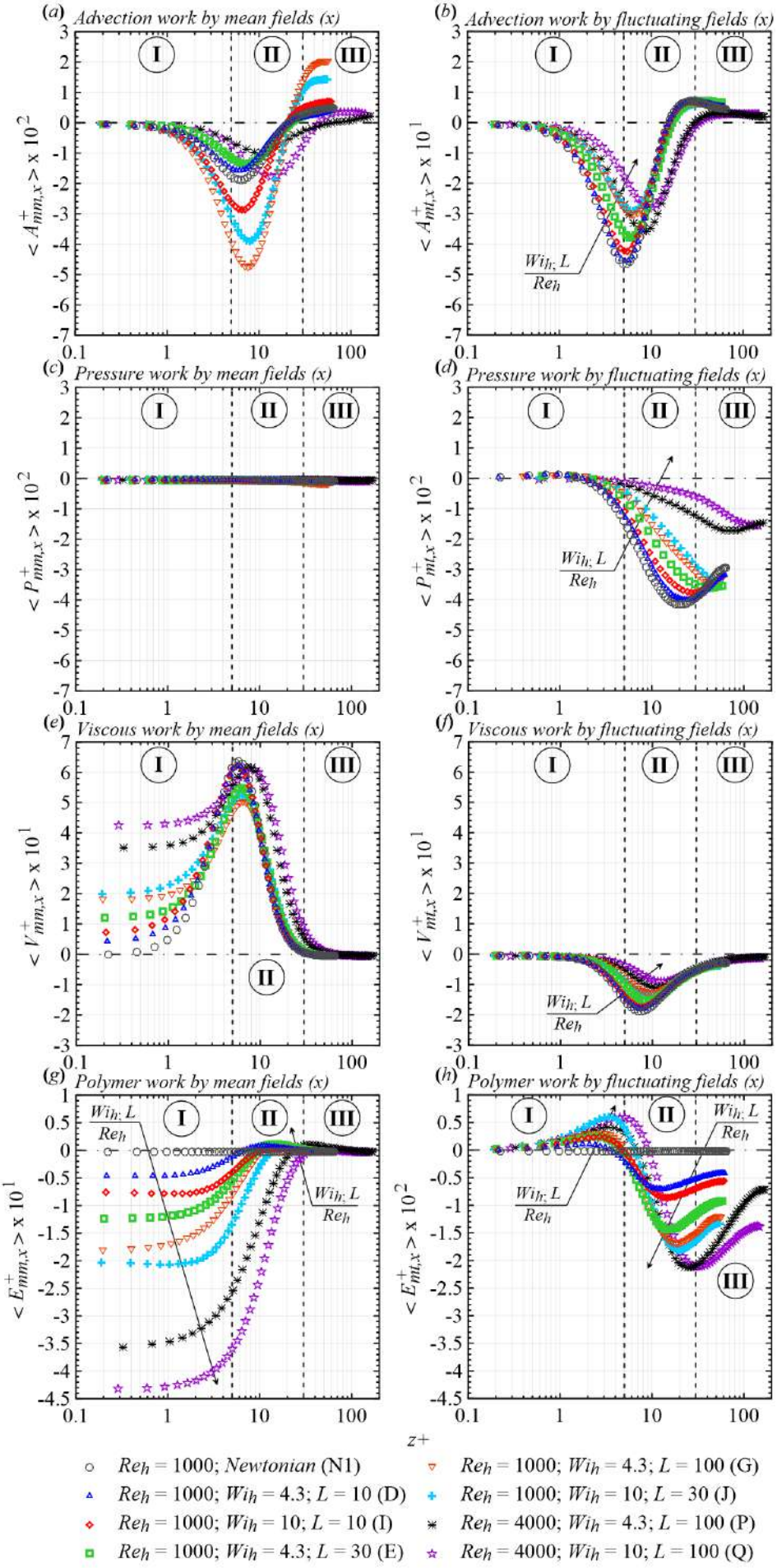

Figure 3.12 – Mean (left column) and fluctuating (high column) polymer work terms across the half-width plane Couette.

polymer energy (production of mean polymeric energy),

$$P_{pm}^{+} = -\overline{\Xi_{ij}^{+}}\ \overline{S_{ji}^{+}}. \tag{3.8}$$

The remaining terms on the right side represent the dissipation rate of MKE (ϵ_m^+), the viscous diffusion of MKE due the solvent ($D_{m\nu}^+$), the pressure transport of MKE (D_{mP}^+), the turbulent transport of MKE (D_{mt}^+), and the mean polymeric transport of MKE (D_{pm}^+). As shown by the equation 3.9, the mean flow energy is partitioned to both the turbulence and the polymer (elastic portion).

The transport equation for the turbulent kinetic energy (TKE), $K_t^+ = tr(\boldsymbol{\Xi}^+)/2$, if formed in the usual manner from the fluctuating momentum equation, and is given by

$$\begin{aligned}\frac{DK_t^+}{Dt^+} = P_m^+ - \underbrace{\beta_0\left(\frac{\partial\overline{u_i'^+}}{\partial x_j^+}\right)^2}_{\epsilon_t^+} + \underbrace{\beta_0\left(\frac{\partial^2 K_t^+}{\partial x_j^{+2}}\right)}_{D_{t\nu}^+} + \underbrace{\frac{\partial\left(\overline{p'^+ u_i'^+\delta_{ij}}\right)}{\partial x_j^+}}_{D_{tP}^+} + \\ \underbrace{\frac{\partial\left(\overline{u_i'^+ u_i'^+ u_j'^+}/2\right)}{\partial x_j^+}}_{D_{mt}^+} - P_{pt}^+ + D_{pt}^+,\end{aligned} \tag{3.9}$$

where the first five terms on the right side are the classic Newtonian terms representing the production of fluctuating energy by the mean shear (P_m^+), the dissipation rate of TKE (ϵ_t^+), the viscous diffusion of TKE ($D_{t\nu}^+$) due the solvent, the pressure transport of TKE (D_{tP}^+), and the turbulent transport of TKE (D_{mt}^+). The remaining two terms are an energy exchange term (production of turbulent polymeric energy),

$$P_{pt}^+ = \overline{\Xi_{ij}'^{\,+}\ S_{ji}'^{\,+}}. \tag{3.10}$$

and a polymeric/turbulent transport (polymeric transport of TKE) of,

$$D_{pt}^+ = \frac{\partial\left(\overline{\Xi_{ij}'^{\,+} u_i'^+}\right)}{\partial x_j^+}. \tag{3.11}$$

which provide the energetic connection between the flow turbulent and the polymeric fluid stress.

Figure 3.13 brings out the mean kinetic energy budget across the plane Couette flow half-width for Newtonian and FENE-P turbulent flows. The mean kinetic energy is explored in figure 3.13(a), while the terms of the energy balance (equation 3.9) are displayed in figures 3.13(b)-(h).

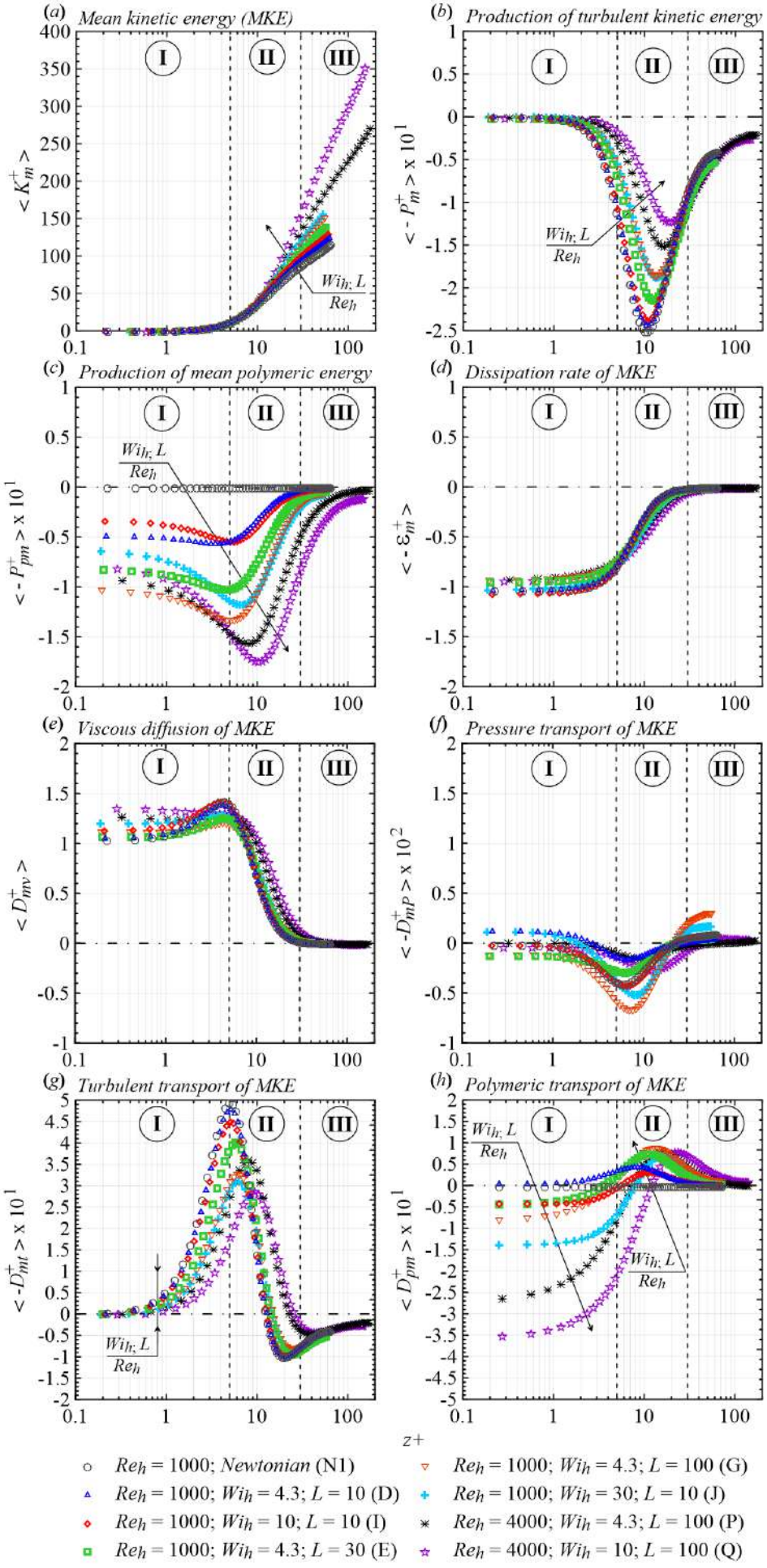

Figure 3.13 – Mean kinetic energy profiles across the half-width plane Couette.

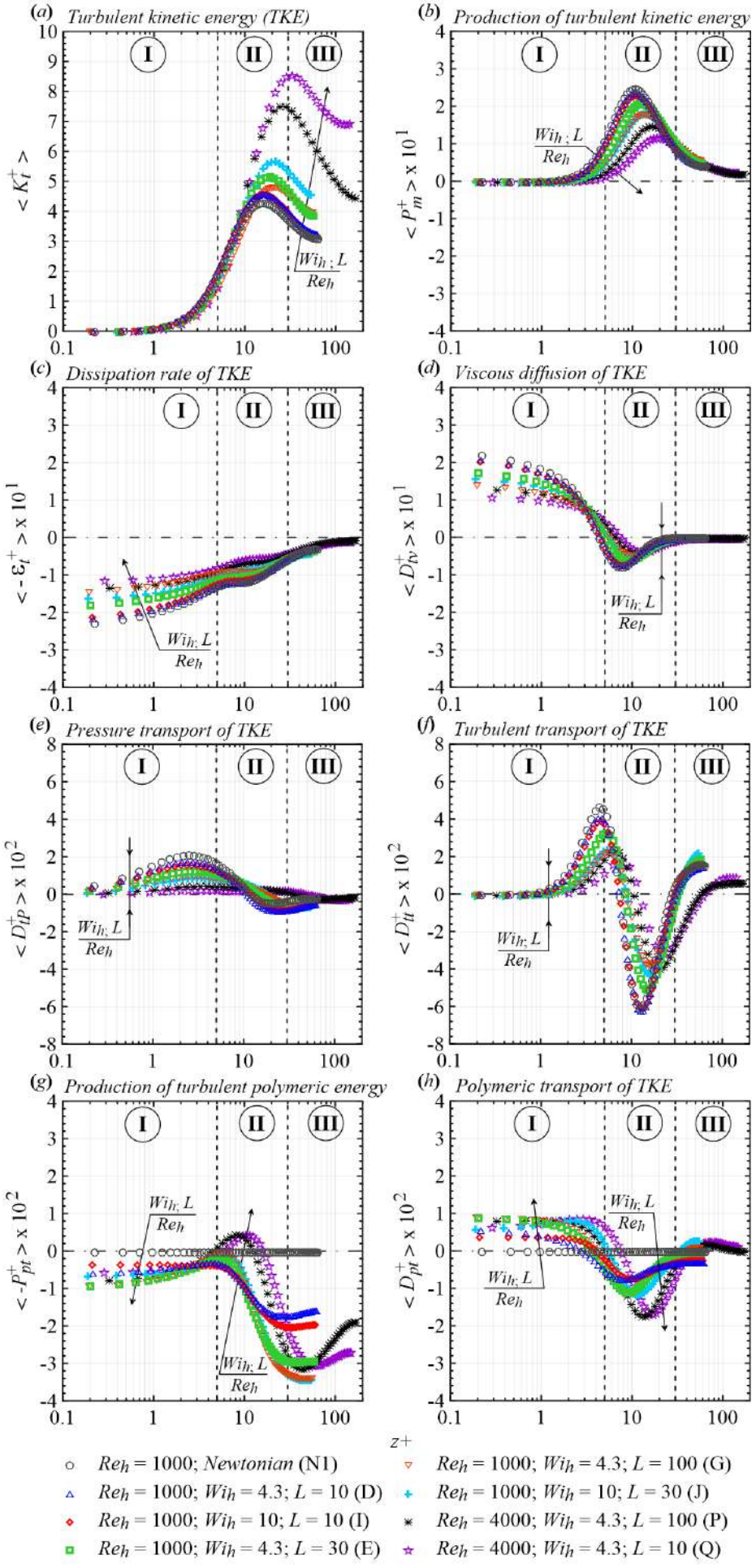

Figure 3.14 – Turbulent kinetic energy profiles across the half-width plane Couette.

Concerning the mean kinetic energy (figure 3.13*a*) resulting from budget discussed above, one can note that $\langle K_m^+ \rangle$ increases with elasticity. Furthermore, the slope of the drag reduction profiles becomes more pronounced while moving increasing DR, which is related the increase in the streamwise mean velocity caused by the polymers.

For the Newtonian mean kinetic budget (grey circles in figures 3.13), the dominating balance in the vicinity of the wall is between the mean viscous dissipation, $\langle \epsilon_m^+ \rangle$, and the viscous diffusion, $\langle D_{mv}^+ \rangle$. As previously pointed out by Thais et al. [86] for a channel flow, at $z^+ \approx 10$, the production of turbulent kinetic energy (or the destruction of mean kinetic energy), $\langle -P_m^+ \rangle$, achieves a minimum and the turbulent transport of MKE, $\langle -D_{mt}^+ \rangle$, reaches its maximum. Since the mean pressure gradient is approximatively equal to zero (figure 3.8*a*), the mean pressure transport, $\langle D_{mP}^+ \rangle$, make no discernible contributions to the energy balance, which is also valid for the viscoelastic flows.

The appearance of the polymeric terms, $\langle D_{pm}^+ \rangle$ and $\langle -P_{pm}^+ \rangle$, which act respectively as a source and sink of MKE, modifies the mean kinetic budget, decreasing the peak magnitude of $\langle -P_m^+ \rangle$, $\langle -D_{mt}^+ \rangle$ and $\langle D_{mv}^+ \rangle$, although the latter is enhanced in near wall region (similar to $\langle V_{mm,\alpha}^+ \rangle$). As the elasticity increases, these peak magnitudes are shifted from the wall towards the centre of the geometry, a further evidence of the enhancement of the buffer layer. Following the analyses concerning $\langle E_{mm,\alpha}^+ \rangle$ shown in figure 3.12(*g*), $\langle D_{pm}^+ \rangle$ and $\langle -P_{pm}^+ \rangle$ indicate that polymers store a significant amount of energy from the mean flow in region I ($\langle D_{pm}^+ \rangle < 0$ and $\langle -P_{pm}^+ \rangle < 0$). Nevertheless, part of this energy is released to the mean velocity field in regions II and III, where $\langle D_{pm}^+ \rangle > 0$.

The turbulent kinetic budget across the plane Couette flow half-width explored in figure 3.14 gives supplementary details about the polymer-flow interactions. As have been shown for turbulent channel flows [87, 86], the turbulent kinetic energy, $\langle K_t^+ \rangle$, increases for viscoelastic fluids relative to the Newtonian case (figure 3.14*a*). Figure 3.14*a* also exemplifies the thickening of the buffer layer, the peak of $\langle K_t^+ \rangle$ moving away from $z^+ \approx 15$ for the case N1 (Newtonian fluid; grey circles), to $z^+ \approx 20$ for the case J ($Re_h = 1000, Wi_h = 10$ and $L = 30$; blue plus symbols) and finally to $z^+ \approx 35$ for the case Q ($Re_h = 4000$, $Wi_h = 10$ and $L = 100$). For the Newtonian turbulent kinetic budget (grey circles in figures 3.14), the typical wall-proximity balance between viscous diffusion, $\langle D_{tv}^+ \rangle$, and viscous dissipation rate, $\langle -\epsilon_t^+ \rangle$, is observed [5]. As reported in Thais et al. [86] by considering a Newtonian channel flow, at $z^+ \approx 12$, the production of TKE, $\langle P_m^+ \rangle$, achieves its peak, been balanced by $\langle -\epsilon_t^+ \rangle$ and contributions from $\langle D_{tv}^+ \rangle$ and $\langle D_{tt}^+ \rangle$. Despite non-negligible, the pressure transport of TKE, $\langle D_{tP}^+ \rangle$, plays a marginal role, which is attenuated as the elasticity increases due to the partial suppression of the pressure gradient fluctuations evidenced in figure 3.8(*b*). Regarding the viscoelastic cases, consistent with the mean kinetic energy budget (figure 3.13), the production of TKE decreases for these cases, having their peak magnitude moved away from the wall. The polymeric transport term $\langle D_{pt}^+ \rangle$ acts as source of turbulent energy in regions I and

III ($\langle D^+_{pt} \rangle > 0$) as well as a sink of it in region II ($\langle D^+_{pt} \rangle < 0$). For the LDR cases, $\langle -P^+_{pt} \rangle$ is negative for all z^+, indicating a destruction of turbulent energy by the polymers. However, it is important to emphasizes that, for the HDR cases, $\langle -P^+_{pt} \rangle$ exhibits a positive peak magnitude just above the bottom limit of the region II, suggesting that the polymers are also acting as a source of turbulence around this location. This maximum positive value increases when increasing Wi_h and L. Lastly, following the fluctuating viscous work analysed in figure 3.12(f), the addition of polymers induces a reduction of the viscous diffusion and dissipations rate of TKE, which is mostly perceived in regions I and II.

3.5 Longitudinal 1D spectra of turbulent kinetic energy

Figure 3.15 show longitudinal 1D spectra of turbulent kinetic energy, $E_{11}/(h\ U_h^2)$, for two Newtonian flows and seven viscoelastic flows at $z^+ = 15$. Around such a location, the production of TKE is maximum for all cases analysed here (see figure 3.14b). Despite the low Reynolds number considered in figure 3.15(a), $Re_h = 1000$, a range of wavenumbers between $1 \leq k_x \leq 3$ for the Newtonian fluid (grey open symbols) shows the classical power law decay, $k_x^{-5/3}$ (dashed line). However, such a decay is modified by the presence of polymers, moving toward $k_x^{-14/3}$ [88]. As a result of the polymer-flow interactions, the high wavenumber structures ($k_x > 10$) are strongly supressed whereas a small increase in $E_{11}/(h\ U_h^2)$ occurs within very small wavenumber structures. Additionally, at $Re_h = 4000$, the Newtonian flow exhibits a clear $k_x^{-5/3}$ power law decay in the range $2 \leq k_x \leq 10$, which again is highly affected by the molecules, getting close to $k_x^{-14/3}$ (dash-dotted line) with increasing elasticity. A last characteristic of the 1D viscoelastic spectra clearly observed at $Re_h = 4000$ is that the low wavenumber energy content in the streamwise direction is an increasing function of the drag reduction level, which contributes to the enhancement of the streamwise velocity fluctuation illustrated in figure 3.2(b) as well as to the increase in the streamwise advection work in region III (figures 3.12a and b). These observations are qualitatively in line with experimental and numerical data obtained from turbulent plane Poiseuille flows of viscoelatic fluids [99, 88].

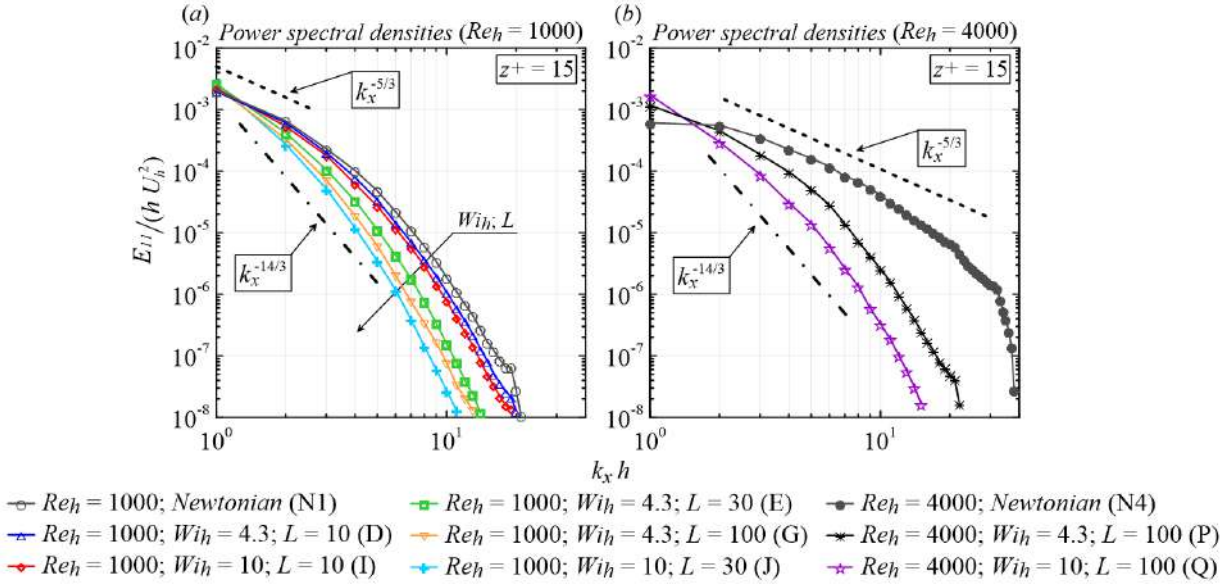

Figure 3.15 – 1D-power spectral density of the streamwise velocity fluctuation at the wall distance $z^+ = 15$. $Re_h = 1000$ (a) and $Re_h = 4000$ (b).

3.6 Polymer-turbulence interaction mechanism

Recently, Pereira et al. [71] numerically provided new details concerning the polymer-turbulence interactions from a drag reduction point of view, which were included in the autonomous regeneration cycle discussed by Dubief et al. [24] and originally conceived for turbulent Newtonian flows by Jiménez and Pinelli [42]. Following the recent contributions of Pereira et al. [71], we increment the referred autonomous regeneration cycle in figure 3.16 taking into the results presented in this work.

The grey dashed arrow in figure 3.16 indicates that, in the viscous sublayer ($z^+ < 5$), the polymers are highly exposed to the mean flow, which acts as a source of polymeric energy ($\langle E^+_{mm,\alpha} \rangle < 0$ in figure 3.12*g*). Additionally, as indicated by the blue dashed arrow, near the wall (at $z^+ \approx 5$), polymers not only release energy to the streaks (purple dashed arrow), but also to the vortical and extensional structures ($\langle E^+_{mt,\alpha} \rangle > 0$ at $z^+ \approx 5$ in figure 3.12*g*). However, polymers can be also pulled around the near-wall vortices, passing through extensional regions and experiencing a significant strain. Fundamentally, within the rotating structures, the polymer stores turbulent energy by applying a counter-torque around the vortices [47], while, in the extensional ones, polymers take energy from the flow by opposing the extensional deformation [71]. As a result, polymers store turbulent energy ($\langle E^+_{mt,\alpha} \rangle < 0$) in regions II and III, which is represented by the red dashed arrow. Lastly, the polymer can be injected (or re-injected) into the very near-wall region, there releasing streamwise turbulent energy and being more exposed to the mean shear.

Despite the enhancement of the streamwise momentum caused by the polymer release of streamwise turbulent energy at $z^+ \approx 5$, it is noteworthy to mention the significant reduction on both the spanwise and the wall-normal velocity fluctuation caused by the molecules (figures 3.2*c* and *d*), which reflects on the morphology of the turbulent structures: their thicknesses and streamwise lengths increase, while their strengths weaken [71]. In consequence, the near-wall advection work decreases, as illustrated by the green dashed arrow in figure 3.16 (see also figures 3.12*a* and *b*). On the other hand, the fact that the turbulent structures become more parallel to the wall favours the advective transport throughout the streamwise direction in region III since the heads of the hairpins (spanwise rotation) completely vanish in this region [46]. Hence, polymers induce a slight increase in the magnitude of $\langle A^+_{mm,\alpha} \rangle$ and $\langle A^+_{mt,\alpha} \rangle$, far from the wall, as represented by orange dashed arrow (figures 3.12*a* and *b*).

The drag reduction mechanism discussed above and sketched in figure 3.16 clarifies the role played by the polymers in the self-sustained wall turbulence interacting with the mean shear, nonlinear interactions, near-wall elliptical and hyperbolic structures in viscoelastic drag reducing flows.

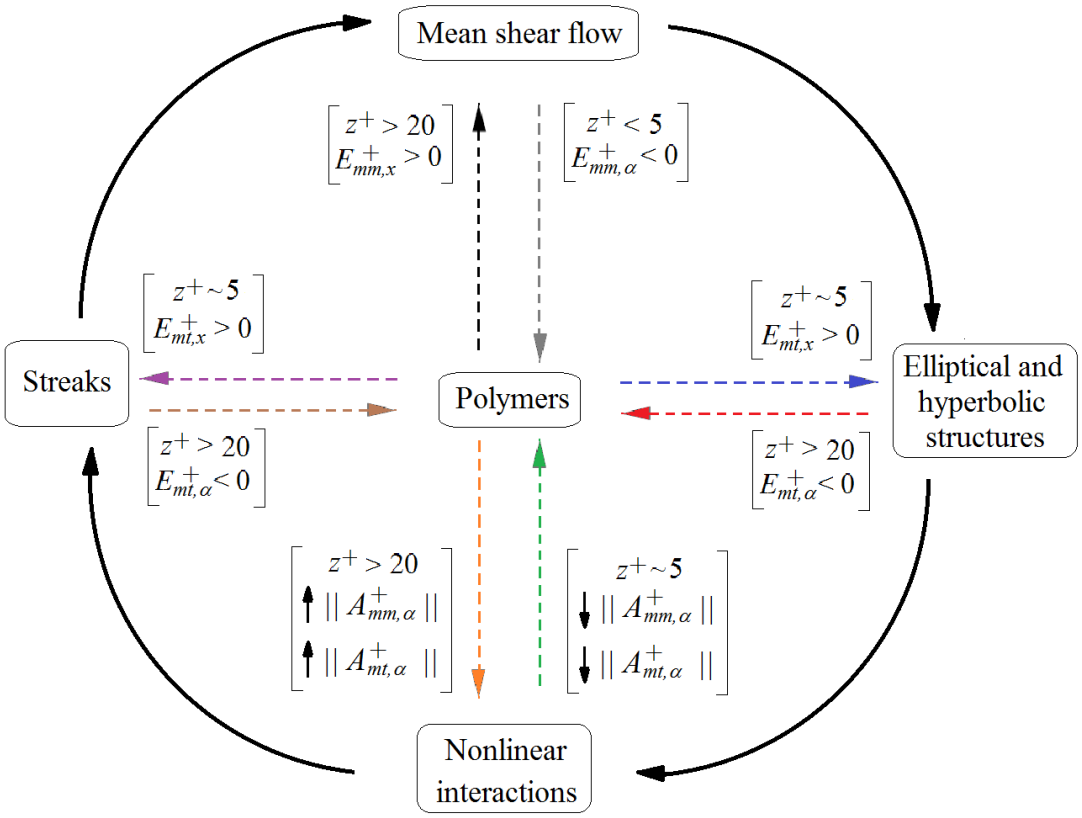

Figure 3.16 – Sketch of the polymer-induced drag reduction mechanism.

3.7 Concluding Remarks

Direct numerical simulations of a FENE-P fluid were used to analyse turbulent viscoelastic flows in a plane Couette geometry. Four Newtonian flows and sixteen viscoelastic flows were examined, keeping the viscosity ratio β_0 fixed at 0.9 and taking into account four different values of the Reynolds number based on the plate velocities ($Re_h = 1000$, $Re_h = 2000$, $Re_h = 3000$ and $Re_h = 4000$). A large range of Weissenberg number based on the plate velocities ($1 \leq Wi_h \leq 10$) and maximum polymer molecule extensibility ($10 \leq L \leq 100$) were explored, which provided drag reduction regimes (DR) from 0.9% up to 52.8% (the simulation details are in table 3.1, Section 3.2).

Polymers modify the velocity field, increasing its streamwise component, which departs from the Prandtl–Kármán law (the onset of DR) up to Virk's asymptote, as DR increases (figure 3.2a). A similar effect is found for the streamwise Reynolds stress normal component (figure 3.2b). Such an effect is related to the increase in the low wavenumber energy observed from the perspective of the longitudinal 1D spectra of turbulent kinetic energy (figure 3.15). Consequently, the advection transport becomes more pronounced in the core zone relative to the Newtonian case. An opposite trend is perceived in the near-wall region ($z^+ < 10$), where the high wavenumber structures are partially suppressed ($k_x > 10$) due to the attenuation of both the normal spanwise and wall-normal Reynolds stress components induced by the polymers (3.2b). As a result, the near-wall advection transport decreases with increasing elasticity.

A careful energy budget analysis allowed us to include more details concerning the polymer-flow interactions on the autonomous regeneration cycle discussed by Dubief et al. [24] and recently explored by Pereira et al. [71] (figure 3.15). Fundamentally, polymers are highly exposed to the mean flow, which acts as the main source of polymeric energy ($\langle E^+_{mm,\alpha} \rangle < 0$ in figure 3.12g) in the vicinities of the wall ($z^+ < 10$), where the molecules are highly stretched. In this region, polymers are also able to interact with the turbulent structures, releasing energy to them ($\langle E^+_{mt,\alpha} \rangle > 0$ in figure 3.12h), which contributes to enhance the streamwise velocity fluctuation. However, these trends completely change as the wall distance increases. Consequently, within turbulent structures located far from the wall, the molecules store energy by applying a counter-torque around the vortices [47] and a counter-stretch in the extensional regions [71]. In contrast, the molecules also release polymeric energy to the mean flow in the core zone, increasing the streamwise mean velocity. Lastly, it is important to remark that the polymer-flow exchanges of energy mentioned above become more pronounced as the drag reduction level increases (Re_h, Wi_h and L).

Chapter 4

Transient aspects of drag reducing plane Couette flows

The addition of a small amount of polymers of high molecular weight can lead to a decrease in the pressure drop in turbulent flows. Over the years, numerous studies have been conducted in attempts to make practical use of polymer-induced drag reduction. However, many aspects concerning its main mechanism are still unclear. One of those aspects is the development of the turbulent structures and polymer deformation over time in the beginning of the phenomenon. As an attempt to further understand the drag reduction over this developing time, we analyse a turbulent Couette flow of a FENE-P fluid with the aid of direct numerical simulations. We show that the initial interactions between the mean shear flow, turbulent structures, and polymer stretching are the key to understanding the step-by-step evolution of the drag reduction (DR). A few instants after the beginning of the simulation, the DR assumes a significantly negative value before starting to increase and reaches its maximum. When the DR is a minimum, the polymers experience their highest deformation state. The energy necessary to initially stretch them comes mainly from the mean shear flow, which causes a decrease of the DR until its minimum and negative value. After this point, the polymers start to strongly interact with the turbulent structures, which are partially suppressed, and the DR starts to increase. Part of the energy stored by the molecules is then released to the mean flow, increasing the DR to a maximum level while the polymer extension decreases. Lastly, DR reduces, reaching an asymptotic and positive value, which indicates the beginning of the statistical steady flow state.

4.1 Introduction

The drag reducing flows by polymers has been analysed since the pioneering works of Forrest and Grierson [28], Toms [93], and Mysels and Metzner [61]. Among its appli-

cations there is a great variety of processes, such as fire-fighting operations, transport of liquids in pipes, transport overseas, blood flow resistance, and many others [27, 15, 80, 29, 3]. The fundamentals of drag reduction (DR) together with many of its practical aspects can be found in [52, 51, 96, 84, 102]. From these papers one can mainly understand how the concentration, molecular weight, and temperature affect the DR.

Phenomenological explanations for polymeric drag reduction gravitate around two major ideas: the viscous theory, independently proposed by Lumley [52] and Seyer and Metzner [81], and the elastic theory postulated by Tabor and de Gennes [84]. Additional details regarding the DR mechanism have also been reported by Dubief et al. [24], Dimitropoulos et al. [21] and Thais et al. [86].

An aspect of the DR that has not been sufficiently analysed is its dependence on time, which is particularly significant at the begging of the phenomenon and will be the main focus of this work. When polymers are introduced into a fully developed turbulent flow, they cause an abrupt disturbance. The mean shear flow and the turbulent structures are strongly changed and a new steady state takes time to be reached, as numerically shown by Dimitropoulos et al. [21] and Tamano et al. [85] and experimentally confirmed by Andrade et al. [2]. The level of drag reduction can even assume negative values at the very beginning of the phenomenon (when the polymers are injected into a turbulent flow, for example). In fact, DR is zero at the beginning and decreases until a minimum value, before starting to increase and achieve its maximum value after a significant period, called the *developing time* [65, 64]. The details concerning the polymer–turbulence interactions during this period remain, however, unclear.

Despite the fact that DR has been widely studied, its transient aspect has not not yet been systematically investigated. The focus of our work is to carefully analyse, with the aid of a numerical simulation of a FENE-P fluid, the transient aspects of drag reducing plane Couette flows during the developing time. The initial interactions between the polymers and the flow are fundamental to fully understanding the variations in the level of the drag reduction, which can even assume negative values at the beginning of the simulations. The evolution of DR over time is confronted here with the evolution of the polymer stretching and turbulent structures. In addition, we also analyse the total kinetic energy budget, which is quite a good tool to further understand polymer–turbulence interactions. We believe that the comprehension of these interactions is the key to understanding the DR mechanism.

This work is organized as follows. The details concerning our numerical methodology are exposited in Section 4.2. Following the description of the methodology, our main results are finally presented in Section 4.3, where the transient aspects of drag reduction are analysed.

4.2 Numerical methodology

In order to analyse the interaction of the polymer molecules with the turbulence from the very beginning to the steady state, the initial conditions for the conformation tensor were the identity tensor, $\boldsymbol{I}$ ($\boldsymbol{C} = \boldsymbol{I}$ at the beginning of the simulations). In addition, for each viscoelastic case, both the velocity and the pressure fields were initially started from the same Newtonian fully developed turbulent flow. As a result of this methodology, the DR exhibits a significant transient behaviour before achieving its statistical steady state, as we will show in the next section.

The parameters for the turbulent FENE-P plane Couette flows studied here are summarized in Table 4.1. We simulated our viscoelastic cases fixing the Reynolds number based on the plate velocities, $Re_h = hU_h/\nu_{tot}$, at 3000 and β_0 at 0.9. Three combinations of Weissenberg number, $Wi_h = \lambda U_h/h$, and L were explored: $Wi_h = 10$ and $L = 100$; $Wi_h = 4.3$ and $L = 100$; $Wi_h = 10$ and $L = 30$. Both the size of the domain ($L_x \times L_y \times L_z = 12\pi \times 4\pi \times 2$) and the number of mesh points ($N_x \times N_y \times N_z = 384 \times 256 \times 129$) were kept the same for all cases, which leads to a grid resolution of $11.69 \leqslant \Delta x^+ \leqslant 13.40$, $5.85 \leqslant \Delta y^+ \leqslant 6.70$, and $0.31 \leqslant \Delta z^+ \leqslant 4.36$.

Re_h	$Re_{\tau 0}$	Wi_h	$Wi_{\tau 0}$	L	u_τ	Δ_x^+ **x** Δ_y^+ **x** $\Delta_{z,min}^+$	$\Delta_{z,max}^+$	**DR [%]**
3000	119.1	10	47.3	100	0.040	11.69 x 5.85 x 0.31	3.81	47 (HDR)
3000	136.5	4.3	26.7	100	0.046	13.40 x 6.70 x 0.35	4.36	30 (LDR)
3000	136.5	10	62.1	30	0.046	13.40 x 6.70 x 0.35	4.36	30 (LDR)

Table 4.1 – Parameters for the turbulent FENE-P plane Couette flows. In this paper, three FENE-P flows were examined keeping $Re_h = 3000$ and $\beta_0 = 0.9$ fixed. In addition, both the size of the domain ($L_x \times L_y \times L_z = 12\pi \times 4\pi \times 2$) and the number of mesh points ($N_x \times N_y \times N_z = 384 \times 256 \times 129$) were kept the same for all cases.

For the present study, we define the percentage of DR in time as follows:

$$DR(t) = \left(1 - \frac{< \tau_w(t) >}{< \tau_w(t=0) >}\right) \times 100, \tag{4.1}$$

where $< \tau_w(t) >$ is the wall shear stress at a given instant t and $< \tau_w(t=0) >$ is the wall shear stress at the very beginning of the simulation when the polymers are totally coiled. Two drag reducing regimes are obtained from our drag reducing flows after a statistical steady state was reached: the high drag reduction (HDR; $DR > 40\%$) observed for our most elastic case ($Wi_h = 10$ and $L = 100$) in which $DR = 47\%$; the low drag reduction (LDR; $DR \leqslant 40\%$) related to our least elastic cases ($Wi_h = 4.3$ and $L = 100$; $Wi_h = 10$ and $L = 30$) for which $DR = 30\%$. Physically, the main difference between these two regimes consists in the fact that for LDR flows, the Reynolds stresses play a major role, whereas in the HDR regime, the near-wall dynamics of the flow is dominated by the polymer stresses [102].

4.3 Results and Discussion

The focus of our work has been to carefully analyse, with the aid of a numerical simulation of a FENE-P fluid, a drag reducing flow over time. The polymer–turbulence interactions are complex and fundamental to clarifying the mechanism of DR, which can even assume negative values at the beginning of the simulation. Such negative values are not intuitive at first glance, and deserve our attention. In fact, the drag reduction is a consequence of the polymer's deformation (here estimated by $tr(\boldsymbol{C})/L^2$) and its interaction with the turbulent structures over time. The comprehension of this relationship is important to understand the mechanism of DR and the simulations shown here are a further step in this direction. The variations of DR over time are confronted here with the evolution of polymer stretching and turbulent structures. Lastly, the total kinetic energy budget is also considered, which represents quite a good tool for further explaining DR. We simulated three viscoelastic cases fixing Re_h at 3000 and β_0 at 0.9. The parameters of the FENE-P fluid are in Table 4.1. All data are presented here in terms of wall units and at a dimensionless time tU_h/h, where h is the half-gap between the upper and bottom plates and U_h is the absolute value of their velocities.

The evolution of the vortical structures over time can be recognized in figure 4.1, in which the three-dimensional isosurfaces of Q are displayed. The use of such a kind of entity to identify turbulent structures is quite common and is known as the *Q-criterion*, in which vortical (or elliptical) structures are defined as the positive values of the second invariant of the velocity gradient tensor, computed for incompressible flows by

$$Q = \frac{1}{2}\left(\|\boldsymbol{W}\|^2 - \|\boldsymbol{S}\|^2\right) > 0, \tag{4.2}$$

where $\|\boldsymbol{W}\|$ and $\|\boldsymbol{S}\|$ denote the Euclidean norms of $\boldsymbol{W}$ and $\boldsymbol{S}$, respectively[1]. On the other hand, negative values of Q indicate extensional (or hyperbolic) regions. For more details about such a criterion, see [38]. The structures shown in figure 4.1 come from the simulation of our most elastic FENE-P fluid ($Wi_h = 10$ and $L = 100$). From the top to the bottom, there are displayed four instantaneous three-dimensional structures of Q. For clarity, exceptionally in figure 4.1(a), we fixed $Q = 1$, since, at the very beginning of the simulation, $tU_h/h = 0.3$, the flow is full of structures and the isosurfaces of $Q = 0.1$ completely fill the domain. Hence, only to distinguish the structures, we show in figure 4.1(a) the isosurfaces of $Q = 1$. The colours on the isosurfaces depict the level of the relative polymer stretching, measured by the trace of the conformation tensor (normalized by the maximum polymer extension length), $tr(\boldsymbol{C})/L^2$. At the very first instants of the simulation, the molecules are totally coiled, $tr(\boldsymbol{C})/L^2 \approx 0$

[1] The Euclidean norm of a generic second order tensor $\boldsymbol{A}$ is $\|\boldsymbol{A}\| = \sqrt{tr\left(\boldsymbol{A}\cdot\boldsymbol{A}^{\boldsymbol{T}}\right)}$.

(the blue colour is dominant). Without any interaction between the polymers and turbulent structures, we see an apparently Newtonian fluid flow and the drag reduction is negligible ($DR \approx 0\%$), which is expected. It is known that in turbulent flows of Newtonian fluids, the morphology of the vortical structures follows an organized hierarchy over the domain (see figure 4.1). In the vicinity of the wall ($z^+ < 20$), eddies are found in pairs of counter-rotating quasi-streamwise vortices, while for $z^+ > 30$, these eddies resemble *hairpins* (the so-called *horseshoe vortices*; see also [1]) composed of three well defined parts: the *legs* (where the rotation is quasi-aligned with the streamwise direction), the *head* (a rotation part aligned with the spanwise direction), and the *necks* (connections between the legs and the head of the hairpin). A few instants later, at $tU_h/h = 9$, figure 4.1(b), the Newtonian morphology is completely changed. The polymers are abruptly stretched and the turbulent structures are partially destroyed (the vortices with $Q = 1$ have completely vanished). The isosurfaces of $Q = 0.1$ do not completely fill the domain anymore, even though the number of structures is widely spread over it. The surfaces are coloured from blue ($tr(\mathbf{C})/L^2 \approx 0$) to red ($tr(\mathbf{C})/L^2 \approx 0.8$), which indicates a distribution of the polymeric deformation over the domain. The stretching is higher close to the wall, where the mean shear stress is more intense (we will go back to this point later). We would like to emphasize here that at $tU_h/h = 9$, the drag reduction reaches its minimum negative value ($DR \approx -60\%$), despite the disappearance of a great number of turbulent structures. This fact really deserves our attention because it is not intuitive. If DR is a process in which a turbulent flow approaches a laminar state at the same Reynolds number, how is it possible to have the drag increased at the same instant when the turbulent structures are reduced? Numerical simulations of FENE-P fluid which show a drag increase have also been reported by Dimitropoulos et al. [21] and Tamano et al. [85], who argue that polymers take the great part of the necessary energy for stretching from the mean shear flow and such a significant loss of energy is the main cause of an initial drag increase, even restraining part of the vortices. The same explanation was used by Andrade et al. [2] who performed a number of experiments to take into account the drag increase and its dependence on the polymer's concentration and molecular weight.

In the sequence of the simulation, at $tU_h/h = 100$, figure 4.1(c), the turbulent structures with $Q = 0.1$ are strongly suppressed and the flow experiences its maximum level of drag reduction ($DR \approx 60\%$). The morphology of the vortices is very different from the Newtonian case at the beginning of the simulation, displayed in figure 4.1(a). Their thicknesses and streamwise lengths increase, while they become parallel to the wall. Hence, the classic Newtonian hierarchical organization mentioned before is no longer observed. At the same time, the polymers are weakly stretched (colours are midway blue and green). After the maximum DR is reached, a significant amount of structures appear again before finding their statistical steady state at $tU_h/h > 300$. In

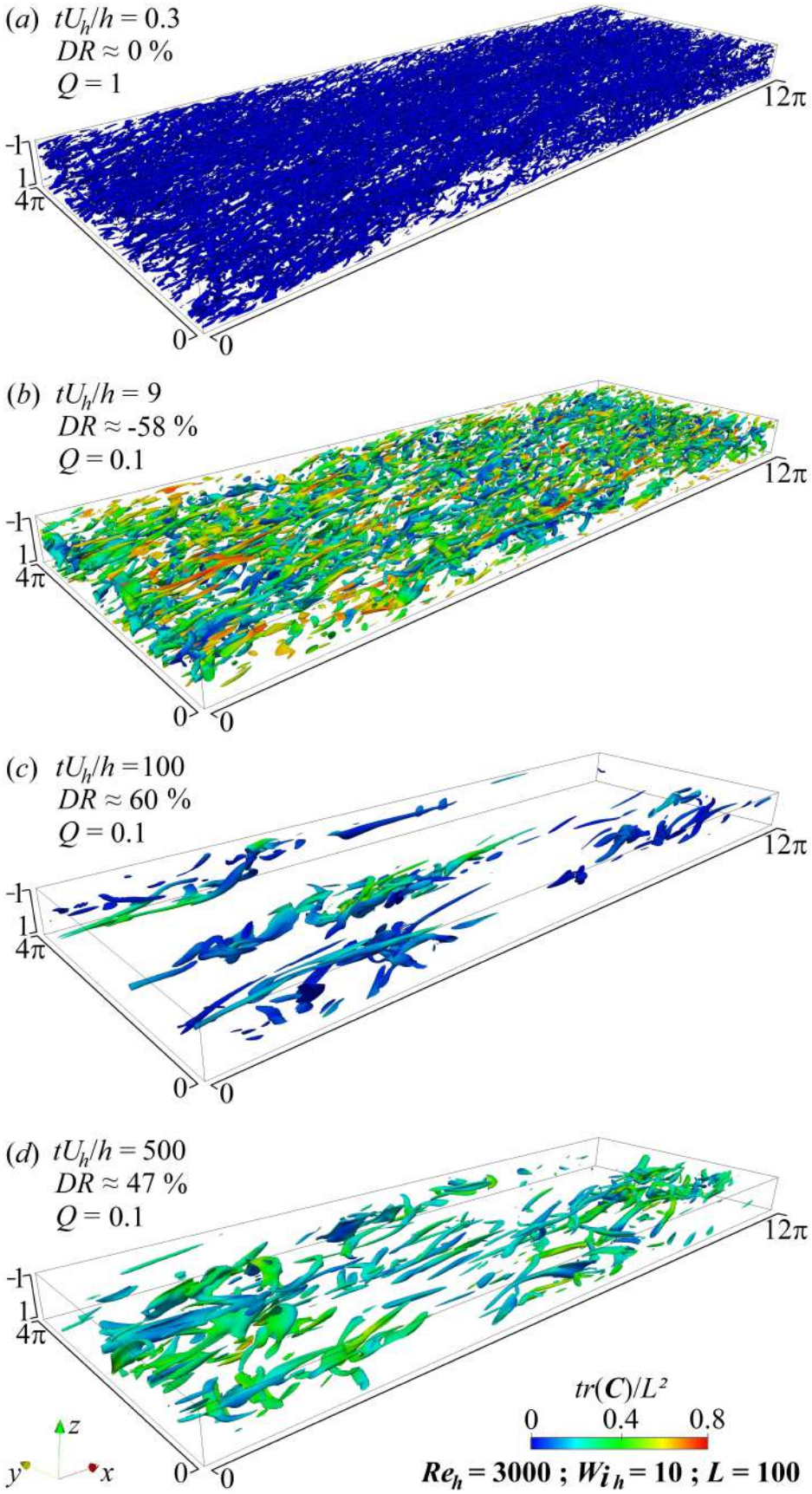

Figure 4.1 – The three-dimensional structures represent isosurfaces of vortical regions defined as a positive value of the second invariant of velocity gradient tensor, $\nabla \boldsymbol{u}$. The colours indicate the polymer stretching, $tr(\boldsymbol{C})/L^2$.

figure 4.1(d) we see the isosurfaces at $tU_h/h = 500$, in which the final value of DR is around 47%. The difference between the maximum value of DR and its asymptotic one ($DR_{max} - DR_{asy}$), which is smaller, is not obvious and deserves an explanation. This point will be discussed in the following paragraphs.

It is worth mentioning that the polymers interact with the turbulent shear flows, weakening not only the vortical structures ($Q > 0$; as shown in figure 4.1), but also the extensional ones ($Q < 0$; not shown here), which induces an enhancement of the parabolic domain ($Q = 0$). These initial interactions between the polymers and turbulent structures impose a transient behaviour on the drag reduction level at the very beginning of the phenomenon, as highlighted in figure 4.2(b) for our three viscoelastic cases. The drag reduction level is compared with the spatial average of the relative polymer stretching, $< tr(\boldsymbol{C})/L^2 >_{xyz}$, presented in figure 4.2(a), revealing an asynchronism between these two quantities. At the very beginning, there is no interaction between the polymers and turbulent structures and, consequently, the DR and $< tr(\boldsymbol{C})/L^2 >_{xyz}$ are zero. A few instants later, despite the fact that the polymers also take a non-negligible amount of energy from the turbulent structures, the molecules start to be stretched mainly by the mean shear flow, and $< tr(\boldsymbol{C})/L^2 >_{xyz}$ increases until reaching its maximum value (such a maximum value occurs at $tU_h/h = 9$ for the most viscoelastic FENE-P fluid). Simultaneously, the DR significantly falls and, at the same time, its maximum negative value of -60% is reached, which indicates a significant drag increase. Thus, the minimum DR (or the maximum drag increase) occurs when the molecules have their maximum mean length, which is a diametrical asynchronism. As we mentioned before, it occurs because the polymers take their energy for stretching primarily from the mean shear flow, and the consequence is the decrease of the DR. As the elastic parameters are incremented, the drag increase becomes more evident ($DR \approx -20\%$ for $Wi_h = 10$ and $L = 30$, and $DR \approx -60\%$, for $Wi_h = 10$ and $L = 100$). This is in accordance with the experiments available in Andrade et al. [2]. The increase of polymer concentration or molecular weight in a solution induces an increase in the drag at the very start of the drag reducing flow. The authors argue that the necessary energy used to change the polymers from their coiled state to a stretched new configuration increases when more molecules are introduced into the solvent. The same happens if the molecular weight is increased since a larger molecule stores more energy when stretched.

After its minimum value, DR starts to increase and simultaneously $< tr(\boldsymbol{C})/L^2 >_{xyz}$ decreases until the maximum value of drag reduction is reached. Such a maximum occurs at the dimensionless time equal to 100 for the most viscoelastic FENE-P fluid (grey circles). Some instants later, the phenomenon achieves its steady state regime, from an average point of view. As pointed out before, the maximum and the minimum values of DR are increasing functions of L and Wi_h, which is fully in accordance with

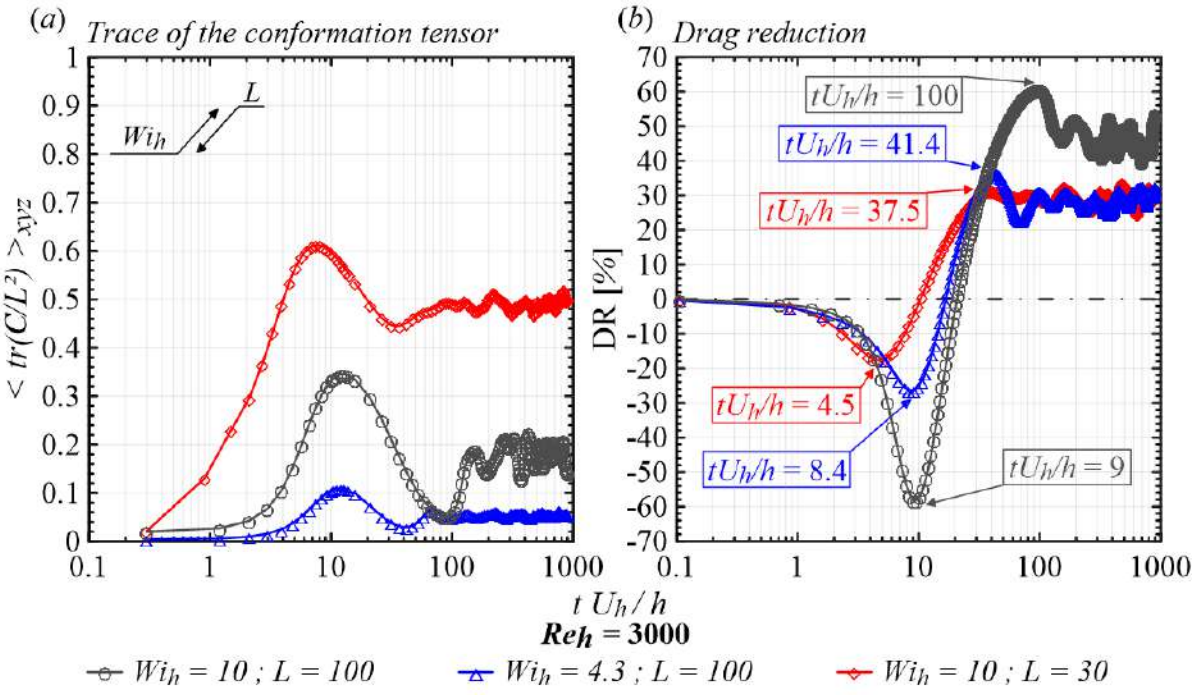

Figure 4.2 – Evolution of the spatial average of the relative polymer stretching as a function of the normalized time, tU_h/h (a). Average drag reduction, DR, as a function of the normalized time (b).

the experiments. Thus, the polymer stretching and the drag reduction do not follow the same rate. In fact, they are totally asynchronous. Such a behaviour was also observed by Dimitropoulos et al. [21], analysing a turbulent flow of FENE-P fluid in a different geometry. Hence, the turbulent flow is disturbed by the polymers within a very few instants of the beginning of the process. There is a exchange of energy between the mean flow, the vortices, and the polymers. This interaction induces a highly transient behaviour, which reaches its statistical steady state after a period of time, called here the 'developing time', t_d. This time is also an increasing function of the elasticity (L and Wi_h). Again, this is in accordance with the experiments in Andrade et al. [2], where a t_d that increases with polymer concentration and molecular weight is observed.

It is worth noting in figure 4.2(a) how L and Wi_h affect the polymeric deformation. Hence, let us compare the grey circles ($Wi_h = 10$; $L = 100$) and the red diamonds ($Wi_h = 10$; $L = 30$). It can be clearly seen that the relative polymer extension decreases with increasing L, which suggests that larger polymer molecules are less susceptible to chain scission, as pointed out by Pereira and Soares [65]. In an opposing trend, $tr(\boldsymbol{C})/L^2$ increases with Wi_h. If the relaxation time increases, the polymers can interact with a more extensive spectrum of turbulent structures [19]. Thus, their stretching must be more pronounced. This is also in agreement with Pereira and Soares [65].

In order to better understand the changes in the conformation of the molecules during the begging of the drag reduction phenomenon, we display in figure 4.3 how the

polymers are stretched relative to the wall distance at different instants. The average values in the $x-y$ plane of the trace of the normalized conformation tensor, $\langle tr(\boldsymbol{C})/L^2\rangle$, are displayed as a function of the normalized wall distance z^+ for our three combinations of L and Wi_h. We have chosen some very specific instants for each viscoelastic case, such as those for the maximum drag increase and drag reduction (values of tU_h/h inside the boxes in figure 4.2*b*), in addition to an instant at the very beginning of the simulation and at that corresponding to the statistical steady state. It is mainly shown that the polymers are stretched near the wall, within the *viscous sublayer* ($0 < z+ < 5$; region I), where the mean turbulent shear flow is very intense. The maximum deformation occurs within region II ($5 < z+ < 30$) and it dramatically decreases in the region III ($z^+ > 30$; region III). In the core zone, region III, the polymers are also stretched since the fluctuations in the velocity field also interact with the polymers, being a source of polymeric energy [86], but with a much lower intensity. Obviously, at the very start of the simulation, $tU_h/h = 0.3$, the mean polymer stretching is zero (grey circles). It reaches its maximum value some instants later (blue triangles), before decreasing again until finding a new minimum (red diamonds). At dimensionless times 500 and 1000, the polymer deformation is at its statistical steady state. In turbulent Newtonian flow studies, the boundaries of regions I, II and III are used to define the *viscous sublayer*, the *buffer layer* and the *log-law region*, respectively.

The interactions between the polymers and the turbulence can be also evaluated from the perspective of the streamwise velocity component, as shown in figure 4.4. The velocity profiles are analysed at the same five characteristic instants used in figure 4.3, for our three viscoelastic cases. Each point in the figure is an average in the $x-y$ plane along z^+. In order to compare our profiles with the classical ones available in the literature, the velocity of the bottom plate was subtracted from the velocity field, resulting in a relative streamwise component, u_{rx} given by $u_{rx} = u_x - (-U_h)$. Close to the wall, region I, all velocity profiles fall down in the *viscous law* ($< u_{rx}^+ >= z^+$; solid grey line), as expected. At the very start of the simulation, $tU_h/h = 0.3$, the polymers were totally coiled and the velocity profile fitted the Newtonian *log-law* (grey dots). Hence, at the beginning of the simulation the FENE-P behaves as a Newtonian fluid, because the molecules are not significantly stretched. Some instants later, when the maximum drag increase is reached, the velocity profile is below the Newtonian (blue triangles). This is quite representative and a clear picture of what happens to the mean flow, which is retarded when the polymers take energy from it to be stretched. Such retardation is very impressive for the case of the most viscoelastic FENE-P fluid. The velocity profile for the maximum drag reduction conduction is in red diamonds in (*a*), (*b*) and (*c*). It is worth noting that the MDR asymptote (red dash-dotted line; [96]) is achieved for the most viscoelastic case ($Wi_h = 10$ and $L = 100$), at $tU_h/h = 100$, when the maximum DR is reached, before decreasing to find its steady state (green squares and orange inverted

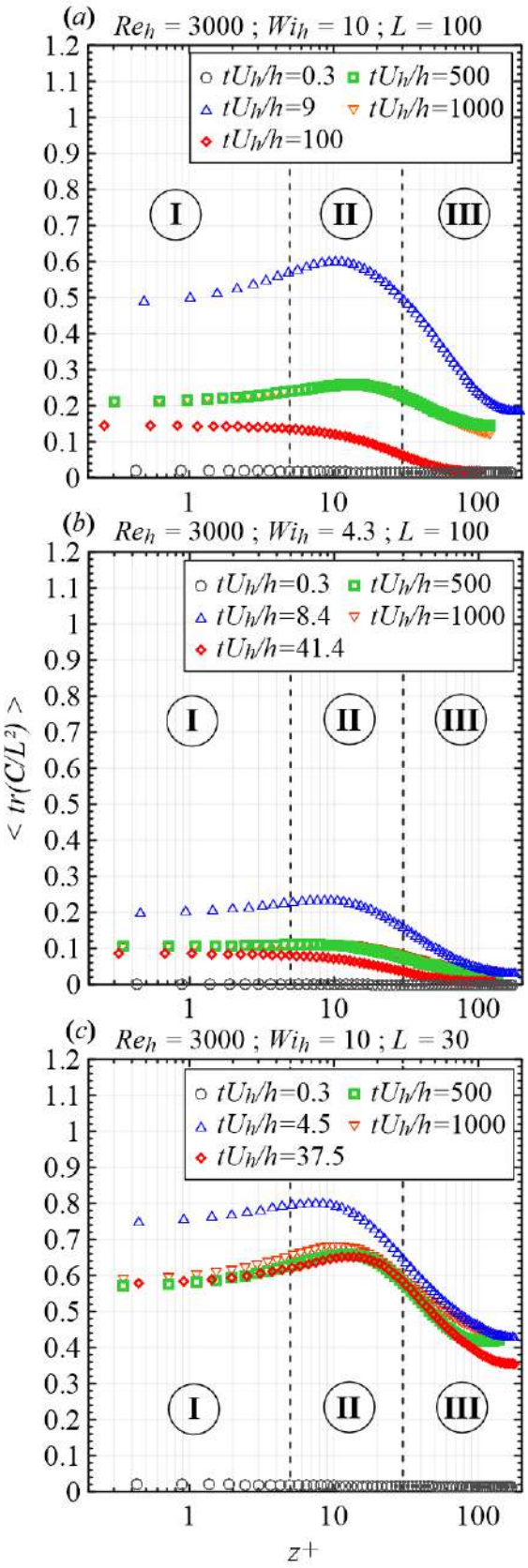

Figure 4.3 – Average values in the $x-y$ plane of the trace of the normalized conformation tensor, $\langle tr(\boldsymbol{C})/L^2 \rangle$, as a function of the normalized wall distance for three FENE-P turbulent flows: $Re_h = 3000$, $Wi_h = 10$ and $L = 100$ (a); $Re_h = 3000$, $Wi_h = 4.3$ and $L = 100$ (b); $Re_h = 3000$, $Wi_h = 10$ and $L = 30$ (c). For each viscoelastic flow, the relative polymer extension is analysed at four normalized instants, tU_h/h.

triangles).

Taking into account these results, the difference $DR_{max} - DR_{asy}$ can be explained. Why is the maximum drag reduction not sustained, but instead falls, reaching an asymptotic value below its maximum one? From an experimental point of view, this is expected, since polymers degrade or de-aggregate, but our current model does not take into account any degradation. In fact, we can detach the phenomenon as being dependent on three distinct entities: the polymers; the mean shear flow; and the turbulent structures. We can identify and compute the energy from each of these quantities. Thus, following the phenomenon step-by-step, we observe a Newtonian flow at the very beginning, when the polymers are totally coiled ($tr(\boldsymbol{C})/L^2 \approx 0$). After a few instants, the polymers are stretched and the necessary energy comes mainly from the mean shear flow, but a smaller part also comes from the structures. The part of the energy which comes from the vortices (one can see that in figure 4.1b the structures are reduced in comparison to figure 4.1a) works to increase the DR, but that part which comes from the mean shear flow is much larger and the consequence is a significant increase in the drag. The maximum drag increase at $tU_h/h = 9$ for our most elastic fluid imposes a retardation in the flow. We see in figure 4.4(a) a velocity profile (blue triangles) significantly below the Newtonian curve (grey dotted line). At that very moment, the mean velocity reaches its maximum retardation (see figure 4.4a). The polymers start to strongly interact with the turbulent structures, inhibiting them, and the DR starts to increase. In other words, the main reason for an increasing DR over time, after its minimum value is achieved, is the suppression of the turbulent structures. In addition, part of the energy stored by the polymers is released to the mean flow when their mean length is decreasing, which helps the DR to increase. This process continues until DR_{max} is reached at $tU_h/h = 100$ for $Wi_h = 10$ and $L = 100$. In addition, as the mean flow also acts as a source of turbulent energy [86], the increasing mean velocity tends to strengthen the vortices, which works in this sense to reduce the DR. After reaching their minimal stretching, the polymers start to deform again, but, unlike in the beginning, the mean shear stress is also minimal, since the velocity gradient near the wall is at its minimum value. Hence, in this new period of increasing deformation, the level of stretching reached is less pronounced. Again, the polymers take energy from the mean flow and the DR decreases until its final asymptotic value. Such a process is periodic, but after a sufficiently long time, the developing time (t_d), everything happens around a mean level which constitutes a statistical steady state in which the polymers interact with the flow following a coil–stretch cycle [24]. Finally, the fact that DR_{asy} is smaller than DR_{max} is expected and can be explained. The exchange over time of energy between the mean flow, the turbulent structures, and that stored by the polymers is the key of the mechanism.

The results discussed above indicate a significant interaction between the polymer

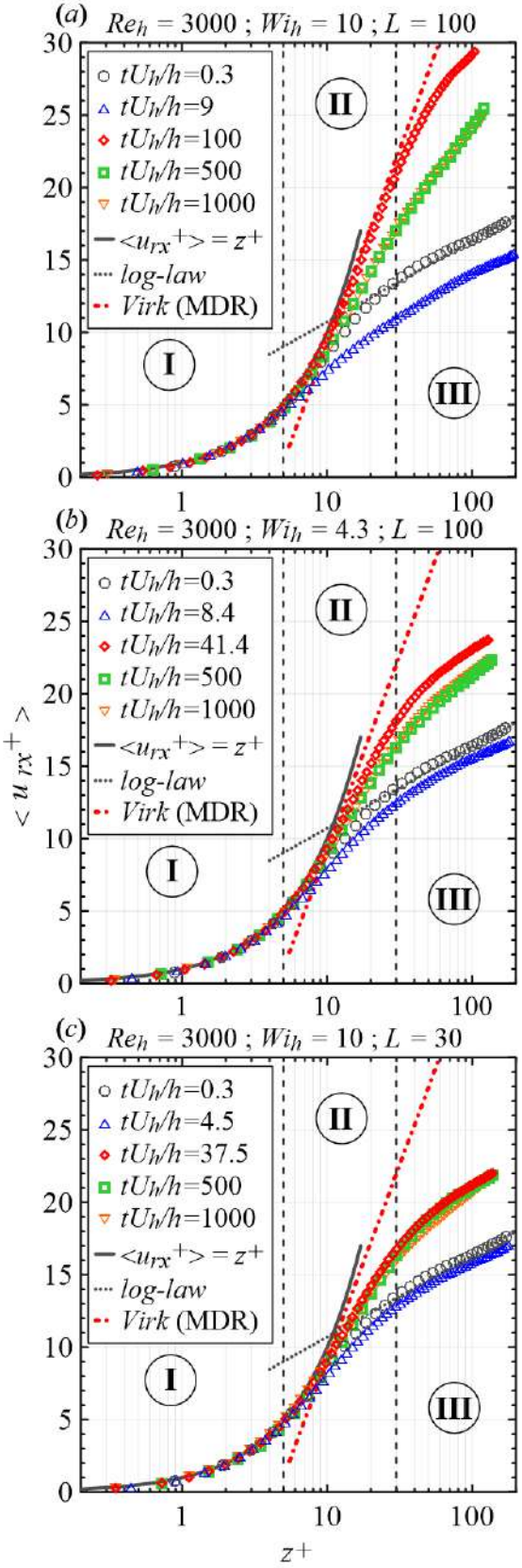

Figure 4.4 – Average values in the $x-y$ plane of the streamwise relative velocity, $\langle u_{rx}^+ \rangle$, as a function of the normalized wall distance for three FENE-P turbulent flows: Re_h = 3000, Wi_h = 10 and L = 100 (a); Re_h = 3000, Wi_h = 4.3 and L = 100 (b); Re_h = 3000, Wi_h = 10 and L = 30 (c). For each viscoelastic flow, the streamwise relative velocity is analysed at four normalized instants, tU_h/h.

and the flow in the beginning of the drag reduction phenomenon, followed by significant energy exchanges. These energy exchanges are taken into account by multiplying the momentum equation (1.2) by the velocity, which leads to the work equation:

$$\underbrace{\left[\frac{1}{2}\frac{\partial\left(u_\alpha^{+2}\right)}{\partial t^+}\right]}_{T_\alpha^+} = \underbrace{\left[-u_\alpha^+\frac{\partial\left(u_\alpha^+u_i^+\right)}{\partial x_i^+}\right]}_{A_\alpha^+} + \underbrace{\left[-u_\alpha^+\frac{\partial p^+}{\partial x_\alpha^+}\right]}_{P_\alpha^+} + \underbrace{\left[(\beta_0)\,u_\alpha^+\frac{\partial^2 u_\alpha^+}{\partial x_i^{+2}}\right]}_{V_\alpha^+} + \underbrace{\left[u_\alpha^+\frac{\partial \Xi_{\alpha i}^+}{\partial x_i^+}\right]}_{E_\alpha^+}, \tag{4.3}$$

where the instantaneous polymer work term, E_α^+, indicates the amount of energy stored ($E_\alpha^+ < 0$) or released ($E_\alpha^+ > 0$) by the polymers from the velocity field in the α direction, u_α^+. The complementary work terms denote the advection A_α^+, the pressure redistribution P_α^+, and the viscous stress V_α^+. The sum $A_\alpha^+ + P_\alpha^+ + V_\alpha^+$ is referred to as the *Newtonian work*, N_α^+, and T_α^+ is the time derivative term.

It is worth mentioning that the energy exchanges in the x direction constitute more than 90% of that considering the streamwise, the spanwise and the wall-normal directions. Hence, in figures 4.5 and 4.6, only the $x-y$ plane average of the instantaneous streamwise total kinetic energy budget, provided by equation 4.3, against the normalized wall distance is considered.

Figure 4.5 shows the spatial average of the streamwise energy budget, equation 4.3, as a function of the dimensionless time. The same three FENE-P cases are shown here. From this figure we can get quite a good picture of the energy exchange between the polymers and the turbulent flow. The polymeric work $< E_x^+ >_{xyz}$ is null at the beginning of the simulation, since the molecules are mainly coiled at this moment (blue crosses). The total energy $< T_x^+ >_{xyz}$ is balanced by the Newtonian work (the grey circles and the orange inverted triangles collapse into a single curve). Thus, at the very start of the simulation, the flow behaves as a Newtonian one. Some instants after the beginning, the energy balance totally changes, the polymeric work start to decrease, achieving negative values, meaning that the polymers are being stretched and energy is taken from the flow. The minimum value of $< E_x^+ >_{xyz}$ occurs at $tU_h/h \approx 9$ for the most viscoelastic case ($< E_x^+ >_{xyz} \approx -0.29$) displayed in figure 4.5(*a*). At the very same moment, the viscous work $< V_x^+ >_{xyz}$ reaches its maximum value (green squares; $< V_x^+ >_{xyz} \approx 0.3$) and the drag increase is around 60% (see figure 4.2*b*). Concerning the instantaneous velocity (figure 4.4*a*), we observe a significant retardation of the flow, since $< u_{rx}^+ >$ is below the classic Newtonian profile at $tU_h/h = 9$. Hence, the polymer work is balanced by the viscous work. In other words, the main energy stored by the polymers comes from the mean shear flow. After this point, part of the energy stored by the polymers is released to the mean flow while the mean extension of the molecules decreases (figure 4.2*a*). Consequently, the streamwise velocity increases and $< T_x^+ >_{xyz}$ also increases. At $tU_h/h = 100$ for our most elastic case, DR_{max} is reached, $< E_x^+ >_{xyz}$ approaches zero,

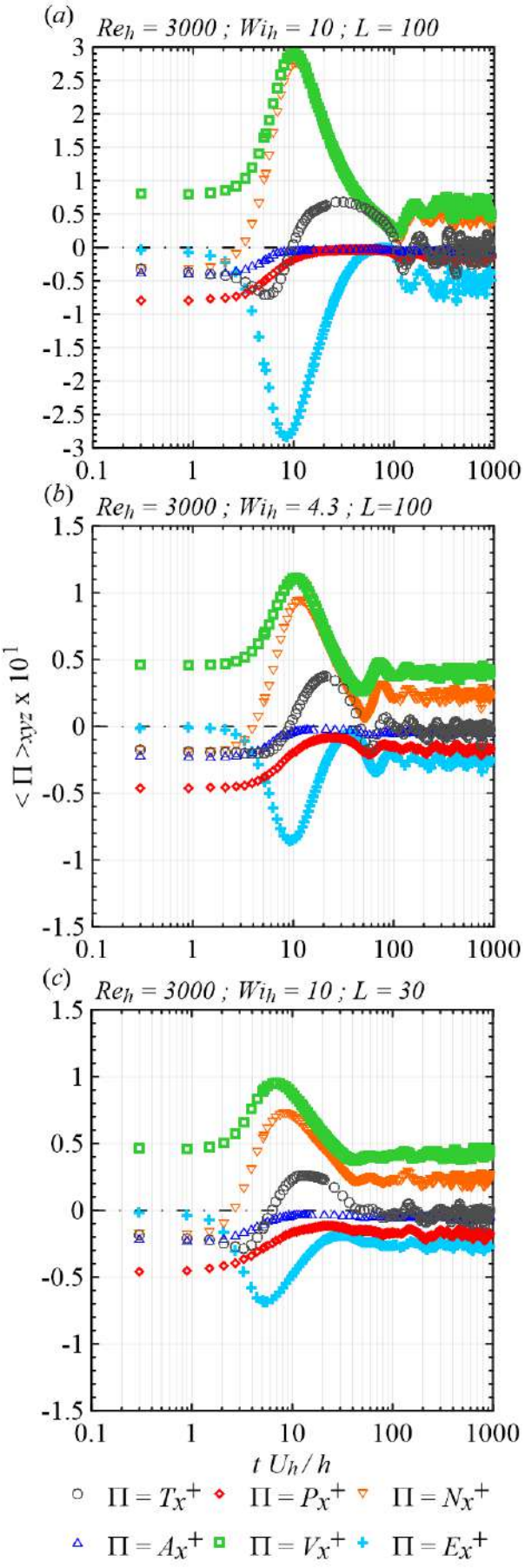

Figure 4.5 – Spatial average of the streamwise energy budget terms as a function of the normalized time, tU_h/h.

and a flow condition of minimum wall shear stress is achieved. Then, the polymers start to interact with this flow condition, stretching moderately until a constant mean level. At this final stage ($tU_h/h > 300$), $< T_x^+ >_{xyz}$ fluctuates around zero and the energy exchanges are mainly balanced by the polymeric work and the viscous work following the significant suppression of both the advection (blue triangles) and the pressure (red diamonds) related to the weakening of the turbulent structures shown in figure 4.1. As described by Dubief et al. [24], at the statistical steady state, the molecules work in their coil–stretch cycle, alternately storing energy in the flow and obtaining energy from the flow. Thus, the asymptotic value of $< E_x^+ >_{xyz}$ oscillates around its time-averaged value ($< E_x^+ >_{xyz} \approx -0.05$ for the most elastic case), which is clearly an increasing function of Wi_h and L.

Lastly, in figure 4.6 we can see the kinetic energy distribution as a function of the wall distance. The analysis is restricted to the most viscoelastic FENE-P fluid ($Wi_h = 10$ and $L = 100$). Again we see that, at the very beginning, $tU_h/h = 0.3$, the polymeric work (blue crosses) is zero and the kinetic energy is balanced by the Newtonian terms (orange inverted triangles). The advection term $< A_x^+ >$ balances the viscous work $< V_x^+ >$. Both quantities are nulls at the wall and reach their maximum values in the region II, just above the viscous sublayer ($z^+ \approx 5.5$). It seems that $< A_x^+ >$ and $< V_x^+ >$ are the main terms in the flow of Newtonian fluids, the former being the most important one as pointed by Graham [31]. In region III, both the terms are significantly reduced. Such a behaviour is expected, since the viscous work in flows of Newtonian fluids are related to the small scale fluctuations, which are null very close to the walls and less significant in the core region. After $tU_h/h = 9$, the energy distribution dramatically changes (figure 4.6*b*). The polymeric work starts to play a very important role in the flow. At this time, when the maximum drag increase occurs, the energy is exclusively balanced by the polymeric work and the viscous work, since $< A_x^+ >$ is strongly suppressed across the plane Couette half-width and $< P_x^+ >$ plays a minor role. As discussed previously, the polymers are primarily stretched by the mean shear flow close to the wall, which implies an intense polymeric work in the viscous sublayer, region I. In addition, the turbulent structures interact with the molecules, providing a supplementary polymer extension over the geometry. In other words, the mean shear flow is responsible for a significant polymer pre-stretching, which is increased since the turbulent structures interact with the polymer molecules, providing a supplementary polymer extension. After the polymer deformation in the beginning of the simulation, the molecules reduce their mean length and release energy to the mean flow. A significant increase in the advection term $< A_x^+ >$ is then perceived in figure 4.6(c), which results from the fact that the mean flow also acts as a source of turbulent energy. At this time, $tU_h/h = 100$, we observe the maximum drag reduction ($DR \approx 60\%$). Lastly, the energy in the statistical steady state condition, figure 4.6(d), is balanced by the polymeric work, the viscous

work, and the advection terms. In fact, comparing figures 4.6(a) and (d), we observe that $< A_x^+ >$ is strongly reduced due to the presence of the polymers within region II and slightly increased in region III, as a consequence of the morphological changes in the turbulent structures evidenced in figure 4.1.

4.4 Concluding Remarks

Direct numerical simulations of a FENE-P fluid are used to analyse a time-dependent drag reducing flow between parallel plates for a turbulent regime at $Re_h = 3000$. We simulated three viscoelastic cases, changing the values of Wi_h and L, but keeping the same viscosity rate $\beta_0 = 0.9$. Our main interest was to capture and emphasize some transient features of the drag reducing flow throughout parallel plates in an attempt to further understand its mechanism. The analyses of the simulations clearly show that three entities play a very important role in $DR(t)$, namely: the mean shear flow, the polymeric stretching, and the turbulent structures. Energy is constantly exchanged between these quantities from the beginning of the simulation until its statistical steady state, and it is the key to understanding drag reduction as a function of time.

Figure 4.7 summarizes the principal four stages related to the DR mechanism at the beginning of the phenomenon. The open symbols denote the mean streamwise velocity profiles, while the worm-like structures represent vortical (or elliptical) regions and the purple line illustrates the polymers. The exchanges of energy between these three entities at each stage are represented by the arrows. Firstly, at the stage 1 (figure 4.7a), polymers (purple line), initially coiled, store a significant amount of energy ($|E_x^+|$, increases) which primarily comes from the mean shear flow (grey circles), as indicated by the grey solid arrow. In addition, a smaller part of this energy comes from the turbulent structures (elliptical and hyperbolic ones, although only the former are represented in the sketch), as shown by the black solid arrow in figure 4.7(a). These polymer–flow interactions not only weaken the turbulent structures, as they decrease the magnitude of the advection ($|A_x^+|$), but also impose a retardation in the streamwise velocity. As a result, the DR decreases while the molecules stretch considerably, increasing the viscous work ($|V_x^+|$) near the wall. At stage 2 (figure 4.7b), the velocity profile reaches its maximum retardation (blue triangles) and $DR = DR_{min}$. Nevertheless, the polymers continue to interact with the turbulent structures, storing their energy and reducing $|A_x^+|$ (black solid arrow in figure 4.7b). At a certain point, molecules deformation cannot be sustained since the streamwise velocity and the turbulent structures are significantly weak. Consequently, the polymers start to partially coil, releasing energy to the mean flow (purple solid arrow), which helps DR and the mean streamwise velocity (red diamonds) to increase to their maximum level, as illustrated in figure 4.7(c) (stage 3). As the mean flow also acts as a source of turbulent energy [86], the increasing mean

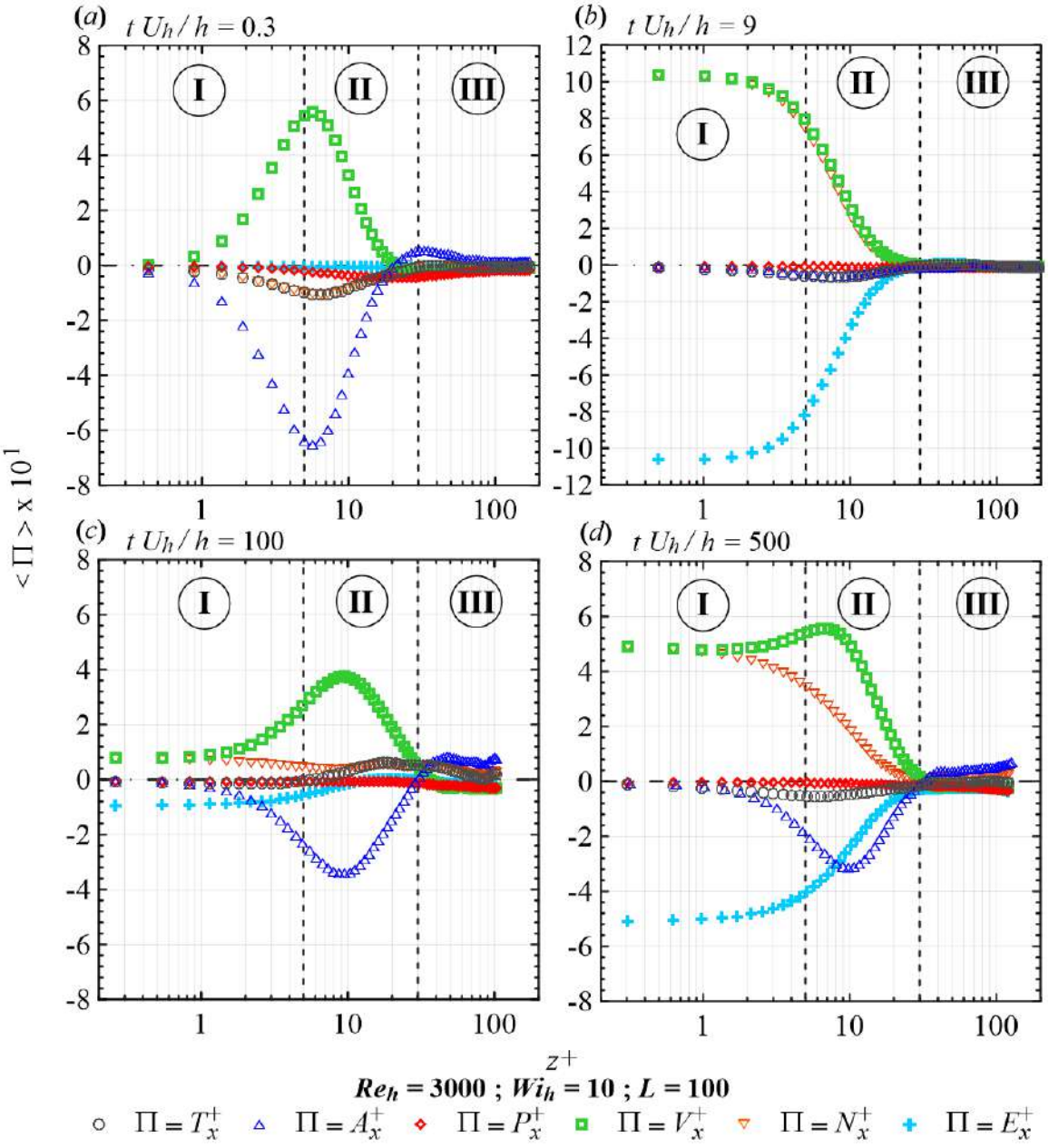

Figure 4.6 – Average values in the $x-y$ plane of the streamwise total kinetic energy budget against the normalized wall distance.

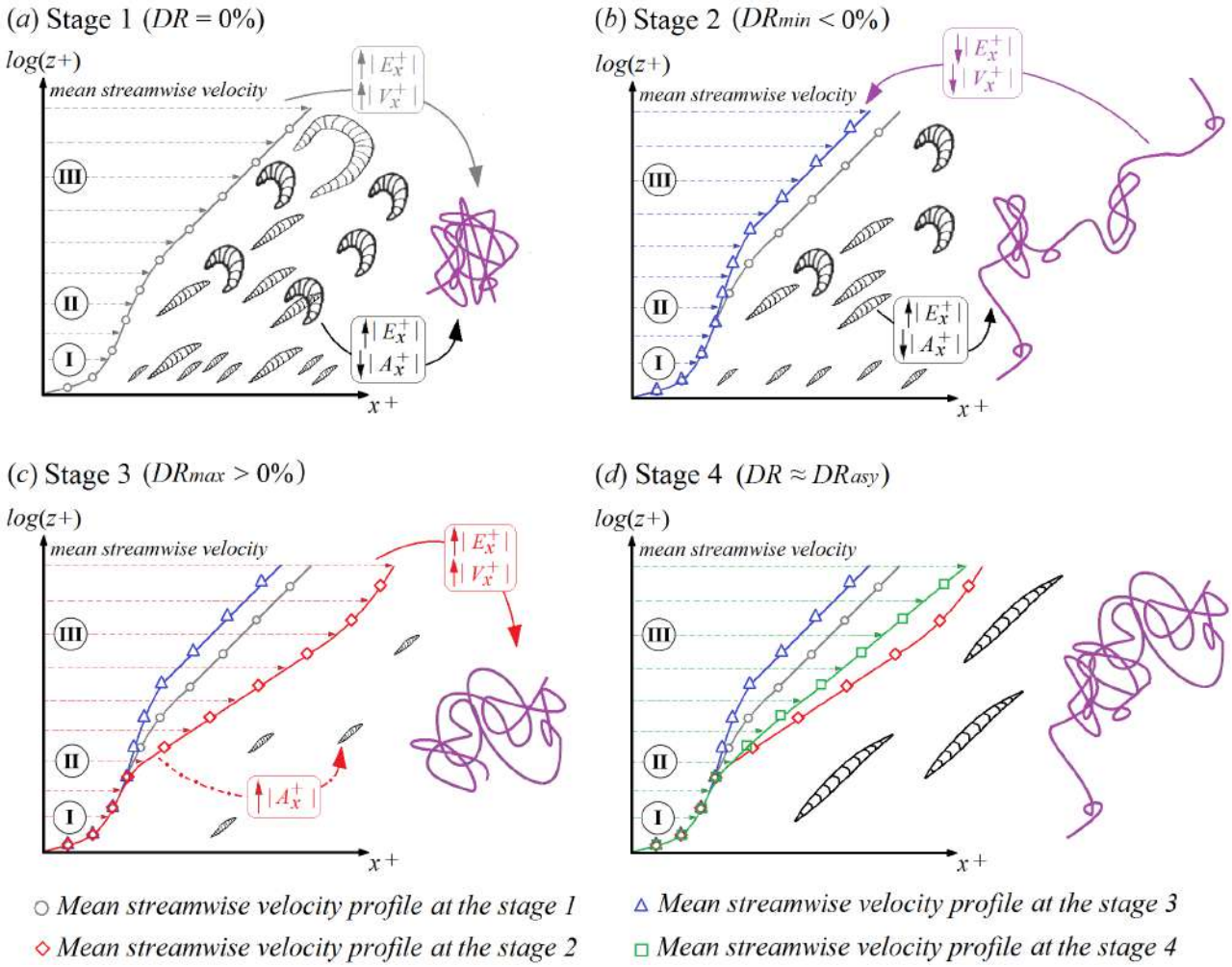

Figure 4.7 – Sketch of the polymer–flow interactions during the developing time. The open symbols denote the mean streamwise velocity profiles, while the worm-like structures represent vortical (or elliptical) regions and the purple line illustrates the polymers. The exchanges of energy between these three entities at each stage are represented by the arrows.

velocity tends to strengthen the turbulent structures ($|A_x^+|$ slightly increases at stage 3, as illustrated by the red dash-dotted arrow in figure 4.7*c*), reducing the DR. After reaching their minimal stretching, polymers start to deform again. However, differently from the beginning, the mean shear stress is minimal, since the velocity gradient near the wall is in its minimum value. Thus, in this period of increasing deformation, the level of stretching reached is less pronounced. Lastly, the polymers take energy from mean flow (red solid arrow in figure 4.7*c*) and the DR decreases until its asymptotic value, DR_{asy}, as shown in figure 4.7(*d*) (stage 4). In this statistical steady state, the polymers interact with the flow following the coil-stretch cycles described by Dubief et al. [24].

Lastly, it is important to emphasize that the asymptotic drag reduction is below its maximum value, which is explained here by means of fluid dynamics. In fact, $DR(t)$

and $< tr(\boldsymbol{C})/L^2 >_{xyz}$ oscillate until finding a statistical steady state after a long time due to the strong exchanges of energy, which dramatically modify the flow over time as well as the drag reduction level and the polymer conformation.

Chapter 5

Elliptical, parabolic, and hyperbolic exchanges of energy in drag reducing plane Couette flows

The Q-criterion is used to partition the domain into elliptical, parabolic, and hyperbolic subdomains corresponding to regions where the magnitude of vorticity surpasses, is equal, or is lower than the magnitude of the rate of strain. Although the importance of the hyperbolic parts is stressed in some works in fluid mechanics, only recently hyperbolic structures were recognized to play a crucial role on the drag reduction phenomenon of viscoelastic turbulent flows. More specifically, not only vortical structures are weakened by the action of polymers in turbulent flows, but also hyperbolic structures are attenuated in the same direction, in a process that can be referred to as *flow parabolization*. In the present work we investigate the polymer-turbulence interaction by discriminating the mechanical response of this system accordingly to the different subdomains, elliptical, parabolic, and hyperbolic, where this response is allocated. To this end, we employ Direct Numerical Simulations (DNS) of a viscoelastic Finite Extensional Nonlinear Elastic model with the Peterlin approximation (FENE-P) to examine the transient evolution and statistically steady regimes of a plane Couette flow which was perturbed from a laminar flow at an initial time and developed a turbulent regime as a result of this perturbation. We have found that even more activity is located within the confines of the hyperbolic structures when compared to what happens in the elliptical ones, which highlights the importance of considering the role of hyperbolic structures on the drag reduction mechanism.

5.1 Introduction

The turbulence of viscoelastic fluids is a subject that receives increasing attention in the literature. Turbulence is considered one of most challenging subjects of physics and, therefore, if the fluid that experiences such regime has a viscoelastic character, there is a substantial amplification of complexity of the flow. Besides that, the polymer induced drag reduction phenomenon (DR), i.e. the decrease in the friction factor originated by the addition of small amounts of polymers on a Newtonian turbulent flow [28, 93, 61], motivates considerably the investigation of viscoelastic turbulence, since important industrial processes can be economically impacted by a controlled DR procedure [15, 80, 29].

Although one can find efforts on modelling the flow using a Reynolds average approach [55, 56], or even Large Eddy Simulations (LES) [90], the main approaches used to investigate the DR are Direct Numerical Simulations (DNS) and experiments. This happens because the DR is not completely understood and, therefore, there is a need for fundamental studies that are able to explore new aspects of this problem and enhance our comprehension on the underlying physics of the polymer-turbulence interaction. Marginally to the prolific discussion around the two main theories that try to explain, in a simplistic form, the exceedingly non-linear nature of the DR, i.e. the viscous theory [52, 81, 51] and the elastic theory [84], there is an effort on understanding the effects of the interactions between polymers and turbulence by investigating how these two entities, representatives of material and flow, are correlated to each other. This correlation has been investigated in some fronts, as described below.

An intuitive and first investigated approach to understand polymer-turbulence interaction is to compute the effects of the polymer action on average quantities like mean velocity and Reynolds stress tensor. This line of investigation is responsible for the finding of the maximum drag reduction (MDR) or Virk's asymptote, an universal bound for the DR presented by Virk and co-workers [97, 98, 96, 95]. The categories *low drag reduction* (LDR) and *high drag reduction* (HDR) regimes are also an output of this approach. The Reynolds stress tensor is also highly affected by the action of polymers. Apart from the decrease of the shear stress component, there is a 'stretching' of the Reynolds stress ellipsoid in the streamwise direction, i.e. a growth on the magnitude of the streamwise normal component, accompanied with a decrease of the normal components in wall and spanwise directions [74, 99, 103, 23, 87].

A valuable approach is to analyse the energy budget equation and evaluate in which conditions the energy associated to the polymeric contribution is stored or released. This front was explored by Dubief et al. [24]. They found an unexpected release of polymer energy near the wall and proposed an autonomous regeneration cycle of polymer wall turbulence, i.e. a mechanism that could explain the energy interchanges

between polymer and turbulence. Pereira et al. [71] also analysed the energy-budget equation from this perspective. A new aspect of this cycle was observed, namely that the changes in the energy budgets are more significant on the Newtonian terms than the polymeric ones, showing a compensation of these Newtonian terms with respect to the polymeric one and revealing a clear non-linear effect of this interaction. A relevant contribution to the investigation of viscoelastic turbulence is the recognition of intermittent events that are hidden by time averages. In this connection, an important finding is the alternation between *active* and *hibernating* turbulence reported by the Graham's group [105, 106, 30]. The framework of nonlinear dynamic systems was employed to explain particularities of the flow, extolling the importance of extracting information from the time series produced by main variables. The study of the transient aspect of the polymer-turbulence interaction was considered by Pereira et al. [72], taking the Newtonian turbulent flow as a base flow where, at time $t = 0$, occurs the addition of a FENE-P polymer (Finite Extensible Nonlinear Elastic with the Peterlin approximation; [73, 14]).

A different approach that is used to correlate polymers and turbulence is to analyse how main features of polymer molecules like *shape* and *orientation* are connected to the *organization* of the turbulent flow considered. From the DNS perspective, it became usual to employ the Finite Extensible Nonlinear Elastic with the Peterlin approximation (FENE-P) due to a physically realistic representation of the finite extensibility of a polymer molecule combined with simplicity. This mesoscale approach belongs to the family of models in which the main features of the polymer are captured by the conformation tensor. In this sense, polymer shape and orientation are evaluated by their model counterparts which are the eigenvalues and principal directions of the conformation tensor that in turn are directly related to average dyadic of the end-to-end vector. Usually this information is condensed into the first invariant of the conformation tensor and the eigenvector associated to the highest eigenvalue. From the turbulent viewpoint of the polymer-turbulence nonlinear relation, important features of how this chaotic motion is organized can be grasped by its spectrum of different time and length scales or the instantaneous Reynolds stress tensor. Nevertheless, it is recognized that a crucial manifestation of turbulence is how this motion is structured. How to educe turbulent structures is a subjective issue and different approaches have been employed in this direction. It is not the aim of the present work to go through all the details in this matter, but a brief discussion is worthwhile. Going through the literature it is hard to distinguish in a clear way the expressions: *turbulent structures* and *coherent structures*. Sometimes these expressions can also be interchangeable with the expression *vortical structures*. In the 80's and 90's, Cantwell [16], Hussain [39, 40], Robinson [78], and others have developed the concept of coherent structures in turbulent flows. The vortex concept is still a non-consensual matter, as reported in a number of articles [18, 41, 107,

17, 34]. One widely used criterion for vortex identification is the Q-criterion presented in Hunt et al. [38]. Besides delineating the *eddy zones* what is usually interpreted as 'vortices from the Q-criterion perspective', this work also framed what they called the *convergent zones* as zones of convergence and divergence of streamlines. In a similar fashion, Weiss [101] alluded to regions vorticity-dominated and regions strain-rate-dominated using the expressions *elliptical mode* and *hyperbolic mode*, respectively. Haller [34] also refer to the *elliptical domain* and *hyperbolic domain* as regions where the flow defies the tendency dictated by the rate-of-strain tensor or corroborates that tendency, respectively. The expression 'parabolic domain' was employed to refer to 2D-boundaries between elliptical and hyperbolic domains. Inspired by these ideas, Pereira et al. [71] employed the expressions *elliptical structures* and *hyperbolic structures* based on the Q-criterion. These structures are obtained as a function of time and are manifolds of connected regions in space of constant values of Q, being elliptical if $Q > 0$, and hyperbolic if $Q < 0$. Several articles in the literature that investigate the DR places vortical (or elliptical) structures under scrutiny and have found unequivocal connection between the action of polymers in a turbulent flow and weakening of vortical structures [47]. Nevertheless, Pereira et al. [71] found that hyperbolic structures as captured by the Q-criterion, are also diminished by the influence of polymer activities. The preliminary results have shown that the process that occurs at the hyperbolic domain is not less important than the corresponding process in the elliptical domain, which is more established in the literature. What was shown by Pereira et al. [71] is that the action of polymer on turbulence induces an evolution towards a parabolic state where elliptical and hyperbolic structures get weaker as a consequence of elastic effects.

In the present work, we investigate the polymer-flow interactions within elliptical, parabolic and hyperbolic parts, separately, from a kinetic energy budget perspective. Employing the viscoelastic FEPE-P model, direct numerical simulations are conducted in order to examine the transient evolution and statistically steady regimes of drag reducing plane Couette flows which was perturbed from a laminar condition at an initial time and developed to a turbulent regime as a result of this perturbation. Two Newtonian fluids and two viscoelastic fluids are considered.

This work is organized as follows. In Section 5.2, we present the physical formulation and the numerical methodology considered for our simulations. Following the methodology description, our main results are displayed in Section 5.3, where the elliptical, parabolic, and hyperbolic exchanges of energy in drag reducing plane Couette flows are analysed. Finally, the conclusions are drawn in the closing section.

5.2 Numerical methodology

The parameters for the turbulent Newtonian and FENE-P plane Couette flows studied here are summarized in Table 5.1. We simulated our viscoelastic cases fixing the Weissenberg number, $Wi_h = \lambda U_h/h$, at 10, L at 100 and β_0 at 0.9. In addition, two values of Reynolds number based on the plate velocities, $Re_h = hU_h/\nu_{tot}$, were explored: $Re_h = 1500$ and $Re_h = 4000$. In order to investigate the polymer addition effects on the fluid dynamic, these viscoelastic flows were compared with two Newtonian cases at the same Re_h. The size of the domain was kept the same for all DNS presented here ($L_x \times L_y \times L_z = 12\pi \times 4\pi \times 2$) while the number of mesh points was $N_x \times N_y \times N_z = 768 \times 512 \times 257$ for the higher Re_h case and $N_x \times N_y \times N_z = 384 \times 256 \times 129$ for the lower one. This leads in a grid resolution of $11.69 \leq \Delta x^+ \leq 13.40$, $5.85 \leq \Delta y^+ \leq 6.70$, and $0.31 \leq \Delta z^+ \leq 4.36$.

Re_h	$Re_{\tau 0}$	Wi_h	$Wi_{\tau 0}$	L	u_τ	Δ_x^+ **x** Δ_y^+ **x** $\Delta_{z,min}^+$	$\Delta_{z,max}^+$	**DR [%]**
1500	93	-	-	-	0.062	9.13 x 4.56 x 0.19	2.84	0
1500	64	10	27.5	100	0.043	6.28 x 3.14 x 0.19	1.96	50
4000	220	-	-	-	0.055	10.80 x 5.40 x 0.19	3.81	0
4000	150	10	56.3	100	0.038	7.36 x 3.68 x 0.19	2.60	52

Table 5.1 – Parameters for the turbulent Newtonian and FENE-P plane Couette flows. In this work, two FENE-P flows were examined keeping $Wi_h = 10$, $L = 100$, and $\beta_0 = 0.9$ and varying the Reynolds number ($Re_h = 1500$; $Re_h = 4000$). The number of mesh points was $N_x \times N_y \times N_z = 768 \times 512 \times 257$ for the higher Re_h case and $N_x \times N_y \times N_z = 384 \times 256 \times 129$ for the lower one. The size of the domain was kept the same for all cases ($L_x \times L_y \times L_z = 12\pi \times 4\pi \times 2$).

For the present study, we define the percentage of DR as a function of time as follows:

$$DR(t) = \left(1 - \frac{<\tau_w(t)>}{<\tau_{w,N}(t)>}\right) \times 100, \tag{5.1}$$

where $<\tau_w(t)>$ is the area-average of the FENE-P wall shear stress at a given instant t and $<\tau_{w,N}(t)>$ is the area-average of the Newtonian wall shear stress at the same instant t. The following steady unidirectional shear field was used as initial velocity and pressure conditions for the DNS: $u_x(x,y,z) = z$, $u_y(x,y,z) = 0$, $u_z(x,y,z) = 0$, and $p(x,y,z) = 0$. Additionally, for the viscoelastic DNS, the initial conformation tensor field

was given by the stationary analytical solution:

$$\begin{cases} C_{xx} = \frac{1}{f\{\mathrm{tr}(\boldsymbol{C})\}}\left[1 + \frac{2\ We_h^2}{f^2\{\mathrm{tr}(\boldsymbol{C})\}}\left(\frac{du_x}{dz}\right)^2\right] \\ C_{xy} = C_{yz} = 0 \\ C_{xz} = \frac{We_h}{f^2\{\mathrm{tr}(\boldsymbol{C})\}}\left(\frac{du_x}{dz}\right) \\ C_{yy} = C_{zz} = \frac{1}{f\{\mathrm{tr}(\boldsymbol{C})\}} \\ f\{\mathrm{tr}(\boldsymbol{C})\} = \frac{2}{3}\cosh\frac{\phi}{3} + \frac{1}{3}, \end{cases} \tag{5.2}$$

with $\phi = \cosh^{-1}\left(\frac{27}{2}\ \Omega^2 + 1\right)$, $\Omega = \left(\sqrt{2}\ We_h/Lp + 1\right)\frac{du_x}{dz}$ and $\frac{du_x}{dz} = 1$ since $u_x = z\ \forall z \in [-1, 1]$. Aiming to analyse the interaction of the polymer molecules with the turbulent structures from the very beginning of the DR phenomenon ($DR = 0\%$) to its steady state ($DR > 0\%$ and statistically constant), turbulence was triggered by a initial perturbation consisting of four pairs of counter-rotating vortices with axes of rotation aligned with the x-direction:

$$\begin{cases} u'_{init} = 0 \\ v'_{init} = -A\left(x - \frac{L_x}{2}\right)\left(y - \frac{L_y}{2}\right)\exp\left[-\left(x - \frac{L_x}{2}\right)^2 - \left(y - \frac{L_y}{2}\right)^2\right]\left(1 - 6z^2 + 5z^4\right) \\ w'_{init} = A(z)\left(1 - z^2\right)^2\left(x - \frac{L_x}{2}\right)\exp\left[-\left(x - \frac{L_x}{2}\right)^2 - \left(y - \frac{L_y}{2}\right)^2\right]\left[1 - 2\left(y - \frac{L_y}{2}\right)^2\right], \end{cases} \tag{5.3}$$

where u'_{init}, v'_{init}, and w'_{init} are the initial velocity increments responsible for disturb the flow in each direction and A is the amplitude coefficient (A was kept fixed at 5 for the cases shown in 5.1). As a result of this methodology, DR exhibits a high transient behaviour before achieving its statistical steady state, as we will show in the next section.

5.3 Results and discussion

As discussed in section 5.1, Pereira et al. [71] showed that not only the elliptical structures but also the hyperbolic ones play an important role on the drag reduction mechanism. Both types of structures tend to evolve towards a parabolic state, which is a fingerprint of the laminar viscometric regime, when interacting with polymers. In the present work, we will employ a strategy of investigation that splits a general quantity of interest into relative intensities associated to each of these structure forms.

Figure 5.1 shows subfigures of the evolution in time of elliptical and hyperbolic structures originated from a turbulence perturbation superposed onto a laminar viscoelastic shear flow at dimensionless time $t/U_h h = 0$ for the case at $Re_h = 4000$, $Wi_h = 10$

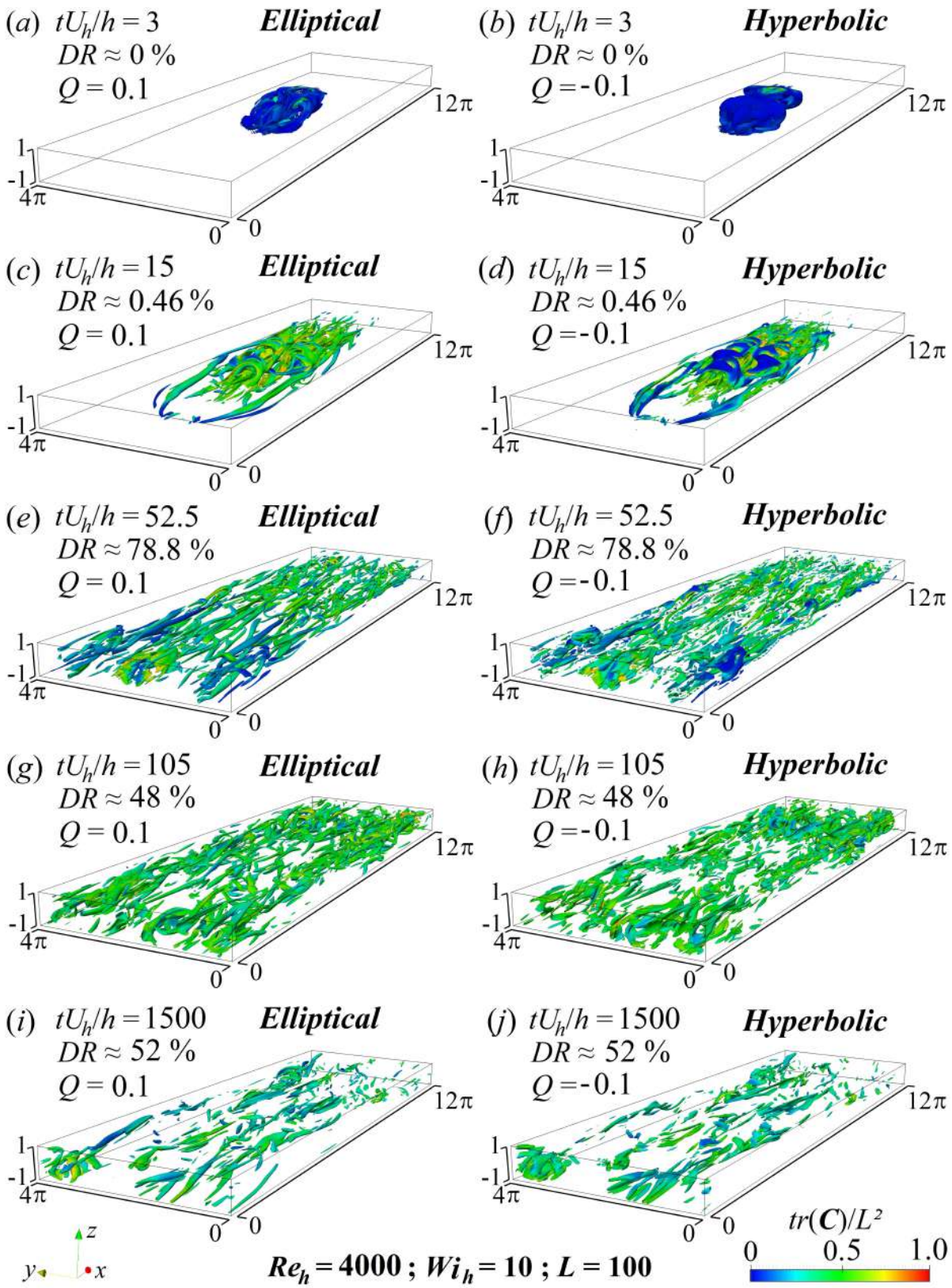

Figure 5.1 – The three-dimensional structures represent isosurfaces of elliptical and hyperbolic structures defined respectively as a positive and negative value of the second invariant of velocity gradient tensor, $\nabla \boldsymbol{u}$. The colors indicate the polymer stretch, $\mathrm{tr}(\boldsymbol{C})/\mathrm{L}^2$.

and $L = 100$. These structures are determined by isosurfaces of Q [38]. For incompressible flows, $Q = \frac{1}{2}\left(\|\boldsymbol{W}\|^2 - \|\boldsymbol{S}\|^2\right)$, where $\|\ \|$ denotes the Euclidean norm of a given tensor. On the left column in figure 5.1, we find how the elliptical structures associated to $Q = 0.1$ evolves in time, while on the right, hyperbolic structures characterized by the same intensity, $Q = -0.1$, are displayed. The color of the structures indicates the stretch level of the polymers as measured by the quantity $\mathrm{tr}(\boldsymbol{C})/\mathrm{L}^2$. Figures 5.1($a$) and 5.1($b$), related to the dimensionless time, $tU_h/h = 3$ (three units after the perturbation injection), show that, elliptical and hyperbolic structures form a volume with quite similar sizes. These structures are predominantly blue, indicating that the polymers are coiled at the beginning. At this moment, the level of DR is negligible ($DR \approx 0$). From figures 5.1(c) and 5.1(d), we notice that, at $tU_h/h = 15$, elliptical and hyperbolic structures advance in the domain exhibiting a similar overall shape. At this instant, the polymer chains are more stretched showing a distribution of colors predominantly green, i.e. $\mathrm{tr}(\boldsymbol{C})/\mathrm{L}^2 \approx 0.5$. The polymers associated to the hyperbolic structures are less stretched around the upper plate (more bluish), while around the lower plate they are more stretched in both hyperbolic and elliptical structures, what is illustrated by the yellow color. When time advances to $tU_h/h = 52.5$ and the drag reduction is around $DR \approx 78\%$, the structures corresponding to the magnitude $|Q| = 0.1$ are spread all over the domain. The main difference between the hyperbolic and the elliptical parts is that the former is more fragmented than the latter.

A worth noticing fact, is that there was a significant change in DR from $tU_h/h = 52.5$ to $tU_h/h = 105$ (from $\approx 78\%$ to $\approx 48\%$) with a insubstantial corresponding change in the structure level of both types. On the other hand, a small change in DR from $tU_h/h = 105$ to $tU_h/h > 200$ had a remarkable change in the number of hyperbolic and elliptical structures. We will return to this point later.

The changes in the flow during the development of the initial perturbation are evaluated from a turbulent structure perspective in figures 5.2, where the spatial average over the whole domain ($< >_{xyz}$) of the percentage of elliptical (grey circles), parabolic (blue triangles) and hyperbolic (red diamonds) structures is shown as a function of the dimensionless time, tU_h/h, for the four cases considered here: the Newtonian flow at $Re_h = 1500$ (figure 5.2a); the Newtonian flow at $Re_h = 4000$ (figure 5.2b); the viscoelastic flow at $Re_h = 1500$, $Wi_h = 10$ and $L = 100$ (figure 5.2c); the viscoelastic flow at $Re_h = 4000$, $Wi_h = 10$ and $L = 100$ (figure 5.2d). In the early stages of evolution, when the flow is essentially laminar, there is a dominance of the parabolic state, as expected, for all cases. Besides that, the hyperbolic and the elliptical structures are equally distributed, occupying 10% of the flow (5% of elliptical parts and 5% of hyperbolic ones). From this percentage viewpoint, the effect of changing the Reynolds number in the Newtonian case is almost indistinguishable (figure 5.2a and b). For all four cases, as the initial perturbation advances in the domain, the number of elliptical

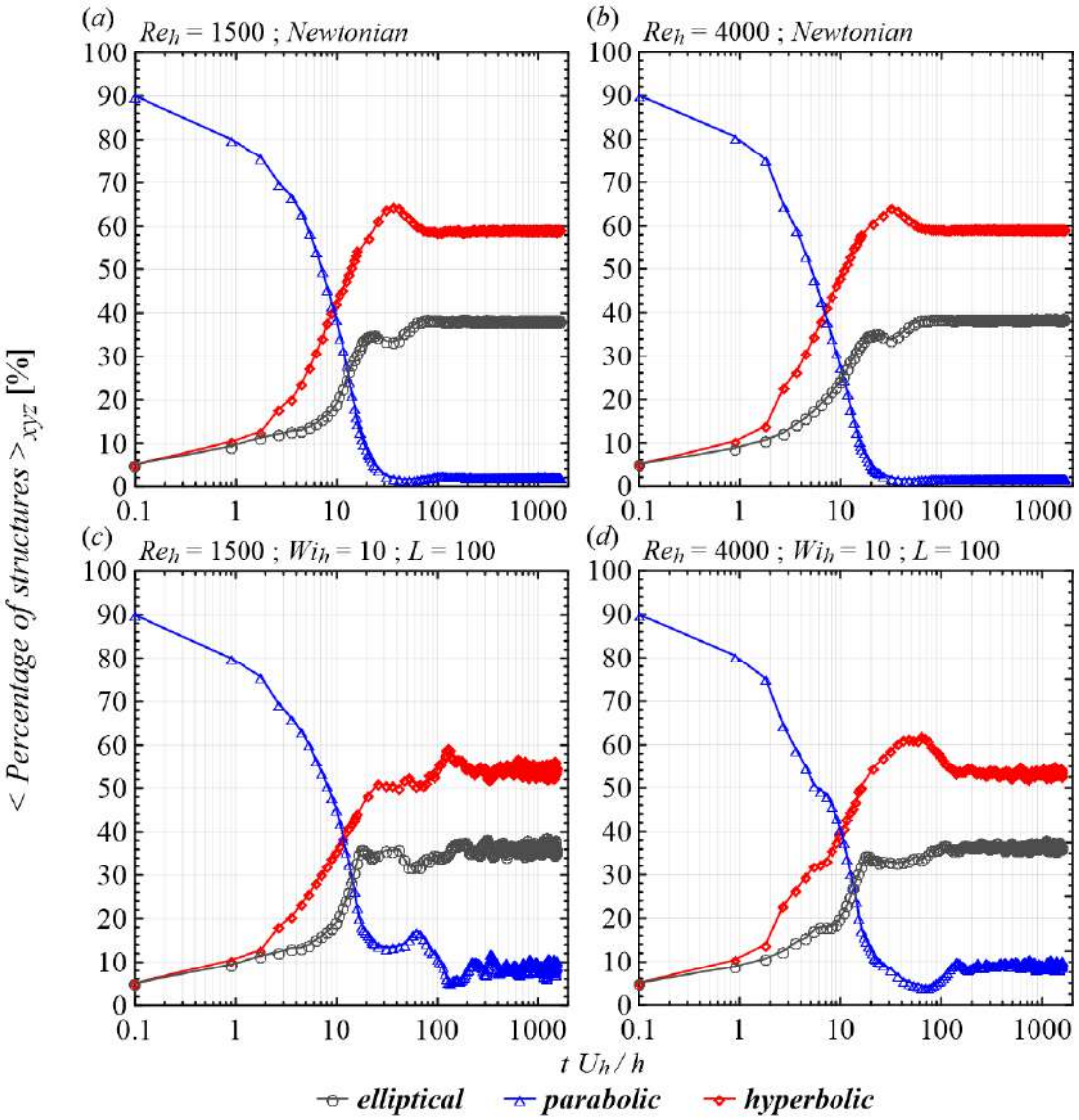

Figure 5.2 – Percentage of coherent structures as function of the dimensionless time, tU_h/h.

and hyperbolic structures increases whereas the percentage of parabolic parts associated with the laminar regime strongly decreases. It is worth noting that after $tU_h/h \approx 1$, the quantity of hyperbolic structures increases more sharply than that of the elliptical ones. Except for the viscoelastic case at $Re_h = 1500$, just before the achievement of the steady state, the percentage of hyperbolic structures has a peak whereas elliptical percentage of structures have a valley. The viscoelastic cases do also present a valley in the percentage of parabolic states. Once the statistically steady state regime is achieved, we can find very well defined plateaus for each percentage of structures. During this period, the percentage of parabolic parts is negligible compared with the hyperbolic ($\approx 60\%$) and elliptical ($\approx 40\%$) distributions, for the Newtonian cases. In contrast, a non-negligible amount of parabolic parts is observed for the viscoelastic flows. In general, it can be said that the viscoelastic fluids redistribute the percentage of structures, favouring the enlargement of the parabolic domain and decreasing the percentage number of hyperbolic and elliptical structures, as previously discussed in Pereira et al. [71].

The picture given by an evolution in time as presented in figure 5.2 can be enriched from a location perspective as shown in figure 5.3, where the average values in the $x-y$ plane of the time-averaged percentage of structures is displayed as a function of the wall distance. The percentage of structures was averaged in time over some 500 flow snapshots spanning several eddy turnover times after the statistical steady state was achieved (the same methodology employed by [**Thais-13**, 87]). Our four flows are analysed. All the cases show a predominance of a parabolic state near the wall, while hyperbolic and elliptical structures are more frequent far from the wall. Another common feature these cases share is that hyperbolic structures are more present than elliptical ones in the entire domain. It is noteworthy the intense redistribution that occurs within the space of the first wall unit (region I, $0 < z^+ < 5$). Taking the Newtonian case at $Re_h = 4000$ as an example (figure 5.3*b*), we can see that the parabolic parts go down from 100% at the wall to $\approx 5\%$ at $z^+ = 1$. From $z^+ = 0.2$ to $z^+ = 1$, the hyperbolic structures have increased from 0% to $\approx 75\%$, while the percentage of elliptical structures have increased from 0% to $\approx 20\%$. This redistribution is less intense in the low Re_h case (figure 5.3*a*), but still very high. This intense activity very near the wall may be responsible for the poor description obtained from the Large Eddy Simulation approach where even in wall resolved version, the first grid point is typically of one or more wall distance units. If we continue to increase the wall distance, we find that, at the end of the viscous sublayer ($z^+ = 5$), the percentage of parabolic states is negligible and the redistribution of domains are restricted to hyperbolic and elliptical ones. In this case, we can see that as wall distance gets higher, more elliptical structures are formed at the expense of the hyperbolic ones. For the Newtonian cases, it seems that the minimum distance between the percentage of hyperbolic and elliptical structures is achieved at the upper limit of the buffer layer ($z^+ = 30$). Comparing the viscoelastic

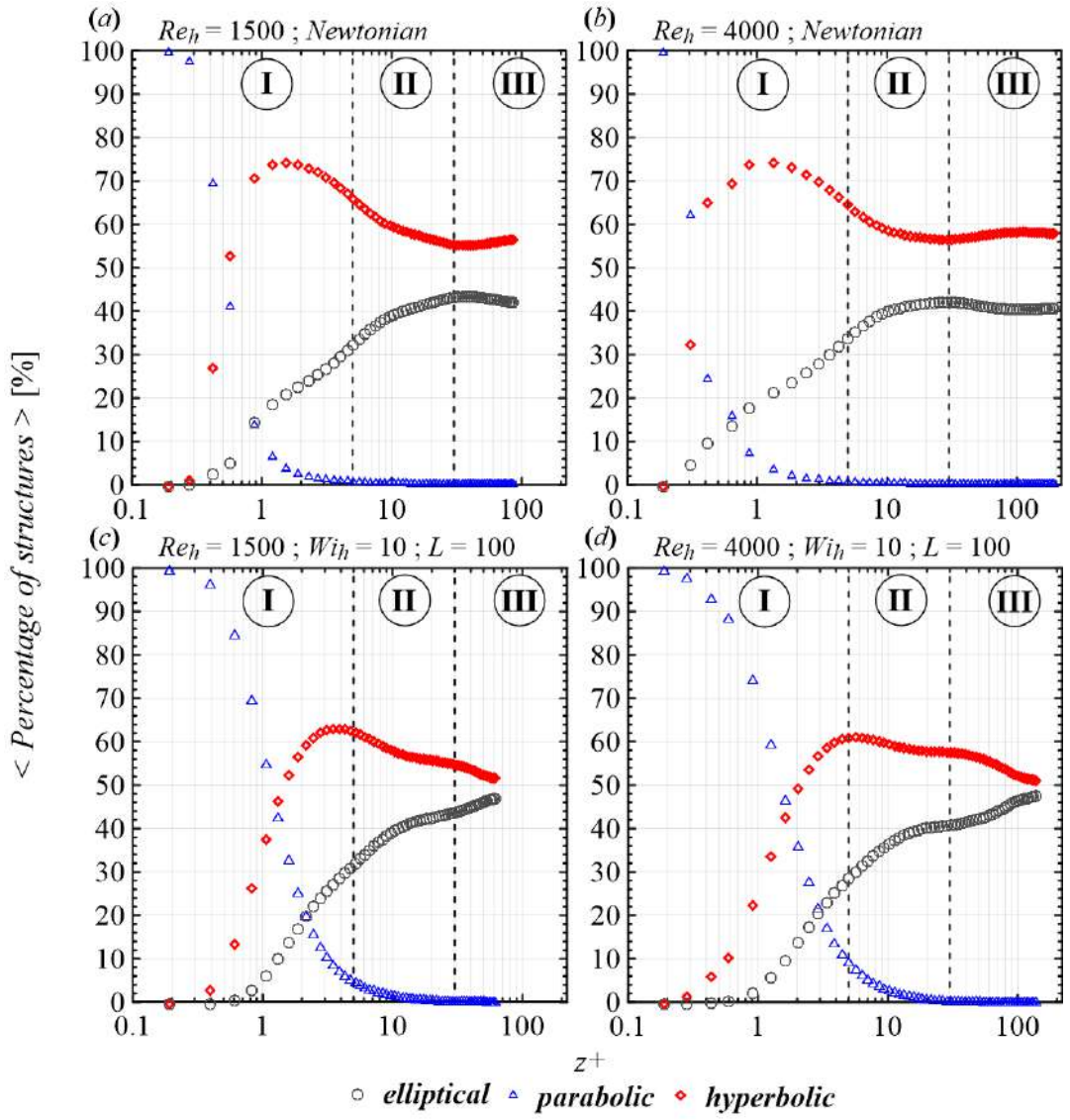

Figure 5.3 – Percentage of coherent structures as function of the dimensionless wall distance.

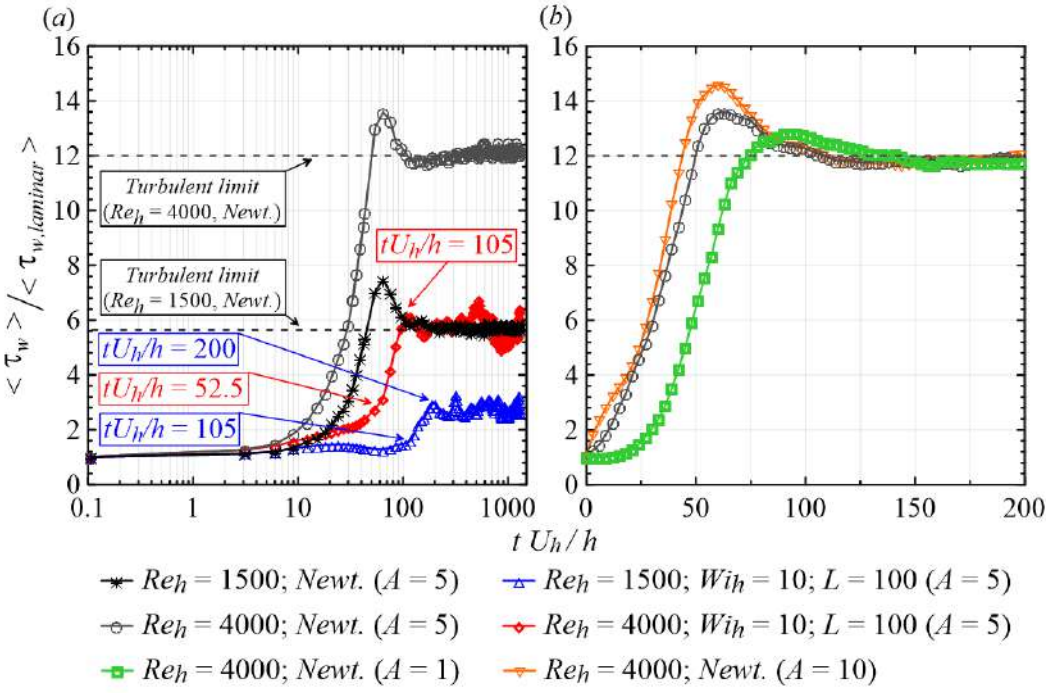

Figure 5.4 – Evolution of the wall shear stress, τ_w, made dimensionless by its laminar value, $\tau_{w-laminar}$, as function of the dimensionless time, tU_h/h.

cases with their Newtonian counterparts, we can observe a significant extension of the near-wall region where the parabolic parts are accompanied with both elliptical and hyperbolic structures $z^+ = \in [2, 30]$. Taking the case at $Re_h = 4000$, $Wi_h = 10$ and $L = 100$, we notice that at $z^+ = 1$ the percentage of parabolic parts is still $\approx 74\%$ against $\approx 5\%$ of the Newtonian case. This fact may suggest that the decrease of the parabolic domain can be used as a criterion for inferring the size of the viscous sublayer for viscoelastic wall turbulence. After the upper limit of the region II ($5 < z^+ < 30$), another remarkable difference in viscoelastic flow is the continuous decrease in the gap between hyperbolic and elliptical structures as we move towards the centre of the geometry. This behaviour is in contrast to the Newtonian cases where a minimum gap between the percentage number of hyperbolic and elliptical structures coincides with the limit between the buffer and s. If this criterion is used to define this transition, one would conclude that the buffer layer would continue until the centre line while the log-law layer would be suppressed. This conclusion is in accordance to the works of White and co-workers [102, 104] who put in light the suppression of the log-law layer in viscoelastic turbulence and criticized the use of a log-law to describe the maximum drag reduction limit. Relative to the Newtonian flows, the viscoelastic cases exhibit a less numerous near-wall elliptical and hyperbolic parts (region I). In region III ($z^+ > 30$), a higher percentage of elliptical structures is observed, while the hyperbolic ones appear in a smaller number than the corresponding Newtonian case.

In order to better understand effects the of the Reynolds number and the elasticity

on the drag, we analyse in figure 5.4(a) how the average of the wall stress in $x-y$ plane evolves over time, taking as reference the wall shear stress at the laminar regime ($\langle\tau_w\rangle/\langle\tau_{w,\ laminar}\rangle$). Because of this reference, all curves start from unity. Our four cases are considered. Examining the two Newtonian curves, we can see a dramatic difference between the two levels of stresses at the wall when the Reynolds number increases from $Re_h = 1500$ (black stars) to $Re_h = 4000$ (grey balls), although they exhibit similar shapes. The ratio $\langle\tau_w\rangle/\langle\tau_{w,\ laminar}\rangle$ departs from 1 at the very few instants after the very beginning of the simulations. At $tU_h/h \approx 3$, inertia (Re_h) and elasticity (Wi_h, L) start play a role as can be noticed by the detachment of the different curves. It is worth noting that, specifically for the Newtonian cases, the asymptotic value is preceded by an overshoot in the wall shear stress. The occurrence of the overshoot explains the significant decrease in DR with no corresponding changes in the turbulent structures shown in figure 5.2. This is a Newtonian effect. Figure 5.4(b) reveals that this overshoot emerges from inertial effects related to the value of the amplitude of the initial perturbations, A. Comparing our standard results obtained with $A = 5$ (grey circles), with the results with new amplitudes, $A = 1$ (green squares) and $A = 10$ (orange inverted triangles), it is clearly perceived that the overshoot is a increasing function of A. Since polymers suppress inertial effects, no overshoot is observed for the viscoelastic cases analysed in figure 5.4(a). Furthermore, polymers delay the development of the turbulent structures. At $tU_h/h = 105$, for instance, the wall shear stress for the Newtonian flow at $Re_h = 1500$ already achieved its asymptotic level (black stars) while the correspondent viscoelastic wall shear stress barely started to increase (blue triangle). Hence, for viscoelastic cases, the asymptotic plateau is reached at higher dimensionless times compared to their Newtonian counterparts, which is in accordance with the recent experimental results reported by Andrade et al. [2], who evidenced that the development of turbulent structures is delayed by the polymers.

Regarding the increase in the viscoelastic wall shear stress towards its asymptotic value, it is possible to distinguish at least three stages. During the first stage, $\langle\tau_w\rangle/\langle\tau_{w,\ laminar}\rangle$ slightly increases. Considering, for instance, the viscoelastic case at $Re_h = 4000$ (red diamonds), the initial stage occurs for the dimensionless time $3 < tU_h/h < 52.5$. However, at $tU_h/h = 52.5$, the slope of $\langle\tau_w\rangle/\langle\tau_{w,\ laminar}\rangle$ dramatically increases, characterizing the second stage of the flow development. The same tendency is observed for the case of $Re_h = 1500$ (blue triangles curve) at $tU_h/h = 105$. As we will show later, the initial and smaller slope is related to the interactions between polymers and turbulent structures while the second and accentuated slope is linked with strong energy exchanges between the polymers and the mean flow. Lastly, during the third stage (the statistical steady state), $\langle\tau_w\rangle/\langle\tau_{w,\ laminar}\rangle$ oscillates around its time-averaged value.

As discussed in Section 5.2 (equation 5.1), the instantaneous drag reduction level

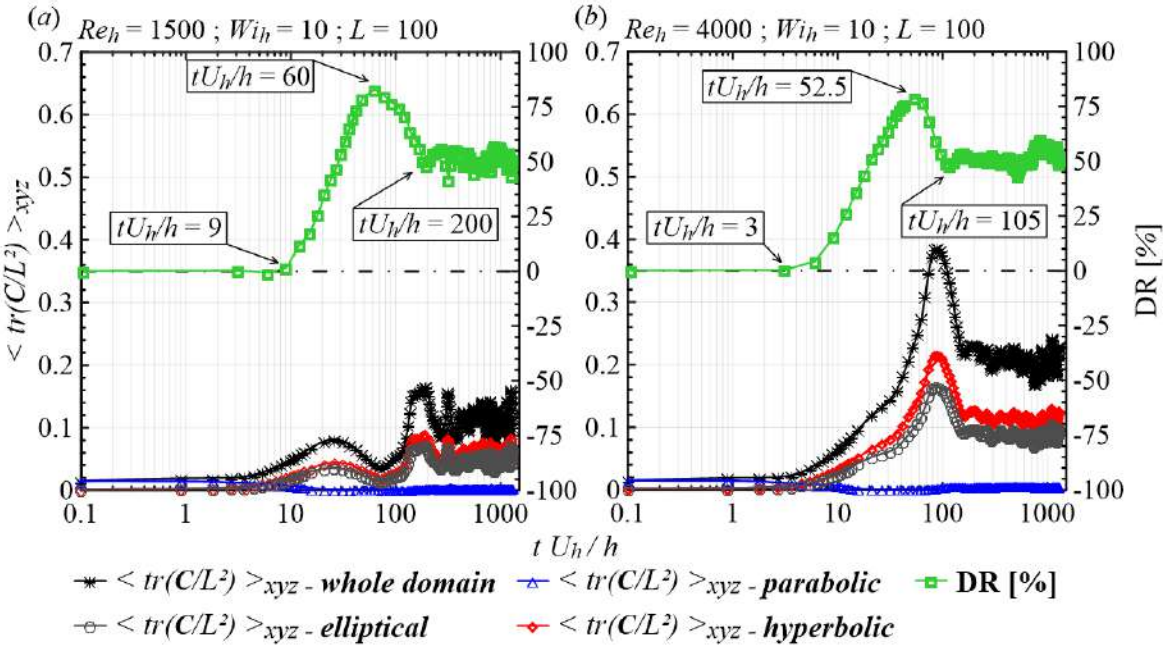

Figure 5.5 – Evolution of the spatial average of the relative polymer stretch as function of the dimensionless time, tU_h/h. Average drag reduction, DR, as function of the dimensionless time.

is calculated by dividing the viscoelastic wall shear stress curve by its corresponding Newtonian one, the both shown in figure 5.4(a). The evolution over time of the drag reduction level is displayed in figures 5.5(a) and (b) (green squares) together with instantaneous spatial averages of the relative polymer stretching, $\langle \mathrm{tr}(\boldsymbol{C})/\mathrm{L}^2 \rangle_{xyz}$. The former is evaluated by considering not only the whole domain (black stars), but also each subdomain, i.e. the elliptical (grey circles), parabolic (blue triangles) and hyperbolic (red diamonds) ones.

Analysing the green square curve in figure 5.5(b), we first notice that DR starts to increases at $tU_h/h \approx 3$, achieving its maximum value at $tU_h/h \approx 52.5$. As shown in figure 5.4(a), at this dimensionless time, the Newtonian wall shear stress is very close to its peak while the viscoelastic one is increasing sharply. As a consequence, DR decreases during the next instants until reaching its asymptotic plateau ($\approx 52\%$) at $tU_h/h \approx 105$. A similar behavior is perceived at $Re_h = 1500$, as illustrated by the green squares in figure 5.5(a). The only difference between the two viscoelastic cases is the retardation in the flow development which happens at $Re_h = 1500$. In this case, DR is shifted from zero at $tU_h/h \approx 9$ and reaches its maximum level at $tU_h/h \approx 60$. In addition, its asymptotic wall shear stress plateau is achieved at $tU_h/h \approx 200$. It is important to remark that, for the both viscoelastic cases, the polymer conformation (black stars) is still strongly varying over time when the asymptotic wall shear stress plateau is achieved. Therefore, the fact that the asymptotic $\langle \tau_w \rangle$ was reached does not indicate the begging of the statistical steady state [21, 72]. At $Re_h = 4000$, for instance, the final flow condition

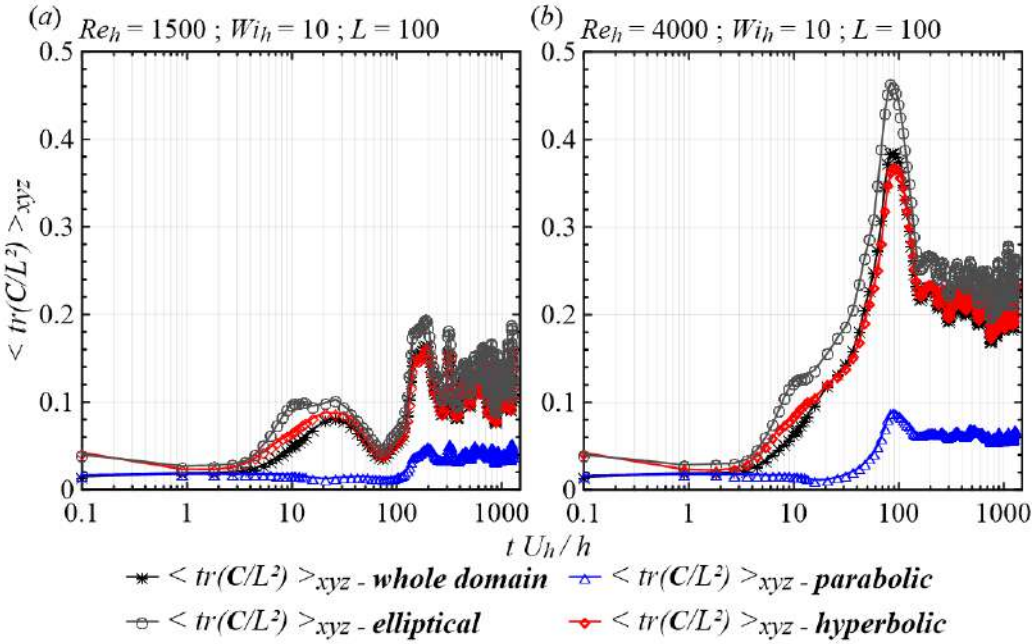

Figure 5.6 – Evolution of the spatial average of the relative polymer stretch normalized by the size of each subdomain as function of the dimensionless time, tU_h/h.

is only observed for $tU_h/h > 200$, when both the velocity and the conformation tensor fields oscillated around their mean values. At $Re_h = 1500$, the statistical steady state is observed for $tU_h/h > 300$.

Concerning the relative polymer stretching, it is noted that, a few instants after the beginning of the simulations, $\langle \mathrm{tr}(\boldsymbol{C})/\mathrm{L}^2 \rangle_{xyz}$ increases from approximately zero to its peak. For the viscoelastic case represented by the black stars in figure 5.5(b), the increase in the polymer extension becomes more pronounced between $tU_h/h \approx 52.5$ and $tU_h/h \approx 90$, when $\langle \mathrm{tr}(\boldsymbol{C})/\mathrm{L}^2 \rangle_{xyz}$ is maximum (≈ 0.38). Then, the polymers release part of their energy to the flow and $\langle \mathrm{tr}(\boldsymbol{C})/\mathrm{L}^2 \rangle_{xyz}$ decreases to its statistical steady value ($\langle \mathrm{tr}(\boldsymbol{C})/\mathrm{L}^2 \rangle_{xyz} \approx 0.2$ for $tU_h/h > 200$). Furthermore, from figure 5.5, we can observe that in the parabolic domain the polymers are remarkably shrunk, as indicated by the blue triangles. In contrast, accentuated values of $\langle \mathrm{tr}(\boldsymbol{C})/\mathrm{L}^2 \rangle_{xyz}$ are found in both the elliptical and hyperbolic parts. The polymer extension curves evolve in a similar way within these two turbulent structures. Nevertheless, polymers are slightly more stretched in the hyperbolic domain than in the elliptical one. Therefore, we can conclude that hyperbolic and elliptical structures are constantly donating energy to polymers, in order to maintain their stretching level. On the other hand, in a parabolic state where a turbulent structure is not present, the polymers are able to relax and assume an isotropic configuration.

The results shown in figure 5.5 are a direct consequence, not only to the ability of a certain subdomain (elliptical, parabolic, hyperbolic) to stretch the polymers but also, to the portion each subdomain occupies in the whole domain. We have already shown

(see figure 5.3) that the hyperbolic subdomain is the largest one, since it overcomes the other two outside and in a part of the viscous sublayer. Therefore, we have not answered the question of which subdomain has a higher ability to stretch the polymers, since the size of the domain enters the computation of figure 5.5. In order to asses this question, we plotted in figure 5.6 the same averaged evolution over time, but now normalized by the size of each subdomain. What can be seen in this figure is that the relative stretching in each subdomain is higher in the elliptical one, followed by the hyperbolic case. Therefore, we can conclude that the parabolic subdomain has the least ability on stretching the polymers. The main conclusion is that, from the perspective of the Q-criterion, there are more stretched polymers in the hyperbolic subdomain because its size is larger than the size of the elliptical subdomain and not because of its ability to stretch polymers.

In order to better understand the changes on the molecules conformation during the begging of the drag reduction phenomenon, we displayed in figure 5.7 how polymers are stretched relatively to the wall distance at different instants. Average values in the $x-y$ plane of the trace of the normalized conformation tensor, $\langle \mathrm{tr}(\boldsymbol{C})/\mathrm{L}^2 \rangle$, are displaced as a function of the dimensionless wall distance, z^+, for our viscolestic case at $Re_h = 4000$. We choose some very specific instants for each viscoelastic case, as those indicate inside the boxes in figures 5.4(a) and 5.5(b) as well as that corresponding to the statistical steady state $tU_h/h = 1500$. The whole domain is considered in figure 5.7(a), while the relative polymer stretch is partitioned among elliptical, parabolic and hyperbolic parts in figures 5.7(b), (c), and (d), respectively. Hence, for each specific instant, the superposition of the profiles displayed in figures 5.7(b), (c), and (d) is equal to that shown in figures 5.7(a).

During the initial instants, except for the small perturbation in the middle of the geometry, the flow is essentially laminar and dominated by a parabolic state. The linear streamwise velocity profile $u_x = z$ leads to a constant and weak velocity gradient for $tU_h/h \leq 3$. Consequently, $\tau_w = \tau_{w,laminar}$ and a very low and constant relative polymer stretch profile exclusively related to the parabolic regions is observed at $tU_h/h = 0.3$ (grey circles in figures 5.7a and c) and at $tU_h/h = 3$ (blue triangles in figures 5.7a and c). Additionally, at these instants, both the elliptical and the hyperbolic domains barley begun to develop, which makes $\langle \mathrm{tr}(\boldsymbol{C})/\mathrm{L}^2 \rangle \approx 0$ within these turbulent structures, as illustrated by the grey circles and the blue triangles in figures 5.7(b) and (d). At $tU_h/h = 52.5$, when the increase in τ_w becomes more accentuated, polymers exhibit a strong deformation profile that departs from $\langle \mathrm{tr}(\boldsymbol{C})/\mathrm{L}^2 \rangle \approx 0.095$ at the wall, increasing exponentially until it reaches its maximum level ($\langle \mathrm{tr}(\boldsymbol{C})/\mathrm{L}^2 \rangle \approx 0.3$) at the middle of the plane Couette geometry. Very close to the wall, $z^+ < 1$, the polymer stretch essentially takes place within parabolic and hyperbolic domains. Nevertheless, the former vanishes as we move towards the centreline and, in the core zone (III; where $\langle \mathrm{tr}(\boldsymbol{C})/\mathrm{L}^2 \rangle$ is

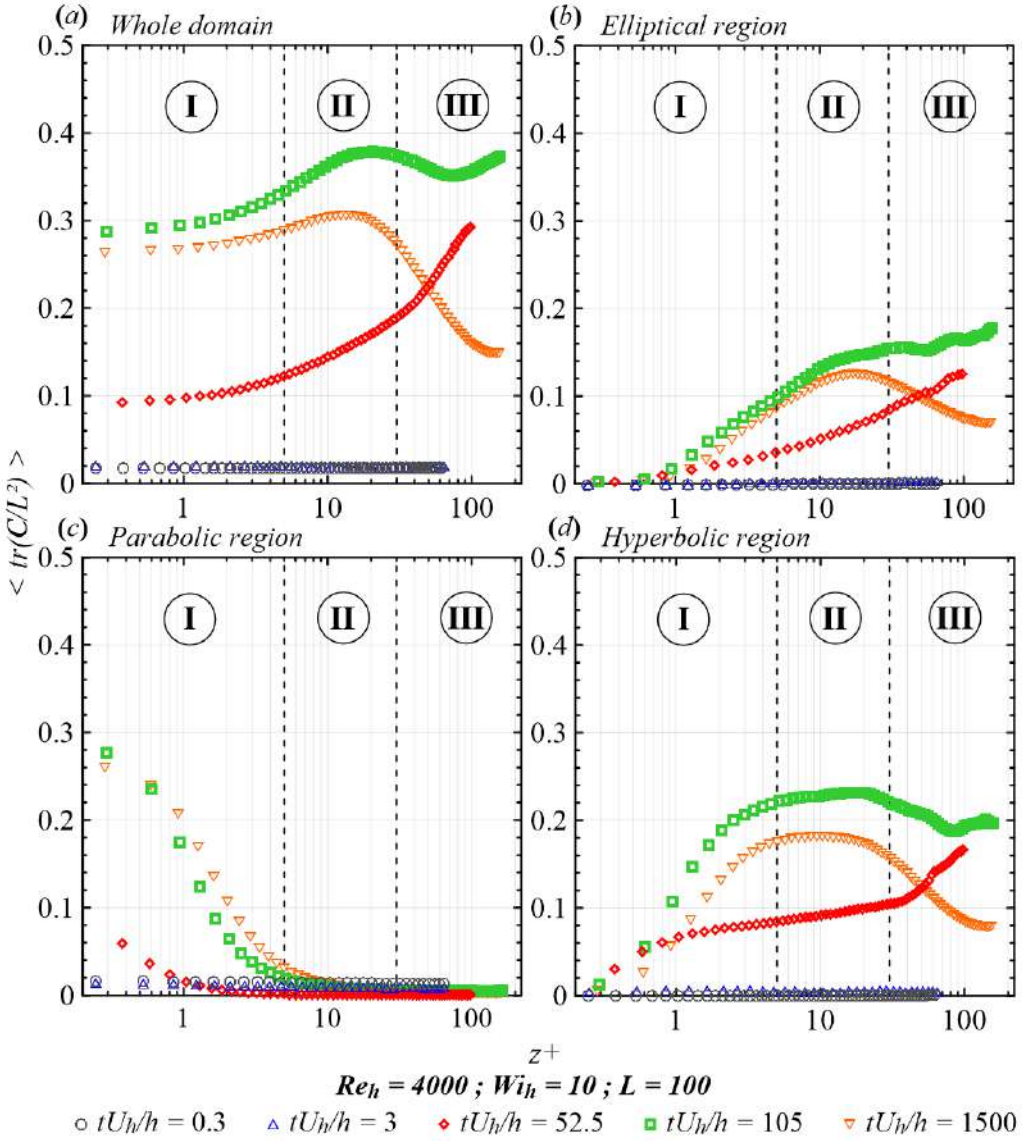

Figure 5.7 – Average values in the $x-y$ plane of the trace of the normalized conformation tensor, $\langle \mathrm{tr}(\boldsymbol{C})/\mathrm{L}^2 \rangle$, as function of the dimensionless wall distance for the most elastic case: $Re_h = 4000$, $Wi_h = 10$ and $L = 100$. The relative polymer extension is analysed at five dimensionless instants, tU_h/h.

maximum), the polymer deformation is driven by both the elliptical and hyperbolic structures, as indicated by the red diamonds. In other words, in the beginning of the process, the DR achieves its maximum value following the significant molecules deformation due to their interactions with the turbulent structures situated in the core zone. This is in accordance with the elastic theory postulated by Tabor and de Gennes [84], who claimed that the polymer drag reduction is not a wall–dependent phenomenon. Additionally, at $tU_h/h = 52.5$, the development of the turbulent structures have dramatically modified the velocity gradient and polymers start to strongly interact with the mean flow, storing its energy and increasing $\partial\tau_w/\partial t$ (figure 5.4*a*) as a consequence. At $tU_h/h = 105$, when the wall shear stress reaches its peak, although $\langle \mathrm{tr}(\boldsymbol{C})/\mathrm{L}^2 \rangle$ is large within parabolic parts located in the vicinity of the wall ($\langle \mathrm{tr}(\boldsymbol{C})/\mathrm{L}^2 \rangle \approx 0.28$ at $tU_h/h = 105$), the relative polymer stretch achieves its highest values in regions II and III, where the molecules deformation is mainly driven by the turbulent action on the elliptical and hyperbolic domains (green squares in figures 5.7*b* and *d*). However, during their initial stretch process, polymers store a considerable amount of energy from these turbulent structures, weakening them. Thus, after $tU_h/h = 105$, the high molecular deformation cannot be sustained since the elliptical and hyperbolic parts are significantly weak. Consequently, the molecules situated in regions II and III start to partially coil, releasing energy to the mean flow and slightly decreasing τ_w. The polymer extension profile moves downward, assuming the shape represented by the orange inverted triangles. Lastly, τ_w oscillates around it asymptotic level, which indicates the beginning of the statistical steady flow ($\tau_w \approx 5.6\ \tau_{w,laminar}$ for $tU_h/h > 200$, as pointed out in figure 5.4). During the statistical steady state illustrated by the profiles evaluated at $tU_h/h = 1500$ (orange inverted triangles in figure 5.7), it is firstly observed that polymers are considerably stretched near the wall, where the mean turbulent shear flow is intense. The maximum $\langle \mathrm{tr}(\boldsymbol{C})/\mathrm{L}^2 \rangle$ occurs in the region II and it dramatically decreases in the region III. Nevertheless, in the core zone, polymers are still stretched since the turbulent structures were not completely suppressed. Hence, the fluctuations on the velocity field also interact with polymers, being a source of polymeric energy [**Thais-13**], but in a much lower intensity. In this final stage, the polymer stretching near the wall is due to the parabolic subdomain (see the comparison between figures 5.7*a* and 5.7*c*). The decrease of the parabolic polymer stretching is compensated by the increase of the elliptical and hyperbolic contributions to this stretching at the end of the viscous sublayer and most of the (Newtonian) buffer layer. From the end of region II going through the entire region III the polymer stretching decreases in elliptical and hyperbolic subdomains.

The interactions between polymers and turbulence can be also evaluated from the perspective of the streamwise velocity component, as shown in figure 5.8. The velocity profile are analysed at the same five characteristic instants used in figure

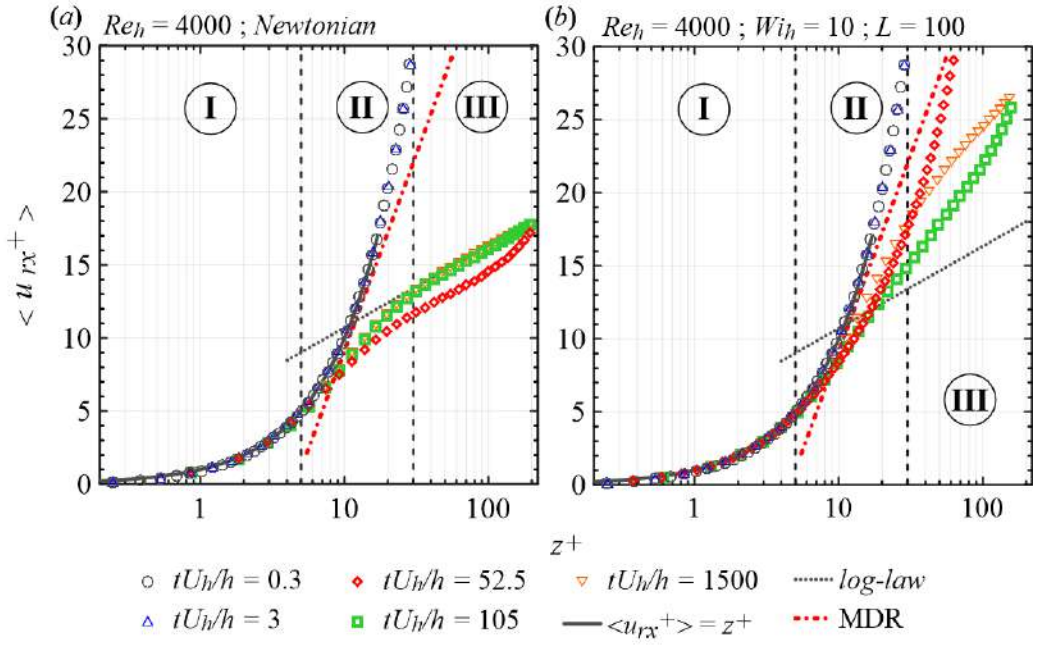

Figure 5.8 – Average values in the $x-y$ plane of the streamwise relative velocity, $\langle u_{rx}^{+} \rangle$, as function of the dimensionless wall distance: $Re_h = 4000$, Newtonian (a); $Re_h = 4000$, $Wi_h = 10$ and $L = 100$ (b). For each flow, the streamwise relative velocity is analysed at five dimensionless instants, tU_h/h.

5.7, for our two cases at $Re_h = 4000$. The polymer effect on the velocity profile are evaluated by confronting the Newtonian (figure 5.8a) and the viscoelastic flow (figure 5.8b). Each point in the figure is an average in the $x-y$ plane along z^+. In order to compare our profiles with the classical ones available in literature, the velocity of the bottom plate was subtracted from the velocity field, resulting in a relative streamwise component, u_{rx} given by $u_{rx} = u_x - (-U_h)$. At instants $tU_h/h = 0.3$ and $tU_h/h = 3$, both the Newtonian and the viscoelastic flows exhibit a laminar character and the coincidence of the velocity profile with the curve $u_{rx}^{+} = z^{+}$ surpasses the viscous sublayer. However, the development of the turbulent structures starts to significantly modify the flows. The velocity, then, decreases while the wall shear stress becomes more accentuated, as displayed in figure 5.4. At $tU_h/h = 52.5$, significant differences between the Newtonian and the viscoelastic cases are observed. The former presents a streamwise velocity profile (red diamonds in figure 5.8a) below the classic log-law one, which can be seen in figure 5.8(a) by comparing the red diamonds and the grey dots. In addition, its wall shear stress is very close to the maximum level (grey circles in figure 5.4). In contrast, the latter, whose the wall shear stress is still small, presents a streamwise velocity profile very close to the MDR one (red dash-dotted). Lastly, for $tU_h/h > 100$, the Newtonian velocity fits the classic log-law while the wall shear stress reaches its mean level. However, for the viscoelastic case, u_{rx}^{+} undergoes some changes before achieving the statistical steady state at $tU_h/h = 200$. In other words, the addition of polymers

retards the development of the steady state velocity profile.

In face of the results presented previously, we can now describe, from a dynamic point of view, the development of the polymer drag reduction phenomenon trigged by an initial perturbation superposed onto a laminar viscoelastic shear flow. This phenomenon can be detached as being dependent on three distinct entities: polymers, mean shear flow, and turbulent structures (elliptical and hyperbolic parts). Following $\tau_w(t)$, step-by-step, we observe a laminar flow at the very beginning which is not able to stretch the molecules ($\langle \mathrm{tr}(\boldsymbol{C})/\mathrm{L}^2 \rangle_{xyz} < 0.02$ at $tU_h/h = 0$). Consequently, $\tau_w = \tau_{w,laminar}$ and $DR = 0\%$. Nevertheless, after few instants, polymers are extended and the necessary energy comes from the elliptical and hyperbolic structures related to the initial perturbation located in the middle of the geometry. Hence, polymers firstly exhibit an accentuated stretch within regions II and III, while a less significant $\langle \mathrm{tr}(\boldsymbol{C})/\mathrm{L}^2 \rangle$ is observed in the vicinity of the wall (red diamonds in figure 5.7). The development of the turbulent structures increases τ_w and modify the mean shear flow, making the latter a source of polymeric energy for the molecules situated close to the wall. Then, $\langle \mathrm{tr}(\boldsymbol{C})/\mathrm{L}^2 \rangle$ tends to increase in region I (green squares in figure 5.7), while u_{rx}^+ is delayed (green squares in figure 5.8*b*). This retardation of u_{rx}^+ increases τ_w more markedly until its peak. However, at this point, the high molecular deformation in the core zone can not be sustained since the elliptical and hyperbolic structures become weak, following the significant polymer-turbulence interactions. Consequently, the molecules situated in regions II and III start to partially coil, releasing energy to the mean flow. This releasing of energy increases u_{rx}^+ and slightly decreases τ_w toward their final stages (orange inverted triangles in figure 5.8*b* and red diamonds in figure 5.4, respectively).

The results discussed above indicate a strong interaction between the polymer and the flow in the beginning of the drag reduction phenomenon followed by a significant energy exchanges. These energy exchanges are taken into account by multiplying the momentum equation (1.2) by the velocity, which leads to the work equation

$$\underbrace{\left[\frac{1}{2}\frac{\partial\left(u_\alpha^{+2}\right)}{\partial t^+}\right]}_{T_\alpha^+} = \underbrace{\left[-u_\alpha^+\frac{\partial\left(u_\alpha^+ u_i^+\right)}{\partial x_i^+}\right]}_{A_\alpha^+} + \underbrace{\left[-u_\alpha^+\frac{\partial p^+}{\partial x_\alpha^+}\right]}_{P_\alpha^+} + \underbrace{\left[(\beta_0)\,u_\alpha^+\frac{\partial^2 u_\alpha^+}{\partial x_i^{+2}}\right]}_{V_\alpha^+} + \underbrace{\left[u_\alpha^+\frac{\partial \Xi_{\alpha i}^+}{\partial x_i^+}\right]}_{E_\alpha^+}, \tag{5.4}$$

where the instantaneous polymer work term, E_α^+, indicates the amount of energy stored ($E_\alpha^+ < 0$) or released ($E_\alpha^+ > 0$) by the polymers from the velocity field in the α direction, u_α^+. The complementary work terms denote the advection A_α^+, the pressure redistribution P_α^+, and the viscous stress V_α^+. The sum $A_\alpha^+ + P_\alpha^+ + V_\alpha^+$ is referred as the *Newtonian work*, N_α^+, and T_α^+ is the local time derivative term. It is worth mentioning that the energy exchanges in the x direction constitute more than 90% of the total energy, including the streamwise, the spanwise and the wall-normal directions. Hence, in figures 5.9, 5.10,

5.11, and 5.12 only the $x-y$ plane average of the instantaneous streamwise total kinetic energy budget, provided by equation 5.4, against the dimensionless wall distance is considered.

Figure 5.9 shows the spatial average of the streamwise energy budget, equation 5.4, as function of the dimensionless time. The Newtonian (left column) and viscoelastic (right column) cases $Re_h = 4000$ are shown here. The whole domain energy budget (a and b) is divided into the elliptical (c and d), parabolic (e and f), and hyperbolic (g and h) parts. From these subfigures, we can get a quite good picture of the energy exchanges between polymers and the turbulent structures during the developing time. Concerning the viscoelastic case, it is observed in figure 5.9(b) that the polymeric work $\langle E_x^+ \rangle_{xyz}$ is null at the beginning of the simulation, since the molecules are mainly coiled at this moment (blue plus symbols). The local time derivative term $\langle T_x^+ \rangle_{xyz}$ is identical to the Newtonian work (the grey circles and the orange inverted triangles collapse in a single curve) which, during this stage, is mainly composed by the pressure term. Some instants after the beginning of the process, the balance of energy totally changes. The initial perturbation advances in the domain (figure 5.1), changing the flow and increasing the magnitude of $\langle T_x^+ \rangle_{xyz}$. The polymeric work starts to decrease achieving negative values, which means that the molecules are being stretched, following their interactions with the turbulent structures. During the interval $tU_h/h \in \approx [20, 100]$ the local time derivative term $\langle T_x^+ \rangle_{xyz}$ is mainly explained by the polymeric term. At $tU_h/h \approx 80$, the polymeric contribution starts to decrease after its valley ($\langle E_x^+ \rangle_{xyz} \approx -0.18$) while $\langle V_x^+ \rangle_{xyz}$ starts to increase with more intensity, showing a maximum (together with τ_w) at $tU_h/h = 105$ and being the main contribution to the Newtonian term. At this stage, u_{rx}^+ appears closer to the log-law profile (green squares in figure 5.8b). These trajectories suggest that the mean flow is now acting as a source polymeric energy. Therefore, both the Newtonian and polymeric terms contribute to the increase of $\langle T_x^+ \rangle_{xyz}$ until the flow reaches its statistically steady state. This regime shows a very low local time derivative of the kinetic energy obtained from a balance between a positive Newtonian (almost viscous) and a negative polymeric contributions of the same order of magnitude, i.e. $\langle N_x^+ \rangle_{xyz} \approx -\langle E_x^+ \rangle_{xyz} \approx 0.05$. In other words, while in the Newtonian case the viscous term counteracts the pressure work contribution, $\langle P_x^+ \rangle_{xyz} \approx -0.2$, in the viscoelastic case the viscous work increases counteracting the drainage of energy provided by the new work term, the polymeric one. This increase in the viscous work can be responsible for the decrease of the turbulent structures and the raise of the parabolic domain.

The analysis conducted above for the whole domain can gain additional insight if we understand how each term of equation 5.4 is distributed among the subdomains, i.e. elliptical, parabolic, and hyperbolic as illustrated by the next subfigures of figure 5.9. Confronting the Newtonian and viscoelastic cases shown in the left and the right columns, it is observed that, although for the whole domain the advective term,

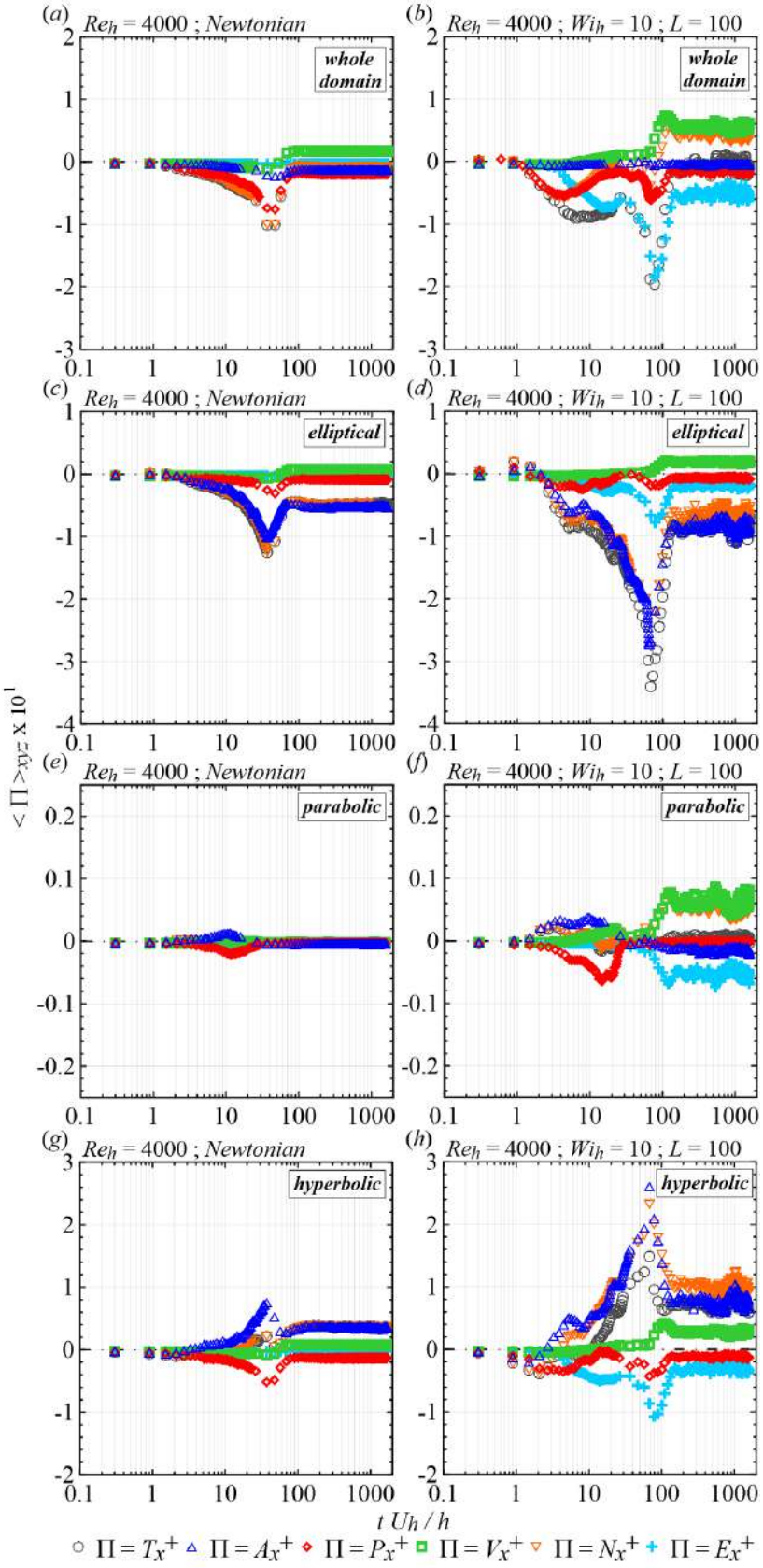

Figure 5.9 – Spatial average of the streamwise energy budget terms as function of the dimensionless time, tU_h/h.

$\langle A_x^+ \rangle_{xyz}$ (blue triangles), is negligible, the same cannot be said about its subdomains counterparts, especially hyperbolic and elliptical ones. The Newtonian case exhibits non-negligible contributions of these structures but, in the presence of polymers the magnitude of $\langle A_x^+ \rangle_{xyz}$ increases in both the elliptical and hyperbolic subdomains without changing its overall value, which is close to zero. The contribution of the parabolic subdomain is negligible (please notice that the scale of the parabolic curves is one order of magnitude lower). Comparing figures 5.9(c) and (d), and figures 5.9(g) and (h), it is interesting to note that the morphological changes in the turbulent structures caused by the addition of polymers increases the streamwise advection within both the elliptical and hyperbolic parts. In other words, although the polymers strongly reduce the quantity of elliptical and hyperbolic structures and change their morphology, the modified (and less numerous) turbulent structures which emerges from the polymer-flow interactions exhibit a more accentuated A_x^+. This result is an additional motivation for including the hyperbolic structures in the analysis of turbulent flows. The elliptical structures, identified as vortices in the literature, cannot be the only source of the connection between the turbulent structures and the physical explanation of the flow.

Analysing figures 5.9(d), (f) and (h), it can be seen that the polymeric energy, differently from the advective term, has contributions of elliptical, parabolic, and hyperbolic subdomains in the same direction, i.e. a negative contribution to $\langle T_x^+ \rangle_{xyz}$. These contributions come primarily from the hyperbolic structures. During the statistical steady state ($tU_h/h > 200$), for instance, the magnitude of $\langle E_x^+ \rangle_{xyz}$ in the hyperbolic parts ($\langle E_x^+ \rangle_{xyz} \approx -0.04$) is approximatively two times greater than that observed in the elliptical ones ($\langle E_x^+ \rangle_{xyz} \approx -0.02$), while a less significant quantity of energy (approximatively ten times smaller) is stored in the parabolic domain. The viscous term increases from the Newtonian to the viscoelastic case in every subdomain. Again, one can verify a near symmetric value of $\langle V_x^+ \rangle_{xyz}$ with respect to the polymeric contribution after the statistically steady state has been achieved.

Similarly to the rationale that was employed with respect to the results shown in figure 5.5, which originated figure 5.6, the same concern is applied to figure 5.9, i.e. it would be illustrative to understand each term of equation 5.4 looking separately to each subdomain as our universe of analysis. This is done in figure 5.10, where figures 5.10(a) and (b) are coincident with figures 5.9(a) and (b). Interestingly, the main difference between figures 5.9 and 5.10 is the fact that some the terms of equation 5.4, like $\langle A_x^+ \rangle_{xyz}$, $\langle N_x^+ \rangle_{xyz}$, and $\langle T_x^+ \rangle_{xyz}$ in the elliptical subdomains have a higher relative magnitude when compared to what is taking place in the hyperbolic subdomain, although the sign relation is maintained. In other words, a quantity like $\langle A_x^+ \rangle_{xyz}$, for example, has its contribution equilibrated in elliptical and hyperbolic regions because hyperbolic regions are more numerous, what balances the fact of being less intense in this subdomain. The polymeric contribution, $\langle E_x^+ \rangle_{xyz}$, has also slightly changed to a situation where

hyperbolic and elliptical regions have more similar values.

It is worth noting that the developing time reported in Pereira et al. [72] and the one presented here are very different from each other. In the former work, the polymers are initially stretched and the velocity and the pressure fields are started from a Newtonian fully developed turbulent flow. The mean flow exhibits, then, an accentuated velocity gradient (especially near the wall), which allows it to act as the primarily source of energy to the molecules. Consequently, during the first seconds of simulation, polymers strongly interact with the mean shear flow, storing part of its energy. This storage of energy imposes a retardation in the mean velocity, which increases the drag (τ_w) and moves DR from zero to negative values. In contrast, in the present work, since the initial laminar shear flow is not capable to deform the molecules, the energy necessary to initially stretch the polymers comes from the elliptical and hyperbolic structures related to the initial perturbation located in the middle of the geometry. As these turbulent structures weaken, DR moves from zero (at the very beginning of the simulations) to positive values. The differences between the two referred works show that the development of DR is highly dependent not only on the initial molecules conformation, as experimentally evidenced by Andrade et al. [2], but also on the flow condition at the very beginning of the process. However, it is important to stress that, once the statistical steady state is reached, all the simulated flows follow the wall turbulence regeneration cycle described in Pereira et al. [71]. In other words, despite the dynamic differences during their developing time, in the statistical steady state, the viscoelastic turbulent flows reported here and in Pereira et al. [72] converge to the same polymer–flow mechanism. Some important aspects of this polymer–flow mechanism are explored here from a time–average perspective. In this connection, the averaging of the energy terms shown in equation 5.4 is taken over time using 500 flow snapshots spanning several eddy turnovers times. The starting point is the mean work equation,

$$\underbrace{\left[\frac{1}{2}\frac{\partial\left(u_\alpha^{+2}\right)}{\partial t^+}\right]}_{T^+_{m,\alpha}} = \underbrace{\left[-u_\alpha^+\frac{\partial\left(u_\alpha^+u_i^+\right)}{\partial x_i^+}\right]}_{A^+_{m,\alpha}} + \underbrace{\left[-u_\alpha^+\frac{\partial p^+}{\partial x_\alpha^+}\right]}_{P^+_{m,\alpha}} + \underbrace{\left[(\beta_0)\,u_\alpha^+\frac{\partial^2 u_\alpha^+}{\partial x_i^{+2}}\right]}_{V^+_{m,\alpha}} + \underbrace{\left[u_\alpha^+\frac{\partial \Xi^+_{\alpha i}}{\partial x_i^+}\right]}_{E^+_{m,\alpha}}, \tag{5.5}$$

where the time–averaged amount of energy which is stored ($E^+_{m,\alpha} < 0$) or released ($E^+_{m,\alpha} > 0$) by polymers from the velocity in the α direction, u_α^+, is represented by $E^+_{m,\alpha}$. The complementary work terms denote the mean advection $A^+_{m,\alpha}$, the mean pressure redistribution $P^+_{m,\alpha}$, and the mean viscous stress $V^+_{m,\alpha}$. The sum $A^+_{m,\alpha} + P^+_{m,\alpha} + V^+_{m,\alpha}$ is referred as time–averaged *Newtonian work*, $N^+_{m,\alpha}$, and $T^+_{m,\alpha}$ is the term associated to the time–averaged local time derivative of the kinetic energy. In figure 5.11, we can

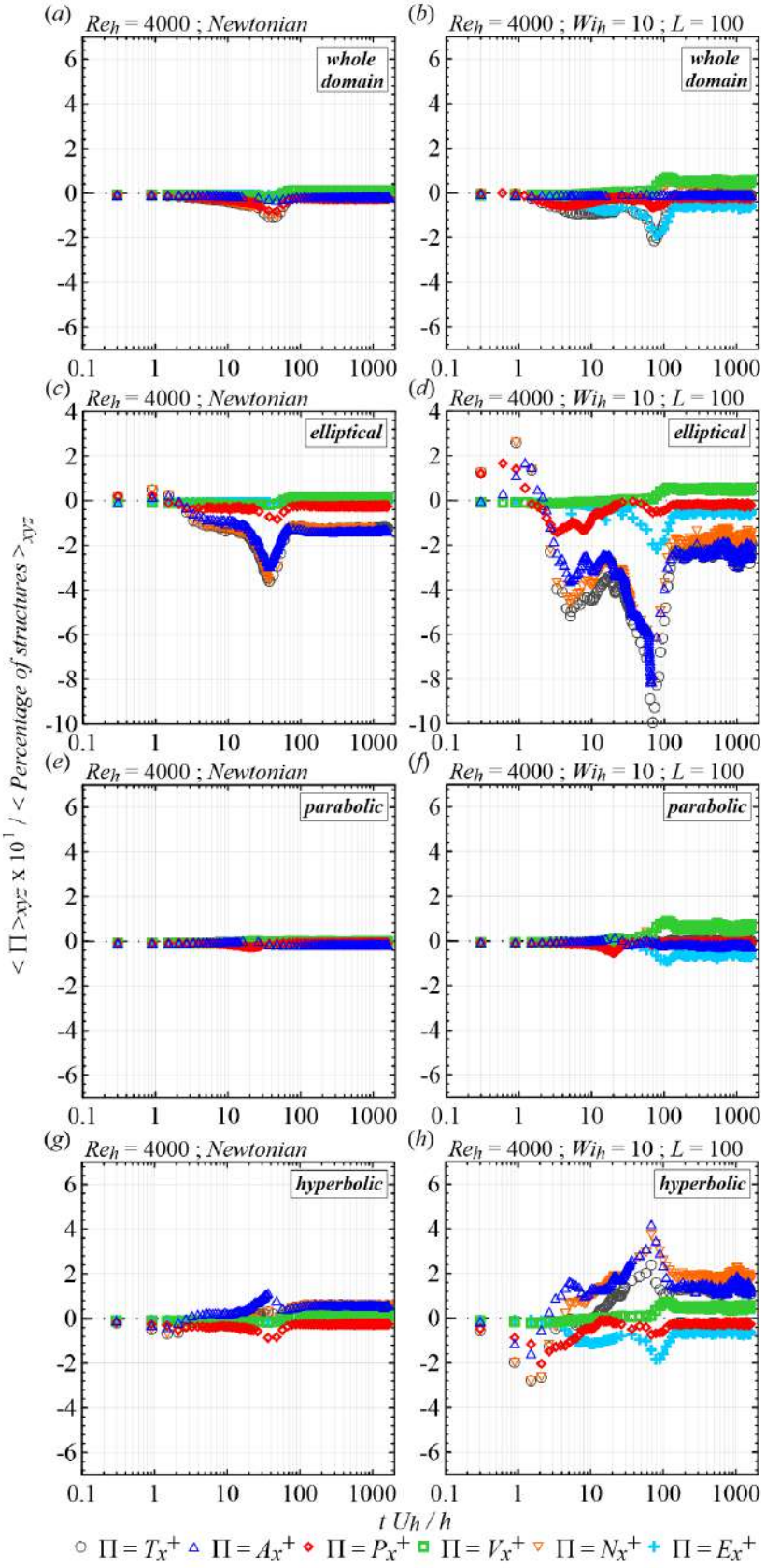

Figure 5.10 – Spatial average of the streamwise energy budget terms as function of the dimensionless time, $t\,U_h/h$.

see the $x-y$ plane average of the mean kinetic energy distribution as a function of the wall distance. The analysis is restricted to the Newtonian and viscoelastic cases at $Re_h = 4000$. Again, we split the domain into elliptical, parabolic and hyperbolic flow subdomains in order to clarify the specific exchanges of energy.

Firstly, regarding the Newtonian flow shown in figure 5.11(a), we observe that the advection term, $\langle A^+_{m,x}\rangle$, balances the viscous one, $\langle V^+_{m,x}\rangle$. Both quantities are nulls at the wall and reach their maximum values in the region II, just above the viscous sublayer ($z^+ \approx 5.5$). It seems that $\langle A^+_{m,x}\rangle$ and $\langle V^+_{m,x}\rangle$ are the main terms in flow of Newtonian fluids, the former being the most important one as reported by Graham [31]. In region III, both the terms significantly reduce. Such a behavior is expected, since the viscous work in flows of Newtonian fluids are related to the small scale fluctuations, which are nulls very close to wall and less significant in the core zone. As pointed out in figures 5.11(c), (e), and (g), the most significant values of $\langle A^+_{m,x}\rangle$ occurs within elliptical structures situated in the region II. In contrast, within these structures, $\langle V^+_{m,x}\rangle$ is slightly smaller than in the hyperbolic ones. The results displayed in figure 5.11(b) indicate that energy distribution dramatically changes when polymers are introduced in Newtonian fluids. The polymeric work starts to play a very important role in the flow. In region I, the energy is primarily balanced by the polymeric term and the viscous one. The latter departs from an accentuated value at the wall, while the former reaches its peak in region II ($\langle V^+_{m,x}\rangle \approx 0.59$ at $z^+ \approx 7.0$). However, a slightly reduction of $\langle V^+_{m,x}\rangle$ is also noted in region II, by comparing figures 5.11(a) and (b). Furthermore, in this region, polymers partially suppress the advection work, of which the maximum absolute value is two times smaller than that observed for the Newtonian flow shown in figure 5.11(a). In the opposite sense, in region III, the addition of polymers slightly increases $\langle A^+_{m,x}\rangle$, which seems to be closely related to the fact that, in viscoelastic flows, the turbulent structures become more parallel to the wall, while their thicknesses and streamwise lengths increase [46]. Moreover, as shown in figures 5.3(c) and (d), the viscoelastic flows exhibit a larger number of elliptical structures within region III than their Newtonian counterparts, which also could justify the increase in $|\langle A^+_{m,x}\rangle|$ observed far from the wall (figure 5.11d).

The elliptical, parabolic, and hyperbolic exchanges of energy are illustrated in figures 5.11(d), (f), and (h), respectively, for a viscoelastic fluid. Figure 5.11(f) shows that, for $z^+ < 1$, polymers store energy primarily from the near-wall parabolic domain ($\langle V^+_{m,x}\rangle < 0$). In addition, the highest values of $\langle V^+_{m,x}\rangle$ are also linked with the parabolic parts situated in the vicinity of the wall (figure 5.11f). Moving from region I to region II, the elliptical and the hyperbolic exchanges of energy become important (figures 5.11d and h), while the parabolic ones vanish (figure 5.11f). At $z^+ \approx 3.5$, $\langle E^+_{m,x}\rangle$ reaches its peak within both the elliptical and hyperbolic parts. Furthermore, for this two parts, the maximum value of $\langle V^+_{m,x}\rangle$ occurs at $z^+ \approx 7.5$. Comparing the Newtonian results

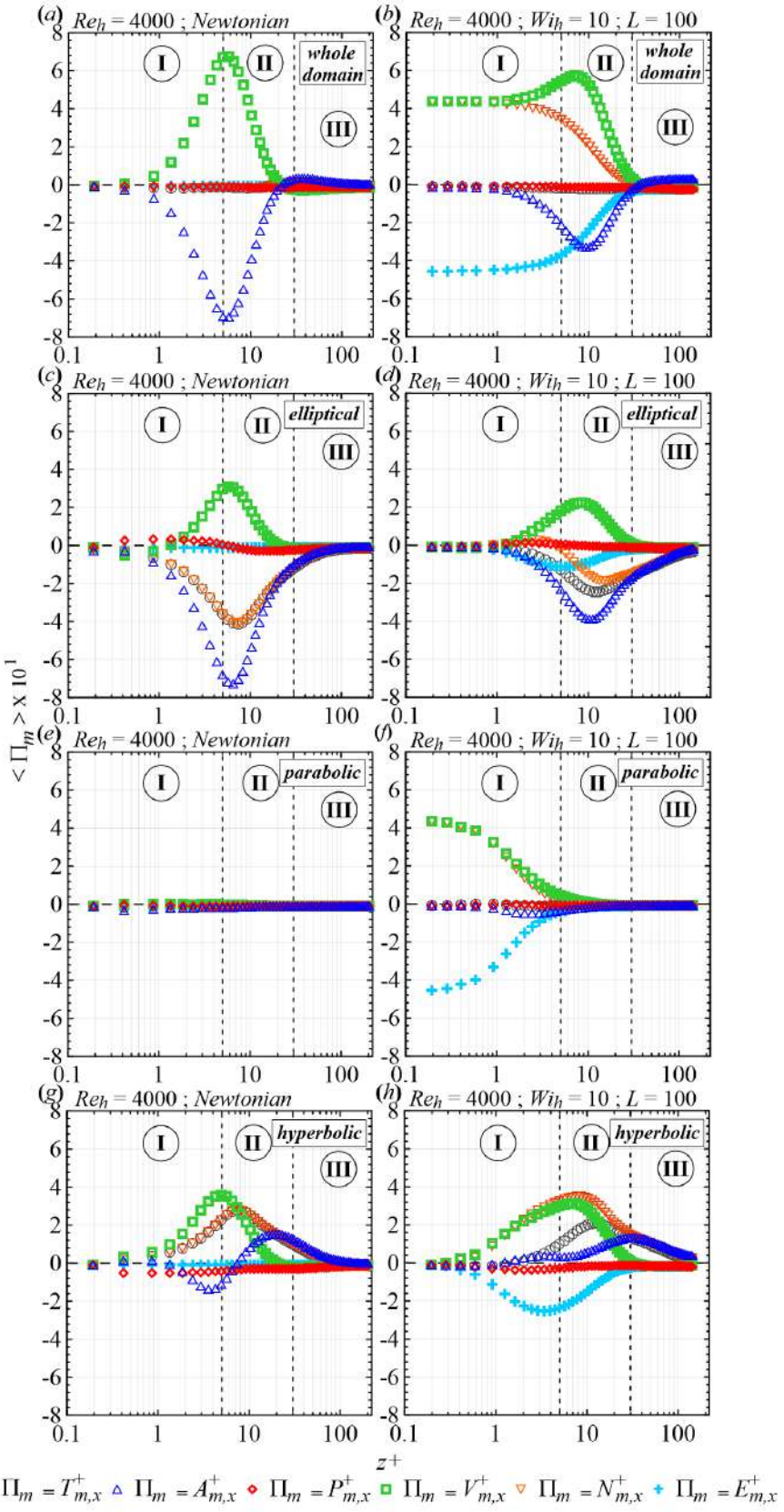

Figure 5.11 – Average values in the $x-y$ plane of the streamwise kinetic energy budget against the dimensionless wall distance: $Re_h = 4000$, $Wi_h = 10$ and $L = 100$.

with the viscoelastic ones, it can be clearly seen that the most significant advection suppression occurs within elliptical structures situated in region II. In contrast, for elliptical and hyperbolic parts located in region III, $|\langle A^+_{m,x}\rangle|$ is greater than that of the Newtonian case at the same Re_h, which is linked with the morphological changes in the turbulent structures as well as the increase in the number of elliptical structures far from the wall (see figures 5.3*c* and *d*). Hence, we can conclude that the reduction in the percentage number of hyperbolic and elliptical structures caused by the polymers (see figure 5.2) decreases the peak of $\langle A^+_{m,x}\rangle$ in region II. However, the morphological changes experienced by these structures favor the streamwise advection in region III, since they become more parallel to the wall and their thicknesses and streamwise lengths increase [46]. Lastly, it is important to observe that the addition of polymers shifts the peak away from the wall. For both the Newtonian and viscoelastic cases, $\langle T^+_{m,x}\rangle$ and $\langle P^+_{m,x}\rangle$ are null along the plane Couette half-width.

Finally, during the statistical steady state, the time–averaged polymer work term can be related to both the mean and fluctuating fields

$$E^+_{m,x} = \underbrace{\left[\overline{U^+_x}\frac{\partial \overline{\Xi^+_{x,i}}}{\partial x^+_i}\right]}_{E^+_{mm,x}} + \underbrace{\left[\overline{u'^+_x\frac{\partial \Xi'^+_{x,i}}{\partial x^+_i}}\right]}_{E^+_{mt,x}}, \tag{5.6}$$

where $E^+_{mm,x}$ and $E^+_{mt,x}$ denote the quantity of energy stored ($E^+_{mm,x} < 0$ and $E^+_{mt,x} < 0$) or released ($E^+_{mm,x} > 0$ and $E^+_{mt,x} > 0$) by the polymers from the mean and the fluctuating velocity fields, respectively, in the streamwise direction. The average values of these quantities in the $x-y$ plane across one-half of the geometry is highlighted in figure 5.12. Our two viscoelastic cases are considered and the results are quite similar. Analysing $\langle E^+_{mm,x}\rangle$ for the whole domain (black stars in figures 5.12*a* and *b*), it is clearly seen that polymer extract a considerable amount of energy from the flow within region I. This energy comes mainly from the mean shear flow through the parabolic parts (for $z^+ < 1$; blue triangles) and the hyperbolic ones ($1 < z^+ < 5$). In region II, significant negative values of $\langle E^+_{mm,x}\rangle$ are still observed within the elliptical (grey circles) and hyperbolic (red diamonds) structures. However, $\langle E^+_{mm,x}\rangle$ increases along the region II and reaches a positive peak around $z^+ \approx 30$, which is more accentuated within hyperbolic parts. The insets in figures 5.12(*a*) and (*b*) indicate that the release of energy by the polymers in region III is small, but non-negligible if compared with $\langle E^+_{mt,x}\rangle$ shown in figures 5.12(*c*) and (*d*). The latter exhibits an opposite behavior with respect to $\langle E^+_{mm,x}\rangle$. As shown by the black stars in figures 5.12(*a*) and (*b*), $\langle E^+_{mt,x}\rangle$ departs from zero at the wall (were the velocity fluctuations are nulls) and gradually increases across the region I until achieving its maximum value at $z^+ \approx 4$. This polymeric energy is exclusively released to elliptical and hyperbolic parts. After this point, $\langle E^+_{mt,x}\rangle$ decreases and

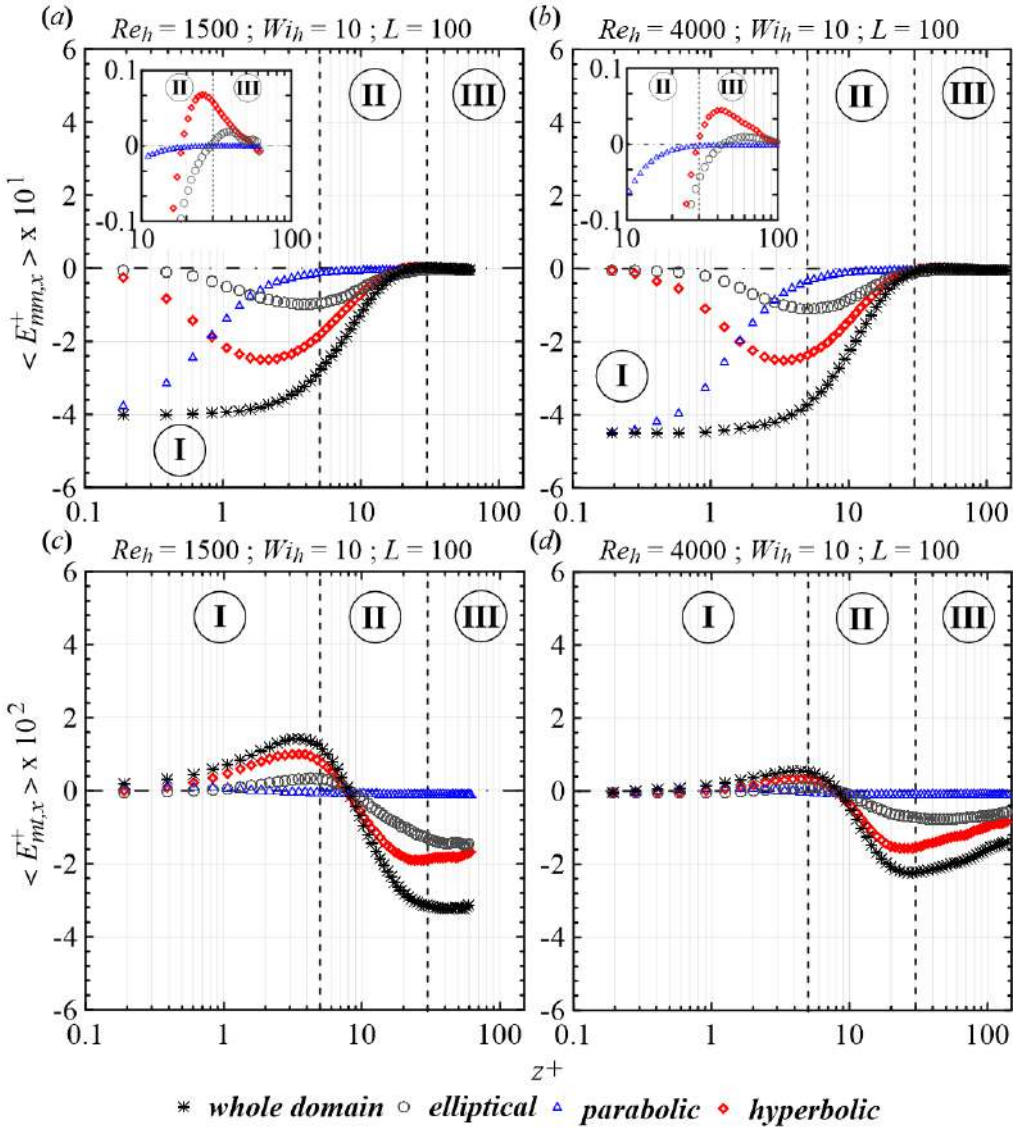

Figure 5.12 – Average values in the $x-y$ plane of both the mean and turbulent streamwise kinetic energy budget against the dimensionless wall distance.

reaches its minimum and negative value in region II, at $z^+ \approx 25$. Negative values of $\langle E^+_{mt,x} \rangle$ are also observed in region III, where polymers store energy from both the elliptical and hyperbolic structures. In short, figures 5.12 highlights how complex the interactions between polymers, the mean shear flow, and the velocity fluctuations are. In region I, polymers basically extract a significant amount of energy from the mean flow ($\langle E^+_{mm,x} \rangle < 0$) and release a smaller part of it to the velocity fluctuations ($\langle E^+_{mt,x} \rangle > 0$). Nevertheless, these trends completely change along region II and, as a result, in region III, polymers simultaneously dampen the turbulent structures and release part of their energy to mean shear flow. In other words, polymers interact with the mean flow and with the fluctuating velocity following opposite trends across the geometry.

5.4 Concluding remarks

Direct numerical simulations of FENE-P fluid are used to analyse a time–dependent drag reducing flow between parallel plates for turbulent regimes at $Re_h = 1500$ and $Re_h = 4000$. In order to investigate the polymer addition effects on the fluid dynamic, these viscoelastic flows were compared to two Newtonian cases at the same Reynolds numbers. We simulated our viscoelastic cases fixing Wi_h at 10, L at 100 and β_0 at 0.9. Aiming to analyse the interaction of the polymer molecules with the turbulent structures from the very beginning of the DR phenomenon ($DR = 0\%$) to its steady state ($DR > 0\%$ and statistically constant), turbulence was triggered by an initial perturbation consisting of four pairs of counter-rotating vortices superimposed onto a laminar viscoelastic shear flow (see details in Section 5.2). Our primary focus was to capture and emphasize some transient features of the drag reducing flow which emerges from the interaction between the polymers and the turbulent structures. These turbulent structures were defined from the perspective of the Q-criterion of flow classification [38]. Hence, the flow was divided into three distinct subdomains: an elliptical (or vortical) one where the second invariant of the velocity gradient tensor is positive ($Q > 0$), a hyperbolic (or extensional) subdomain which is determined by the negative values of the second invariant of the velocity gradient tensor ($Q < 0$), and a parabolic intermediary subdomain for which $Q = 0$. The polymer-turbulence exchanges of energy were then investigated for each one of these subdomains.

Figure 5.13 summarizes the principal four stages related to the DR mechanism at the beginning of the phenomenon. Firstly, at the stage 1 (figure 5.13*a*), the flow is primarily laminar and, consequently, the wall shear stress is equal to the laminar one ($\tau_w = \tau_{w,laminar}$; see figure 5.4). The polymers, practically coiled ($\mathrm{tr}(\boldsymbol{C})/\mathrm{L}^2 \approx 0$, $DR = 0$), store a significant amount of energy ($E^+_x > 0$) which initially comes from the elliptical (curved arrows) and hyperbolic (straight arrows) structures related to the small perturbation located in the middle of the geometry. As a results, at stage 2 (figure 5.13*b*),

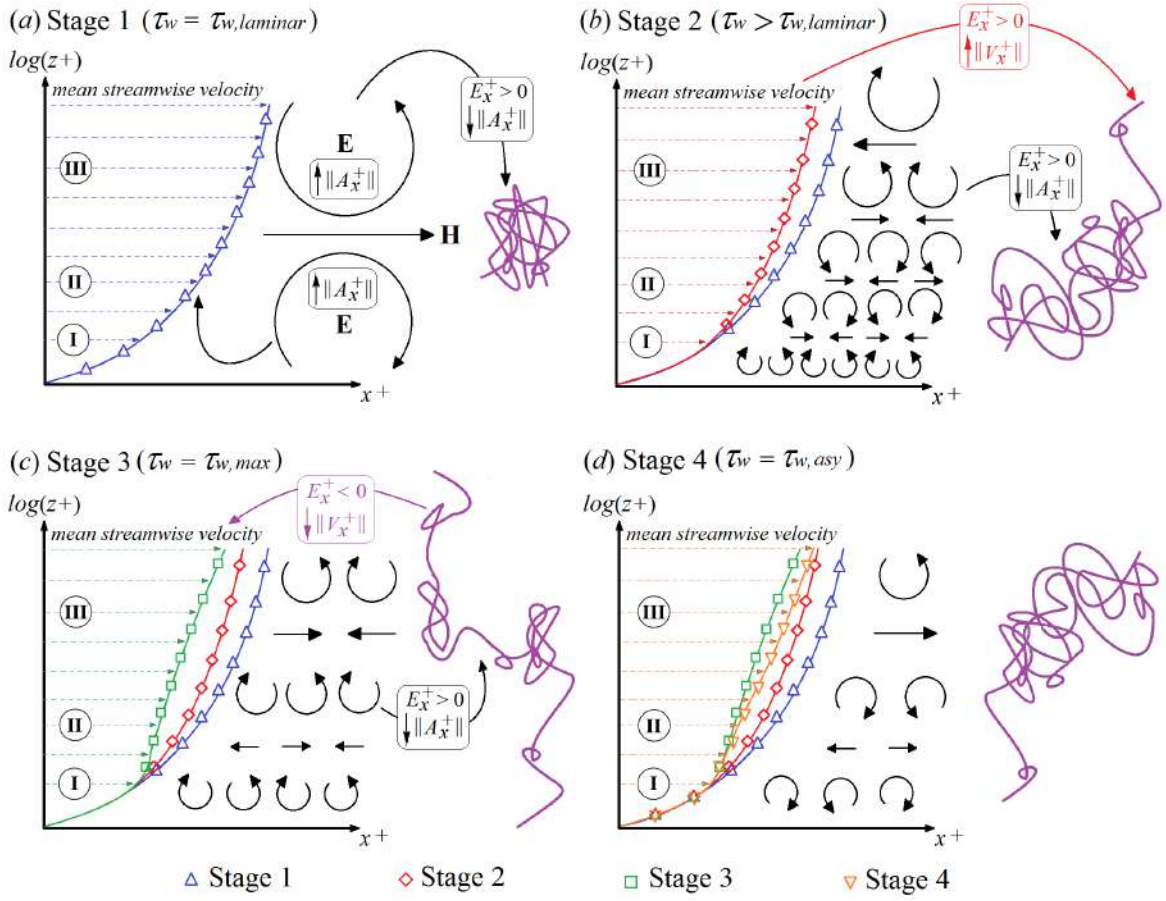

Figure 5.13 – Sketch of the polymer–flow interactions during the developing time.

the molecules start to stretch within regions II ($5 < z^+ < 30$) and III ($z^+ > 30$), while the turbulent structures are partially suppressed, which reduces the advection magnitude, $|A_x^+|$ and increases DR to its maximum value ($DR = DR_{max}$). During their development, the turbulent structures also interact with the laminar mean shear flow, changing the latter and making it able to act as an important source of polymeric energy within parabolic parts. Hence, at the stage 3 (figure 5.13*c*), the polymers exhibit a significant deformation not only in regions II and III, but also in region I ($0 < z^+ < 5$), where the modified mean shear flow plays a major hole for the polymer stretch mechanism. The mean velocity is then delayed, which increases the wall shear stress until its maximum value ($\tau_w = \tau_{w,max}$), decreasing the DR ($DR < DR_{max}$). However, a few instants after at this point, the high molecular deformation in the core zone cannot be sustained since the elliptical and the hyperbolic structures become weak, following the significant polymer-turbulence interactions. As a consequence, the molecules situated in regions II and III start to partially coil, releasing energy to the mean flow. As a result, u_{rx}^+ increases and τ_w slightly decreases toward their final and statistical steady state (stage 4, figure 5.13*d*). During this final period, the polymers interact with the flow following the coil-stretch cycle described by Pereira et al. [71].

Chapter 6

Active and hibernating turbulence in drag reducing plane Couette flows

We analyse the active and hibernating turbulence in drag reducing plane Couette flows using direct numerical simulations of viscoelastic FENE-P fluids. The polymer-turbulence interactions are studied from an energetic standpoint for a range of Weissenberg number, fixing the Reynolds number, the viscosity ratio and the maximum polymer molecule extensibility. The qualitative picture which emerges from this investigation is a cyclic mechanism of energy exchange between the polymers and turbulence that drives the flow through an oscillatory behaviour.

6.1 Introduction

The reduction of the energy dissipation in turbulent flows by polymers has been widely analysed over the years since the observations reported by Toms [93]. Despite the discrepancies between the most prominent theories concerning the nature of the polymer induced drag reduction (DR; [52, 84]), it is well known that the phenomenon is bounded by two major laws: the Prandtl–Kármán law (when DR is null) and the so-called maximum drag reduction regime (MDR) or Virk's asymptote (when DR is maximum; [97]). The existence of the MDR's limit represents one of the most important issues in the DR context since changing the polymer concentration, the molecular weight or even chemical characteristics of the additives produces no effect on this maximum drag reduction level.

Recently, an important contribution to understating the MDR's limit was given by Xi and Graham [105, 106], who defined the MDR as a turbulent flow that fluctuates between two distinct regimes: *active* and *hibernating*. The former is related to the basic dynamical elements of Newtonian near-wall turbulence, exhibiting a higher drag. In contrast, during the latter regime, the turbulent structures almost vanish, which

reduces the drag. Performing direct numerical simulation (DNS) of turbulent plane Poiseuille flows of viscoelastic finitely extensible nonlinear elastic, with the Peterlin approximation (FENE-P fluids), Xi and Graham [105, 106] pointed out that the flow oscillations between active and hibernating regimes, which exist in the Newtonian turbulence, are accentuated by the presence of polymers.

In attempt to better understand the polymer-flow interactions in the MDR scenario, we investigate in the present work the active and hibernating turbulence regimes in drag reducing plane Couette flows. The polymer effect on these two turbulent regimes are explored taking into account a range of Weissenberg numbers, which provides drag reduction levels from 11% up to 54%. Our DNS are performed keeping the Reynolds number (based on the plate velocities), the viscosity ratio and the maximum polymer molecule extensibility fixed. The results which emerge from energy budget and spectral analyses bring out new details concerning the effects of the polymers on the oscillatory behaviour of turbulent viscoelastic flows through the active and hibernating regimes.

The organization of the work is as follows. The description of the physical formulation and numerical methodology are presented in Section 6.2. Our main results are discussed in Section 6.3, where energy budget and spectral analyses are conducted. Finally, conclusions are drawn in the closing section.

6.2 Physical formulation and numerical methodology

We follow here the same numerical methodology used in Pereira et al. [72] and all details of the scheme employed are given by Thais et al. [89]. As in Pereira et al. [72], we analyse here the interaction of the polymer molecules with the turbulence from the very beginning (when polymers are totally coiled) until the steady state regime. The initial condition for the conformation tensor is the identity tensor, i.e. ($\boldsymbol{C}(t=0)=\boldsymbol{I}$). In addition, for each viscoelastic case, both the velocity and the pressure fields are initially started from the same Newtonian fully developed turbulent flow. As a result of this methodology, the DR exhibits a marked transient behaviour before achieving its asymptotic value, from a statistical point o view. We define the percentage of DR in time as

$$DR(t) = \left(1 - \frac{<\tau_w(t)>}{<\tau_w(t=0)>}\right) \times 100, \tag{6.1}$$

where $<\tau_w(t)>$ is the area-averaged wall shear stress at a given instant t and $<\tau_w(t=0)>$ is the area-averaged wall shear stress at the very beginning of the simulation, when the polymers are in an isotropic configuration (coiled from an experimental point of view).

For the present study, we simulate the viscoelastic cases fixing the Reynolds number based on the plate velocities, $Re_h = hU_h/\nu_{tot}$, at 4000, β_0 at 0.9 and L at 100. Five

cases are studied by setting the following Weissenberg numbers based on the plate velocities ($Wi_h = \lambda U_h/h$): 2, 4.3, 10, 20 and 30. The respective asymptotic drag reduction values, DR_{asy}, are: 11%, 33%, 50%, 53 % and 54%. Lastly, both the size of the domain ($L_x \times L_y \times L_z = 12\pi \times 4\pi \times 2$) and the number of mesh points ($N_x \times N_y \times N_z = 768 \times 512 \times 257$) are kept fixed for all cases, which leads to a grid resolution of $7.2 \leqslant \Delta x^+ \leqslant 9.5$, $3.6 \leqslant \Delta y^+ \leqslant 4.8$, and $0.2 \leqslant \Delta z^+ \leqslant 3.4$.

6.3 Results and Discussions

Our primary focus here is on the oscillatory behaviour of the turbulent viscoelastic flow through the active and hibernating regimes, which is achieved by following the numerical methodology detailed in Pereira et al. [72]. Hence, at the very first instant of the simulation, the molecules are totally coiled, $tr(\boldsymbol{C})/L^2 \approx 0$, the DR level is null, and the turbulent velocity field still exhibits a Newtonian-like nature. The flow is then characterized by the presence of a considerable number of turbulent structures, some of which are illustrated in figures 6.1(*a*) and 6.2(*a*) by using the Q-criterion of flow classification[1] [38] for the most elastic case ($Re_h = 4000$, $Wi_h = 30$ and $L = 100$). In figures 6.1 and 6.2, the vortical and extensional structures respectively described by $Q = 0.05$ and $Q = -0.05$ are colored from blue ($tr(\boldsymbol{C})/L^2 = 0$) to red ($tr(\boldsymbol{C})/L^2 = 1$), what indicates a distribution of the relative polymeric deformation over the domain. Since the development along time of the DR was already discussed in our previous work [72], we present here only a brief overview of the beginning of the phenomenon (shown in figures 6.1*a-e* and 6.2*a-e*) and we concentrate our attention on the active and hibernating regimes illustrated in figures 6.1(*f-j*) and 6.2(*f-j*).

At the very beginning, $tU_h/h = 0.3$ (figures 6.1*a* and 6.2*a*), the polymers are totally coiled and the turbulent structures appear with a Newtonian morphology [1]. The drag reduction at this instant is still negligible ($DR \approx 0\%$). The departure from this state develops toward highly negative values as the simulation evolves over time, moving from $DR \approx -6\%$ at $tU_h/h = 3$ (figures 6.1*b* and 6.2*b*) to its minimum value of $DR \approx -112\%$ at $tU_h/h = 9.6$ (figures 6.1*c* and 6.2*c*). After that, the DR starts an increasing trajectory, reaching its positive peak of $DR \approx 77\%$ at $tU_h/h = 300$ (figures 6.1*d* and 6.2*d*) before it decreases towards an oscillatory state of a lower mean value (an asymptotic value from an statistical point of view). During this period, the molecules strongly interact with the flow, stretching (especially near the wall, as displayed in figures 6.1*c* and 6.2*c*) and partially suppressing the turbulent structures. At $tU_h/h \approx 525$

[1] The vortical (or elliptical) and extensional (or hyperbolic) structures are defined as the respective positive and negative values of the second invariant of the velocity gradient tensor, computed for incompressible flows by $Q = \frac{1}{2}\left(\|\boldsymbol{W}\|^2 - \|\boldsymbol{S}\|^2\right)$, where $\|\boldsymbol{W}\|$ and $\|\boldsymbol{S}\|$ denote the Euclidean norms of $\boldsymbol{W}$ and $\boldsymbol{S}$. The Euclidean norm of a generic second order tensor $\boldsymbol{A}$ is $\|\boldsymbol{A}\| = \sqrt{tr\left(\boldsymbol{A} \cdot \boldsymbol{A}^{\boldsymbol{T}}\right)}$.

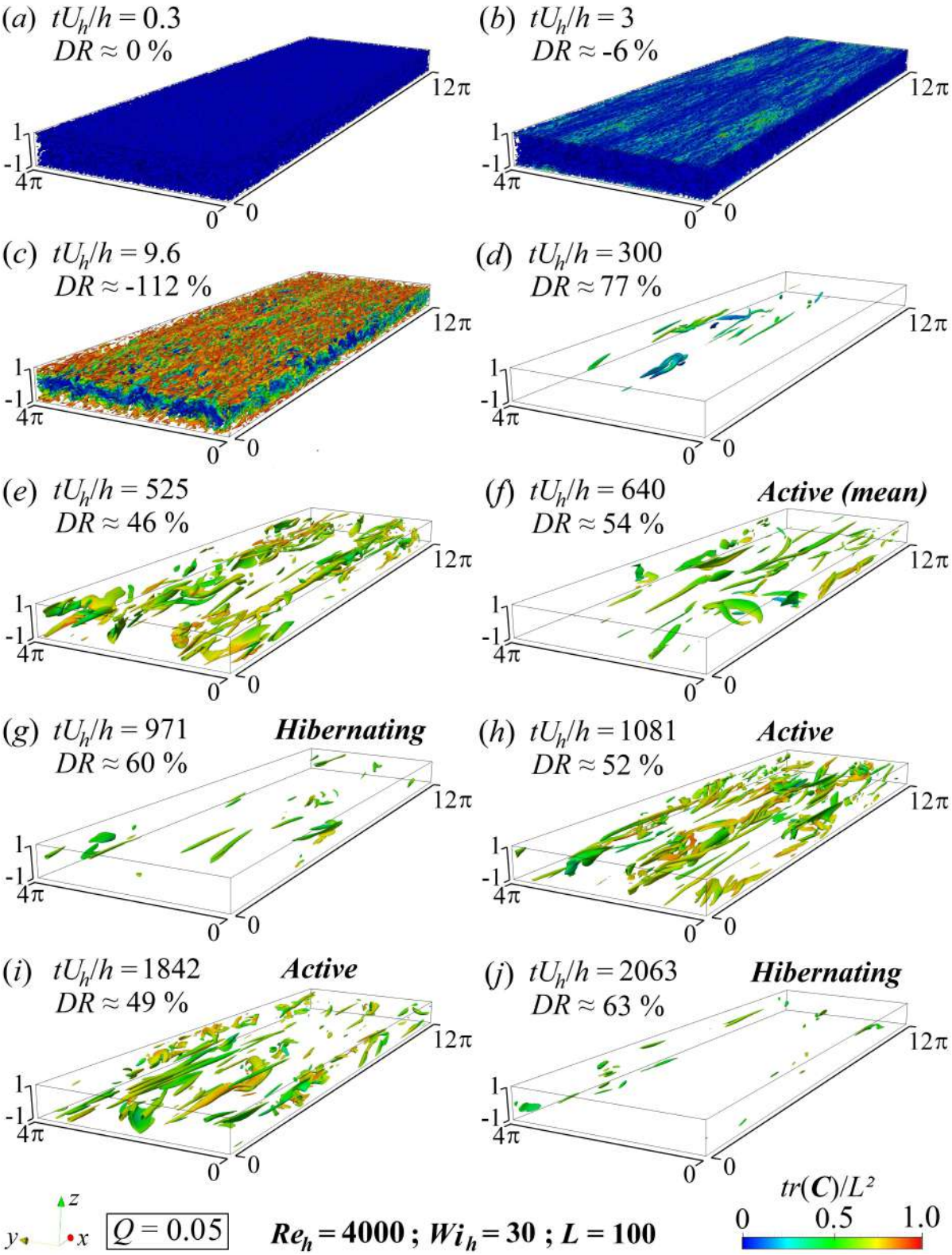

Figure 6.1 – The three-dimensional structures represent isosurfaces of vortical (or elliptical) regions defined as a positive value of the second invariant of velocity gradient tensor, $\nabla \boldsymbol{u}$. The colours indicate the relative polymer stretching, $tr(\boldsymbol{C})/L^2$.

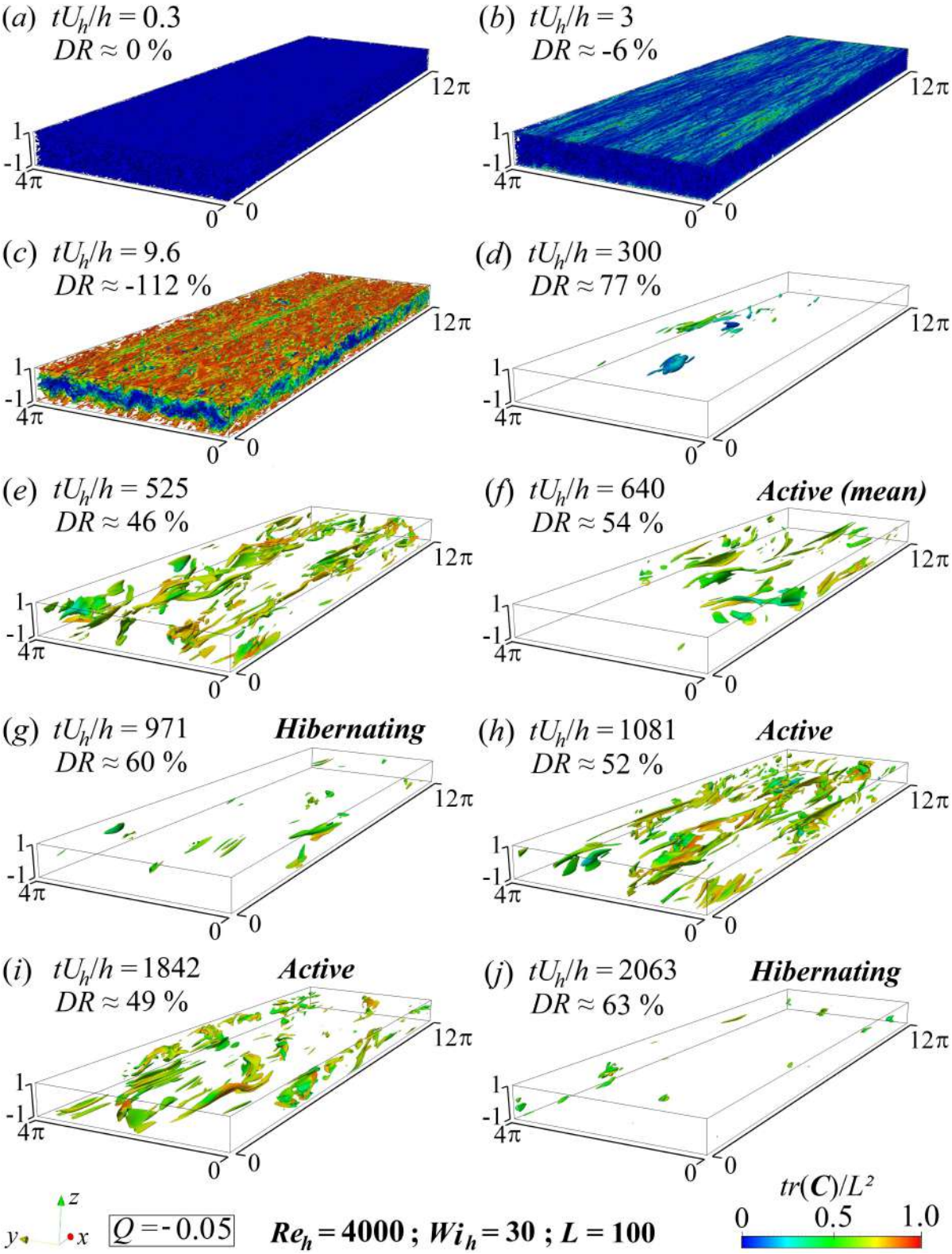

Figure 6.2 – The three-dimensional structures represent isosurfaces of extensional (or hyperbolic) regions defined as a negative value of the second invariant of velocity gradient tensor, $\nabla \boldsymbol{u}$. The colours indicate the relative polymer stretching, $tr(\boldsymbol{C})/L^2$.

(figures 6.1*e* and 6.2*e*), DR starts to fluctuate around its time-averaged value (DR_{asy}), indicating the beginning of the statistically steady state flow. A more detailed physical description of such *developing time* is founded in Pereira et al. [72].

At the dimensionless time $tU_h/h = 640$, the DR level is equal to 54%, which represents its asymptotic value, DR_{asy}. Nevertheless, once the statistically steady state is reached ($tU_h/h > 525$), the turbulence starts to oscillate between periods of strong activation and hibernation. The differences between these two regimes can be observed by comparing the turbulent structures pictured in figures 6.1(f) and 6.2(f) (our reference for the active state) with the others structures displayed in sequence. During highly active periods (figures 6.1*h*-*i* and 6.2*h*-*i*), the flow is dominated by the expected three-dimensional turbulent structures, the drag increases and, in consequence, DR appears smaller than DR_{asy}. In contrast, within hibernating periods (figures 6.1*g*, 6.1*j*, 6.2*g* and 6.2*j*), the structures with $Q = \pm 0.05$ almost vanish, which is a distinct characteristic of the MDR. As a consequence, the drag decreases and DR assumes more pronounced values. At $tU_h/h = 2063$, for instance, DR approaches 63 %, a value around 14% greater than that observed at $tU_h/h = 1842$.

It is worth noting that the molecules are more stretched in the active regime than in the hibernating one. This can be seen more clearly in figure 6.3, where the evolution of both the spatial average of the relative polymer stretching, $< tr(\boldsymbol{C}/L^2) >_{xyz}$ (blue triangles), and the area-averaged wall shear stress dimensionalized by its asymptotic value, $< \tau_w > / < \tau_{w,asy} >$ (red diamonds), are shown as functions of tU_h/h. Only the statistically steady state is considered ($500 < tU_h/h < 3000$). Two cases are displayed: $Re_h = 4000$, $Wi_h = 20$ and $L = 100$ (figure 6.3*a*); and $Re_h = 4000$, $Wi_h = 30$ and $L = 100$ (figure 6.3*b*). The rectangular green boxes indicate the hibernating periods, which are identified by considering the criteria proposed by Xi and Graham [105]. The authors considered a hibernation the period of 50 seconds in which $< \tau_w > / < \tau_{w,asy} >$ drops below a cutoff value of 0.9, indicated by the black line in figure 6.3. Clearly, the fraction of the total time of hibernation in our simulation increases with Wi_h, which corroborates the results reported by Xi and Graham [105, 106]. Furthermore, the reduction of stress also becomes more significant as Wi_h increases. Lastly, it is worth mentioning that the polymer stretching is in phase with the wall shear stress, what means that the molecules are more stretched in the active periods.

The profile of the relative polymer extension is plotted in figure 6.4 (left column) together with the streamwise velocity (right column). Each point in this figure is an average in the $x-y$ plane along z^+. The channel half-width is divided into three distinct regions: I ($0 < z^+ < 5$), II ($5 < z^+ < 30$), and III ($z^+ > 30$). In order to compare our profiles with those available in literature, the velocity of the bottom plate was subtracted from the velocity field, resulting in a relative streamwise component, u_{rx}. Three cases with $Re = 4000$ and $L = 100$ are shown: $Wi_h = 30$ (figures 6.4*a* and *b*);

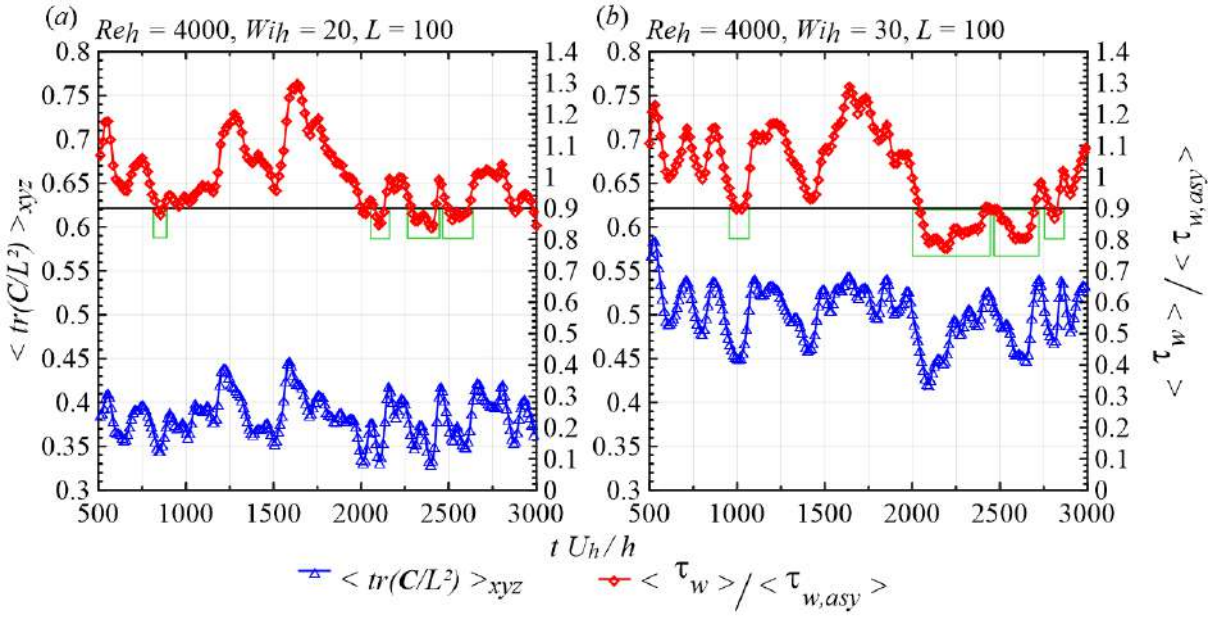

Figure 6.3 – Evolution of the spatial average of the relative polymer stretching as a function of the dimensionless time, tU_h/h (blue triangles). Area-averaged wall shear stress made dimensionless by its asymptotic value, $< \tau_w > / < \tau_{w,asy} >$, as a function of the dimensionless time (red diamonds).

$Wi_h = 10$ and (figures 6.4*c* and *d*); $Wi_h = 4.3$ (figures 6.4*e* and *f*). For each case, three different instants are considered: an instant for a moderately active regime characterized by $< \tau_w > / < \tau_{w,asy} >= 1$ and, thus, $DR = DR_{asy}$ (grey circles); an instant when the turbulence is highly active, corresponding to peak of $< \tau_w > / < \tau_{w,asy} >$ (blue triangles); and, finally, an instant when an intense hibernation occurs, relative to valley of $< \tau_w > / < \tau_{w,asy} >$ (red diamonds). It is clearly observed that the differences between the active (Act) and the (Hib) hibernating regimes become more pronounced as Wi_h increases. In other words, the intensity of the hibernation is accentuated by the presence of polymers. For $Wi_h = 4.3$, the curves practically collapse in a single one. The differences slightly increase for $Wi_h = 10$ and becomes quite clear for $Wi_h = 30$. At this level of elasticity, the hibernating velocity profile (red diamonds) approaches the Virk's asymptote (red dash-dotted line). Moreover, the u_{rx} profile corresponding to the most active case (blue diamond) is markedly below the curve that represents the time-averaged asymptotic profile (grey circles), getting close to the log-law profile represented by the grey dotted line. Concerning the most elastic case, it is also important to remark that the polymers appear more extended in the active periods. In contrast, in the hibernating periods, the molecules are in their least stretched configuration. Such an observation is rigorously the same phenomenon reported by Xi and Graham [105, 106] for turbulent plane Poiseuille flows.

In an attempt to further understand the role played by the active and hibernating turbulence regimes in drag reducing flows, we conduct an analysis from the energy

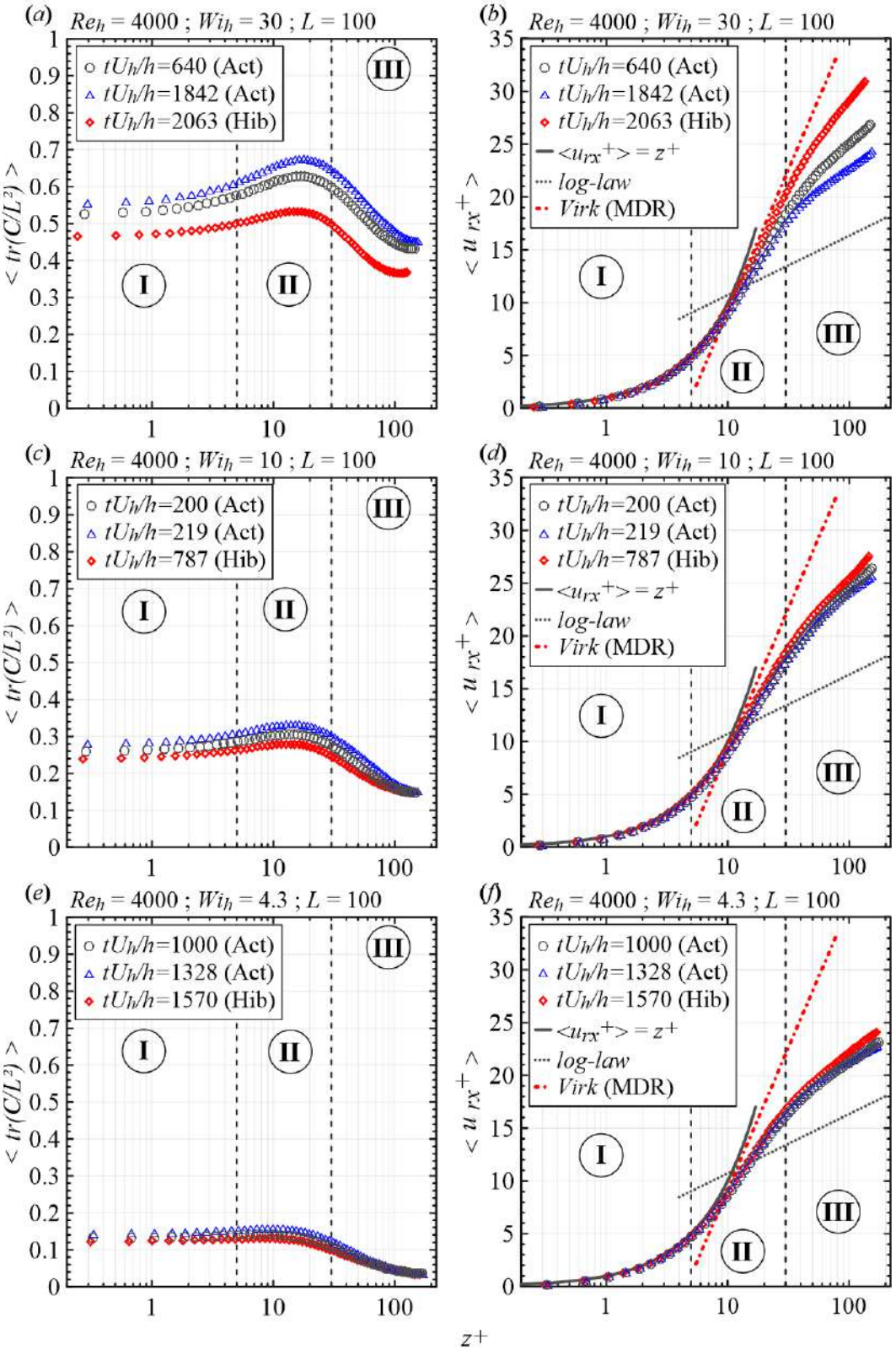

Figure 6.4 – Left column: average values in the $x-y$ plane of the relative polymer stretching, $\langle tr(\boldsymbol{C})/L^2 \rangle$, as a function of the dimensionless wall distance. Right column: average values in the $x-y$ plane of the streamwise relative velocity, $\langle u_{rx}^+ \rangle$, as a function of the dimensionless wall distance. Three FENE-P turbulent flows are analysed: Re_h = 4000, Wi_h = 30 and L = 100 (a and b); Re_h = 4000, Wi_h = 10 and L = 100 (c and d); Re_h = 3000, Wi_h = 4.3 and L = 100 (e and f). For each viscoelastic flow, $\langle tr(\boldsymbol{C})/L^2 \rangle$ and $\langle u_{rx}^+ \rangle$ are analysed at three dimensionless instants, tU_h/h.

budget and the spectral perspectives, which are displayed in figures 6.5, 6.6 and 6.7. Figure 6.5 shows the average values in the $x-y$ plane of the instantaneous kinetic energy terms obtained from the work equation [72]

$$\underbrace{\left[\frac{1}{2}\frac{\partial\left(u_x^{+2}\right)}{\partial t^+}\right]}_{T_x^+} = \underbrace{\left[-u_x^+\frac{\partial\left(u_x^+u_i^+\right)}{\partial x_i^+}\right]}_{A_x^+} + \underbrace{\left[-u_x^+\frac{\partial p^+}{\partial x^+}\right]}_{P_x^+} + \underbrace{\left[(\beta_0)\,u_x^+\frac{\partial^2 u_x^+}{\partial x_i^{+2}}\right]}_{V_x^+} + \underbrace{\left[u_x^+\frac{\partial \Xi_{xi}^+}{\partial x_i^+}\right]}_{E_x^+}, \tag{6.2}$$

where the instantaneous polymer work term, E_x^+, indicates the amount of energy stored ($E_x^+ < 0$) or released ($E_x^+ > 0$) by the polymers from the velocity field in the streamwise direction, u_x^+. The complementary work terms denote the advection, A_x^+, the pressure redistribution, P_x^+, and the viscous stress, V_x^+. The sum $A_x^+ + P_x^+ + V_x^+$ is referred to as the *Newtonian work*, N_x^+, and T_x^+ is the local time derivative term. The $x-y$ plane averages of these terms are plotted as a function of z^+. The profiles are evaluated at $tU_h/h = 1842$ (a peak of the active regime; figure 6.5*a*) and $tU_h/h = 2063$ (a valley of hibernation; figure 6.5*b*) for the most elastic case. In fact, a careful analysis on the energy exchange for the drag reducing flow between parallel plates was reported in Pereira et al. [72]. In the present work it is worth noting the main difference between each term of the kinetic energy in the active and hibernating states, displayed in figures 6.5(*a*) and (*b*). The main difference is concerned with the polymeric (plus blue symbol) and the viscous (green squares) works within the viscous sublayer (region I). The energy stored by the polymers near the wall is clearly less pronounced during the hibernating regime. This term is balanced by the viscous work, which also decreases in the hibernation.

There are striking differences between the active and hibernating states that appear in figure 6.6, where the $x-y$ averages of fluctuating work terms are displayed across the channel half-width for the most elastic case. These energy terms are that exclusively related to the fluctuating fields which appear in the right-hand side of the streamwise work fluctuation equation, which in turn is obtained by decomposing the variables of the streamwise momentum equation into mean flow ($\bar{U}_x^+$, $\bar{p}^+$ and $\bar{\Xi}_{xj}^+$) and fluctuations ($u_x'^+$, p'^+ and $\Xi_{xj}'^+$), and then multiplying the resulting equation by the streamwise velocity fluctuation ($u_x'^+$). The work terms exclusively linked with the fluctuating fields are then: $E_x'^+ = \left(u_x'^+\frac{\partial \Xi_{xj}'^+}{\partial x_j^+}\right)$, $A_x'^+ = \left[-u_x'^+\frac{\partial\left(u_x'^+u_j'^+\right)}{\partial x_j^+}\right]$, $P_x'^+ = \left(-u_x'^+\frac{\partial p'^+}{\partial x^+}\right)$ and $V_x'^+ = \left[(\beta_0)\,u_x'^+\frac{\partial^2 u_x'^+}{\partial x_j^{+2}}\right]$. The instantaneous polymer work term, $E_x'^+$, indicates the amount of energy stored ($E_x'^+ < 0$) or released ($E_x'^+ > 0$) by the polymers from the fluctuating velocity field in the streamwise direction, $u_x'^+$ (the fluctuations are denoted by the superscript '$\prime$'). The supplementary fluctuating work terms denote the advection, $A_x'^+$, the pressure redistribution, $P_x'^+$, and the viscous stress, $V_x'^+$. The sum $A_x'^+ + P_x'^+ + V_x'^+$ is referred to as the *Newtonian fluctuating work*, $N_x'^+$. Following the profiles shown in figure 6.6,

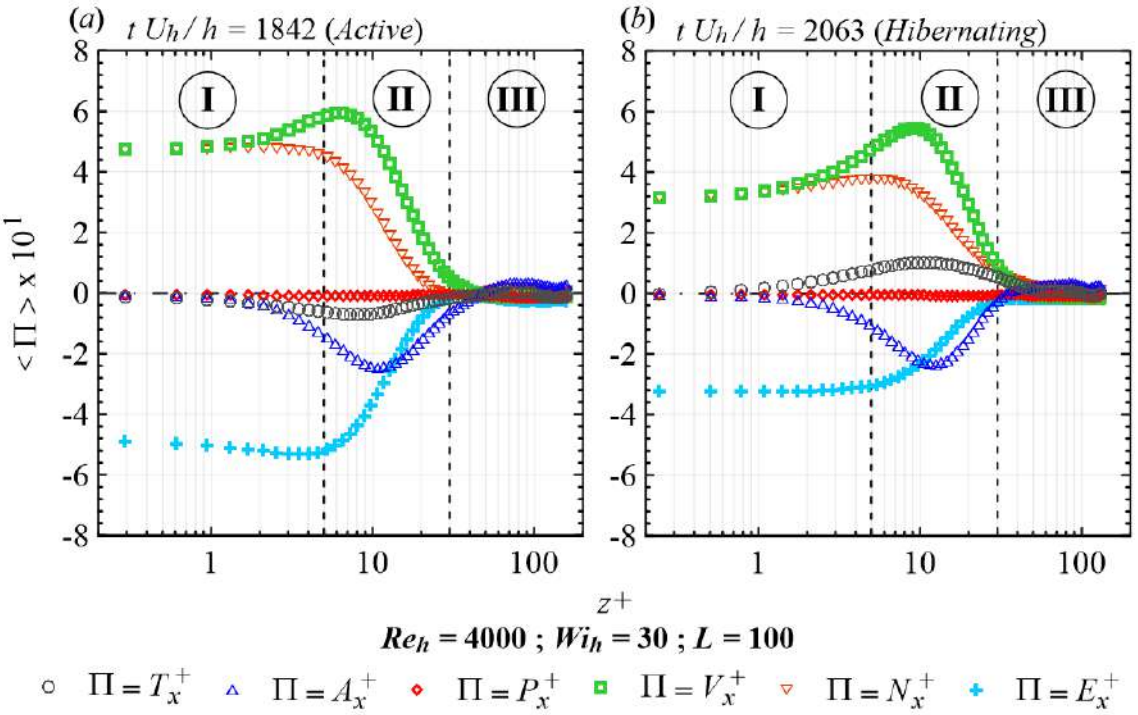

Figure 6.5 – Average values in the $x-y$ plane of the streamwise total kinetic energy budget against the dimensionless wall distance. Two dimensionless instants, tU_h/h, are analysed.

it is clearly seen that, when the flow regime changes from the active (figure 6.6*a*) to the hibernating one (figure 6.6*b*), the magnitude of both the advection ($|A_x'^+|$) and the pressure ($|P_x'^+|$) work fluctuations decrease far from the wall (region III). However, $|A_x'^+|$ increases within the region II. The same tendency is observed for $|V_x'^+|$. It is worth noting that, in the active regime, the molecules located in the regions II and III store energy from the fluctuating velocity field ($E_x'^+ < 0$). However, this scenario considerably changes during the hibernation since significant positive values of $E_x'^+$ are perceived within the region II, which indicates a release of polymeric energy in the fluctuating velocity field. Hence, we can conclude that, especially during the hibernating state, the polymers act as an important source of turbulent kinetic energy in region II. In other words, the turbulence tends to be re-activated by the polymers, which, lastly, increases $|N_x'^+|$, as indicated by the orange inverted triangles in figure 6.6(*b*). The polymer-turbulence exchanges of energy in the hibernating regime may provide a reasonable explanation for the MDR's limit. Xi and Graham [105] argue that the MDR regime is a state in which hibernating turbulence is the norm, with active turbulence arising intermittently.

Finally, figure 6.7 shows the longitudinal 1D spectra of the turbulent kinetic energy, $E_{11}/(h\,U_h^2)$, at $z^+ = 15$ for the most elastic case. Around this point, $|N_x'^+|$ is maximum for both the active and hibernating regimes (see figure 6.6). For the former regime, illustrated by the grey solid line and the blue dashed line, a range of wavenumbers

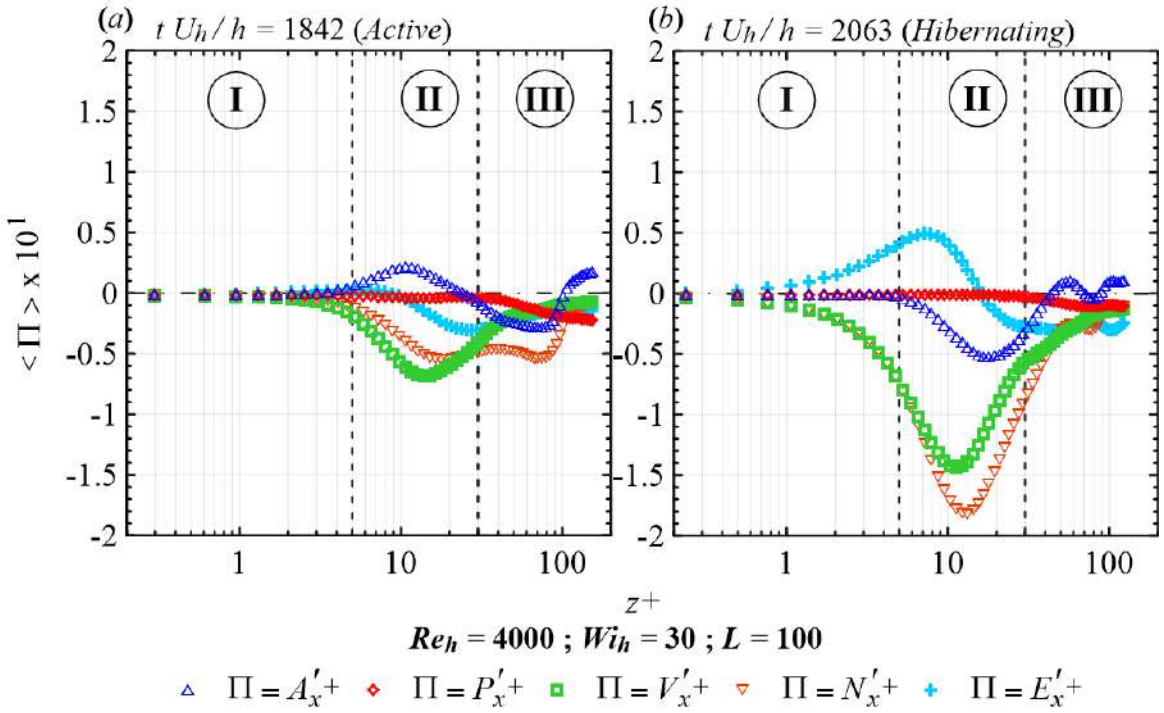

Figure 6.6 – Average values in the $x-y$ plane of the streamwise fluctuating kinetic energy budget against the dimensionless wall distance. Two dimensionless instants, tU_h/h, are analysed.

between $3 \leq k_x \leq 9$ exhibits the typical power law decay related to drag reducing flows, $k_x^{-14/3}$ (black solid line) [88]. However, such a decay is modified in the hibernating period, moving from $k_x^{-14/3}$ towards k_x^{-8} (black dotted line). Consequently, the large wavenumber structures ($k_x > 15$) are strongly suppressed. In contrast, within very small wavenumbers, no significant changes in $E_{11}/(h\ U_h^2)$ are perceived by comparing the three curves plotted in figure 6.7. Hence, we can conclude that the oscillatory behaviour of the turbulence between the active and hibernating regimes affects basically the small-scale structures (high frequencies), which in turn tend to be suppressed during the hibernation while the large structures (low frequency) are preserved. Lastly, it is important to emphasize that the active and hibernating profiles of $E_{11}/(h\ U_h^2)$ collapse into a single one at $Wi_h \leq 10$ (not shown, for brevity).

6.4 Concluding Remarks

Direct numerical simulations of FENE-P fluids were used to analyse the active and hibernating turbulence regimes in drag reducing plane Couette flows. Five viscoelastic flows were examined, keeping the Reynolds number, Re_h, the viscosity ratio, β_0, and the maximum polymer molecule extensibility, L, fixed. A large range of Weissenberg number based on the plate velocities was explored ($2 \leq Wi_h \leq 30$), which provided asymptotic drag reduction levels, DR_{asy}, from 11% up to 54%.

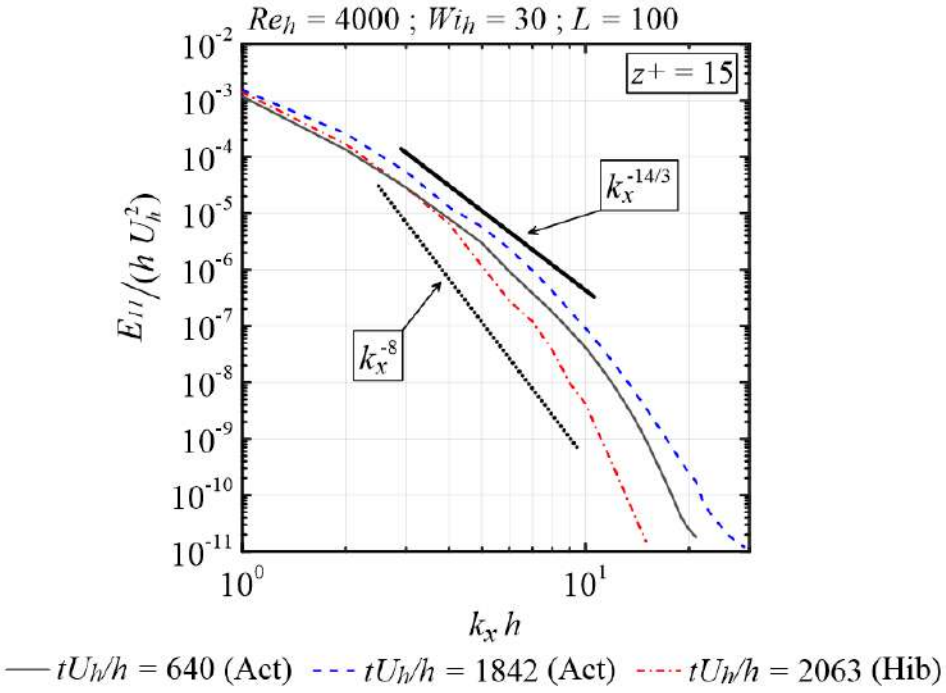

Figure 6.7 – Power spectral densities of the streamwise velocity component at the wall-normal position, $z^+ = 15$. Three dimensionless instants, tU_h/h, are analysed.

The qualitative picture that emerges from our energy transfer and spectral analyses is a cycle which begins when the polymer-flow interactions in the active turbulence regime favour the extension of the molecules. In their stretching process, polymers reduce the mean fluid velocity and partially suppress the turbulent structures (the small-scale ones), driving the flow towards a very weak turbulent hibernating regime in which the polymers tend to relax. Hence, their level of stretching decreases while a significant amount of polymeric energy is released into the flow, increasing its mean velocity towards the MDR asymptote. Additionally, a significant part of the polymeric energy is directly injected into the fluctuating velocity field, favouring the re-activation of turbulence. Finally, the active turbulence stretches the molecules again, reinitiating the cycle.

Chapter 7

Drag reducing flow considering the effects of polymer degradation

We analyse the effects of polymer degradation on a drag reducing plane Couette flow using direct numerical simulations of a viscoelastic FENE-P fluid. A new molecular scission model based on relative polymer extension is developed. It is shown that, as the polymer degradation evolves over time, both the drag reduction level and the streamwise velocity decrease while the number of turbulent structures enhances. The polymer-flow interactions are significantly attenuated by the molecular scissions, especially in the viscous sublayer, which is evidenced by an energy budget analysis.

7.1 Introduction

Polymer-induced drag reducing flow has been investigated for over 60 years. One reason for this is that the drag reducers in turbulent flow systems have been successfully applied and represent a significant potential benefit to many industrial processes. However, the efficiency of the additives is not constant. Turbulence is also responsible for breaking the polymer molecules, decreasing their ability to reduce drag [65].

Experimentally, turbulent flow degradation of polymers in different geometries have been studied by a number of researchers [58, 60, 65, 64, 82]. For instance, Pereira et al. [65] analysed various parameters for polymer degradation in turbulent flows in a cylindrical double gap geometry, such as the Reynolds number, polymer concentration, molecular weight, and temperature. They concluded that increasing concentration and molecular weight delay the observed effects of degradation whereas both the Reynolds numbers and the temperature produce an opposite effect. These results are rather in line with that recently obtained by Soares et al. [82] who performed turbulent pipe flow experiments.

Numerically, as far as we know, the polymer degradation process in turbulent drag

reducing flows was never explored in the literature, a scarcity certainly related to the constraints involving the strong numerical instabilities associated with turbulent viscoelatic flows. Nevertheless, the development of numerical models capable to compute the molecular scission in such scenario could open new tracks for understanding the polymer-flow interactions in turbulent flows and, consequently, the drag reduction phenomenon.

In attempt to better understand the polymer degradation process in drag reducing flows, we conduct in the present work direct numerical simulations (DNS) of a turbulent plane Couette flow of a FENE-P fluid taking into account the molecular scissions. To this end, a molecular scission model is developed based on relative polymer extension. The effects of the polymer degradation on the flow over time are evaluated from statistical and energy budget perspectives.

The organization of this work is as follows. The description of the molecular scission model is presented in Section 8.2. Our main results are discussed in Section 7.3, where statistical analyses concerning the polymer degradation and its impact on the flow are conducted. Finally, conclusions are presented in the closing section.

7.2 Numerical methodology (molecular scission model)

A molecular scission model based on the relative polymer extension is developed in order to compute the effects of polymer degradation in turbulent drag reducing flows. More specifically, we consider a temporal and local field of maximum polymer extension length, $L(x,y,z,t)$ instead of the unique and constant value of L typically used in the classical FENE-P model. At the beginning of the simulation, $L(x,y,z,t)$ is uniform and equal to an initial value, $L_i = 30$. As the simulation progresses, a degradation criterion based on the trace of the conformation tensor divided by L_i^2, $tr(\boldsymbol{C}(x,y,z,t)/L_i^2)$, is employed to modify $L(x,y,z,t)$ within the channel. At particular time-steps during the simulation, if $tr(\boldsymbol{C}(x,y,z,t)/L_i^2) > 0.5$, then $L(x,y,z,t)$ is reduced by 2%. Since $L(x,y,z,t)$ is used to calculate a local Peterlin function at each time-step (which is related to the polymer forces), a decreasing $L(x,y,z,t)$ reduces the polymer contribution on the momentum equation, increasing the drag. Aiming to minimize numerical instabilities, the degradation criterion is applied every 10 seconds (physical time). In addition, we propose an evolution equation for $L(x,y,z,t)$ in order to transport the degraded molecules within the flow,

$$\frac{\partial L}{\partial t} + \left(u_x \frac{\partial L}{\partial x} + u_y \frac{\partial L}{\partial y} + u_z \frac{\partial L}{\partial z} \right) = k_L \left(\frac{\partial^2 L}{\partial x^2} + \frac{\partial^2 L}{\partial y^2} + \frac{\partial^2 L}{\partial z^2} \right), \tag{7.1}$$

in which L represents the local and instantaneous maximum polymer extension length and u_x^+, u_y^+, and u_z^+ dictate the respectively local velocity components in the

streamwise (x^+), spanwise (y^+) and wall-normal (z^+) direction. The explicit dissipative elliptic term in equation 7.1 is an artifice used to remove non-physical high wave-number instabilities typically induced by the chaotic nature of viscoelastic turbulent flows, when computed with a high-order spectral code. Hence, k_L represents a constant of artificial diffusivity. Here, this constant is considerably small, $k_L = 10^{-6}$, and, as a result, the transport of L is dominated by advection. Lastly, the Dirichlet boundary condition is used to $L(x,y,z,t)$ at the walls ($L(x,y,z,t) = L_i$).

For the present study, we simulate one viscoelastic case fixing the Reynolds number, $Re_h = hU_h/\nu_{tot}$ at 1000, the Weissenberg number, $Wi_h = \lambda U_h/h$, at 10, and the viscosity ratio, β_0, at 1000, 10 and 0.9. At the beginning of the simulation, the field of L is uniform and equal to 30. However, L decreases as the polymer degradation becomes important, which increases the drag over time. We define the percentage of DR in time as

$$DR(t) = \left(1 - \frac{<\tau_w(t)>}{<\tau_{w,N}(t)>}\right) \times 100, \tag{7.2}$$

where $<\tau_w(t)>$ and $<\tau_{w,N}(t)>$ denote the area-averaged wall shear stress for the polymer solution and the Newtonian solvent, respectively, at a given instant t. Lastly, both the size of the domain ($L_x \times L_y \times L_z = 12\pi \times 4\pi \times 2$) and the number of mesh points ($N_x \times N_y \times N_z = 384 \times 256 \times 129$) are kept fixed for all cases, which leads to a grid resolution of $\Delta x^+ \approx 9.2$, $\Delta y^+ \approx 4.1$, and $0.2 \leqslant \Delta z^+ \leqslant 1.6$ at the beginning of the simulation and $\Delta x^+ \approx 9.7$, $\Delta y^+ \approx 4.4$, and $0.21 \leqslant \Delta z^+ \leqslant 1.7$ when L reaches its asymptotic value.

7.3 Results and Discussions

The goal of our work has been to evaluate the effects of the polymer degradation on the drag reduction phenomenon by using the molecular scission model presented previously. As the simulation evolves in time, the number of degraded molecules increases and, consequently, the role played by the extra-tensor in the moment equations becomes less important. As a result, DR falls over time, as indicated by the grey circles in figure 7.1. At the beginning of the process, the drag reduction is about 28%. However, every 10 seconds, new molecular scissions take place, reducing DR towards its final level, $DR_{final} \approx 18\%$, which is reached at $tU_h/h \approx 1800$. Following a similar tendency, the spatial average of the maximum polymer extension length, $< L/L_i >_{xyz}$, moves from its initial value ($< L/L_i >_{xyz} = 1$) to its asymptotic one ($< L/L_i >_{xyz} \approx 0.7$), as illustrated by the blue triangles.

The increase in the drag over time is closely related to the growing number of structures illustrated in figure 7.2 by using the Q-criterion [38]. For instance, at the beginning of the simulation ($tU_h/h = 0.3$; figure 7.2*a*), when $L = 1$ for the whole domain, $DR \approx 28\%$ and a moderate number of vortical (blue) and extensional (red) structures

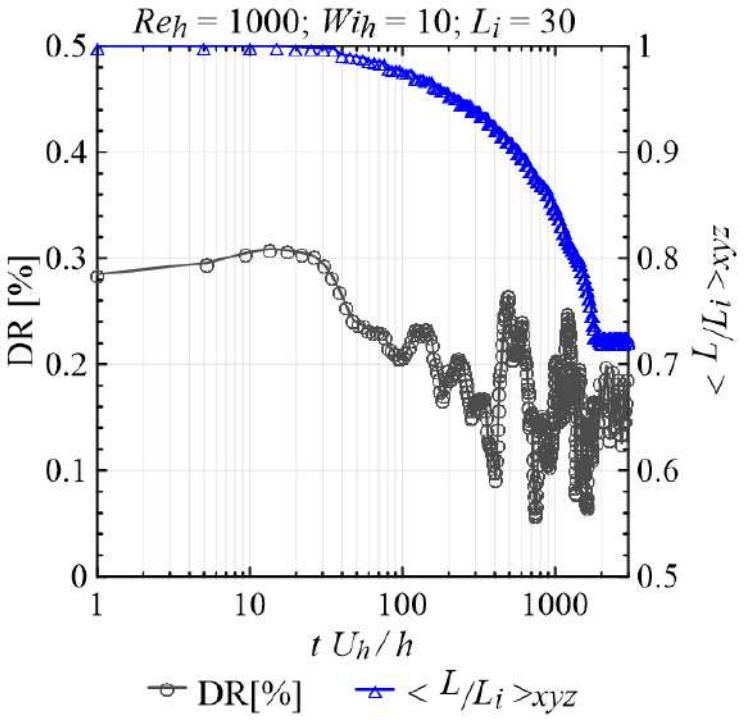

Figure 7.1 – Drag reduction, DR (grey circles) as a function of the dimensionless time, tU_h/h, together with evolution of the spatial average of the maximum polymer extension length made dimensionless by its initial value, $< L/L_i >_{xyz}$ (blue triangles).

with Q equal to 0.1 and −0.1, respectively, are observed across the channel. Nevertheless, these structures almost fill the geometry at $tU_h/h = 1800$, when $0.7 < L/L_i < 1$ and $DR \approx 18\%$.

In figure 7.3, the contours of L/L_i in the centre $x-y$ plane (high column) are compared with that of the norm of the velocity vector made dimensionless by the plate velocity, $\|\boldsymbol{u}\|/U_h$ (left column), in the same plane. Two dimensionless instants are considered: 650 (*a*-*b*) and 1800 (*c*-*d*). At $tU_h/h = 650$ (figure 7.3*b*), values of L/L_i close to the unity (red) are more frequent. However, at $tU_h/h = 1800$ (figure 7.3*d*), $L/L_i < 0.85$ for the entire centre $x-y$ plane. Comparing figures 7.3(*a*) and (*b*), it is interesting to note that smaller values of L/L_i (blue contours) appear in the regions where $\|\boldsymbol{u}\|/U_h$ is pronounced (yellow contours). The same correlation is observed by comparing figures 7.3(*c*), which suggests that the polymer degradation is accentuated within the streaks. A further comparison between the velocity contours in figures 7.3(*a*) and (*c*) reveals that the flow becomes more disturbed with increasing degradation.

More details concerning the effects of the molecular scissions on the flow are shown in figure 7.4 in which the profile of the streamwise velocity (figure 7.4*b*) is plotted together with the relative polymer extension (figure 7.4*a*). Each point in this figure is an average in the $x-y$ plane along z^+. The channel half-width is divided into three distinct regions: I ($0 < z^+ < 5$), II ($5 < z^+ < 30$), and III ($z^+ > 30$). Three different instants, tU_h/h, are considered: 0.3, 650 and 1800. In order to compare our profiles with

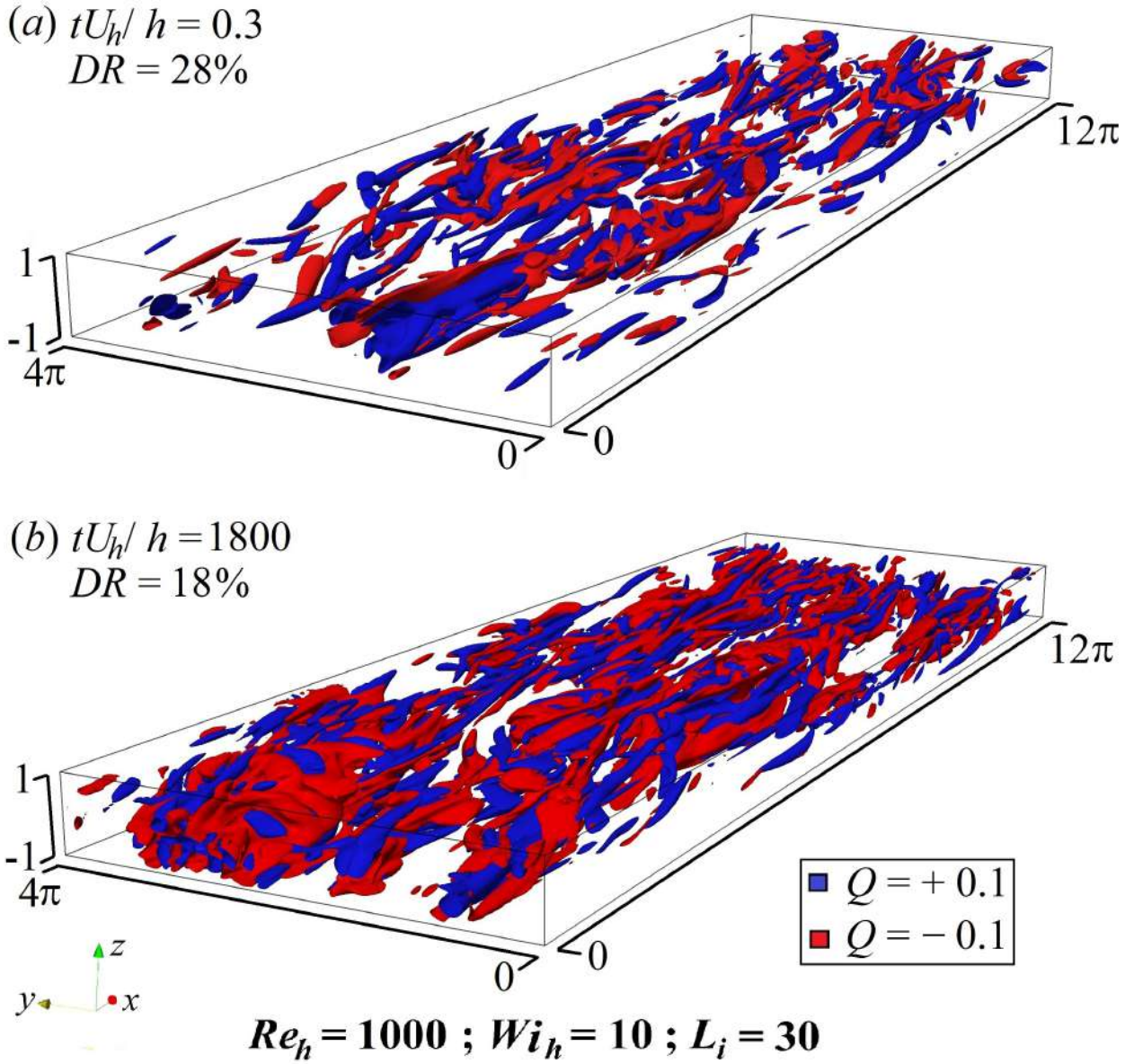

Figure 7.2 – The three-dimensional structures represent isosurfaces of vortical (or elliptical) and extensional (or hyperbolic) regions respectively defined as a positive (blue) and a negative (red) value of the second invariant of velocity gradient tensor, $\nabla \boldsymbol{u}$.

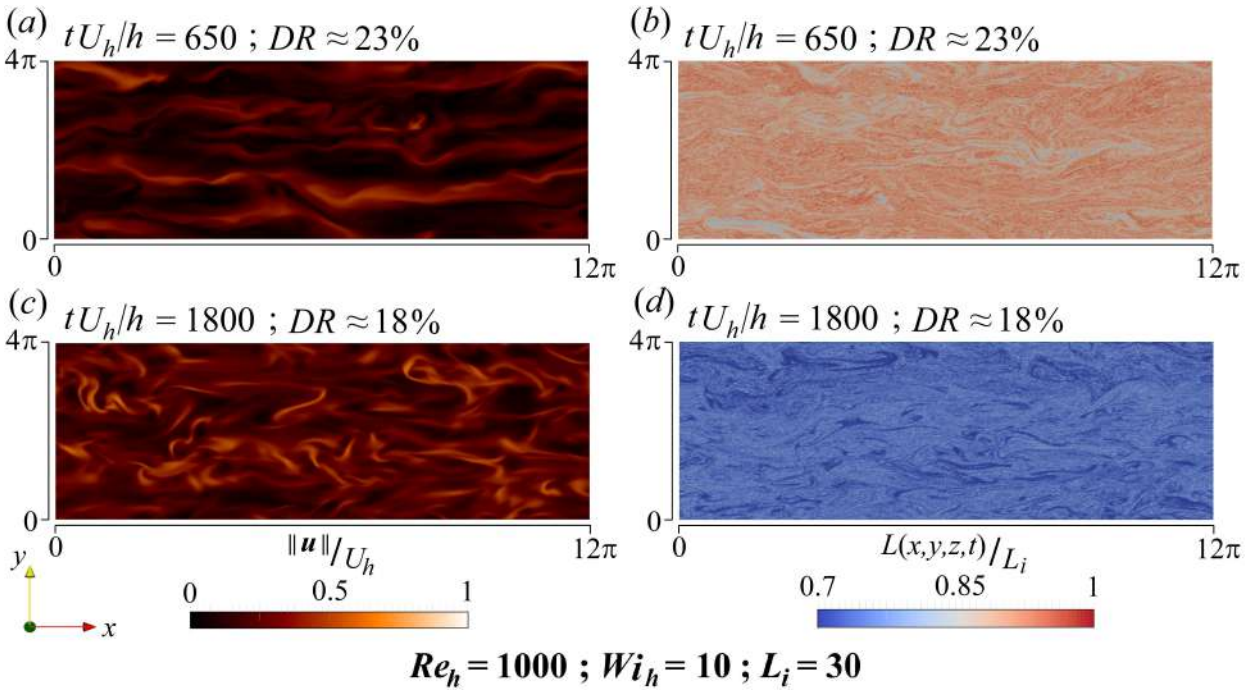

Figure 7.3 – Contours of L/L_i in the centre $x-y$ plane (high column) compared with that of the norm of the velocity vector made dimensionless by the plate velocity, $\|\boldsymbol{u}\|/U_h$ (left column), in the same plane. Two dimensionless instants are considered: 650 (a-b) and 1800 (c-d).

those available in literature, the velocity of the bottom plate was subtracted from the velocity field, resulting in a relative streamwise component, u_{rx}. It is clearly observed that the differences between the curves become more pronounced as the simulation evolves in time and, consequently, the number of degraded molecules increases. Since no molecular scissions were computed until $tU_h/h = 10$, at $tU_h/h = 0.3$ the velocity profile exhibits its highest values (grey circles), figuring in between the maximum drag reduction asymptote (MDR; [97]) indicated by the red dash-dotted line and the log-law represented by the grey dotted line. Nevertheless, instants later, the degradation starts to play an important role and, as a result, the velocity profile moves towards the log-law, a tendency indicated by the black arrow. Lastly, concerning the relative polymer deformation displayed in figure 7.4(a), it is noted that $< tr(\boldsymbol{C}/L^2) >$ is an increasing function of the degradation for all z^+. These results are rather in line with those concerning the effects of the reduction of L on the relative polymer deformation available in the literature (see, for instance, [71]). It is worth noting that more significant differences between the polymer deformation profiles at $tU_h/h = 0.3$ and $tU_h/h = 1800$ occur within the region I, where the degradation is intense due to the high polymer stretching level in the vicinities of the wall.

The molecular degradation also affects the polymer-flow exchanges of energy, as pointed out in figure 7.5. This figure shows the average values in the $x-y$ plane of the

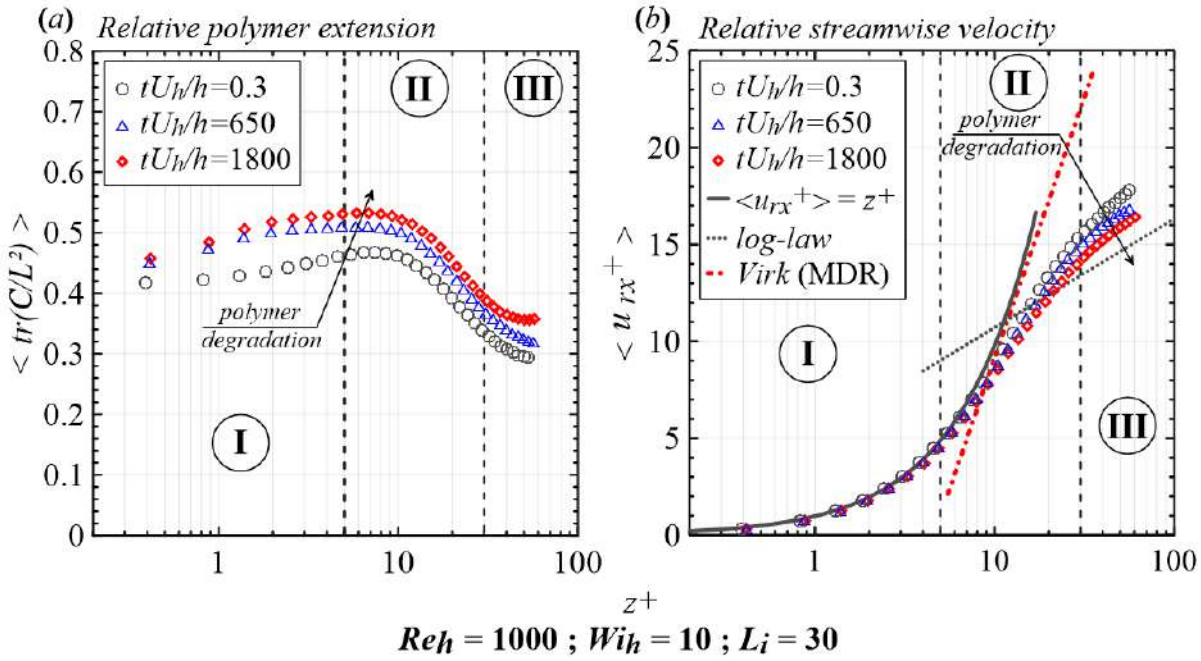

Figure 7.4 – (a): average values in the $x-y$ plane of the relative polymer stretching, $\langle tr(\boldsymbol{C})/L^2 \rangle$, as a function of the dimensionless wall distance. (b): average values in the $x-y$ plane of the streamwise relative velocity, $\langle u_{rx}^+ \rangle$, as a function of the dimensionless wall distance. The quantities are analysed at three distinct dimensionless instants, tU_h/h: 0.3, 650 and 1800.

energy terms obtained from the streamwise work equation,

$$\underbrace{\left[\frac{1}{2}\frac{\partial\left(u_x^{+2}\right)}{\partial t^+}\right]}_{T_x^+} = \underbrace{\left[-u_x^+\frac{\partial\left(u_x^+u_i^+\right)}{\partial x_i^+}\right]}_{A_x^+} + \underbrace{\left[-u_x^+\frac{\partial p^+}{\partial x^+}\right]}_{P_x^+} + \underbrace{\left[(\beta_0)\,u_x^+\frac{\partial^2 u_x^+}{\partial x_i^{+2}}\right]}_{V_x^+} + \underbrace{\left[u_x^+\frac{\partial \Xi_{xi}^+}{\partial x_i^+}\right]}_{E_x^+}, \tag{7.3}$$

where the instantaneous polymer work term, E_x^+, indicates the amount of energy stored ($E_x^+ < 0$) or released ($E_x^+ > 0$) by the polymers from the velocity field in the streamwise direction, u_x^+. The complementary streamwise work terms denote the advection, A_x^+, the pressure redistribution, P_x^+, and the viscous stress, V_x^+. The sum $A_x^+ + P_x^+ + V_x^+$ is referred to as the streamwise *Newtonian work*, N_x^+, and T_x^+ is the local time derivative term. The energy terms are taken into account by multiplying the momentum equation by the velocity and their $x-y$ plane averages are plotted as a function of z^+. The profiles are evaluated at two dimensionless instants, tU_h/h: 0.3 (figure 7.5a) and 1800 (figure 7.5b). Fundamentally, as reported by [72], the energy is balanced by the polymeric work, the viscous dissipation, and the advection terms. Comparing figures 7.5(a) and (b), it is noted that the polymer storage of energy ($E_x^+ < 0$) is considerably attenuated by the molecules scission, especially in the region I, as indicated by the blue plus symbols. In other word, the polymer-flow exchanges of energy are weakened by the molecular

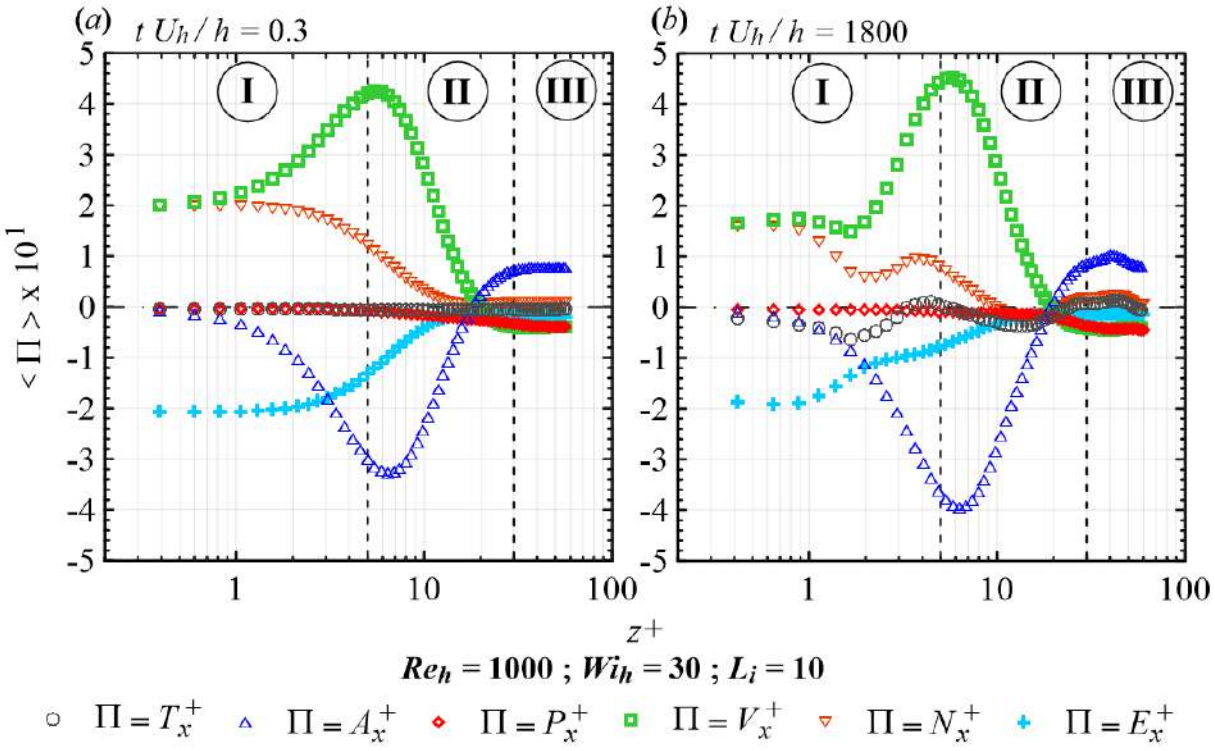

Figure 7.5 – Average values in the $x-y$ plane of the streamwise total kinetic energy budget against the dimensionless wall distance. Two dimensionless instants, tU_h/h, are analysed: 650 and 1800.

scissions. In addition, although the peak magnitude of V_x^+ exhibits a highest value at $tU_h/h = 1800$, the viscous term also decreases in the near wall region with increasing degradation. In contrast, the magnitude of both the advection and the pressure terms appear as increasing functions of the molecular scissions, which is strongly related to the increasing number of turbulent structures shown in figure 7.2. As a result, a more disturbed flow emerges, which, finally, slightly increases $|T_x^+|$.

7.4 Concluding Remarks

Direct numerical simulation of a FENE-P fluid was used to analyse a turbulent viscoelastic flow in a plane Couette geometry fixing the Reynolds number, Re_h, the Weissenberg number, Wi_h, and the viscosity ratio, β_0, at 1000, 10 and 0.9. A new model based on the polymer extension was developed in order to compute the effects of the molecular scissions on the drag reduction phenomenon. A temporal-local field of maximum polymer extension length, L, is considered instead of the constant value typically used in the classical FENE-P model.

At the beginning of the simulation, the field of L is uniform and equal to 30 while the drag reduction level (DR) is about 28%. However, L drops to 21 as the polymer degradation becomes important, which reduces the contribution of the extra-tensor to

the moment equations. Consequently, DR decreases over time to about 18%, the drag reduction final level, while the number of turbulent structures grows and the mean velocity decreases towards the log-law profile. An energy budget analysis revealed that the polymer-flow interactions are significantly attenuated by the molecular scissions, especially in the viscous sublayer.

Chapter 8

General conclusions

8.1 Contribution to the understanding of DR

In this thesis, we have investigated in depth the transient aspects of the drag reducing flows related to the states A, B and C shown in figure 1.1. To this end, we conducted direct numerical simulations of turbulent plane Poiseulle and Couette flows of viscoelastic FENE-P fluids taking into account different values of Reynolds number, Re_h, Weissenberg number, Wi_h, and maximum polymer molecule extensibility, L. Our main contributions to the understanding of the drag reduction mechanism contained in the different chapters of this dissertation are gathered and summarized below:

(a) *Investigation of the drag reduction phenomenon from its very beginning (Chapters 4 and 5)*;

We have analysed the development of the drag reduction phenomenon from its very beginning (when the drag reduction, DR, is null), which is represented by the stage A and referred to as the *developing time*. It was showed that, during this period, the shape of the DR curve is highly affected by the initial flow condition (velocity field), the initial polymer configuration (tensor conformation field) and the elasticity (Wi_h and L). In addition, as the latter increases, the developing time becomes more pronounced.

(b) *Development of a methodology to analyse the polymer-turbulence interactions (Chapters 2 and 5)*;

The polymer-turbulence interactions have been analysed by discriminating the mechanical response of this system accordingly to the different subdomains defined by the Q-criterion of flow classification [38]: elliptical (or vortical); parabolic; hyperbolic (or extensional). The exchanges of energy between these subdomains and the polymers were highlighted.

(c) *Detailed description of the mechanism of polymer coil–stretch (Chapters 2 and 3)*;

Using statistics and tensor analysis, we were able to provided a detailed description of the mechanism of polymer coil–stretch, which concerns the stage B in figure 1.1. In short, the mean flow acts as the main source of polymeric energy near the wall. In this region, polymers also interacts with the elliptical and hyperbolic structures, releasing their energy. Nevertheless, these trends completely change as the wall distance increases. The molecules can be pulled by the turbulent structures towards the centre of the channel, applying a counter-torque around the vortices and a counter-stretch in the extensional subdomains, storing their energy. Lastly, in the core zone, the molecules also release polymeric energy to the mean flow, increasing the streamwise mean velocity.

(d) *Refinement of the understanding of active and hibernating turbulence in drag reducing flows (Chapter 6)*;

When the level of elasticity becomes pronounced, even the stage B exhibits a transient character since the flow starts to strongly oscillate between two different turbulent regimes: active and hibernating [105]. This oscillatory behaviour is closely related to the maximum drag reduction (MDR) asymptote and the effects of the polymers on it were investigated from energy budget and spectral perspectives. Fundamentally, it was shown that, when the elasticity is accentuated, the polymer damping of turbulent structures drives the flow towards a very weakly turbulent hibernating regime. During hibernation, polymers tend to relax towards equilibrium, releasing a significant amount of polymeric energy into the flow. Consequently, the mean velocity increases towards the MDR asymptote while the velocity fluctuations are intensified, favouring the re-activation of the turbulence.

(e) *Development of a new model to compute polymer degradation (Chapter 7)*;

A new and simple polymer scission model based on the molecule strain level was developed in order to numerically reproduce the stage C in Figure 1.1.

(f) *Evaluation of the effects of polymer degradation on the drag reduction phenomenon (Chapter 7)*;

Using the new model referred above, we were able to qualitatively evaluate the polymer degradation effects on the drag reduction phenomenon. As expected, it was observed that the polymer-flow exchanges of energy are significantly attenuated by the molecular scissions.

8.2 Future prospects

The present dissertation has led to a better understanding of several important issues related to the polymer induced drag reduction. In this context, new paths have been opened for the investigations of the polymer-flow interactions. For instance, the exchanges of energy between the polymers and the elliptical, parabolic and hyperbolic subdomains were studied here in the light of the Q-criterion, which in turn can vary with respect to a reference frame (the Q-criterion is non-objective). In order to avoid such variations, a similar methodology can be employed by considering objective flow classification criteria [92, 91, 54], which, lastly, could reveals more details concerning the drag reduction mechanism.

It was also shown in this work that the polymers considerably accentuate the flow oscillations between the active and the hibernating regimes. Consequently, when the elasticity becomes pronounced, estimating uncertainties with respect to the different entities obtained from the statistics of DNS becomes a difficult task. In such a scenario, the development of new methodologies to estimate the statistical errors associated with the direct numerical simulations becomes highly desirable.

Finally, concerning the simulations of the polymed degradation, a new model was proposed. This model represents a initial efforts to better understand the process of molecular scission in drag reducing flows and the results that emerges from it are still preliminary. However, they open new tracks for the development of more realistic models. In this connection, a promising methodology which has been explored by our research group is the addition of degradation parameters on the basis of the FENE model, which shall be natural incorporated into the FENE-P model, after proceeding to the Peterlin approximation.

Bibliography

[1] Roland J. Adrian. "Hairpin vortex organization in wall turbulence". In: *Physics of Fluids* 19 (2007), pp. 041301–1–041301–16.

[2] R. M. Andrade, A. S. Pereira, and E. J. Soares. "Drag increase at the very start of drag reducing flows in a rotating cylindrical double gap device". In: *Journal of Non-Newtonian Fluid Mechanics* 212 (2014), pp. 73–79.

[3] R. M. Andrade, A. S. Pereira, and E. J. Soares. "Drag reduction in synthetic seawater by flexible and rigid polymer addition into a rotating cylindrical double gap device". In: *Journal of Fluids Engineering* 138 (2016), pp. 021101–1–021101–10.

[4] S. W. Armfield and R. L. Street. "Fractional step methods for the Navier–Stokes equations on non-staggered grids". In: *ANZIAM J* 42(E) (2000), pp. C134–C156.

[5] V. Avsarkisov et al. "Turbulent plane Couette flow at moderately high Reynolds number". In: *Journal of Fluid Mechanics* 751 (2014), pp. 1–9.

[6] F. Bagheri et al. "Statistics of polymer extensions in turbulent channel flow". In: *Physical Review E* 86 (2012), pp. 056314–1–056314–10.

[7] K. Bech et al. "An investigation of turbulent plane Couette flow at low Reynolds numbers". In: *Journal of Fluid Mechanics* 286 (1995), pp. 291–325.

[8] R. Benzi. "A short review on drag reduction by polymers in wall bounded turbulence". In: *Physical D* 239 (2010), pp. 1338–1345.

[9] R. Benzi et al. "Identification and calculation of the universal asymptote for drag reduction by polymers in wall-bounded turbulence". In: *Physical Review Letters* 95 (2005), pp. 194502–1–194502–4.

[10] R. Benzi et al. "Turbulence statistics in fully developed channel flow at low Reynolds number". In: *Journal of Fluid Mechanics* 551 (2006), pp. 185–195.

[11] M. Bernardini, S. Pirozzoli, and P. Orlandi. "The effect of large-scale turbulent structures on particle dispersion in wall-bounded flows". In: *International Journal of Multiphase Flow* 51 (2013), pp. 55–64.

[12] H. W. Bewersdorff. "Effect of a centrally injected polymer thread on drag in pipe flow". In: *Rheologica Acta* 21 (1982), pp. 587–589.

[13] H. W. Bewersdorff and R. P. Singh. "Rheological and drag reduction characteristics of xanthan gum solutions". In: *Rheologica Acta* 27 (1988), pp. 617–627.

[14] R. Bird, R. Armstrong, and O. Hassager. *Dynamics of Polymeric Liquids. Kinetic Theory*. Wiley-Interscience, 1987.

[15] E. D. Burger and L. G. Chorn. "Studies of drag reduction conducted over a broad range of pipeline conditions when flowing Prudhoe Bay crude oil". In: *J. Rheology* 24 (1980), p. 603.

[16] B. J. Cantwell. "Organized motion in turbulent flow". In: *Annual Review of Fluid Mechanics* 13 (1981), pp. 457–515.

[17] P. Chakraborty et al. "On the relationships between local vortex identification schemes". In: *Journal of Fluid Mechanics* 535 (2005), pp. 189–214.

[18] M.S. Chong, A.E. Perry, and B.J. Cantwell. "A general classification of three-dimensional flow field". In: *Physics of Fluids* 2 (1990), pp. 765–777.

[19] V. Dallas, J. C. Vassilicos, and G. F. Hewitt. "Strong polymer–turbulence interactions in viscoelastic turbulent channel flow". In: *Physical Review E* 82 (2010), pp. 066303–1–066303–19.

[20] E. De Angelis et al. "Drag reduction by a linear viscosity profile". In: *Physical Review E* 70 (2004), pp. 055301–1–055301–4.

[21] C. D. Dimitropoulos et al. "Direct numerical simulation of polymer-induced drag reduction in turbulent boundary layer flow". In: *Physics of Fluids* 17 (2005), pp. 1–4.

[22] Y. Dubief, V. E. Terrapon, and J. Soria. "On the mechanism of elasto-inertial turbulence". In: *Physics of Fluids* 25 (2013), pp. 110817–1–110817–16.

[23] Y. Dubief et al. "New Answers on the Interaction Between Polymers and Vortices in Turbulent Flows". In: *Flow, Turbulence and Combustion* 74 (2005), pp. 311–329.

[24] Y. Dubief et al. "On the coherent drag-reducing and turbulence-enhancing behaviour of polymers in wall flows". In: *J. Fluid Mech* 514 (2004), pp. 271–280.

[25] M. P. Escudier, F. Presti, and S. Smith. "Drag reduction in the turbulent pipe flow of polymers". In: *Journal of Non-Newtonian Fluid Mechanics* 81 (1999), pp. 197–213.

[26] M. P. Escudier et al. "Turbulent flow of viscoelastic shear-thinning liquids through a rectangular duct: Quantification of turbulence anisotropy". In: *Journal of Non-Newtonian Fluid Mechanics* 160 (2009), pp. 2–10.

[27] A. G. Fabula. "Fire-fighting benefits of polymeric friction reduction". In: *Trans ASME J Basic Engng* (1971), pp. 93–453.

[28] F. Forrest and G. A. Grierson. "Friction losses in cast iron pipe carrying paper stock". In: *Paper Trade Journal* 92 (1931), pp. 39–41.

[29] J. Golda. "Hydraulic transport of coal in pipes with drag reducing additives". In: *Chem Engng Commun* 45 (1986), pp. 53–67.

[30] M. D. Graham. "Drag reduction and the dynamics of turbulence in simple and complex fluids". In: *Physics of Fluids* 26 (2014), pp. 101301–1–101301–24.

[31] M. D. Graham. "Turbulence spreads like wildfire". In: *Nature* 526 (2015), pp. 508–509.

[32] H. L. Greene, R. F. Mostardi, and R. F. Nokes. "Effects of drag reducing polymers on initiation of atherosclerosis". In: *Polym Engng Sci* (1980), pp. 20–449.

[33] A. Gyr and T. Tsinober. "On the rheological nature of drag reduction phenomena". In: *Journal of Non-Newtonian Fluid Mechanics* 73 (1995), pp. 153–162.

[34] G. Haller. "An objective definition of a vortex". In: *Journal of Fluid Mechanics* 525 (2005), pp. 1–26.

[35] J. M. Hamilton, J. Kim, and F. Waleffe. "Regeneration mechanism of nea-wall turbulence structures". In: *Journal of Fluid Mechanics* 287 (1995), pp. 317–348.

[36] H. C. Hershey and J. L. Zakin. "A molecular approach to predicting the onset of drag reduction in the turbulent flow of dilute polymer solutions". In: *Chemical Engineering Science* 22 (1967), pp. 184–187.

[37] S. Hoyas and J. Jiménez. "Scaling of the velocity fluctuations in turbulent channels up to $Re_\tau = 2003$". In: *Physics of Fluids* 18 (2006), pp. 011702–1–011702–4.

[38] J. C. R. Hunt, A. A. Wray, and P. Moin. "Eddies, stream, and convergence zones in turbulent flows". In: *Center for Turbulence Research - Proceedings of Summer Program* Report CTR-S88 (1988), pp. 193–208.

[39] A.K.M.F. Hussain. "Coherent structures–reality and myth". In: *Physics of Fluids* 26(10) (1983), pp. 2816–2850.

[40] A.K.M.F. Hussain. "Coherent structures–reality and myth". In: *Journal of Fluid Mechanics* 173 (1986), pp. 303–356.

[41] J. Jeong and F. Hussain. "On the identification of a vortex". In: *Journal of Fluid Mechanics* 285 (1995), pp. 69–94.

[42] J. Jiménez and A. Pinelli. "The autonomous cycle of near-wall turbulence". In: *Journal of Fluid Mechanics* 389 (1999), pp. 335–359.

[43] D. D. Joseph. *Fluid Dynamics of Viscoelastic Liquids*. New York: Springer Verlag, 1990.

[44] V. N. Kalashnikov. "Dynamical similarity and dimensionless relations for turbulent drag reduction by polymer additives". In: *Journal of Non-Newtonian Fluid Mechanics* 75 (1998), pp. 209–230.

[45] J. Kim, P. Moin, and R. Moser. "Turbulence statistics in fully developed channel flow at low Reynolds number". In: *Journal of Fluid Mechanics* 177 (1987), pp. 133–166.

[46] K. Kim et al. "Effects of polymer stresses on eddy structures in drag-reduced turbulent channel flow". In: *Journal of Fluid Mechanics* 584 (2007), pp. 281–299.

[47] K. Kim et al. "Effects of polymer stresses on eddy structures in drag-reduced turbulent channel flow". In: *Physics of Fluids* 100 (2008), pp. 134504–1–134504–4.

[48] O. Kitoh and M. Umeki. "Experimental study on large-scale streak structure in the core region of turbulent plane Couette flow". In: *Physics of Fluids* 20 (2008), pp. 025107–1–025107–11.

[49] J. Komminaho, A. Lundbladh, and A. Johansson. "Very large structures in plane turbulent Couette flow". In: *Journal of Fluid Mechanics* 320 (1996), pp. 259–285.

[50] A. G. Kravchenko, H. Choi, and P. Moin. "On the relation of near-wall streamwise vortices to wall skin friction in turbulent boundary layers". In: *Physics of Fluids A* 5 (1993), pp. 3307–3309.

[51] J. L. Lumley. "Drag Reduction in Turbulent Flow by Polymer Additives". In: *Journal of Polymer Science: Macromolecular Reviews* 7 (1973), pp. 263–290.

[52] J. L. Lumley. "Drag reduction by additives". In: *Annual Review of Fluid Mechanics* 11 (1969), pp. 367–384.

[53] V. S. L'vov et al. "Drag reduction by polymers in wall bounded turbulence". In: *Physical Review Letters* 92 (2004), pp. 244503–1–244503–4.

[54] R. S. Martins et al. "An objective perspective for classic flow classication criteria". In: *Comptes Rendus Mecanique* 344 (2016), pp. 52–59.

[55] M. Masoudian et al. "A viscoelastic k-eps-v2-f turbulent flow model valid up to the maximum drag reduction limit". In: *Journal of Non-Newtonian Fluid Mechanics* 202 (2013), pp. 99–111.

[56] M. Masoudian et al. "Reynolds-averaged modeling of polymer drag reduction in turbulent flows". In: *Journal of Non-Newtonian Fluid Mechanics* 165 (2010), pp. 376–384.

[57] K. Melnikov, T. Kreilos, and B. Eckhardt. "Long-wavelenght instability of coherent structures in plane Couette flow". In: *Physical Review E* 89 (2014), pp. 043008–1–043008–8.

[58] E. W. Merrill and A. F. Horn. "Scission of macromelecules in dilute solution: Extensional and turbulent flows". In: *Polymer Communications* 25 (1984), pp. 144–146.

[59] T. Min et al. "Drag reduction by polymer additives in a turbulent channel flow". In: *Journal of Fluid Mechanics* 486 (2003), pp. 213–238.

[60] T. Moussa and C. Tiu. "Factors affecting polymer degradation in turbulent pipe flow". In: *Chemical Engineering Science* 49 (1994), pp. 1681–1692.

[61] K. J. Mysels. "Flow of thickened fluids". In: *U.S. Patent* 2 Dec. 27 492 (1949), p. 173.

[62] P. Orlandi. "A tentative approach to the direct simulation of drag reduction by polymers". In: *Journal of Non-Newtonian Fluid Mechanics* 60 (1996), pp. 277–301.

[63] R. W. Paterson and F.H. Abernathy. "Turbulent flow drag reduction and degradation with dilute polymer solutions". In: *J. Fluid Mech* 43 (1970), pp. 689–710.

[64] A. S. Pereira, R. M. Andrade, and E. J. Soares. "Drag reduction induced by flexible and rigid molecules in a turbulent flow into a rotating cylindrical double gap device: Comparison between Poly (ethylene oxide), Polyacrylamide, and Xanthan Gum". In: *Journal of Non-Newtonian Fluid Mechanics* 202 (2013), pp. 72–87.

[65] A. S. Pereira and E. J. Soares. "Polymer degradation of dilute solutions in turbulent drag reducing flows in a cylindrical double gap rheometer device". In: *Journal of Non-Newtonian Fluid Mechanics* 179 (2012), pp. 9–22.

[66] A. S. Pereira et al. "Active and hibernating turbulence in drag reducing plane Couette flows". In: *Under consideration for publication in Physical Review Fluids* (2016).

[67] A. S. Pereira et al. "Analyses statistiques et tensorielles de l'étirement des polymères dans les écoulements viscoélastiques turbulents en canal plan". In: *Rhéologie* 27 (2015), pp. 34–42.

[68] A. S. Pereira et al. "Drag reducing flows considering the effects of polymer degradation". In: *to be submitted to Physics of Fluids* (2016).

[69] A. S. Pereira et al. "Elliptical, parabolic, and hyperbolic exchanges of energy in drag reducing plane Couette flows". In: *Under consideration for publication in Physics of Fluids* (2016).

[70] A. S. Pereira et al. "On the drag reducing plane Couette flows". In: *Under consideration for publication in Journal of Non-Newtonian Fluid Mechanics* (2016).

[71] A. S. Pereira et al. "Statistics and tensor analysis of polymer coil-stretch mechanism in turbulent drag reducing channel flow". In: *Under consideration for publication in Journal of Fluid Mechanics* (2016).

[72] A. S. Pereira et al. "Transient aspects of drag reducing plane Couette flows". In: *Under consideration for publication in Journal of Non-Newtonian Fluid Mechanics* (2016).

[73] A. Peterlin. "Streaming birefringence of soft linear macromolecules with finite chain length". In: *Polymer* 2 (1961), pp. 257–291.

[74] F. T. Pinho and J. H. Whitelaw. "Flow of Non-Newtonian flluids in a pipe". In: *Journal of Non-Newtonian Fluid Mechanics* 34 (1990), pp. 129–144.

[75] S. Pirozzoli, M. Bernardini, and P. Orlandi. "Large-scale motions and inner/outer layer interactions in turbulent Couette-Poiseuille flows". In: *Journal of Fluid Mechanics* 680 (2011), pp. 534–563.

[76] I. Procaccia, V. S. L'vov, and R. Benzi. "Colloquium: Theory of drag reduction by polymers in wall-bounded turbulence". In: *Reviews of Modern Physics* 80 (2008), pp. 225–247.

[77] P. K. Ptasinski et al. "Experiments in turbulent pipe flow with polymer additives at maximum drag reduction". In: *Flow, Turbulence and Combustion* 66 (2001), pp. 159–182.

[78] S. Robinson. "Coherent motions in the turbulent boundary layer". In: *Annual Review of Fluid Mechanics* 23 (1991), pp. 601–639.

[79] G. Ryskin. "Turbulent drag reduction by polymers: A quantitative theory". In: *Physical Review Letters* 59 (1987), pp. 2059–2062.

[80] R. H. J. Sellin et al. "The effect of drag reducing additives on fluid flows and their industrial applications Part II: Present applications and future proposals". In: *Journal of Hydraulic Research* 20 (1982), pp. 235–292.

[81] F. A. Seyer and A. B. Metzner. "Turbulence phenomena in drag reducing systems". In: *AIChE Journal* 15 (1969), pp. 426–434.

[82] E. J. Soares et al. "Loss of efficiency of polymeric drag reducers induced by high Reynolds number flows in tubes with imposed pressure". In: *Physics of Fluids* 27 (2015), pp. 125105–1–125105–23.

[83] R. Sureshkumar, A. N. Beris, and R. A. Handler. "Direct numerical simulation of the turbulent channel flow of a polymer solution". In: *Physics of Fluids* 9 (1997), pp. 743–755.

[84] M. Tabor and P. G. de Gennes. "A cascade theory of drag reduction". In: *Europhysics Letter* 2 (1986), pp. 519–522.

[85] S. Tamano, M. D. Graham, and Y. Morinishi. "Streamwise variation of turbulent dynamics in boundary layer flow of drag-reducing fluid". In: *Journal of Fluid Mechanics* 686 (2011), pp. 352–377.

[86] L. Thais, T. B. Gatski, and G. Mompean. "Analysis of polymer drag reduction mechanisms from energy budgets". In: *International Journal of Heat and Fluid Flow* 43 (2013), pp. 52–61.

[87] L. Thais, T. B. Gatski, and G. Mompean. "Some dynamical features of the turbulent flow of a viscoelastic fluid for reduced drag". In: *Journal of Turbulence* 13 (2012), pp. 1–26.

[88] L. Thais, T. B. Gatski, and G. Mompean. "Spectral analysis of turbulent viscoelastic and Newtonian channel flows". In: *Journal of Non-Newtonian Fluid Mechanics* 200 (2013), pp. 165–176.

[89] L. Thais et al. "A massively parallel hybrid scheme for direct numerical simulation of turbulent viscoelastic channel flow". In: *Computers and Fluids* 43 (2011), pp. 134–142.

[90] L. Thais et al. "Temporal large eddy simulation of turbulent viscoelastic drag reduction flows". In: *Physics of Fluids* 22 (2010), p. 013103.

[91] R. L. Thompson, R. D. A. Bacchi, and F. J. Machado. "What is a vortex?" In: *Proceedings of the 20th International Congress of Mechanical Engineering (COBEM), Gramado-RS, Brazil* (2009).

[92] Roney L. Thompson. "Flow classification for viscoelastic materials". In: *International Journal of Advances in Engineering Sciences and Applied Mathematics* 1 (2009), pp. 69–83.

[93] B. A. Toms. "Some Observations on the flow of linear polymer solutions through straight tubes at large Reynolds numbers". In: *Proceedings of the International Congress of Rheology, Holland, North-Holland, Amsterdam, Section II* (1948), pp. 135–141.

[94] J. M. J. den Toonder, F. T. M. Nieuwstadt, and G. D. C. Kuiken. "The role of elongational viscosity in the mechanism of drag reduction by polymer additives". In: *Applied Scientific Research* 54 (1995), pp. 95–123.

[95] P. S. Virk. "Drag reduction by collapsed and extended polyelectrolytes". In: *Nature* 253 (1975), pp. 109–110.

[96] P. S. Virk. "Drag reduction fundamentals". In: *AIChE Journal* 21 (1975), pp. 625–656.

[97] P. S. Virk, H. S. Mickley, and K. A. Smith. "The Toms phenomenom: Turbulent pipe flow of dilute polymer solutions". In: *Journal of Fluid Mechanics* 22 (1967), pp. 22–30.

[98] P. S. Virk, H. S. Mickley, and K. A. Smith. "The ultimate asymptote and mean flow structure in Toms' phenomenon". In: *ASME-Journal of Applied Mechanics* 37 (1970), pp. 488–493.

[99] M. D. Warholic, H. Massah, and T. J. Hanratty. "Influence of drag-reducing polymers on turbulence: Effects of Reynolds number, concentration and mixing". In: *Experiments in Fluids* 27 (1999), pp. 461–472.

[100] T. Wei and W. W. Willmarth. "Modifying turbulent structure with drag-reducing polymer additives in turbulent channel flows". In: *Journal of Fluid Mechanics* 245 (1992), pp. 619–641.

[101] J. Weiss. "The dynamics of enstrophy transfer in 2-dimensional hydrodynamics". In: *Physica D* 48 (1991), pp. 273–294.

[102] C. M. White and M. G. Mungal. "Mechanics and Prediction of Turbulent Drag Reduction Whit Polymer Additives". In: *Annual Review of Fluid Mechanics* 40 (2008), pp. 235–256.

[103] C. M. White, V. S. R. Somandepalli, and M. G. Mungal. "The turbulence structure of drag-reduced boundary layer flow". In: *Experiments in Fluids* 36 (2004), pp. 62–69.

[104] C. M. White et al. "Re-examining the logarithmic dependence of the mean velocity distribution in polymer drag reduced wall-bounded flow". In: *Physics of Fluids* 24 (2012), pp. 021701–1–021701–6.

[105] L. Xi and M. D. Graham. "Active and hibernating turbulence in minimal channel flow of Newtonian and polymerc fluids". In: *Physical Review Letters* 104 (2010), pp. 218301–1–218301–4.

[106] L. Xi and M. D. Graham. "Dynamics on the laminar-turbulent boundary and the origin of the maximum drag reduction asymptote". In: *Physical Review Letters* 647 (2012), pp. 028301–1–028301–5.

[107] J. Zhou et al. "Mechanisms for generating coherent packets of hairpin vortices in channel flow". In: *Journal of Fluid Mechanics* 387 (1999), pp. 353–396.

Contents

Transient aspects of the polymer induced drag reduction phenomenon

Abstract

The addition of a small amount of polymers of high molecular weight can lead to a pressure drop decrease in turbulent flows. Over the years, numerous experimental and numerical studies have been conducted in attempts to make practical use of polymer-induced drag reduction, including long-distance transport of liquids, oil well operations, firefighting, transport of suspensions and slurries, and biomedical applications. The polymers successively stretch and coil by interacting with the turbulent structures, which changes the turbulent flow and further imposes a transient behaviour on the drag reduction (DR) as well as the subsequent mechanical polymer degradation. As a result, DR undergoes at least three stages over time: A, B, and C. In stage A, referred to as the *developing time*, DR departs from zero and assumes negative values due to a significant polymer stretching at the beginning of the process, which requires energy from the flow. After the minimum DR is reached, the polymers start their coil-stretch cycle and, in consequence, DR increases in response to the development of turbulent structures, achieving a maximum value, which makes for the beginning of stage B. However, during their coil-stretch cycle, polymers can be mechanically degraded as a result of an intense polymer stretching, which reduces their ability to act as energy exchange agents. Hence, when polymer degradation becomes pronounced, DR decreases until achieving a final value which indicates that the degradation has stopped and the molecular weight distribution has reached a steady state. The polymer degradation process characterizes the stage C. In the present work, numerical analyses are conducted aiming to investigate the stages A, B and C. The transient aspects of the polymer induced drag reduction phenomenon are explored with the aid of direct numerical simulations of turbulent plane Poiseulle and Couette flows of viscoelastic FENE-P fluids taking into account a wide range of Reynolds number, Weissenberg number and maximum polymer molecule extensibility. Stages A and B are carefully studied from tensor, statistical, energy budget and spectral perspectives. Additionally, a new and simple polymer scission model based on the molecule strain level is developed in order to numerically reproduce the stage C. It is found that the significant transient behaviour of DR within stage A is related to important exchanges of energy between the polymers, the mean flow and the turbulent structures, which is accentuated as the elasticity increases. In stage B, the dynamics of the flow is described by an autonomous regeneration cycle. The effects of polymers on such a cycle are attenuated by the molecules degradation during the stage C.

Keywords: direct numerical simulation, turbulent flow, fene-p model, drag reduction, transitory aspects, polymer degradation.

Laboratoire de Mécanique de Lille (LML)
Av. Paul Langevin – Cité Scientifique – 59650 Villeneuve d'Ascq – France

Des aspects transitoires du phénomène de réduction de la traînée induite par des polymères

Résumé

La dilution en très faible concentration de chaînes polymériques longues dans un fluide newtonien peut réduire considérablement la traînée turbulente, phénomène nommé ici DR (*drag reduction*). Au cours des dernières années, de nombreuses études expérimentales et numériques ont été menées motivées par les applications pratiques de la DR, à savoir le transport à grandes distances des liquides par pipelines, le transport des boues et des suspensions et des applications médicales. Les polymères s'étirent et s'enroulent successivement, en interaction avec les structures turbulentes, ce qui modifie l'écoulement turbulent, imposant à DR un comportement transitoire et provoquant la dégradation polymérique. Il en résulte que la DR traverse au moins trois stades. Lors du premier, connu sous le nom de temps de développement, la DR démarre à zéro et descend à des valeurs négatives en raison d'un étirement considérable du polymère au début du processus, ce qui exige de l'énergie de l'écoulement. Une fois atteint le niveau minimal de réduction de la traînée, les polymères commencent leur cycle d'étirement-enroulement et, par conséquent, la DR augmente en réponse au développement de structures turbulentes, pour en arriver à une valeur maximale, menant au début du deuxième stade. Cependant, lors de leur cycle d'étirement-enroulement, les polymères peuvent subir une dégradation mécanique à la suite d'un étirement polymérique intense, ce qui réduit leurs capacités de servir d'agents d'échange d'énergie. Lorsque la dégradation polymérique devient assez prononcée, la DR redescend pour atteindre une valeur finale qui indique que la dégradation s'est arrêtée et que la distribution de la masse moléculaire s'est stabilisée. Le processus de dégradation polymérique caractérise le troisième stade. Dans le présent travail, des analyses numériques ont été menées dans le but d'examiner ces trois stades. Les aspects transitoires du phénomène de réduction de la traînée induite par des polymères sont explorés à l'aide de simulations numériques directes d'écoulements turbulents viscoélastiques FENE-P en géométries du type Poiseuille plan et Couette plan, sur un large éventail de nombres de Reynolds, de nombres de Weissenberg et d'extension maximale de la chaîne polymérique. Les deux premiers stades sont soigneusement étudiés à partir des analyses tensorielle, statistique, énergétique et spectrale. De surcroît, un nouveau modèle de dégradation polymérique basé sur le niveau d'étirement des molécules est proposé afin de reproduire numériquement le stade final. Il a été constaté que le comportement transitoire significatif de la DR lors du premier stade est lié à d'importants échanges d'énergie entre les polymères, l'écoulement moyen et les structures turbulentes, s'intensifiant à mesure que l'élasticité augmente. Lors du deuxième stade, la dynamique de l'écoulement est décrite par un cycle de régénération autonome. Les effets des polymères sur ce cycle s'atténuent par la dégradation moléculaire qui survient lors du troisième stade.

Mots clés : simulation numérique directe, écoulement turbulent, modèle fene-p, réduction de la traînée, aspects transitoires, dégradation du polymère.